NONDESTRUCTIVE LEVEL III DAMAGE EVALUATION AND SYSTEM IDENTIFICATION IN STRUCTURES BASED ON THE RATE OF THE TOTAL ENERGY

A Dissertation

by

ARASH SABZ

Submitted to the Office of Graduate and Professional Studies of
Texas A&M University
in partial fulfillment of the requirements for the degree of

DOCTOR OF PHILOSOPHY

Chair of Committee, J. N. Reddy
Committee Members, Luciana R. Barroso
Mary Beth D. Hueste
John Edward Hurtado
Head of Department, Robin Autenrieth

May 2015

Major Subject: Civil Engineering

ABSTRACT

Nondestructive damage detection methods provide beneficiary bases for planning an economical maintenance program for structures. Economically, detecting and repairing structural damages in their initial stage is desirable, and moreover it may prevent occurrences of disastrous losses especially in areas susceptible to hazardous loads such as earthquakes. Therefore, development of a general damage detection method that alarms degradations of structural properties is of interest.

In this dissertation, a level III non-destructive damage evaluation method, called DITER, is developed based on tracking the rate of the mechanical energy of a structural system. The objective is to simultaneously detect and size variations in the element-wise mass, stiffness, and damping characteristics of a structure, utilizing dynamic response data of the system. The effect of the proportional and non-proportional types of the inherent damping of the structure in the form of viscous resistance to strain of the material and Rayleigh damping, as well as the effect of passive seismic protective devices are considered in the method. Moreover, an iterative algorithm is proposed for the cases with missing load data

A sub-system approach is developed to make DITER applicable to a specific part of a structure. The advantages of this approach are limiting the excitations to the interested area only, and making DITER an appropriate option for structures with seismic protective systems.

While the method is applicable to a general structure, in this dissertation, it is explicitly developed for shear building models as well as for two-dimensional beams and frames. To address the geometrical non-linearity, an extended version of DITER is developed employing von Kármán nonlinearity. Several numerical verifications are presented to study the DITER performance under different types of supports, loadings, and damping characteristics as well as to consider the effects of the type, intensity, and geometry of the imposed damages. In addition, dynamic properties of a three-story office

building are used to experimentally verify the DITER ability in detecting deteriorations in the structural stiffness.

DEDICATION

To my parents and my dear wife

ACKNOWLEDGEMENTS

I would like to express my deepest gratitude to my research advisor, Professor J. N. Reddy, for his great support and invaluable advices throughout this work and also throughout my studies in Texas A&M University. I wish to thank the members of my PhD committee Professors Mary Beth D. Hueste, John E. Hurtado, and Luciana R. Barroso for their helpful suggestions during completion of this dissertation. Moreover, the support of California Department of Transportation to this work is highly acknowledged.

I also wish to acknowledge my former adviser, late Professor Norris Stubbs, whose guidance and advice had been key factors toward the completion of this research.

I would like to give special thanks to Professors John Niedzwecki for his support in the time it was most needed, and I also would like to show my gratitude to Doctor Rashid K. Abu Al-Rub for his guidance at the initial state of my PhD study.

Finally, I am most thankful to my parents and my dear wife who always unconditionally offered me their kindest support.

TABLE OF CONTENTS

Page

ABSTRACT ii

DEDICATION iv

ACKNOWLEDGEMENTS v

TABLE OF CONTENTS vi

LIST OF FIGURES ix

LIST OF TABLES xiv

CHAPTER I INTRODUCTION AND LITERATURE REVIEW 1

- Problem Statement 1
- Background 2
  - Overview 2
  - Review of the Relevant Literature 4
- Shortcomings of the Current Damage Detection Methods 15
- Dissertation Objectives 17
- Significance of the Proposed Work 17
- Organization of the Dissertation 18

CHAPTER II DAMAGE IDENTIFICATION BASED ON THE TOTAL ENERGY RATE 19

- Introduction 19
- Theory of the Proposed Method 20
  - Background 20
  - Derivation of the DITER Equation 21
- Solution of the DITER Equation 28
  - Solution of the DITER Equation for Known Forces 28
  - Contribution of Static Deflections in DITER 32
  - Solution of the DITER Equation with Limited Input Data 34

Page

Damage Index Vector....40
Summary....41

CHAPTER III APPLICATION OF THE DITER METHOD TO SHEAR BEAM STRUCTURES....42

Introduction....42
DITER Equation for Shear Beam Models....42
Problem Formulation....42
Assessment of DITER via Numerical Example Experiments....47
Description of the Test Model....47
Description of the Studied Cases....50
Results and Discussions....53
Summary....80

CHAPTER IV APPLICATION OF THE DITER METHOD TO EULER BERNOULI BEAMS AND FRAMES....82

Introduction....82
DITER Equation for Euler Bernoulli Beams and Frames....82
Part I: Beams....83
Beams with Small Strains and Small Transverse Displacements....83
Beam with Small Strains and Large Rotations....95
Unknown Mass Modification for the Total Displacement Measurement....102
Part II: Frames....104
DITER for Frames....104
DITER for Sub-Systems....105
DITER for Frames Equipped with Isolators and Dampers....111
Summary....122

CHAPTER V ASSESSMENT OF DITER VIA NUMERICAL EXAMPLE EXPERIMENTS....123

Introduction....123
Numerical Experiments....123
Simple Beam Experiment....123
Cantilever Beam Experiment....134
Two Span Beam Experiment....146
Frame Experiment....169
Summary....183

Page

CHAPTER VI DAMAGE DETECTION RESULTS USING EXPERIMENTAL MODAL PARAMETERS 184

Introduction 184
Experimental Data Acquisition 185
Description of the Structure 185
Modal Properties Identification 187
Data Generation 192
Results and Discussions 194
Summary 198

CHAPTER VII CONCLUSION AND FUTURE WORK 200

Summary and Conclusion 200
Future Work 202

REFERENCES 204

APPENDIX A SUPPORTIVE EQUATIONS OF CHAPTER IV 212

A-1: Derivation of Equations (4.48) and (4.50) 212
A-2: Interpolation Functions 215
A-3: Derivation of Equation (4.32) 215

APPENDIX B SUPPORTIVE EQUATIONS OF THE SIMPLE BEAM EXPERIMENT 217

B-1: Derivation of Mode Shapes and Natural Frequencies of a Simple Beam 217
B-2: Determination of Rayleigh Damping Constants 218

LIST OF FIGURES

Page

Figure II-1: Algorithm of the I-DITER method 39

Figure III-1: n-DOFs shear beam model 43

Figure III-2: Selected 7-story shear beam model 48

Figure III-3: Detected damages in the stories' stiffness of the shear beam model, Cases 0i, 0d 55

Figure III-4: Detected damages in the dashpots of the shear beam model, Cases 0i, 0d 56

Figure III-5: Detected damages in the masses of the shear beam model, Cases 0i, 0d 56

Figure III-6: Applied boundaries to the rate of the work (RoW) of case 1i, LNS is the rate of the work computed based on the last known structural properties 58

Figure III-7: Applied boundaries to the rate of the work (RoW) of case 1d, LNS is the rate of the work computed based on the last known structural properties 58

Figure III-8: Loads applied to the 2nd and 7th nodes, Case 1i 59

Figure III-9: Loads applied to the 2nd and 7th nodes, Case 1d 60

Figure III-10: DIV of story stiffness, Cases 1i and 1d 61

Figure III-11: DIV of dashpot constants, Cases 1i and 1d 62

Figure III-12: Variation in the identified loads of case 1i 63

Figure III-13: Variations in the identified loads of case 1d 63

Figure III-14: Convergence of the identified stories' stiffness values of case 1i 64

Figure III-15: Convergence of the identified stories' stiffness values of case 1d 65

Figure III-16: Convergence of the identified dashpot constants of case 1i 65

Figure III-17: Convergence of the identified dashpot constants of case 1d 66

Figure III-18: Top) Noiseless, Bottom) 1% noise-polluted displacement data at the 5th story, Case 0in 67

Figure III-19: Top) Noiseless, Bottom) 2% noise-polluted displacement data at the 5th story, Case 0id 67

Figure III-20: DIV of story stiffness 1% noise-polluted data 70

Figure III-21: DIV of dashpot constants, 1% noise-polluted data 70

Figure III-22: DIV of mass, 1% noise-polluted data 71

Figure III-23: DIV of story stiffness, 2% noise-polluted data 72

Figure III-24: DIV of dashpot constants, 2% noise-polluted data 73

Page

Figure III-25: DIV of mass, 2% noise-polluted data....73
Figure III-26: DIV of story stiffness, 5% noise-polluted data....75
Figure III-27: DIV of dashpot constants, 5% noise-polluted data....75
Figure III-28: DIV of mass, 5% noise-polluted data....76
Figure III-29: DIV of story stiffness for all of the noise intensities....76
Figure III-30: DIV of dashpot constants for all of the noise intensities....77
Figure III-31: DIV of mass for all of the noise intensities....77
Figure III-32: DIV of story stiffness using total and conventional least square based DITER, 3% noise-polluted data....79
Figure III-33: DIV of dashpot constants using total and conventional least square based DITER, 3% noise-polluted data....79
Figure III-34: DIV of mass using total and conventional least square based DITER, 3% noise-polluted data....80
Figure IV-1: Schematic view of a beam....84
Figure IV-2: Internal forces of a beam element, interior nodes are not shown....88
Figure IV-3: A DITER beam element with start node 1 and end note 2 whose local axis oriented with respect to the global coordinates.....103
Figure IV-4: Left) Schematic view of a frame with a sub-system showed by the dashed box Right) the sub-system separated from the system....106
Figure IV-5: Bilinear lateral force-displacement behavior of an isolator....114
Figure V-1: Schematic view of the one span beam....124
Figure V-2: The first three transverse mode shapes of the beam....126
Figure V-3: The sixth transverse mode shapes of the beam....127
Figure V-4: Displacement and velocity of the midpoint of the beam in case 1....128
Figure V-5: Nodes layout at which data are collected in case 1....128
Figure V-6: Sensors layout and excitation forces applied in case 2....129
Figure V-7: Loads applied to the beam in case 2....130
Figure V-8: Displacement and velocity of the middle point of the beam in case 2....130
Figure V-9: Mass identification results of the simple beam, Case 1....131
Figure V-10: Identification of the flexural rigidity of the simple beam, Case 1....131
Figure V-11: Mass identification results of the simple beam, Case 2....133

Page

Figure V-12: Identification of the flexural rigidity of the simple beam, Case 2 133
Figure V-13: The cantilever beam of the second experiment 135
Figure V-14: The normalized WGN load 136
Figure V-15: Velocity and displacement of the tip of the beam in the intact state 137
Figure V-16: Velocity and displacement of the tip of the beam in the damaged state 138
Figure V-17: Transverse displacements at the tip of the beam of the damaged state 139
Figure V-18: Identified EI of the intact state, Part 1 140
Figure V-19: Mass identification of the intact state, Part 1 141
Figure V-20: EI damage detection, Part 1 141
Figure V-21: Mass damage detection, Part 1 142
Figure V-22: Identified viscous damping coefficients, Part 1 142
Figure V-23: Identified EI of the intact state, Part 2 143
Figure V-24: Mass identification of the intact state, Part 2 143
Figure V-25: EI damage detection, Part 2 145
Figure V-26: Mass damage detection, Part 2 145
Figure V-27: Two-span beam 147
Figure V-28: Displacement and velocity responses at x=3m, Part 1 148
Figure V-29: Applied load to the beam of intact state, P_1) Load at x=1.6 m, P_2) Load at x=5m, P_3) Load at x=8.2m, Part 1 148
Figure V-30: Maximum displacement response of the beam located at x=3m, Part 2 149
Figure V-31: Identified stiffness of the intact state 150
Figure V-32: Errors in the identified stiffness of the intact state 151
Figure V-33: Identified mass of the intact state 151
Figure V-34: Errors in the identified mass of the intact state 152
Figure V-35: Identified viscous damping coefficients of the intact state 152
Figure V-36: Identified transverse displacement viscous damping coefficients of the intact state 152
Figure V-37: EI damage detection 153
Figure V-38: Mass damage detection 154
Figure V-39: Identified viscous damping coefficients of the damaged state 154

Page

Figure V-40: Identified transverse displacement viscous damping coefficients of the damaged state....154
Figure V-41: EI damage identification using total displacement data....155
Figure V-42: Sub-system of the two-span beam....155
Figure V-43: Identified stiffness of the sub-system, intact state....156
Figure V-44: Errors in the identified stiffness of the sub-system, intact state....156
Figure V-45: Identified mass of the sub-system, intact state....157
Figure V-46: Errors in the identified mass of the sub system, intact state....157
Figure V-47: Identified viscous damping coefficients of the sub-system, intact state ..158
Figure V-48: Identified transverse displacement viscous damping coefficients of the sub-system, intact state....158
Figure V-49: EI damage identification for the sub-system....159
Figure V-50: Mass damage identification for the sub-system....159
Figure V-51 : Identified viscous damping coefficients of the sub-system, damaged state....160
Figure V-52: Identified transverse displacement viscous damping coefficients of the sub-system, damaged state....160
Figure V-53: Maximum dynamic responses of the beam with Rayleigh damping....161
Figure V-54: EI damage identification of the beam with Rayleigh damping....162
Figure V-55: Mass damage identification of the beam with Rayleigh damping....163
Figure V-56: Static transverse deflection and maximum dynamic transverse deflection of the damaged state of the beam....164
Figure V-57: Transverse static and dynamic displacements for: Top) node 14, Middle) node 15, Bottom) node 16....164
Figure V-58: Stiffness damage identification based on data measured from static equilibrium configuration of the intact state....165
Figure V-59: Mass damage identification based on data measured from static equilibrium configuration of the intact state....165
Figure V-60: Stiffness damaged identification considering static deflections, Part 4 ...166
Figure V-61: Mass damaged identification considering static deflections, Part 4....167
Figure V-62: EI damaged identification considering static deflections, Case 2 of part 5....168

Page

Figure V-63: Mass damaged identification considering static deflections, Case 2, Part 5 168
Figure V-64: One bay frame with isolators and external damper.. 170
Figure V-65: the White Gaussian Noise applied to the frame experiment 174
Figure V-66: Axial rigidity identification of the beam of the sub system, Intact State . 176
Figure V-67: Flexural rigidity identification of the sub system, Intact State 176
Figure V-68: Nodal mass identification of the sub system 177
Figure V-69: Identified effective stiffness of the damper 177
Figure V-70: Identified effective viscous coefficient of the damper 178
Figure V-71: Axial rigidity damage detection of beam elements 179
Figure V-72: Flexural rigidity damage detection 179
Figure V-73: Nodal mass damage detection 180
Figure V-74: Identified shear force-displacement behavior of the isolator based on the identified properties of element number 1 181
Figure VI-1: Lay out of the experimental model, recreated from (Bracci 1992) 186
Figure VI-2: Section 2-2 of the experimental building, recreated from (Bracci 1992).. 187
Figure VI-3: Three story shear beam model of the experimental model 192
Figure VI-4: Applied loads to the experimental model, Top) at first floor, Middle) at second floor, Bottom) at third floor 193
Figure VI-5: Provided and identified story stiffness values of the intact state 195
Figure VI-6: Provided and identified equivalent viscous damping of the intact state ... 195
Figure VI-7: Provided and identified mass values of the intact state 196
Figure VI-8: Measured damage (DP), and identified (DIV) damages of the stiffness of the slightly damaged state 197
Figure VI-9: Measured damage (DP), and identified (DIV) damages of the stiffness of the moderately damaged state 197
Figure VI-10: Measured damage (DP), and identified (DIV) damages of the stiffness of the heavily damaged state 198

LIST OF TABLES

Page

Table III-1: Structural properties and applied excitations in the intact states 48
Table III-2: Structural properties and applied excitations in the damaged states 49
Table III-3: Natural frequencies of the 7-story shear beam model in the intact state 49
Table III-4: Natural frequencies of the 7-story shear beam model in the damaged states 50
Table III-5: Applied damages to the 7-story shear beam model 51
Table III-6: The last known properties of the 7-story shear beam 52
Table III-7: Detected damages in the story stiffness, Cases 0i and 0d 54
Table III-8: Detected damages in the dashpots, Cases 0i and 0d 54
Table III-9: Detected damages in the nodal mass, Cases 0i and 0d 55
Table III-10: Detected damages in the stories' stiffness, Cases 1i and 1d 60
Table III-11: Detected damages in dashpot constants, Cases 1i and 1d 61
Table III-12: Detected damages in the story stiffness, Cases 0i & 0d, 1% noise intensity 69
Table III-13: Detected damages in the dashpots, Cases 0i & 0d, 1% noise intensity 69
Table III-14: Detected damages in mass values, Cases 0i & 0d, 1% noise intensity 69
Table III-15: Detected damages in the stiffness, Cases 0i and 0d, 2% noise intensity 71
Table III-16: Detected damages in the dashpots, Cases 0i & 0d, 2% noise intensity 72
Table III-17: Detected damages in the mass values, Cases 0i & 0d, 2% noise intensity 72
Table III-18: Detected damages in the stiffness, Cases 0i and 0d, 5% noise intensity 74
Table III-19: Detected damages in the dashpots, Cases 0i & 0d, 5% noise intensity 74
Table III-20: Detected damages in the mass values, Cases 0i & 0d, 5% noise intensity 74
Table V-1: Properties of the one span beam 124
Table V-2: The first six natural frequencies of the beam 127
Table V-3: The first six damped frequencies of the beam 129
Table V-4: Identification results of the Rayliegh damping constants, Case 2 133
Table V-5: Properties of the cantilever beam 136
Table V-6: Location, severity, and type of damages of the two-span beam 149
Table V-7: Rayleigh damping coefficient identification, part 4 161

Page

Table V-8: Damping coefficient identification, Case 2 of part 5 168
Table V-9: Properties of the section used in the frame experiment 171
Table V-10: Properties of the isolator 172
Table V-11: Element wise damaged percent values 172
Table V-12: Nodal mass damage values 172
Table VI-1: Provided data for the intact state, source (Bracci 1992) 191
Table VI-2: Provided data for the minor damaged state, source (Bracci 1992) 191
Table VI-3: Provided data for the moderate damaged state, source (Bracci 1992) 191
Table VI-4: Provided data for the severe damaged state, source (Bracci 1992) 191

CHAPTER I
INTRODUCTION AND LITERATURE REVIEW

PROBLEM STATEMENT

Structural integrity assurance is a main concern when structural health is likely to be impaired. After any severe loading incident, such as earthquakes, reoccupation of buildings or reoperation of factories should be subjected to a structural performance assessment. This operation demands intense inspections that are usually time consuming processes. The larger the impacted region, the more time is needed to evaluate the current state of structures. In these cases, the cost of the inspection process is negligible to the expenses of keeping the assets nonfunctional. Hence, development of promising damage detection methods not only can save lives but also may decrease potential economic losses.

Since structures are designed for a designated lifetime utilization, decisions must be made regarding the remaining useful life of the structure. If reliability of the structure can be estimated continuously in a satisfactory manner, then the replacement could be postponed to a later time. The benefits of such analyses will be more obvious when components of infrastructures such as bridges, dams, or massive offshore drilling units are of concern. Likewise, a reliability check of the structures of a tolerant design philosophy is inevitable. Therefore, implementation of a robust health monitoring system would be beneficial.

Amongst other methods, nondestructive damage evaluation (NDE) is considered one of the most welcome methods to monitor and assess structural integrity. Any method that is capable of detecting damages in a structure without introducing any further damages is called an NDE method. NDEs may be applied continuously to locate damages and thus, provide a narrow resolution of the in-demand parts of the structure without initiating or aggravating any possible damages.

The final goal of implementing NDE to a system is to provide a framework based on which decisions can be made about the current state of the system as well as about

predicting the future maintenance. These decisions may include doing nothing, repairing the structure, or replacing the structure. However, the success is inherently dependent on the accuracy and capability of the adopted NDE approach. This capability is heavily dependent on the performance of the employed damage detection method (DDM) of the NDE. If the applied DDM identifies different types of damages such as reduction in mass or stiffness in structural component or isolators, then the utilized NDE method will be more practical and effective. Thus, after nearly 30 years of intense study in this area, research still continues in developing more sophisticated damage detection and evaluation methods.

BACKGROUND

Overview

Before studying NDE methods, it is necessary to define "damage". Extensive literature is available that has studied and classified different kinds of damages in structural components. In general, damage is any changes in a system that adversely affects the system performance. This includes changes in the material and geometrical properties of the system such as stiffness, mass, boundary conditions and system connectivity (Farrar and Worden 2007). Thus, the damage is directly related to the reliability of a system and its diagnosis is critical to identifying system performance. A further restricted definition of damage is offered by Worden and Dulieu-Barton (2004) where they define it as a state in which structure is still usable but in a suboptimal manner. For numerical implementation, however, it is common to address structural damages by reducing the modulus of elasticity or damping coefficients of members and isolators (Jauregui 1998 ; Stubbs et al. 1990; Stubbs and Osegueda 1990). Correspondingly, it is also common to make cuts in sections of structural components to simulate damages (Farrar and Jauregui 1998; Tang et al. 2012; Wang and Qiao 2007) in controlled field experiments.

Mostly, DDMs demand a base state, called the undamaged system, against which they can track degradations in structural parameters. An undamaged system may be defined as the initial constructed system whose performance is assumed to be satisfactory.

This definition may be extended further to the last known state of a system with an acceptable performance.

Intense literature is available in DDMs. Thus, it is more convenient to classify the current developed methods into groups and study characteristic of each. Currently, methods of damage detection utilized in NDEs can be classified into local and global methods. Based on the employed instruments, local methods such as x-ray and ultra-sonic, are capable of detecting damages of different types and severity. However, they demand dense sensor layouts and hence are merely practical in specific locations. In addition, the prospect area should be known approximately and be accessible. In contrast, global methods need less sensor instruments and can be applied to a large portion of a structure. In general, one may use local, global, or a combination of the methods based on the dimension of a structure in order to perform NDEs in an economic way.

Global methods may be further classified into static and vibration-based damage detection methods. The dynamic properties of a structure such as accelerations, velocities, displacements, mode shapes, and natural and damped frequencies (dynamic features) are correlated to the mechanical properties of the structure. Thus, variations of mass, stiffness and damping properties of a structure can potentially be detected by monitoring the dynamic responses of the structure. Additionally, DDMs can be classified based on their selected features (tracking of which reveal the damages) or based on the domain from which the features are extracted. For instance, they can be classified into time domain, frequency domain, and modal domain methods (Fan and Qiao 2011). Another class of DDMs are response based methods, which are built merely upon the experimental dynamic response data collected from the intact and unhealthy states of a structure.

Regardless of the type of a DDM, Rytter (1993) introduced a four level damage identification as follows:

Level I. identify if damage has occurred

Level II. identify if damage has occurred and locating the damage

Level III. identify if damage has occurred, locating the damage place, and estimating the severity of the damage

Level IV. identify if damage has occurred, determine its place and estimating the severity, and finally evaluating the structural performance and estimating the remaining useful life of the structure

Level one methods are capable of identifying the existence of damage in a system. In this level, usually, the focus is on developing methods with as little false prediction as possible. Also, the type of damage that a method can detect does play an important role in the efficacy of the method. In level two, the damage identification method should also determine the location of damages. In level three, the extent of the damage is measured. Based on the type of damage, this level may come up with different measurements. The goal of level four is to determine the reliability of the structure in terms of its performance. In this level probabilistic and damage evolution models may need to be combined to acquire a proper conclusion. Later, Worden and Dulieu-Barton (2004) proposed adding a new level called "classification" in which the type of damage is determined before the assessment.

Review of the Relevant Literature

As mentioned previously, currently, numerous DD methods have been proposed for which some reviews and surveys can be found in (Carden and Fanning 2004; Chang et al. 2003; Doebling et al. 1996; dos Santos et al. 2008; Fan and Qiao 2011; Housner et al. 1997; Li 2010; Mottershead and Friswell 1993; Salawu 1997; Yan et al. 2007). For instance, Doebling et al. (1996) have summarized and compared major DDMs developed by the time of the paper. They tabulated a summarization of the methods based on their utilized schemes and the outcome levels. We may categorize common DDMs into: a) Static-based methods, b) Modal parameter-based methods, c) System Identification and model updating based methods, d) Wavelet-based methods, and e) Other methods. It is also common to classify categories (b), (c), and (d) as dynamic based methods.

Damage detection methods based on modal parameters

a. Natural frequency-based damage detection methods

Damage detection methods based on changes in natural frequencies are categorized in both forward and inverse approaches (Doebling et al. 1998). In a forward approach, the type of damage is known and modeled mathematically. The experimentally obtained frequency should be compared to the model to detect the presumed type of damage (Doebling et al. 1996). While forward problems are in level 1 category, the inverse approach also includes level two and three methods. Early works can be found in Adams et al. (1978) where they employed reacceptance analysis. They developed a natural frequency-based damage detection method for 1D components. They used the axial modes of bars to detect and estimate the damages. Later, Cawley and Adams (1979) employed finite element analysis instead of reacceptance technique to expand their method to locate damages in 2D structures. They assumed that changes in stiffness were independent of the frequencies and related the variations of the two modes' frequencies to the position vector of possible damages. Thus, the possible damage location would be the place where the ratio of eigenvalues of the FE model of the structure equals the ratio of the experimentally measured frequencies. Stubbs and Osegueda (1990) developed a level III sensitivity-based method that compares the modal stiffness of the intact and damaged states of structures following the structural frequency shifts. Narkis (1994) presented a method to calculate natural frequencies of a cracked beam. Employing an inverse approach, he showed that the crack can be located utilizing the first two natural frequencies data.

Measuring natural frequencies demand a few number of sensors, it is relatively simple and cost efficient (Kim and Stubbs 2003), and it is less sensitive to the noises. However, natural frequency-based methods are not sensitive enough to small magnitude of damages (Yan et al. 2007), and hence their applicability in real structures are in doubt (Fan and Qiao 2011). At least five percent changes in a natural frequency must happen before a damage can be detected (Salawu 1997). In addition, a specific change in natural frequency may attribute to different damage locations by which false positive damage results are expected (Yan et al. 2007).

b. Mode shape-based damage detection methods

Compared to natural frequencies, mode shapes determination requires more measurement tools, and it is more sensitive to noises (Messina et al. 1998). However, mode shapes contain spatial information of the structure. Thus, theoretically, comparing the mode shapes of damaged and undamaged states of a structure may identify the existence and locate multiple damage occurrences. Also, in contrast to the natural frequencies, they are less sensitive to environmental conditions (Farrar and James III 1997).

Mode shape-based DDMs track changes of mode shapes, modal stiffness, modal flexibility, or modal damping acquired from an intact structure (baseline) and the current state of the structure. In the absence of data of the undamaged structure, it is common to create a FE model of the structure to simulate the baseline data. The FE model usually is calibrated by comparing the modal parameters of the real and simulated structures. More details can be found in (Hemez 2004). As the FE models contains more DOFs than the experimental extracted mode shapes, either modal expansion or model reduction become necessary.

Early works were focused on tracking mode shape changes to locate damages in a structure. However, those attempts could not achieve their objective sophisticatedly. For example, Farrar and Cone (1994) showed that mode shapes do not change if a damage occurs on the modal nodes. Ji et al. (2011) studied a full-scale experimental test of a four-story moment frame steel structure. They gathered acceleration data of the structure while it was shaking over a shaking table. Although the structure had been damaged due to the applied strong ground motion, the final result showed negligible changes in the mode shapes. Thus, other modal values were taken into consideration.

To cover the above shortcoming, Pandey and Biswas (1994) proposed a utilization of tracking changes in structural modal flexibility to locate damages. In the original proposition, just a column of the modal flexibility was used to determine damage location. Later, Zhang and Aktan (1995) enhanced the method by incorporating the whole flexibility matrix in the model. Catbas et al. (2008) employed modal curvature and modal

flexibility to locate damages in a bridge structure. These methods usually are capable of qualitatively assess the damage severity. They only need a few lower mode shapes to construct modal flexibility matrix with acceptable accuracy. The reason is that the mode shapes' contribution becomes less in magnitude as a result of the appearance of the modal frequency in the dominator of the flexibility matrix. However, mass normalized mode shapes are necessary to create modal flexibility matrix. Thus, the application of these methods for output response only cases are limited.

c. Curvature Mode shape, strain mode shape, and modal strain energy based damage detection methods

Pandey et al Pandey et al. (1991) proposed the usage of curvature mode shapes (CMS) instead of displacement mode shapes to develop a level III DDM. They determined the CMS of the displacement mode shapes using a central difference approximation of vertical dynamic displacements. They successfully located damage in a cantilever and simply supported beams by tracking the local growth of the CMS of the damaged beam and comparing it to the intact CMS. However, in large damaged areas CMS may fail.

Based on (Pandey et al. 1991) work, Ratcliffe (1997) used curvature mode shapes to detect damage in a cantilever and free-free beam when data were only provided from the damaged structure. He fitted a cubic polynomial at each DOF (where the curvature mode shapes were determined) using adjacent four node CMS data. He located damages based on the difference of the fitted polynomial and the acquired CMS obtained at each measured point. He also proposed to use strain mode shapes to increase the accuracy of the method. While the method showed capability of detecting small damages (as 0.5% reduction in stiffness), its locating accuracy lessened as the damage magnitude became smaller. Besides, the method was not studied for a multi damaged state.

Followings their previous work (Stubbs and Osegueda 1990), Stubbs et al. (1992) introduced a damage index method based on the modal strain energy fractions and Stubbs et al. (1995) verified its performance using I-40 bridge data. Jauregui (1998) and Farrar and Jauregui (1998) did a comparative study of 5 damage detection methods including damage index method, mode shape curvature method, change in flexibility method,

change in uniform load surface method, and change in stiffness method using the extracted experimental and numerical modal data of I-40 bridge . In contrast to the other methods, the damage index method performed showed acceptable capability in locating multiple damages without any false positive damage detection.

Kim and Stubbs (2003) extended the work of (Stubbs and Osegueda 1990) to a level III method. They introduced an error index that computed the difference of the ratio of the fractional changes in the eigenvalues and the modal sensitivity of the modal stiffness for which previously large number of measured frequencies were required before a damage could be detected. To address the issue they used measured mode shapes instead of numerically calculating the sensitivity matrix. They also used the relation of the fractional changes of the modal strain energy to the fractional changes of the modal frequencies to assess the severity of the crack like damages in an Euler Bernoulli beam structures.

Barroso and Rodriguez (2004) applied the damage index method on an ASCE benchmark problem. To acquire the required data of the undamaged structural properties, they developed a non-iterative method based on the ratio of the mode shapes and the eigen values. The method is applicable on shear beam model of structures. Acceptable results are demonstrated for large damage amounts.

d. System identification and model updating methods

A broad range of damage detection methods is inspired by updating the model parameters of a mathematical model of a system. In model updating-based DDM, the model is basically constructed from governing equations of motion (mostly based on the conservation of linear momentum). The model parameters will be updated by calibrating the parameters of the model employing the measurements of the structure.

There are two general approaches in the model updating methods. In the first approach, prior knowledge of structural parameters is assumed. Here, an objective function may be constructed to minimize the discrepancy of the measured and the identified modal parameters. The optimization function is the modal force error that arises when the eigen values and eigen vectors of the damaged structure are substituted into the

eigen problem of the undamaged state of the structure. The updated values of the stiffness and/or mass matrices are achieved once the optimization is completed.

The second approach (also known as System identification (SI) methods) is intended to identify structural properties. This identification reveals the state of the structure at different time instants. By tracking the identified properties, the possible location and severity of damages are determined. A system identification is mostly performed by comparing the structural responses with the prediction of its corresponding FE model. Similar to the first approach, the discrepancy between the prediction and observation will be used to update the FE model by altering the structural parameters such as Young moduli and boundary conditions. The process includes creating an objective function to minimize the discrepancy between observation and prediction that can be either modal characteristics or dynamic responses. Modal characteristics include mode shapes (either real or complex), natural frequencies, and damping ratio; and the dynamic responses are accelerations, velocities, or displacements of the instrumented nodes. For instance, Moaveni et al. (2013) performed a level three damage identification on a 3-story, 2-bay, RC frame employing the model updating method. They updated the model by minimizing the discrepancy between the identified and predicted natural frequencies and mode shapes of the structure. They divided the FE model of the structure into sub-structures and modeled damages as Young modulus reductions occurred uniformly through each sub-structure.

The system identification can be either applied in an online or offline manner. In the online methods, the unknown parameters are updated constantly as the data is being collected (Huang et al. 2010; Yang et al. 2014; Yang et al. 2014). These methods are particularly of interest when the structure is behaving in non-linear manner. Damage identification during an earthquake falls in this category. Recursive approaches such as recursive LSE or unsent Kalman filter are usually employed for these cases. In contrast, in offline approaches an ensemble of data will be fed to the model in one shot and the system will be identified accordingly.

Vast numbers of level three SI-based damage detection methods have been proposed. Wang and Haldar (1994) proposed a response-based iterative least square method (ILS_UI) to identify mass and stiffness of shear beam models. They divided the problem for two general cases, a) when the excitation is applied at just one node, as in earthquakes, and b) when other nodes can also be excited. To avoid singularity in case (a) and case (b), initial guesses of the input forces were provided for merely the first four and two time steps, respectively. The first estimates of the structural parameters re obtained using the equation of motions and the initial guesses of the forces. Next, the parameters are used to estimate the forces at all-time steps. The procedure is repeated until the variation of the two consecutive identified force vectors are less than a predefined threshold. Later, based on the work of Hoshiya and Sutoh (1993) , Wang and Haldar (1997) developed a method using an extended Kalman filter with a weighted global iteration (KF-WGI) to enhance the previous ILS_UI (Wang and Haldar 1994) method for shear beam systems. However, the number of excitation nodes must be limited and their locations must be known, otherwise the initial values of the Kalman filter remain unknown.

In the case of using Rayleigh damping in the equation of motions, the final least square objective function of ILS_UI method will become non-linear. Thus, the method will fail. To solve the issue, Ling and Haldar (2004) proposed a modified ILS_UI method. They eliminated the non-linearity by estimating the spatial derivative of the objective function using first order Taylor series. Later, Katkhuda et al. (2005) extended the iterative least square with unknown input (ILS-UI) method to be applicable to frame structures with a limited number of elements. However, for beam elements with large defects the method failed in assessing the severity of damages. Katkhuda et al. (2010) applied the method on the steel frame with semi-rigid connections by modifying the mass and stiffness matrices of each element.

Collecting data from all DOFS, Xu et al. (2012) proposed a weighted adaptive iterative least square estimation method, WAILSE-IME, to identify a shear beam structural properties with an unknown excitation input. To enhance the convergence, a

learning coefficient variable was employed to update the estimated forces at each iteration. Additionally, they used a weight matrix to improve the method performance. They examined the method performance with data collected from a numerical and an experimental shear beam structure.

Huang et al. (2010) proposed an adaptive quadratic sum-squares error to track changes of known structural parameters while some forces are unknown. They provided an analytical solution to the recursive problem and verified it for an experimental three story shear beam model with degraded stiffness values. They assumed complete knowledge of the state of the system at the time of the beginning of collecting data.

Yang et al. (2014) applied the method mentioned above in conjunction with a reduced finite element model to boost the computational efficiency of the method. They utilized a static condensation method in order to decrease the number of unknown parameters and the number of DOFs. They verified the approach experimentally for a shear beam structure in which joints were damaged.

A major drawback of EOMs-based DD method is that, as time passes, the size of the coefficient matrix of the optimization problem grows rapidly and increases the computational cost. Alternatively, energy-based DDM may be used to mitigate this issue.

Energy based damage detection methods were first introduced and developed for a shear beam model by Topole (1993). The approach has been validated for a 3-DOF shear story model (Topole 1993) and later for a damped 10-story shear beam model, representing high rise buildings, by Hyung (2007). The method is efficient and can create a baseline structure on its own. It is conveniently applicable to the structures with different type of dampers. However, it has neither developed nor verified for other structural elements such as beams and plates. The method has ignored the body forces of the structure. The mass must be known completely and only the free dynamic response data must be used. More importantly, it is not customizable to a specific region of a structure and data of the whole structure is always required.

e. Wavelet-based methods

Most of the DDMs need to compare the undamaged state of a system to its damaged state to locate or assess possible damages. However, the information of structural properties of an intact structure is not always available (Stubbs et al. 2000). A solution to this problem is to create a baseline by studying the as-built plan of the structure and using provided system identification models (e.g. (Stubbs et al. 2000) and (Stubbs and Kim 1996)). Subsequently, a finite element model of the structure is created to simulate the undamaged state or the baseline of the structure (Lee et al. 2004) . Another remedy to the unavailability of the intact structure data is to use response-based methods, also known as output only methods, that request data only from the current state of the structure.

A class of level 2 output only damage methods has been introduced based on wavelet analysis. Damages cause perturbations in the dynamic response of a structure. These perturbations can be identified in finer resolution spanned by wavelets. It is shown that wavelet-based methods successfully locate damages in beams and plates components. (e.g. (Liew and Wang 1998; Loutridis et al. 2005)). Recently Young Noh et al. (2011) proposed the utilization of wavelet energies to create damage sensitive features. They used a Morlet wavelet transform of acceleration responses of a structure (responses can be non-stationary) and determined the wavelet energy at a particular time and scale. Based on the energies, they introduced three damage sensitivity features to capture the damage evolution either at its low or high level of severity. A major drawback of wavelet methods is that high spatial resolution of the interested signal (e.g. mode shapes) is required (Fan and Qiao 2009).

f. Static-based methods

In addition to the dynamic based DDMs, a class of static response based methods has been presented. For instance, Hua et al. (2009) proposed a static based approach to determine damages in girders of cable-stayed bridges. They measured forces at cables at the field and predicted it with a static FE model of the bridge. They searched for the optimal values of structural parameters such as young modulus, mass, and area cross section that made the difference of the predicted and observed forces minimum. The

optimization was performed iteratively using sensitivity matrix of the analytical cables forces. They used penalty method to overcome the ill condition of the sensitivity matrix. More recently, Ghrib et al. (2012) detected and assessed damages in an Euler-Bernoulli beam using the beam deflection data. They used Photogrammetry technique to measure beam deflection and to create the inverse problem.

Compared to dynamic-based methods, static-based methods demand less number of sensor installment and request less data storage (HALDAR et al. 2013). However damages in mass damping characteristic cannot be tracked through static approaches. In addition, the measurement should be done relative to a fixed reference location that is not always available, for instance in offshore structures (Das et al. 2012).

g. Other methods

Besides the reviewed DDMs, there are other methods that do not strictly belong to a specific introduced category. We may introduce new categories such as signal processing and machine learning-based DDMs to classify these methods. Yet, employing too many different categorizations could be confusing instead of being helpful. Various DDMs are developed using the model updating concept, yet, employing genetic algorithm or artificial neural network-based optimization methods. The advantage is the ability of dealing with uncertainty generated either from the model itself or the noise in the data. However, they are computationally intensive, and also they might need training beforehand. Srinivas et al. (2011) presented a multi-stage approach to benefit the GA algorithm while reducing the optimization cost. They used the modal strain energy method to detect damages initially and next applied GA-based optimization algorithm to increase the accuracy of detecting damages' location and severity. The objective function was constructed based on the combination of modal assurance criteria and fractional changes in frequencies.

Huang et al. (1998) introduced "intrinsic mode functions (IMFs)" to characterize nonlinear and non-stationary signals. The IMFs can be considered as posteriori basis function of the signal of which they are generated. To decompose the signal into its IMFs the authors proposed the empirical mode decomposition (EMD) method. The

instantaneous frequency, subsequently, can be identified by taking the Hilbert transformation of the IMFs. Based on the sudden changes in the first IMF of acceleration data, Yang et al. (2004) proposed a method to identify the instant time of changes in structural stiffness. The method, however, was too sensitive to the noises. To address the noise problem, they used the Hilbert-Huang spectrum of the acceleration response of a node. The summation of the amplitude of the analytical signals of each IMFs of a signal is called Hilbert-Huang spectrum. They used the first modal response by filtering out the higher frequencies of the signal and found the damage instant (they assumed damage to be a reduction in stiffness) when the average frequency of the maximum amplitude of the analytical signal in the time-frequency domain had been changed. Cheraghi et al. (2005) and Cheraghi and Taheri (2007) introduced energy damage index (EDI) method to detect damages in systems with piezoelectric sensors. The EDI is the fractional changes of the energy of the first IMF of the signals provided by the sensors for the intact and damaged state of the system. The IMF is based on the first natural frequency of the signal. The accuracy of the EDI in detecting damages in pipe joints were investigated byEsmaeel et al. (2012).

Based on lumped mass shear beam models, Ma et al. (2005) proposed a method to decouple damages in a structure excited with seismic loads. The method converts a MDOF structure into decoupled SDOF system in which the occurrence and size of the damages can be studied individually. This was a relief to the cumbersome solution of large scale inverse problems. The online application of the method successfully verified with a numerical three story shear beam model.

Similar to (Ma et al. 2005), Shan et al. (2013) converted a seismically excited MDOFs shear beam system to several decoupled SDOF systems. Only damages in the place of each SDOF leave an effect on the system responses. In contrast to (Ma et al. 2005), they formulated the DDM to use time domain inter story drift-based structural acceleration measurements to detect damages. Therefore, the output of accelerometers can be employed directly without any hassle of acquiring velocities or displacements. Yet, both methods require constructing a virtually healthy model of the system to monitor the

results and to create the damage detection criteria. The virtual model may be a simplified shear beam model updated to mimic the response of the healthy condition of the structure. The virtual and real structure must be excited identically.

SHORTCOMINGS OF THE CURRENT DAMAGE DETECTION METHODS

Amongst the numerous available DDMs discussed above, there are some promising methods. However, there is no universal consensus that identifies an absolutely superior method. Based on the conditions, a group of DDMs might be more appropriate to be applied in a specific situation. Addressing the shortcomings of the previous methods can be helpful to present a more robust general method.

Static-based methods benefit from demanding less data compared to the dynamic methods. However, they lose their advantages to the problem of noise sensitivity, likelihood of structural overloading (as large loads are required to acquire meaningful displacements data), and the necessity of fixed references.

Modal-based damage detection methods suffer from difficulties in extracting contributing experimental mode shapes. This problem intensifies when mode shapes with close frequencies show high coupling and also when the modes are getting denser, especially in higher frequencies. Capturing higher mode shapes is difficult experimentally and lower frequency modes are less sensitive to the local damages (Farrar and Doebling 1997). Therefore, the accuracy of mode shape-based level three DDMs is of concern.

Model-based methods provide a mathematical model of a system and identify the employed parameters. The mathematical model (often FE model, or in a set of governing PDEs) creates a base, which continuously should be updated to match the experimental data. These methods demand iterative optimization process, which makes them to be computationally expensive. Also, their accuracy is dependent to the data of the undamaged state of the structure that is not always available. In case of utilization of modal parameters, model updating methods become ill-posed problem when dealing with the modal incompleteness. This may result in non-unique system identification outcomes (Mukhopadhyay et al.). Model-based methods may employ structural dynamic responses in physical domain to locate damages. However, when the number of DOFs increases, the

number of equations in the inverse problem grows rapidly. Multiplication of these equations to the number of samples makes the final problem of a large order. Thus, these methods become computationally expensive especially for large complex structures. To address the above difficulties, Hyung (2007) used energy-based approach that was originally introduced by Topole (1993) and was able to reduce the size of the inverse problem. However, the developed time domain method was limited to free dynamic response data, which experimentally is rare. The method considers the whole structure as one system. Therefore, it could not be customized to a particular sub-system. This means that sensors must be spread out to the whole structure even if one is merely interested to the state of a particular part of the structure.

Wavelet-based methods commonly are level II (locate damage only) methods. Thus, they are not suitable for assessing severity of damages. Recently, some level III methods have been developed by employing wavelets in the modal parameter-based DDMs. However, the mentioned difficulties of modal-based methods remain intact.

In summary, while there are some promising global level III methods, their fundamental assumptions and requirements have restricted their applicability in the real world problems. Some examples of common restricting assumptions and requirements are knowing excitation forces and system mass, demanding data from the whole structure, limiting damages merely to the reduction of stiffness, assuming no damping or isolator or merely using modal proportional damping behavior, and considering localized damages in a short length of the structure. Different combinations of the above can be traced in the developed DDMs. In addition, methods that benefit from fewer restrictions either require the current state of the structure to be known beforehand or become computationally costly such that their application might be restricted to shear beam models or small beams.

Considering the above discussion, developing a method with applicability to structures with limited assumptions is appealing to the field. To accomplish this goal, the proposed method needs to be computationally inexpensive particularly for a large number of DOFs. The method must be able to detect and size different type of damages. In

addition, the method should be applicable to sub-systems as one may desire to track local health conditions, for instance, due to a potential sensitivity of a part of a structure.

DISSERTATION OBJECTIVES

On the bases of the discussed potential improvement opportunities for existing level III methods, the objective of this dissertation is to develop a time domain-based computationally efficient level III damage detection method with limited input observation. This method must be able to identify properties of an intact system. It should be capable of identifying exact members at which damages have occurred. Also, it is desired that the method be capable of identifying multiple and broad damage cases, i.e. when damages have occurred in several connected elements. Meanwhile, the method must be insensitive to modal incompleteness. The method is intended to be applicable to frames equipped with passive energy dissipation devices such as isolators and dampers. As a level III method, it must be capable of locating and quantifying the amount of damages. Furthermore, the approach may be customized to be applicable to particular parts of a structure of significant importance. In this study, damage is considered to be changes in stiffness, damping, and/or mass characteristics of a structure.

SIGNIFICANCE OF THE PROPOSED WORK

This work offers a damage detection method that locates and assesses damages in mass, stiffness, and damping characteristics of civil structures. It is applicable to structures with seismic protective systems. It may keep its accuracy in simultaneous multiple damaged cases, and also when the damage has been spread over a large area. The method is computationally efficient and, consequently, it is optimal for large structures with unknown damaged states and with dense sensor layouts. It may absorb geometric nonlinearity effects without adding any extra nonlinearities in the solution process. The method is customizable to sub-systems, and hence if the interest is to identify properties of a part of a structure more accurately, then the method may be applied merely on the sub-system area. In addition, identification results may be used to provide a baseline data for other damage detection methods.

ORGANIZATION OF THE DISSERTATION

The rest of this dissertation are presented in six chapters. In CHAPTER II, based on the rate of the total energy of a general structure, a governing equation of the proposed method (DITER) is derived and its solution is provided. Next, DITER is extended for cases with limited inputs, where "input" refers to the excitation loads. In CHAPTER III, the governing equation is explicitly derived for shear beam type structures and performance of DITER has been numerically verified for a seven degree of freedoms shear beam sample. The limited input case and also noise effects have been studied as well. In CHAPTER IV, the governing equation of DITER has been derived for Euler Bernoulli beams and frames considering small strain conditions with either small or large rotations. Inherent and external damping characteristics have been included in the governing equation as well. Sub-systems implementation and existence of seismic protective systems are discussed at the end of chapter. In CHAPTER V, DITER performance has been numerically verified for beams with various types of boundary conditions and damaged states. The verification is performed for two-dimensional frames with viscous dampers and rubber bearing isolators as well. In CHAPTER VI, the method has been verified using experimentally acquired modal properties of a three story building. Finally, in CHAPTER VII, summary and findings of the research have been presented.

CHAPTER II
DAMAGE IDENTIFICATION BASED ON THE TOTAL ENERGY RATE

INTRODUCTION

Time domain based DDMs are free from the discussed shortcomings of the modal based approaches; nevertheless, they are computationally expensive, and for large complex structures, they might be inapplicable. Most of the time domain based damage detection approaches are built upon the equation of motions (EOMs) originating from the conservation of linear momentum. Thus, at each node, up to a six-dimensional vector of the partial differential equation is required. As data are being collected during time, the data matrix rapidly grows and makes the problem to be computational expensive. In addition, the computational cost intensifies when iterative approaches are required. Important examples of these situations are cases where some nodal forces are unknown.

In this study, a dynamic finite element model has been utilized to define the equation of motions of a general structure. The principle of work and energy is next applied to the obtained EOMs to drive a unique statement of all the equations. The time derivative of the set of equations is taken to create a linear set of equations, called DITER equation, for the damage detection method. Consequently, the DITER equation merely consists of one equation for each time instant. The DIETR equation of an interested system should be developed for various time instants employing acceleration data. These equations together form a set of linear equations, whose inverse solution identifies the system state. Finally, to locate and size damages, the unknown parameters are estimated by solving the set of equations using an iterative least square approach. These steps have been first obtained for a general case, and in next chapters are explicitly formulated for shear beam models, beams, and two-dimensional frames. Finally a customization has been introduced for sub-structures with viscous energy dissipative systems.

Note that in this study, unless otherwise specified, bold capital letters and bold lowercase letters are reserved for matrices and vectors, respectively.

THEORY OF THE PROPOSED METHOD

Background

To identify structural properties, an energy based method has been developed and presented in this chapter. Hereafter, the method will be referred to as DITER (damage identification based on total energy rate).

Employing the conservation of the total energy principle, Topole (1993) introduced an energy based none-destructive evaluation method (here after it is called DICTE). DICTE was efficiently capable of identifying structural properties including stiffness and damping. Based on an assumed analytical model of damping characteristics of a system, his method identified non-linear dampers properties as well. This accomplishment was a significant step for its time when the available modal NDEs were not able to capture those non-linearities satisfactorily. He numerically tested his proposed method to an undamped shear story sample and showed its superiority to the other modal NDEs. Later, Hyung (2007) examined the method successfully on a damped 10-story shear beam model. DICTE is a straight forward method that directly provides interested properties of a shear beam structure through an appropriate equation set. However, DICTE applicability is restricted due to several shortcomings.

DICTE is built upon system's free response. Hence, if the system is exposed to external loads, it either may fail or untraceable errors may emerge. This adversely limits the applicability of the method in real world problems. For example, if it is desired to track damages of a bridge, one has to stop the ongoing traffic to collect free response data. Also, DICTE is not an efficient method to study properties of a sub-system. The reason is that it is difficult to eliminate internal forces in a system that acts as an external excitation to the sub-system. In addition, prior knowledge of the structural mass is required.

In contrast, DITER is based on the changes of rate of the total energy of a system. DITER may apply to each element of components of a damped or undamped structure consisted of truss, beam, column, plate, external damper, and isolator components. The interested properties of each element may be identified by feeding dynamic response data of the system to DITER. As long as the applied loads are known, no mass information is

required. Thus, the structural properties including mass, stiffness, and damping can be determined in an element-wise manner.

Derivation of the DITER Equation

From classic dynamic formulation, e.g. (Hibbeler 2010), based on the principle of conservation of total energy for a system with no external forces on boundaries where only mechanical terms are considered (i.e. neglecting variations of heat and chemical energy), summation of the variation of potential and kinetic energies of the system equals the dissipated energy. Therefore, one can write:

$$\begin{aligned} &T_{t_0,sys.} + U_{t_0,sys.} - D_{t_0 \to t_i} = T_{t_i,sys.} + U_{t_i,sys} \\ &TE_0 = T_{t_0,sys.} + U_{t_0,sys.} = T_{i,sys.} + U_{i,sys} + D_{t_0 \to t_i} \end{aligned} \tag{2.1}$$

where T and U denote kinetic and potential (internal) energy of the system at $t = t_0$ and $t = t_i$ time instants. D represents the dissipated energy of the system and $TE_0 = TE(t_0)$ denotes total energy of the system at $t = t_0$.

For a free dynamic response, equation (2.1) can be rewritten at any time instant as:

$$\begin{aligned} &U_{t_i,sys} - D_{t_0 \to t_i} + T_{t_i,sys.} = TE_0 \\ &t_i \in \left[t_0, \cdots, t_p \right], \end{aligned} \tag{2.2}$$

where t_0 is the instant at which the excitation has been started and t_p shows the final interval up to which the dynamic field data is available.

In general, for an elastic behavior, the potential energy (ignoring body forces) of a solid can be equated to its strain energy. Thus, kinetic and potential energies of a system occupying the volume Ω at the time instant t_i are:

$$\begin{aligned} U_{t_i,sys} &= \int_{\Omega} \frac{1}{2} \boldsymbol{\varepsilon}_d^{e\,T} \mathbf{E} \boldsymbol{\varepsilon}_d^e \, d\Omega \\ T_{t_i,sys.} &= \int_{\Omega} \frac{1}{2} \rho \dot{\mathbf{u}} \dot{\mathbf{u}}^T \, d\Omega \end{aligned} \tag{2.3}$$

where $\boldsymbol{\varepsilon}_d^e = \boldsymbol{\varepsilon}_d^e(t, \mathbf{x})$ is the elastic strain located at $\mathbf{x}$ caused by the dynamic force and $\mathbf{E} = \mathbf{E}(\mathbf{x})$ is the modulus of elasticity. It is assumed that $\mathbf{E}$ remains constant during the excitation period for $t_i \in [t_0, \cdots, t_p]$. $\mathbf{x}$ is the location vector and Ω shows the physical domain of the system. $\rho = \rho(\mathbf{x})$ is the material density and $\mathbf{u} = \mathbf{u}(t, \mathbf{x})$ denotes the displacement vector. Superscript signs "T" and the dot represent the transpose and time derivation, respectively. However, instead of using the above equations, potential and kinetic energies of a system can be approximated by discretizing the system into elements, approximating the energies at each one, and describing the system energy as the summation of energies at the element level. Therefore, it is useful to first consider the equation of motion of a general system in a finite element perspective.

To study a dynamic response of a structure, different modeling methods have already been developed, e.g. see (Clough and Penzien 2010). Describing the equation of motion in the finite element approach, one can write (Reddy 2005):

$$\mathbf{M}\ddot{\mathbf{u}} + \mathbf{C}\dot{\mathbf{u}} + \mathbf{K}\mathbf{u} = \mathbf{f} \tag{2.4}$$

where $\mathbf{M}$ is the assembled mass matrix modeled either in lumped or consistent mass manner, $\mathbf{C}$ represents the assembled damping coefficients matrix including the external dampers, $\mathbf{K}$ is the assembled stiffness matrix, $\mathbf{f}$ is consisted of the external and body forces ,i.e. nodal forces (for a free response $\mathbf{f}$ is a zero vector), and $\mathbf{u}$ is the element wise, i.e. generalized, nodal displacement vector measured from the undeformed configuration, called the total displacement. The superscript dot shows derivatives with respect to time.

The vector $\mathbf{f}$ has been defined at nodes. Thus, for node "n", $\mathbf{f}^n$ in the most general form, may be described as:

$$\mathbf{f}^n = \left[f_1^n, f_2^n, f_3^n, f_4^n, f_5^n, f_6^n \right]^T \tag{2.5}$$

To find $\mathbf{f}^n$ at location $\mathbf{x} = \mathbf{x}_n$, the element-wise forces must be added over the global nodes coincided at node n .

In general $\mathbf{M}$, $\mathbf{C}$, and $\mathbf{K}$ are functions of time, location, and the state of the domain. By state, it is meant the current temperature, chemical situation, and particle

displacements. The displacements have to be measured with respect to the undeformed configuration of the system. However, if it can be assumed that the mentioned matrices are time invariant for a limited time period in which the dynamic response data has been collected, then $\mathbf{u}$ might be measured from the static equilibrium condition of the system and $\mathbf{f}$ consists of the external loads. Consequently, inherent body forces are excluded, and $\mathbf{M}$, $\mathbf{C}$, and $\mathbf{K}$ could be considered to be functions of the location in the system domain. However, in case of stiffness or mass damages (a reduction in values) the initial balance of the body forces and the static deflections will be lost. To make the equations of motion mathematically sound, total displacements must be used; otherwise, it should be kept in mind that the newly calculated responses are now referred to a different static equilibrium state. Yet, if the reduction is small in a sense that the variation of the static deflections are negligible compared to the dynamic responses, then the necessity of using total displacements might be ignored, and the static equilibrium state could be considered unchanged as the deviations in the equations of motion have not violated the equilibrium strongly. Employing total displacements can be helpful to acquire more accurate damage intensities in moderate responses as the stiffness matrix might be dependent on the nodal displacements. However, if the installed sensors do not support such a measurement, like accelerometers, then finding total displacements requires additional unknown identifications. For simplicity, as long as the displacements are small and the instruments are unable to provide total displacements directly, it is recommended to use displacements with respect to the static deflection. If final identifications show considerable damage intensities in the stiffness or mass properties, then one may try to employ total displacements to increase accuracy.

Considering equations (2.3) and (2.4), the kinetic energy of a structure can be described as a summation of kinetic energy of each nodal/ element-wise masses (described in lumped or consistent mass). Likewise, the total potential energy at each time instant would be the summation of the potential energy of each element of the system. Therefore, if the system has been discretized into NEL elements with a stiffness matrix, $\mathbf{K}_j$, and a consistent mass matrix, $\mathbf{M}_j$, then Equation (2.3) can be approximated by:

$$U_{sys}(t) - U_{sys}(t_0) = \sum_{j=1}^{NEL} \int_{\mathbf{u}_{j(t_0)}}^{\mathbf{u}_j(t)} \left(\mathbf{K}_j \mathbf{u}_j\right).d\mathbf{u}_j \tag{2.6}$$

$$T_{sys}(t) - T_{sys}(t_0) = \sum_{j=1}^{NEL} \int_{\mathbf{u}_{j(t_0)}}^{\mathbf{u}_j(t)} \left(\mathbf{M}_j \ddot{\mathbf{u}}_j\right).d\mathbf{u}_j \tag{2.7}$$

where $\mathbf{u}_j$, $\ddot{\mathbf{u}}_j$ are the generalized displacement and acceleration vectors of the nodes of the j^{th} element, respectively.

Energy dissipation in a structure may originate from inelastic behavior of materials or other mechanisms such as heat generations due to frictions between the members of the structure and opening and closing of micro cracks(Chopra 2007). The latter kind of the dissipation is usually modeled as viscous dampers (Chopra 2007). Also, to protect a structure against dynamic forces such as earthquakes energy dissipaters, including isolators and dampers, might be installed in the structure (e.g. (Buckle and Mayes 1990)). Various type of energy dissipaters are available. However, assuming viscous behavior for both inherent damping and external dampers, the dissipated energy of the whole system may be computed as:

$$D_{t_0 \to t} = \sum_{j=1}^{ND} \int_{\mathbf{u}_j(t_0)}^{\mathbf{u}_j(t)} \mathbf{C}_j \dot{\mathbf{u}}_j.d\mathbf{u}_j \tag{2.8}$$

where "ND" is the total number of external dampers and the elements with material damping, and $\mathbf{C}_j$ represents the damping coefficient matrix of the j^{th} damper/ element. Substituting equations(2.6), (2.7), and (2.8) in (2.2) :

$$\sum_{j=1}^{NEL} \int_{\mathbf{u}_{j(t_0)}}^{\mathbf{u}_j(t)} \left(\mathbf{K}_j \mathbf{u}_j\right).d\mathbf{u}_j + \sum_{j=1}^{ND} \int_{\mathbf{u}_j(t_0)}^{\mathbf{u}_j(t)} \mathbf{C}_j \dot{\mathbf{u}}_j.d\mathbf{u}_j = -\sum_{j=1}^{NEL} \int_{\mathbf{u}_{j(t_0)}}^{\mathbf{u}_j(t)} \left(\mathbf{M}_j \ddot{\mathbf{u}}_j\right).d\mathbf{u}_j \tag{2.9}$$

where the kinetic energy term has been moved to the RHS. Note that equation (2.9) is true as long as the body forces are neglected and no external excitation is applied to the structure for the time instants.

Equation (2.9) helps to identify structural parameters such as member's stiffness and damping coefficients if displacements of the structure have been collected from a free

response experiment. To find the properties, equation (2.9) must be constructed for various time instants to create a set of equations. Displacements and velocities of each node may be known either from a numerical model or an experimental measurement. The equation set can be solved in a least square manner in order to find the stiffness and damping of the structure. Later in this study the solving method and related issues have been discussed in more details.

The effect of external and body forces can be added to equation (2.9) using the principle of work and energy (PWE) (e.g. see (Hibbeler 2010)). Considering only mechanical work, PWE description is:

$$\begin{aligned} &T_{t_0,sys.}+U_{t_0,sys.}+W_{t_0\to t}-D_{t_0\to t}=T_{t,sys.}+U_{t,sys.} \\ &W=W_{ext}+W_{\mathrm{B}} \end{aligned} \tag{2.10}$$

where T , U , and D denote kinetic, internal, and dissipated energies respectively. W_{ext}, W_B represent the work of external forces applied on the boundary of the system and the work done by the body forces , $\mathbf{b}$ respectively. If the displacements are measured from the static equilibrium condition, then the work done by the weight force may be ignored i.e. $W=W_{ext}$. Similar to equation (2.2), for a dynamic problem, equation(2.10) may be rewritten as

$$\begin{aligned} &T_{t,sys.}+U_{t,sys}-W_{t_0\to t}+D_{t_0\to t}=TE_0 \\ &t\in\left[t_0,\cdots,t_p\right] \end{aligned} \tag{2.11}$$

where t_0 is the time at which excitations are started, and t_p shows the final time step up to which the dynamic field data is available. Expanding equation (2.11) for all members of a structure, equations (2.12) and (2.13) are obtained as:

$$\sum_{j=1}^{NEL}\int_{\mathbf{u}_{j(t_0)}}^{\mathbf{u}_j(\mathrm{t})}\left(\mathbf{K}_j\mathbf{u}_j\right).d\mathbf{u}_j+\sum_{j=1}^{NEL}\int_{\mathbf{u}_{j(t_0)}}^{\mathbf{u}_j(\mathrm{t})}\left(\mathbf{M}_j\ddot{\mathbf{u}}_j\right).d\mathbf{u}_j+\sum_{j=1}^{ND}\int_{\mathbf{u}_j(t_0)}^{\mathbf{u}_j(\mathrm{t})}\mathbf{C}_j\dot{\mathbf{u}}_j.d\mathbf{u}_j-\sum_{j=1}^{NON}\int_{\boldsymbol{\alpha}_j(t_0)}^{\boldsymbol{\alpha}_j(\mathrm{t})}\mathbf{f}_j.d\boldsymbol{\alpha}_j=0 \tag{2.12}$$

$$\sum_{j=1}^{NEL}\int_{t_0}^{t}\dot{\mathbf{u}}_j^T\mathbf{K}_j\mathbf{u}_j dt+\sum_{j=1}^{NEL}\int_{t_0}^{t}\dot{\mathbf{u}}^T\mathbf{M}_j\ddot{\mathbf{u}}_j dt+\sum_{j=1}^{ND}\int_{t_0}^{t}\dot{\mathbf{u}}^T\mathbf{C}_j\dot{\mathbf{u}}_j.dt-\sum_{j=1}^{NON}\int_{t_0}^{t}\dot{\boldsymbol{\alpha}}_j^T\mathbf{f}_j.dt=0 \tag{2.13}$$

where NON is the total number of the nodes and the rests are described in equation (2.9) . The "." symbol stands for dot product. $\boldsymbol{\alpha}$ is the nodal displacement vector. $\mathbf{f}_j = \mathbf{f}_j\left(t, \mathbf{x}\right)$ represents the nodal external excitation vector and is obtained by adding up the corresponding element-wise forces. Alternatively, the rate of the work can be calculated as

$$\sum_{j=1}^{NON} \int_{t_0}^{t} \dot{\boldsymbol{\alpha}}_j^T \mathbf{f}_j^N dt + \sum_{j=1}^{NEL} \int_{t_0}^{t} \dot{\mathbf{u}}_j^T \mathbf{f}_j^e dt \tag{2.14}$$

where $\mathbf{f}_j^N$ is the load applied directly to the node (sensor location), and $\mathbf{f}_j^e$ denotes the element-wise description of the loads applied at the j^{th} element domain, excluding the weight force, in an either distributed or concentrated manner.

The stiffness and mass matrices of each element are related to the modulus of elasticity and material density of the element, respectively. Thus, $\mathbf{K}_j$ and $\mathbf{M}_j$ can be formulated for unknown values of $\mathbf{E}$ and ρ where it is assumed that $\mathbf{E}$ and ρ remain constants during the data collection. Similarly, the damping matrix is described based on the damping coefficient of each element/ damper. Therefore, equation (2.13) can be used to identify unknown structural parameters including the modulus of elasticity, material density, and damping coefficient at the element level.

To find the unknowns, a set of equations, $\boldsymbol{\Lambda} = \left\{\Lambda_0, \Lambda_1, \cdots, \Lambda_p\right\}^T$, may be created whose i^{th} component refers to equation (2.13) with $t_0 = t_i, t = t_{i+1}$. Thus, the system identification problem reduces into an optimization problem with a $\left(p+1\right)$ number of statements. Most of the time, the mass of the structure can be estimated and considered to be a priori known amount; nevertheless, this assumption is not a necessity in this method.

Creating equation (2.13) at different time instants provides enough information to identify the structural properties. However, approximating the integrations introduces errors to the set of equations especially when $\mathbf{K}_j$, $\mathbf{M}_j$, and $\mathbf{C}_j$ are time dependents . Particularly, the error magnifies when time increments (sampling rate) and/or the response frequencies are relatively large. Thus, instead of the absolute values of the energies, the

time rate of the energies might be used. Differentiating equation(2.11) with respect to time at $t > t_0$:

$$\dot{T}_{t,sys.} + \dot{U}_{t,sys} - \dot{W}_{t_0 \to t} + \dot{D}_{t_0 \to t} = T\dot{E}_{t_0,sys} \tag{2.15}$$

where

$$\begin{aligned}
&\dot{T} = \sum_{j=1}^{NEL} \dot{\mathbf{u}}_j^T \mathbf{M}_j \ddot{\mathbf{u}}_j \\
&\dot{U} = \sum_{j=1}^{NEL} \dot{\mathbf{u}}_j^T \mathbf{K}_j \mathbf{u}_j \\
&\dot{W} = \sum_{j=1}^{NON} \dot{\boldsymbol{\alpha}}_j^T \mathbf{f}_j \quad \text{or} \qquad \dot{W} = \sum_{j=1}^{NON} \dot{\boldsymbol{\alpha}}_j^T \mathbf{f}_j^N + \sum_{j=1}^{NEL} \dot{\mathbf{u}}_j^T \mathbf{f}_j^e \\
&\dot{D} = \sum_{j=1}^{ND} \dot{\mathbf{u}}_j^T \mathbf{C}_j \dot{\mathbf{u}}_j \\
&T\dot{E}_{t_0} = 0
\end{aligned} \tag{2.16}$$

For the case of known inputs, after transferring the external excitation power terms to the RHS, Equation(2.13) changes to:

$$a) \sum_{j=1}^{NEL} \dot{\mathbf{u}}_j^T \mathbf{M}_j \ddot{\mathbf{u}}_j + \sum_{j=1}^{NEL} \dot{\mathbf{u}}_j^T \mathbf{K}_j \mathbf{u}_j + \sum_{j=1}^{ND} \dot{\mathbf{u}}_j^T \mathbf{C}_j \dot{\mathbf{u}}_j = \sum_{j=1}^{NON} \dot{\boldsymbol{\alpha}}_j^T \mathbf{f}_j^N + \sum_{j=1}^{NEL} \dot{\mathbf{u}}_j^T \mathbf{f}_j^e, \ \ \forall t > t_0$$

$$b) \sum_{j=1}^{NEL} \dot{\mathbf{u}}_j^T \mathbf{M}_j \ddot{\mathbf{u}}_j - \sum_{j=1}^{NEL} \dot{\mathbf{u}}_j^T g\bar{\mathbf{m}}_j + \sum_{j=1}^{NEL} \dot{\mathbf{u}}_j^T \mathbf{K}_j \mathbf{u}_j + \sum_{j=1}^{ND} \dot{\mathbf{u}}_j^T \mathbf{C}_j \dot{\mathbf{u}}_j = \sum_{j=1}^{NON} \dot{\boldsymbol{\alpha}}_j^T \mathbf{f}_j^N + \sum_{j=1}^{NEL} \dot{\mathbf{u}}_j^T \mathbf{f}_j^e, \forall t > t_0 \tag{2.17}$$

where the first equation is provided when the displacements are measured from static equilibrium, and the second one is for cases with total displacements. $\mathbf{f}_j^N$ and $\mathbf{f}_j^e$ are as defined is equation (2.14). $g\bar{\mathbf{m}}$ represents the element-wise nodal values of the weight force. The term $\sum_{j=1}^{NEL} \dot{\mathbf{u}}_j^T g\bar{\mathbf{m}}_j$ accounts for the rate of the work done by the body force. It has been written explicitly to avoid disambiguates once one desires to employ total displacements for unknown mass problems. As mentioned before, equation (2.17) benefits

from the elimination of integration computation. Therefore, the above equations should be used and be named as DITER equation. The final form of the equation is shown in equation (2.22).

Note that to avoid the coupling of the mass and stiffness parameters, the mass, damping, and stiffness matrices and element's DOFs, $\mathbf{u}$, should be derived in local coordinates while the forces and nodal displacements, $\boldsymbol{\alpha}$,are described in global coordinates. The associated rotation matrix could be simply formed considering the geometry of the structure and the nodal displacements.

SOLUTION OF THE DITER EQUATION

Solution of Equation (2.17) may determine the unknown structural parameters including axial and flexural stiffness, mass, and damping coefficients. However, the excitation forces on the RHS are not always known. Thus, the solution to DITER equation in case of known forces and forces with limited observation are separately discussed.

Solution of the DITER Equation for Known Forces

To begin, it is assumed that the static deflection and all external forces are known. If the stiffness and density of each element are approximated by equivalent values, that remain constant for the whole element domain, then the first, second, and the third terms of the LHS of equation (2.17) may be rewritten as follows:

$$\left[\left(\sum_{j=1}^{NEL}\dot{\mathbf{u}}_j^T\mathbf{M}_j\ddot{\mathbf{u}}_j\right)_{i1}\right]\equiv\mathbf{G}(\dot{\mathbf{u}},\ddot{\mathbf{u}},t,\mathbf{x})\boldsymbol{\theta}_m \text{ or } \left[\left(\sum_{j=1}^{NEL}\dot{\mathbf{u}}_j^T\mathbf{M}_j\ddot{\mathbf{u}}_j-\sum_{j=1}^{NEL}\dot{\mathbf{u}}_j^T g\bar{\mathbf{m}}_j\right)_{i1}\right]\equiv\mathbf{G}(\dot{\mathbf{u}},\ddot{\mathbf{u}},t,\mathbf{x})\boldsymbol{\theta}_m$$

$$\left[\left(\sum_{j=1}^{NEL}\dot{\mathbf{u}}_j^T\mathbf{K}_j\mathbf{u}_j\right)_{i1}\right]\equiv\boldsymbol{\Gamma}\left(\mathbf{u},\dot{\mathbf{u}},t,\mathbf{x}\right)\boldsymbol{\theta}_k,\qquad i=1,2,...,p+1 \tag{2.18}$$

where known matrices $\mathbf{G}$ and $\boldsymbol{\Gamma}$ are of size $(p+1)\times\sum_{j=1}^{NEL}l_j^m$ and $(p+1)\times\sum_{j=1}^{NEL}l_j^k$ respectively. Vectors $\boldsymbol{\theta}_m$ and $\boldsymbol{\theta}_k$ represent the element-wise unknown parameters regarding mass (mass and/or mass inertia per unit length) and stiffness/rigidity (axial

and/or flexural) respectively. $\boldsymbol{\theta}_m$ is of size $\left(\sum_{j=1}^{NEL} l_j^m\right)\times 1$ and $\boldsymbol{\theta}_k$ is of the size $\left(\sum_{j=1}^{NEL} l_j^k\right)\times 1$. l_j^m and l_j^k show the number of mass and stiffness unknown parameters at j^{th} element, respectively. $\left[(.)_{ij}\right]$ denotes a matrix with $(.)$ component located at row i and column j where at each row $t = t_i$. Finally, $(p+1)$ is the number of collected samples. Note that $\boldsymbol{\theta}_m$ and $\boldsymbol{\theta}_k$ are assumed to be time invariant during the period in which data is collected. The first term of equation (2.18) corresponds to the case in which displacements are measured from the deformed static configuration, and the second one is for the total displacements data.

Similarly the damping term of equation (2.17) can be written as:

$$\left[\left(\sum_{j=1}^{ND} \dot{\mathbf{u}}_j^T \mathbf{C}_j \dot{\mathbf{u}}_j\right)_{i1}\right] \equiv \mathbf{D}(\boldsymbol{\upsilon}, t, \mathbf{x})\boldsymbol{\theta}_c \qquad (2.19)$$
$$i = 1, 2, ..., p+1$$

Where $\boldsymbol{\upsilon}$ is a term based on which the behavior of the damper is described (for instance, it might be nodal velocity or displacement) and $\boldsymbol{\theta}_c$ is a vector that holds the time invariant damping coefficients. Size of $\mathbf{D}$ and $\boldsymbol{\theta}_c$ are $(p+1)\times\sum_{j=1}^{ND} l_j^c$ and $\left(\sum_{j=1}^{ND} l_j^c\right)\times 1$, respectively. l_j^c shows the number of unknown parameter for the j^{th} damper.

The RHS of Equation(2.17) is known by the observation and may be written as:

$$\left[\left(\sum_{j=1}^{NON} \dot{\boldsymbol{\alpha}}_j^T \mathbf{f}_j^N + \sum_{j=1}^{NEL} \dot{\mathbf{u}}_j^T \mathbf{f}_j^e\right)_{i1}\right] \equiv \mathbf{y},\ \mathbf{y} = \mathbf{y}_{(p+1)\times 1}$$
$$i = 1, 2, ..., p+1$$

(2.20)

Substituting equations (2.18), (2.19), and (2.20) into equation (2.17), the DITER equation can be rewritten as:

$$\mathbf{G}(\dot{\mathbf{u}},\ddot{\mathbf{u}},t,\mathbf{x})\boldsymbol{\theta}_m+\boldsymbol{\Gamma}\left(\mathbf{u},\dot{\mathbf{u}},t,\mathbf{x}\right)\boldsymbol{\theta}_k+\mathbf{D}(\upsilon,t,\mathbf{x})\boldsymbol{\theta}_c=\mathbf{y},\ \forall t>t_0 \tag{2.21}$$

and be summarized in the form of:

$$\mathbf{H}\boldsymbol{\theta}+\mathbf{v}=\mathbf{y} \tag{2.22}$$

where $\mathbf{H}=[\boldsymbol{\Gamma},\mathbf{D},\mathbf{G}]$ and $\boldsymbol{\theta}=[\boldsymbol{\theta}_k^T,\boldsymbol{\theta}_c^T,\boldsymbol{\theta}_m^T]^T$. Thus, $\mathbf{H}$ and θ are of size $\left(p+1\right)\times l$ and $l\times 1$ respectively with $l=\left(\sum_{j=1}^{ND}l_j^c+\sum_{j=1}^{NEL}l_j^m+\sum_{j=1}^{NEL}l_j^k\right)$. $\mathbf{v}$ is an error vector consisted of errors originated from data collection and model errors. It is assumed that $\mathbf{v}$ has a normal distribution of $N\left(0,\sigma^2\right)$ and a diagonal covariance matrix $E[\mathbf{v}\mathbf{v}^T]=\mathbf{R},\mathbf{R}=R_{ij}\delta_{ij}$ where δ is Kroneker delta (Yang et al. 2009).

The best estimation of θ, $\hat{\theta}$ can be computed considering following error function:

$$\boldsymbol{\varepsilon}=\mathbf{y}-\hat{\mathbf{y}} \tag{2.23}$$

where $\hat{\mathbf{y}}=\mathbf{H}\hat{\boldsymbol{\theta}}$. The error could be minimized in a least square sense in order to find the unknown parameters of the structure. To find the best estimation of the unknown parameters, the weighted squared ℓ_2 norm of the error function should be created, Υ, and minimized as shown in equation (2.24)

$$\begin{aligned}&\min:\Upsilon=\boldsymbol{\varepsilon}^T\mathbf{R}^{-1}\boldsymbol{\varepsilon}=\mathbf{y}^T\mathbf{R}^{-1}\mathbf{y}+\hat{\boldsymbol{\theta}}^T\mathbf{H}^T\mathbf{R}^{-1}\mathbf{H}\hat{\boldsymbol{\theta}}-\hat{\boldsymbol{\theta}}^T\mathbf{H}^T\mathbf{R}^{-1}\mathbf{y}-\mathbf{y}^T\mathbf{R}^{-1}\mathbf{H}\hat{\boldsymbol{\theta}}\\&\text{Subject to}:\hat{\boldsymbol{\theta}}>0\end{aligned} \tag{2.24}$$

If $\boldsymbol{\tau}$ is a vector consisted of independent variable of unknown parameters stored in $\hat{\theta}$, $\hat{\theta}$ may obtain by minimizing the cost function, Υ, through solving :

$$\begin{aligned}&\frac{\partial\Upsilon}{\partial\boldsymbol{\tau}}=\mathbf{0}\Rightarrow 2\hat{\boldsymbol{\theta}}^T\mathbf{H}^T\mathbf{R}^{-1}\mathbf{H}\mathbf{C}-2\mathbf{y}^T\mathbf{R}^{-1}\mathbf{H}\mathbf{C}=0\Rightarrow\\&\Lambda\equiv 2\mathbf{C}^T\mathbf{H}^T\mathbf{R}^{-1}\left(\mathbf{H}\hat{\boldsymbol{\theta}}-\mathbf{y}\right)=0\end{aligned} \tag{2.25}$$

where

$$\mathbf{C}=\frac{\partial\hat{\boldsymbol{\theta}}}{\partial\boldsymbol{\tau}} \tag{2.26}$$

In general, equation(2.25) is nonlinear. In a simple approach, we may use Newton–Raphson method to linearize the equation and estimate $\hat{\boldsymbol{\theta}}$ as:

$$\Lambda(\boldsymbol{\tau}) \simeq \hat{\Lambda}(\boldsymbol{\tau}) = \mathbf{C}^T\mathbf{H}^T\mathbf{R}^{-1}\left(\mathbf{H}\hat{\boldsymbol{\theta}} - \mathbf{y}\right)|_{\boldsymbol{\tau}_0} + \frac{\partial\left(\mathbf{C}^T\mathbf{H}^T\mathbf{R}^{-1}\left(\mathbf{H}\hat{\boldsymbol{\theta}} - \mathbf{y}\right)\right)}{\partial\boldsymbol{\tau}}|_{\boldsymbol{\tau}_0}\,\Delta\boldsymbol{\tau} \qquad (2.27)$$

where only the first two terms of the Taylor expansion have been considered. Next, an initial value $\boldsymbol{\tau}_0$ should be chosen and $\Delta\boldsymbol{\tau}$ will be obtained solving $\hat{\Lambda}(\boldsymbol{\tau}) = 0$. $\boldsymbol{\tau}$ will be updated as $\boldsymbol{\tau}_1 = \Delta\boldsymbol{\tau} + \boldsymbol{\tau}_0$ and equation $\hat{\Lambda}(\boldsymbol{\tau}) = 0$ will be solved again to find the new $\Delta\boldsymbol{\tau}$. This iteration continues until $\Delta\boldsymbol{\tau}$ become less than a priori determined threshold at $\boldsymbol{\tau} = \boldsymbol{\tau}_k$. Note that in the case of availability, $\boldsymbol{\tau}_0$ can be the last known state of the structure. Assuming $\mathbf{R} = \mathbf{I}$, in a special case where all the unknown parameters are independent variables, i.e. $\boldsymbol{\tau} = \hat{\boldsymbol{\theta}}$, equation (2.24) can be solved as follows:

$$\begin{aligned} &\frac{\partial\Upsilon}{\partial\hat{\boldsymbol{\theta}}} = \mathbf{0} \rightarrow 2\hat{\boldsymbol{\theta}}^T\mathbf{H}^T\mathbf{H} - 2\mathbf{y}^T\mathbf{H} = \mathbf{0} \rightarrow \\ &\hat{\boldsymbol{\theta}} = \mathbf{H}^{\dagger}\mathbf{y} \end{aligned} \qquad (2.28)$$

$\mathbf{H}^{\dagger}$ is the pseudo inverse of $\mathbf{H}$ that is obtained from the singular value decomposition of $\mathbf{H}$. Thus, $\mathbf{H}^{\dagger} = \mathbf{V}\boldsymbol{\Sigma}^{\dagger}\mathbf{U}^T$ where $\mathbf{U}_{(p+1)\times(p+1)}$ and $\mathbf{V}_{l\times l}$ are, respectively, the left and right singular vectors of $\mathbf{H}$, $\boldsymbol{\Sigma}$ is a diagonal matrix

$$\boldsymbol{\Sigma} = \begin{bmatrix} \sigma_1 & & & & & \\ & \ddots & & & & \\ & & \sigma_n & & & \\ & & & 0 & & \\ & & & & \ddots & \\ & & & & & 0 \end{bmatrix}$$

$$\sigma_1 \geq \cdots \geq \sigma_n \geq 0, \qquad n \leq \min(p+1, l)$$

that consists of the singular values of $\mathbf{H}$, and $\boldsymbol{\Sigma}^{\dagger}$ is the same as $\boldsymbol{\Sigma}^T$ whose non zero diagonal terms are inversed. Notice that, due to the noises, zero terms might be substituted

by some positive numbers, yet the values might be eliminated by adjusting the tolerance of the SVD.

Contribution of Static Deflections in DITER

In contrast to the conventional forward dynamic problems, mathematically, the body forces $\mathbf{b}$ should not be ignored in the DITER equation. This statement holds true even if the displacements, $\mathbf{u}$ are measured from the static equilibrium configuration, i.e. where velocity and acceleration at all nodes are zero. The reason is that once the stiffness or mass is damaged the weight of the structure will no longer equate to the multiplication of the static deflection, $\boldsymbol{\delta}_s$ by the current stiffness matrix. For clarity, consider a SDOF system with stiffness k and mass m under excitation of $f(t)$. If u is measured from static equilibrium and δ_s is the static deflection, then $k\delta_s = mg$. Also, let's assume that the system is damaged by reducing the stiffness to k^*. Thus,

$$k^*\left(u + \delta_s + \Delta u_s\right) + m\ddot{u} = f + mg \tag{2.29}$$

where Δu_s is the variation of the static deflection, i.e. $k^*\left(\delta_s + \Delta u_s\right) = mg$. If data is collected in a way that the amount of $\bar{u} = u + \Delta u_s$ is measured, e.g. using accelerometers, then a slight discrepancy of $\delta_s\left(k - k^*\right)$ emerges for the description of the equation of motion shown in equation (2.30).

$$k^*\bar{u} + m\ddot{u} = f \tag{2.30}$$

Dynamic response data mostly are collected with accelerometer sensors. Accelerometers provide displacements, for instance using double integration method, with respect to the initial conditions where the structure was at rest, i.e. a condition with zero velocity and acceleration, or simply at static equilibrium state. In other words, accelerometers provide $\bar{u}$. Thus, $\boldsymbol{\delta}_s$ remains an unknown vector whose role in the damage identification should be accounted for. It is important to note that identification of accurate amount of $\boldsymbol{\delta}_s$ is not the main interest. Instead, its role in reducing the errors occurred by the changes of static deflection in the damage identification is of the main concern. In

addition, the contribution of the static deflection in the objective function is considerably smaller than other structural properties. Consequently, the identified amounts of $\boldsymbol{\delta}_s$ are likely to be less accurate compared to the other unknowns. Therefore, while $\boldsymbol{\delta}_s$ is time invariant and for a specific structure, its identification could be performed only once, it is recommended to consider $\boldsymbol{\delta}_s$ as an unknown vector to increase the reliability of the outcomes of DITER damage identification. However, as $\delta_s\left(k-k^*\right)$ suggests, for small damages one might be willing to ignore the inconsistency and identify parameters with the data measured from the static deflection.

As mentioned above, the static deflation is considered in the objective function to account for any probable deviation in the static equilibrium configuration of the structure due to the imposed damages. Note that the objective is to locate and size damages to the structural properties i.e. mass, stiffness, and damping characteristic and not to identify the static deflection values.

If the element-wise static deflection is shown by $\boldsymbol{\delta}_s$, and the measured element-wise displacements from the accelerometer data are called $\bar{\mathbf{u}}$,then

$$\begin{aligned}\mathbf{u} &= \boldsymbol{\delta}_s + \bar{\mathbf{u}}\\ \dot{\mathbf{u}} &= \dot{\bar{\mathbf{u}}}\\ \ddot{\mathbf{u}} &= \ddot{\bar{\mathbf{u}}}\end{aligned} \tag{2.31}$$

To consider the effect of the variation in static deflection on the energy terms, for the case that the dependency of the **K**, **M**, and **D** matrices on the displacements are negligible, the second term of equation (2.18) has been rewritten as:

$$\sum_{j=1}^{NEL}\dot{\mathbf{u}}_j^T\mathbf{K}_j\mathbf{u}_j = \sum_{j=1}^{NEL}\dot{\mathbf{u}}_j^T\mathbf{K}_j\bar{\mathbf{u}}_j + \sum_{j=1}^{NEL}\dot{\mathbf{u}}_j^T\mathbf{K}_j\boldsymbol{\delta}_{s,j} \equiv \bar{\boldsymbol{\Gamma}}\left(\bar{\mathbf{u}},\dot{\mathbf{u}},t,\mathbf{x}\right)\boldsymbol{\theta}_k + \boldsymbol{\Gamma}_s\left(\dot{\mathbf{u}},t,\mathbf{x}\right)\bar{\boldsymbol{\theta}}_k \tag{2.32}$$

where $\boldsymbol{\theta}_k$ is the same as equation (2.18), and $\bar{\boldsymbol{\theta}}_k$ contains the multiplication of each component of $\boldsymbol{\theta}_k$ to the corresponding nodal static deflection. Thus, the size of $\bar{\boldsymbol{\theta}}_k$ is $\bar{l}\times 1$ where $\bar{l} = \sum_{j=1}^{NEL} l_j^k \bar{h}_j$ for which $\bar{h}_j$ represents the number of DOFs associated to the type of

employed elements. For instance, for a flexural stiffness of the j^{th} element $\bar{h}_j = 4$. The size of $\bar{\mathbf{\Gamma}}$ is the same as $\mathbf{\Gamma}$, while the size of $\mathbf{\Gamma}_s$ is $(p+1)\times\bar{l}$. $\boldsymbol{\delta}_{s,j}$ contains element-wise initial static deflections of the j^{th} element, and it is described in the local coordinates of the element. Therefore, if

$$\begin{aligned}\bar{\mathbf{H}} &= [\bar{\mathbf{\Gamma}}, \mathbf{\Gamma}_s, \mathbf{D}\ , \mathbf{G}\ ] \\ \bar{\boldsymbol{\theta}} &= [\boldsymbol{\theta}_k^T, \bar{\boldsymbol{\theta}}_k^T, \boldsymbol{\theta}_c^T, \boldsymbol{\theta}_m^T]^T\end{aligned} \tag{2.33}$$

the best estimation of $\bar{\theta}, \hat{\bar{\boldsymbol{\theta}}}$,can be found by minimizing the following objective function acquired by employing equation (2.17).

$$\begin{aligned}&\bar{\Upsilon} = \boldsymbol{\varepsilon}^T\mathbf{R}^{-1}\boldsymbol{\varepsilon} = \mathbf{y}^T\mathbf{R}^{-1}\mathbf{y} + \hat{\bar{\boldsymbol{\theta}}}^T\bar{\mathbf{H}}^T\mathbf{R}^{-1}\bar{\mathbf{H}}\hat{\bar{\boldsymbol{\theta}}} - \hat{\bar{\boldsymbol{\theta}}}^T\bar{\mathbf{H}}^T\mathbf{R}^{-1}\mathbf{y} - \mathbf{y}^T\mathbf{R}^{-1}\bar{\mathbf{H}}\hat{\bar{\boldsymbol{\theta}}} \\ &\text{Subject to}: \begin{cases}[\boldsymbol{\theta}_k^T, \boldsymbol{\theta}_c^T, \boldsymbol{\theta}_m^T]^T > \mathbf{0} \\ \mathbf{S}_{LB} \le \bar{\boldsymbol{\theta}}_k \le \mathbf{S}_{UB}\end{cases}\end{aligned} \tag{2.34}$$

where $\mathbf{S}_{LB}$ and $\mathbf{S}_{UB}$ are the lower and upper bound limits of $\bar{\boldsymbol{\theta}}_k$, respectively. The values of the boundaries are not critical to the method and should be estimated with reasonable amounts. To find the unknown structural parameters, it is required to substitute equation (2.24) with equation (2.34) and follow the same solution procedure.

Solution of the DITER Equation with Limited Input Data

In the previous part, DITER method was formulated to find structural properties, including mass, stiffness, and damping coefficients, based on the measured dynamic responses and excitation forces. The unknown parameters can be determined by optimizing equation (2.24). However, in practice, it is not always possible to excite a large structure with controlled forces or collect data of forces at all DOFs. Thus, it is necessary to extend the method for cases in which excitations are not known at some locations. To address the limited input data, approaches such as iterative LSE (Ling and Haldar 2004; Wang and Haldar 1994; Wang and Haldar 1997) and weighted iterative LSE (Xu et al. 2012) have been proposed for time domain SI methods. These methods employ conservation of linear momentum to create objective functions. In this study, an iterative

optimization method has been customized for DITER to solve the unknown excitation problem. For the sake of reference, the method will be called I-DITER.

Iterative algorithm for limited input data

To make I-DITER enable to find the unknown parameters in the case of limited input data, first, it is necessary to make an initial guess of the unknown nodal forces, $\hat{\mathbf{f}}$,for the corresponding sampling time, and next, calculate the rate of the external work. A zero value is an appropriate guess vector. However, in order to speed up the convergence rate, it is recommended to compute the initial approximation of excitations using the last identified mass, stiffness and damping matrices with the current responses as follows:

$$\hat{\mathbf{f}}^0 = \tilde{\mathbf{M}}\ddot{\mathbf{u}} + \tilde{\mathbf{C}}\dot{\mathbf{u}} + \tilde{\mathbf{K}}\mathbf{u} \tag{2.35}$$

where superscript "~" shows the last identified values of damping and stiffness matrices. Note that equation (2.35) should be used to update approximation of forces at DOFs where the excitations are not measured or available.

Having the initial estimation of the unknown forces, the vector $\mathbf{y}$ of equation (2.22) must be updated by adding the rate of the kinetic energy to the presumed external power. Thus,

$$\mathbf{H}\hat{\boldsymbol{\theta}}^0 = \hat{\mathbf{y}}^0 \tag{2.36}$$

where $\hat{\boldsymbol{\theta}}^0$ is the best estimation of the vector of the unknowns and $\hat{\mathbf{y}}^0$ is the summation of the rate of the kinetic energy and external work done on the system corresponding to the initial guess of the excitation vector. The subscript zero denotes the number of the current, here the initial, iteration.

$$\hat{\mathbf{y}}^0 = \left[\left(-\sum_{j=1}^{NEL} \ddot{\mathbf{u}}_j^T \mathbf{M}_j \dot{\mathbf{u}}_j + \hat{\dot{W}}^0 \right)_{i1} \right], i = 1, 2, ..., p+1 \tag{2.37}$$

where

$$\hat{\dot{W}}^0 = \sum_{j_1} \hat{\mathbf{f}}_{j_1}^0 . \dot{\boldsymbol{\alpha}}_{j_1} + \sum_{j_2} \mathbf{f}_{j_2} . \dot{\boldsymbol{\alpha}}_{j_2}$$

Here j_2, j_1 denote the nodes with known and unknown load magnitude respectively. To obtain the unknown parameters of equation(2.36), following iterative optimization algorithm has been presented. In contrast to the structural properties, the absolute amount of the unknown forces are seldom of interest. Thus, the simpler description of $\hat{\mathbf{y}}^0$ is used in equation (2.37). Here, the weight force must be addressed as a part of $\hat{\mathbf{f}}$ and $\mathbf{f}$, i.e. the weight will be included in the description of $\hat{\dot{W}}^0$. However, if it is desired, the weight force might be excluded from the other external forces, and consequently from $\hat{\dot{W}}^0$, by adding the term $\sum_{j=1}^{NEL} \dot{\mathbf{u}}_j^T g \bar{\mathbf{m}}_j$ to the RHS of equation (2.37). In such a case, the weight term must be deducted from $\hat{\mathbf{f}}^0$ of equation (2.35) and be addressed explicitly.

Once the initial values are assigned to the unknown forces, the initial unknown parameters, $\hat{\boldsymbol{\theta}}^{k=0}$ can be obtained by solving equation (2.36) as described in equation (2.24). To update the estimation of the rate of the external work upon the initially obtained parameters, $\hat{\boldsymbol{\theta}}^{k=0}$ should be substituted in the FEM form of the equation of motions, i.e. equation (2.4), and the corresponding forces must be computed as follows:

$$\hat{\mathbf{f}}^k = \mathbf{M}\ddot{\mathbf{u}} + \hat{\mathbf{C}}^k\dot{\mathbf{u}} + \hat{\mathbf{K}}^k\mathbf{u} \tag{2.38}$$

where $\hat{\mathbf{K}}^k$ and $\hat{\mathbf{C}}^k$ are constructed based on the determined $\hat{\boldsymbol{\theta}}^k$ with $\hat{\dot{\mathbf{w}}} = \hat{\dot{\mathbf{w}}}^{k-1}$. If the discrepancy between the known nodal forces, $\mathbf{f}_{j_2}$, and the updated $\hat{\mathbf{f}}_{j_2}^k$ at node j_2 is shown by $\delta\mathbf{f}_{j_2}^k = [(\delta f_{j_2}^k)_{i1}], \mathrm{i} = 1, 2, \cdots, \mathrm{p}+1$ at the k^{th} iteration, then the k^{th} variation of the rate of the work done by the known loads is $\delta\hat{\dot{\mathbf{w}}}^k = \delta\mathbf{f}_{j_2}^k . \dot{\boldsymbol{\alpha}}_{j_2}$. Hence, the rate of the work vector could be updated as:

$$\hat{\dot{\mathbf{w}}}^k = \delta\hat{\dot{\mathbf{w}}}^k + \hat{\dot{\mathbf{w}}}^{k-1} \tag{2.39}$$

where

$$\dot{\mathbf{w}}^{k-1} = [\dot{W}_1^{k-1}, ..., \dot{W}_{p+1}^{k-1}]^T$$

The iteration continues until the Euclidian (l_2) norm of the deviation of the rate of the work vector, $\left\|\delta\hat{\dot{\mathbf{w}}}\right\|_2$, becomes less than a previously determined threshold, i.e.

$$\left\|\delta\hat{\dot{\mathbf{w}}}\right\|_2 \le \xi \tag{2.40}$$

where ξ is a predetermined tolerance and $\left\|(.)\right\|_2$ denotes the l_2 norm.

To enhance the convergence of the above iterative process, boundaries may be introduced to the updated rate of the work done on the system. The boundaries can be determined assuming a rational range of structural damages. One may assign the boundaries to the components of $\hat{\dot{\mathbf{w}}}^k$ at each time instant i, i.e. $t = t_i$, using equation (2.41) where it is assumed that no healing has taken place .

$$\min(\tilde{\dot{\mathbf{w}}}) \le \hat{\dot{\mathbf{w}}}^k \le \max(\tilde{\dot{\mathbf{w}}}) \tag{2.41}$$

where

$$\begin{aligned} &\tilde{\dot{\mathbf{w}}} = [\tilde{\dot{W}}_1, ..., \tilde{\dot{W}}_{p+1}]^T \\ &\tilde{\dot{W}}_i = \sum_{j=1}^{NEL} \dot{\mathbf{u}}^T \left(1-\alpha_j^m\right)\tilde{\mathbf{M}}_j\ddot{\mathbf{u}}_j + \sum_{j=1}^{NEL} \dot{\mathbf{u}}_j^T \left(1-\alpha_j^k\right)\tilde{\mathbf{K}}_j\mathbf{u}_j + \sum_{j=1}^{ND} \dot{\mathbf{u}}_j^T \left(1-\alpha_j^c\right)\tilde{\mathbf{C}}_j\dot{\mathbf{u}}_j \end{aligned} \tag{2.42}$$

at $t = t_i$ and:

$$\alpha_j^m \le \alpha_m, \alpha_j^k \le \alpha_k, \alpha_j^c \le \alpha_c \tag{2.43}$$

In equations (2.42) and (2.43), subscript i denotes time instants and α_j^m, α_j^k, and α_j^c are positive values that represent the expected reduction in mass, stiffness and damping, respectively. α_m, α_k, and α_c are the highest expected value of the above coefficients, which could roughly be estimated based on an engineering judgment. Note that a value of $\alpha_j^k = 1$ means a complete failure of j th member. For limited input data, it is assumed that the mass matrix remains intact and consequently $\alpha_j^m = 0$ and $\tilde{\mathbf{M}} = \mathbf{M}$. To find the minimum or maximum values of $\tilde{\dot{\mathbf{w}}}$, linear programming can be used. If the iteration does not converge we may increase the magnitude of α_j^m, α_j^k, and α_j^c.

It is also possible to consider a slight healing to the last known state of the structure. To do so, it is adequate to change the objective function in equation (2.42) to

$$\tilde{\dot{W}}_i = \sum_{j=1}^{NEL} \dot{\mathbf{u}}^T \left(1 + {}^H\alpha_j^m - \alpha_j^m\right) \tilde{\mathbf{M}}_j \ddot{\mathbf{u}}_j + \sum_{j=1}^{NEL} \dot{\mathbf{u}}_j^T \left(1 + {}^H\alpha_j^k - \alpha_j^k\right) \tilde{\mathbf{K}}_j \mathbf{u}_j + \sum_{j=1}^{ND} \dot{\mathbf{u}}_j^T \left(1 + {}^H\alpha_j^c - \alpha_j^c\right) \tilde{\mathbf{C}}_j \dot{\mathbf{u}}_j \tag{2.44}$$

subject to

$$\begin{aligned} &\alpha_j^m \le \alpha_m, \alpha_j^k \le \alpha_k, \alpha_j^c \le \alpha_c \\ &{}^H\alpha_j^m \le {}^H\alpha_m, {}^H\alpha_j^k \le {}^H\alpha_k, {}^H\alpha_j^c \le {}^H\alpha_c \end{aligned} \tag{2.45}$$

where the superscript "H" refers to the healing process. ${}^H\alpha_j^m$, ${}^H\alpha_j^k$, ${}^H\alpha_j^c$ are positive values representing mass, stiffness and damping healing factors. Healings can happen due to various reasons. For instance, the structure might be repaired, or it might become stiffer due to the variation of temperature. Even damages to the structure may increase the damping of the structure as well. Note that, especial care must be taken to the selection of the healing and reduction factors. Smaller values can enhanced the convergence rate; however, if the damages are underestimated by taking too small reduction factors, then the iteration may not converge. Thus, it is recommended to start with large factors unless the assessor has adequate knowledge about the state of the structure.

The required steps of I-DITER is summarized in the following, and its flowchart is shown in Figure II-1.

1. Initially estimate the unknown external forces using equation (2.35) and calculate the rate of the work done on the system by,

$$\hat{\dot{\mathbf{w}}}^k = \left[\left(\sum_{j_1} \hat{\mathbf{f}}_{j_1}^k . \dot{\boldsymbol{\alpha}}_{j_1} + \sum_{j_2} \mathbf{f}_{j_2} . \dot{\boldsymbol{\alpha}}_{j_2} \right)_{i1} \right], i = 1, 2, ..., p+1$$

2. Compute $\hat{\mathbf{y}}^k$ based on $\dot{W}^k$ for k=0 (equation (2.37))
3. Estimate α_k, α_c based on the engineering judgment. If no information is available, select relatively large values such as 0.5 to 0.8.
4. Solve equation (2.41) to bound $\hat{\dot{\mathbf{w}}}^k$ at k=0

5. Determine $\hat{\boldsymbol{\theta}}^k$ from equation (2.24)
6. Update the estimated forces using equation (2.38)
7. Update the rate of the work done on the system using equation(2.39)
8. Compute $\hat{\mathbf{y}}^k$ based on the last updated $\hat{\dot{\mathbf{w}}}^k$
9. Determine $\hat{\boldsymbol{\theta}}^k$ from step 5 for the current iteration
10. Repeat steps 7 to 11 until $\left\|\delta\hat{\dot{\mathbf{w}}}\right\|_2 \le \xi$,where ξ is a predetermined tolerance value and $\left\|(.)\right\|_2$ denotes the l_2 norm

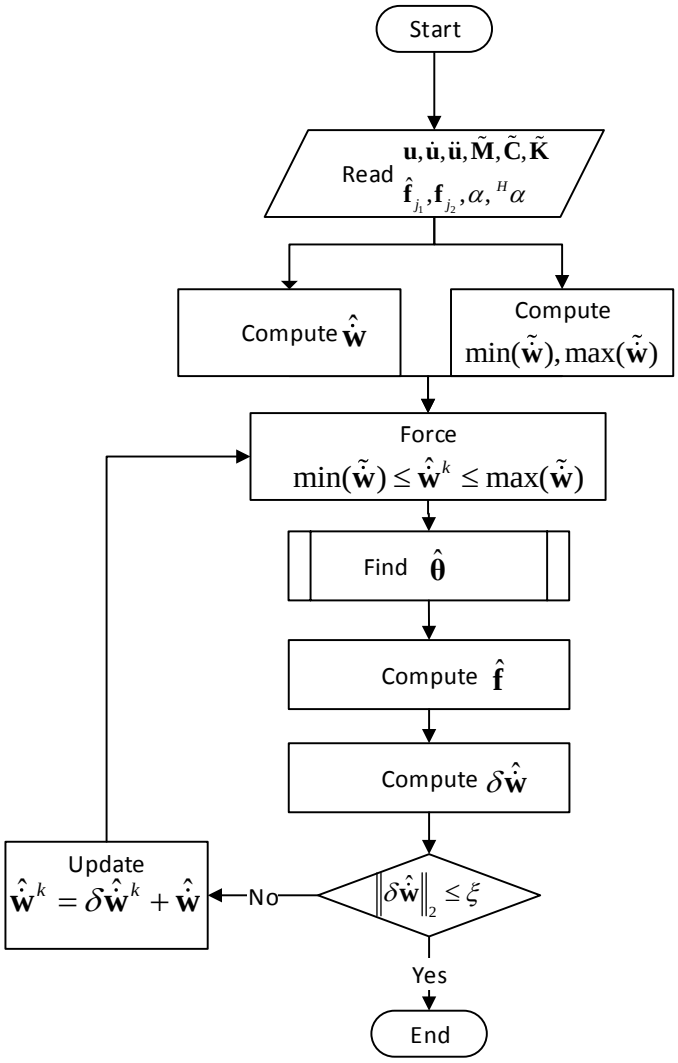

Figure II-1: Algorithm of the I-DITER method

Damage Index Vector

The best estimation of the unknown structural parameters, $\hat{\theta}$, can be determined once equation (2.24) is minimized. However, the final objective of DITER is to locate and size damages of a structure. To address the objective, damage indices are introduced. If $\hat{\boldsymbol{\theta}}^I$ is the identified or given structural parameters of an intact state of a structure, and $\hat{\boldsymbol{\theta}}^C$ is the estimated parameters of the current state of the structure, a Damage Index Vector (DIV), $\boldsymbol{\varphi}$, that corresponds to the damages occurred in the structural parameters is defined as follow:

$$\boldsymbol{\varphi} = \frac{\hat{\boldsymbol{\theta}}^I - \hat{\boldsymbol{\theta}}^C}{\hat{\boldsymbol{\theta}}^I} \tag{2.46}$$

Elements of DIV, φ_i, refer to the type and location of damages, and magnitudes of φ_i represent the severity of damages. The maximum value of each element is restricted to 1. A positive value shows that the corresponding structural element is damaged. A negative value, on the other hand, implies a structural healing. Thus, in a damaged area, each DIV's element has a value in the range of $[0,1]$ where zero means no damage and one implies a complete failure (losing a structural member). Note that DIV is in fact a vector with three sub-vectors, ${}^k\boldsymbol{\varphi}$, ${}^m\boldsymbol{\varphi}$, and ${}^c\boldsymbol{\varphi}$ that are associated with damages occurred to the stiffness, mass, and damping characteristics, respectively. Therefore, a refined definition of DIV can be presented as:

$$\boldsymbol{\varphi} = \left[{}^k\boldsymbol{\varphi}^T, {}^m\boldsymbol{\varphi}^T, {}^c\boldsymbol{\varphi}^T \right]^T \tag{2.47}$$

where a positive value of the i^{th} element of ${}^k\boldsymbol{\varphi}^T$ (i.e. ${}^k\varphi_i$) implies stiffness damages in the i^{th} structural element with the severity correlated to the magnitude of ${}^k\varphi_i$. The same is true for the DIVs of ${}^m\boldsymbol{\varphi}$ and ${}^c\boldsymbol{\varphi}$. Note that in case of unknown excitations, ${}^m\boldsymbol{\varphi}$ should be eliminated from DIV.

Interpretation of DIV of dampers needs special attention. Damping properties of a structure might increase once some damages occur. For instance, Slastan and Pietrzko (1993) observed enlargement in the damping characteristic of an reinforced concrete beam

after initiation of cracks. Therefore, it is more appropriate to consider ${}^{c}\boldsymbol{\varphi}$, as a tool to track the location and magnitude of changes in damping values.

SUMMARY

In this chapter, the DITER equation was derived, and the required objective function was presented for conditions of having either known or unknown excitations. The solution of the objective function contains the interested unknown structural properties. In addition, the effect of the variation of the static deflection on the DITER results was discussed. Additional unknown parameters introduced to the unknown vector to reduce the influence of the variation of the static deflections on the damage detection results. Finally, an iterative LSE approach was developed for the cases with missing load data. A lower and upper boundaries were also proposed to limit the variations of the unknown work rate, which may enhance the convergence of I-DITER.

CHAPTER III
APPLICATION OF THE DITER METHOD TO SHEAR BEAM STRUCTURES

INTRODUCTION

Shear beam models have been employed vastly in structural dynamic literatures to represent the simplest dynamic description of a structure. The idea is to reduce a system into a MDOFs lumped mass model where each node, i.e. lumped mass location, has only one DOF. Thus, the complexity of a real structure is ignored, while the results are still suitable for an initial analysis. Hence, it is a good practice to study DITER performance for shear beam models before applying it to more complex structures such as beams and frames. In this chapter, first, the terms of the DITER equation are obtained for a general n-DOF shear beam model. Next, a seven-story damped shear beam model is presented, and its dynamic responses are obtained numerically. The application of DITER to the model has been studied where different damaged scenarios have been presented by reducing values of mass, stiffness and damping characteristics of the structure. At the end of the chapter, cases with limited input knowledge and effects of noise pollutions are presented.

DITER EQUATION FOR SHEAR BEAM MODELS

Problem Formulation

Consider a n-story shear beam model consisting of n nodal masses (lumped mass) and n viscous type dampers as shown in Figure III-1. Each story has a stiffness of k_i, mass of m_i, and viscous energy dissipaters with a damping coefficient of c_i. To keep the generality of the problem, non-proportional damping has been considered in the system. The structure has been excited by applying a load vector $\mathbf{f}_i$ at each node. In all the above terms, subscript i refers to the story number.

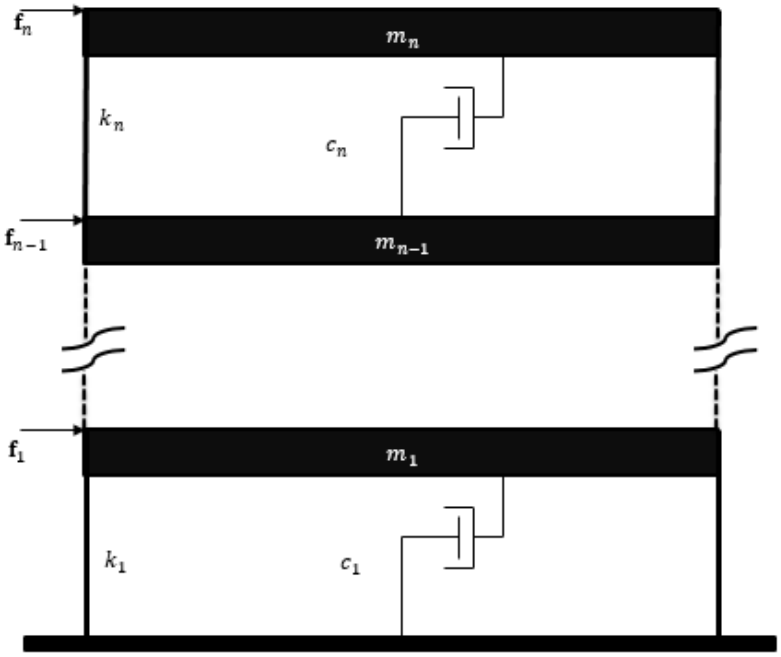

Figure III-1: n-DOFs shear beam model

The structural properties and the dynamic responses of the model are related by the following equation of motions:

$$\mathbf{M}\ddot{\mathbf{u}} + \mathbf{C}\dot{\mathbf{u}} + \mathbf{K}\mathbf{u} = \mathbf{f} \tag{3.1}$$

where $\mathbf{M}$, $\mathbf{K}$, and $\mathbf{C}$ represent mass, stiffness, and damping matrices, respectively. $\mathbf{M}$ is a diagonal matrix whose first element corresponds to the lumped mass of the first story. The stiffness and damping of the model shape the following bounded matrices:

$$\mathbf{M} = \begin{bmatrix} m_1 & & \\ & \ddots & \\ & & m_n \end{bmatrix}$$

$$\mathbf{K} = \begin{bmatrix} k_1 + k_2 & -k_2 & & & \\ -k_2 & \ddots & & & \\ & & k_i + k_{i+1} & -k_{i+1} & \\ & & -k_{i+1} & \ddots & -k_n \\ & & & -k_n & k_n \end{bmatrix} \quad \mathbf{C} = \begin{bmatrix} c_1 + c_2 & -c_2 & & & \\ -c_2 & \ddots & & & \\ & & c_i + c_{i+1} & -c_{i+1} & \\ & & -c_{i+1} & \ddots & -c_n \\ & & & -c_n & c_n \end{bmatrix} \tag{3.2}$$

Vector $\mathbf{u}$ contains nodal displacements. $\dot{(\cdot)}$ and $\ddot{(\cdot)}$ show first and second time derivatives, respectively.

Instead of using the coupled EOMs, the DITER equation may be used to identify the structural parameters. Thus, the rate of the strain and kinetic energy of each story must be obtained along with the power of the excitation forces and the rate of the dissipated energy. Considering the j^{th} story and describing its relative nodal displacements by $r_j = u_{j+1} - u_j$, for any time instants of collected data the followings can be found:

$$\begin{aligned} \dot{T}_j &= \ddot{u}_j \dot{u}_j m_j \\ \dot{U}_j &= \dot{r}_j r_j k_j \\ \dot{W}_j &= f_j \dot{u}_j \\ \dot{D}_j &= \dot{r}_j^2 c_j \end{aligned} \tag{3.3}$$

where $\dot{T}_j$ and $\dot{U}_j$ are the rate of the kinetic and strain energies of the j^{th} story , respectively. $\dot{W}_j$ denotes the rate of the work done by the external forces to this story, and $\dot{D}_j$ is the rate of the dissipated energy.

The DITER Equation for the Complete Input Data

If the applied external forces are available, then DITER might be used to identify the structural mass, stiffness, and damping properties. In such a case, the observations are consisted of the rate of the work done on the system, and equation (2.22) governs the identification problem. Therefore, the next task is to obtain the required elements of this equation.

Equation (3.3) provides adequate information to construct the DITER equation of the shear beam model. Maintaining the assumption of the time-invariant characteristic of the structural properties during the data collection interval, $\mathbf{G}$, $\mathbf{\Gamma}$, $\mathbf{D}$, and the rate of the external work are obtained as follows:

$$\mathbf{G}=\begin{bmatrix} g_{1,0} & \cdots & g_{\mathrm{n},0} \\ & \vdots & \\ g_{1,p} & \cdots & g_{n,p} \end{bmatrix} \qquad \mathbf{\Gamma}=\begin{bmatrix} \gamma_{1,0} & \cdots & \gamma_{\mathrm{n},0} \\ & \vdots & \\ \gamma_{1,p} & \cdots & \gamma_{n,p} \end{bmatrix}$$
$$\mathbf{D}=\begin{bmatrix} d_{1,0} & \cdots & d_{\mathrm{n},0} \\ & \vdots & \\ d_{1,p} & \cdots & d_{n,p} \end{bmatrix} \qquad \dot{\mathbf{w}}=\begin{bmatrix} \dot{w}_0 & \cdots & \dot{w}_p \end{bmatrix}^T \tag{3.4}$$

where

$$g_{j,m}=\ddot{u}_{j,t_m}\dot{u}_{j,t_m} \qquad j=1,2,\cdots,\mathrm{n}$$
$$\gamma_{j,m}=\dot{r}_{j,t_m}r_{j,t_m} \qquad m=0,1,\cdots,p$$
$$d_{j,m}=\dot{r}^2_{j,t_m}$$
$$\dot{w}_m=\sum_{j=1}^{n} f_{j,\mathrm{t}_m}\dot{u}_{j,\mathrm{t}_m}$$

Thus, the components of equation (2.22) can be written as:

$$\mathbf{H}=\begin{bmatrix}\mathbf{\Gamma} & \mathbf{D} & \mathbf{G}\end{bmatrix}$$
$$\mathbf{y}=\dot{\mathbf{w}} \tag{3.5}$$
$$\boldsymbol{\theta}=\begin{bmatrix} k_1 & \cdots & k_n & c_1 & \cdots & c_n\, m_1 & \cdots & m_n \end{bmatrix}^T$$

Substituting the above matrices into equation (2.24), the best estimation of the unknown structural parameters can be obtained. Once $\boldsymbol{\theta}$ is identified for different states of the structure, location and severity of damages may be obtained by forming DIV using equations (2.47).

The DITER Equation for Limited Input Data

It is not always possible or economic to measure the external forces at all DOFs employed in the DITER method. In these cases, the observation vector, $\mathbf{y}$, derived from equation (2.20) is no longer valid, and it must be determined from equation (2.38). The unknown structural properties and the DIV should be computed from the iterative procedure of I-DITER as well.

In I-DITER, the DITER equation should be created and optimized at each iteration until the criterion introduced in equation 2.41 is satisfied. For this purpose, the followings can be acquired for the k^{th} iteration:

$$\begin{aligned}
&\mathbf{H} = \begin{bmatrix} \boldsymbol{\Gamma} & \mathbf{D} \end{bmatrix} \\
&\hat{\mathbf{y}}^k = \hat{\dot{\mathbf{w}}}^k - \dot{\mathbf{T}} \\
&\hat{\boldsymbol{\theta}}^k = \begin{bmatrix} k_1^k & \cdots & k_n^k & c_1^k & \cdots & c_n^k \end{bmatrix}^T
\end{aligned} \tag{3.6}$$

where $\boldsymbol{\Gamma}$ and $\mathbf{D}$ are as described in equation. (3.4). $\dot{\mathbf{T}}$ represents the rate of the kinetic energy as:

$$\begin{aligned}
&\dot{\mathbf{T}} = \begin{bmatrix} T_0 & \cdots & T_p \end{bmatrix} \\
&\dot{T}_m = \sum_{j=1}^{n} m_j g_{j,m}
\end{aligned} \tag{3.7}$$

and $\hat{\dot{\mathbf{w}}}^k$ is computed by.:

$$\begin{aligned}
&\hat{\dot{\mathbf{w}}}^k = \begin{bmatrix} \hat{\dot{w}}_0^k & \cdots & \hat{\dot{w}}_p^k \end{bmatrix}^T \\
&\hat{\dot{w}}_m^k = \sum_{j_1} f_{j_1,\mathrm{t}_m}^{k-1} \dot{u}_{j_1,\mathrm{t}_m} + \sum_{j_2} f_{j_2,\mathrm{t}_m} \dot{u}_{j_2,\mathrm{t}_m} \quad \text{where } j_1 + j_2 = n
\end{aligned} \tag{3.8}$$

where j_2, j_1 denote the nodes with known and unknown load magnitudes , respectively.

If the last known structural properties are available, the convergence process of I-DITER might be enhanced by bounding the updated rate of the work done on the system by employing equation 2.42 whose form for the n-story shear beam model is:

$$\tilde{\dot{W}}_i = \sum_{j=1}^{NEL} \left(1 + {}^{H}\alpha_j^m - \alpha_j^m\right) \ddot{u}_j \dot{u}_j m_j + \sum_{j=1}^{NEL} \left(1 + {}^{H}\alpha_j^k - \alpha_j^k\right) \dot{r}_j r_j \tilde{k}_j + \sum_{j=1}^{ND} \left(1 + {}^{H}\alpha_j^c - \alpha_j^c\right) \dot{r}_j^2 \tilde{c}_j \tag{3.9}$$

In equation (3.9) $\tilde{k}$ and $\tilde{c}$ are respectively the last known stiffness and damping properties of the structure. Other terms are as described in equation (2.44) and equation (2.46).

The excitations at the k^{th} iteration must be updated by first, substituting the obtained parameters of the last iteration into equation (3.2), and then substituting the results in equation (3.1). The iteration continues until the convergence is acquired.

ASSESSMENT OF DITER VIA NUMERICAL EXAMPLE EXPERIMENTS

Description of the Test Model

To verify the proposed approach, a numerical shear beam story example is presented. The model is a 7-story shear beam structure equipped with dashpots to simulate viscous damping behavior (see Figure III-2). The experiment is designed to address the DITER performance in:

- Identifying structural properties in the intact state, i.e. in creating a baseline
- Finding multiple damages in a system with non-proportional damping characteristics under varying excitations
- Identifying unknown forces along with other unknown structural properties
- Detecting damages with noise-polluted data

To extract the dynamic responses, the structure is excited with two sets of White Gaussian Noises (WGN) applied at the second and seventh stories. Linear acceleration method is employed to obtain the displacements, velocities, and accelerations, at the DOFs. Data are collected at frequencies of 100 Hz and 1000 Hz. The intensity of the forces, the values of lumped masses, story stiffness values, and dashpot constants are shown in Table III-1 and Table III-2 for the intact and damaged states of the structure, respectively.

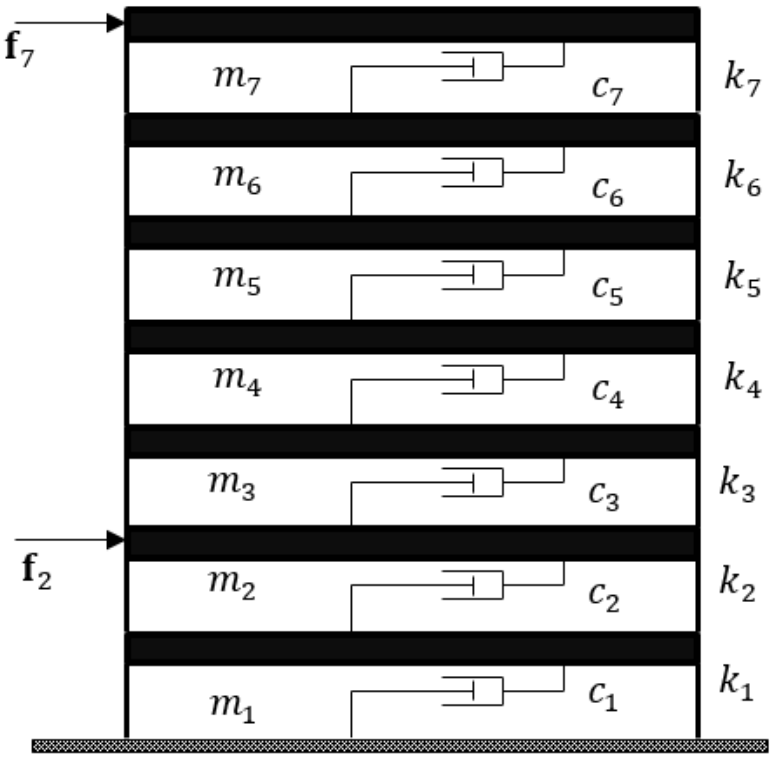

Figure III-2: Selected 7-story shear beam model

Table III-1: Structural properties and applied excitations in the intact states

Story	Stiffness	Dashpot	Mass	Force (WGN)
	kips/in	kips.s/in	kips.s^2/in	Intensity(kips)
1	1800	2.7	2	0
2	1200	2.5	2	210
3	600	3.7	2	0
4	600	1.5	1.5	0
5	550	2	1.5	0
6	550	2	1	0
7	550	1	1	90

Table III-2: Structural properties and applied excitations in the damaged states

Story	Stiffness	Dashpot	Mass	Force (WGN)
	kips/in	kips.s/in	kips.s^2/in	Intensity(kips)
1	1440	2.70	2.0	0
2	840	2.25	1.4	210
3	540	3.70	1.6	0
4	480	0.75	0.9	0
5	495	1.90	1.5	0
6	275	1.60	0.8	0
7	550	0.70	0.5	90

Take note that the forces are generated randomly; hence, while the intensities remain constant, the final magnitude and direction of the excitation forces are different for each case. This helps to observe if the method is affected by the variation of the applied loads.

Natural frequencies of the intact and damaged states of the structure are shown in Table III-3 and Table III-4, respectively. Note that, there is no specific trend that shows the variations in the values of the natural frequencies between the intact and damaged states by which one can determine the possible damages. While the first and the second frequencies show a slight growth, the third and the last ones experienced a small reduction. This is the result of the simultaneous changes happened in the mass and stiffness constants, which adversely affects the damage identification results of the natural frequency-based methods.

Table III-3: Natural frequencies of the 7-story shear beam model in the intact state

No.	1	2	3	4	5	6	7
f (Hz)	0.853	2.221	3.455	4.369	5.423	6.461	6.925

Table III-4: Natural frequencies of the 7-story shear beam model in the damaged states

No.	1	2	3	4	5	6	7
f (Hz)	0.864	2.261	3.392	4.399	5.861	6.491	6.728

Description of the Studied Cases

It is intended to study the performance of DITER when the structure suffers a multiple-damaged state in which its mass, stiffness and/or damping properties are simultaneously degraded. To make the experiment more realistic, the excitations vary from case to case. This helps to observe if the method's performance is affected by the variation of the applied loads as the model is exposing to the damages. To address the goals, six different cases have been studied. Data sampling is performed in 100 Hz for the first four cases; while, sampling of 1000 Hz is preferred for the last two cases.

1. **Case 0i**

This case is designed to identify the intact structural properties. The results form a baseline for the further monitoring of the structure. In this case, the data are assumed to be noiseless and the forces are known. Here, the main purpose is to study the system identification aspect of DITER.

2. **Case 0d**

A damaged scenario is applied to the structure to study the method's effectiveness in dealing with multiple damages with small to large magnitudes. A damage parameter, φ, (DP) is employed to reduce the stiffness, mass and dashpot constants of the stories of the structure. The damage parameter is defined as follow (similar to DIV):

$$\varphi = -\frac{(.)^{*} - (.)}{(.)}$$

The employed damage parameters for case 0d are shown in Table III-5. The natural frequencies of the damaged state can be found in Table III-4.

Table III-5: Applied damages to the 7-story shear beam model

Story	φ_k	φ_c	φ_m
1	20%	0%	0%
2	25%	10%	25%
3	10%	0%	20%
4	20%	35%	35%
5	10%	5%	0%
6	35%	20%	20%
7	0%	25%	30%

Zero values of DPs are intentionally introduced to keep some parameters undamaged to investigate for damage leakage. Damage leakage refers to an effect in which existence of damage in a member, here a story, affects the identification accuracy of the adjacent members' properties. Damage leakage is undesired as it might result in false positive damage detections.

3. Case 1i

The purpose of this case is to assess the ability of DITER when the excitations are unknown. To generate the data, the intact structure is excited similarly to case 0i. As described in the second chapter, it is more efficient, but not necessary, to use the last known structural properties to make the initial estimates of the unknown forces. Thus, hypothetically, the parameters shown in Table III-6 have been selected to be the last known properties of the structure. The parameters are selected close to the range of the intact values; however, to keep the generality, the values are deviated arbitrarily from the corresponding intact values. In other words, it is assumed that the values presented in Table III-6 have been provided from the last application of DITER on the structure. These values, have been used to impose the upper and lower boundaries to the work rate term of the DITER equation (see equation (2.43) to equation (2.46)).

Table III-6: The last known properties of the 7-story shear beam

Story	Stiffness	Dashpot	Mass
	kips/in	kips.s/in	kips.s^2/in
1	2250	2.70	2.0
2	1500	3.25	2.0
3	810	4.81	2.0
4	810	2.18	1.5
5	743	2.00	1.5
6	550	2.90	1.0
7	1100	1.10	1.0

4. Case 1d

The ultimate goal of DITER is to locate damages and assessing their severities. Thus, it is important to check DITER results accuracy when damages occur to the structure while limited information is available about the forces. Thus, in this case, damages introduced in case 0d are imposed to the model, and the response data is collected while the excitations applied at the second and last floors are unknown. Comparing the results of case 1d to case 1i, the performance of I-DITER method might be assessed under the unknown excitation circumstances.

5. Case 0in

The assumption of noiseless data is not always realistic. Noises may contain instruments (such as accelerometers) inaccuracy or model uncertainties. To consider the effect of noises to the results of the intact system identification, artificial White Gaussian Noises (WGN) with certain intensities have been added to the measured responses of each DOF. Following the same approach employed by Ling and Haldar (2004), the intensities are considered to be 1%, 2%, 3% and 5% of the root mean square (RMS) of the measured responses at each DOF. In the noisy circumstances, finer data resolution helps to obtain more accurate results. Thus, a 1 kHz sampling frequency is employed to collect the required data. For the same reason, duration of the data collection is increased from four seconds to thirty two seconds.

6. Case 0dn

In the case 0dn, identical damage parameters of case 0d have been applied to the structural parameters. The data are assumed to be noise-polluted by adding artificial noises following the same pattern introduced in the case 0in. The DIV is obtained using the results of cases 0dn and 0in.

Beside the regular LSE method, DIV has been obtained by applying a total least square estimation method as well. The justification for this attempt is the fact that both sides of the DITER equation have been perturbed by the noises simultaneously. A comparison is made between the results accuracy obtained using the conventional least square estimation and the total least square estimation methods. This comparison is performed for the case in which the data are polluted with noises of three percent intensity.

Results and Discussions

1. Case 0i and case 0d

Cases 0i and 0d refer to the experiments in which excitations are provided and noiseless-data are collected with sampling frequency of 100 Hz for four seconds.

Results of the structural properties identification including stiffness, dashpot and mass constants are respectively tabulated in Table III-7 through Table III-9. As the tables imply, the baseline identification is performed accurately for all the properties, which verifies the identification ability of DITER.

Detected damages for the above properties are shown in Figure III-3 through Figure III-5. Comparison between the introduced damage parameters and the obtained DIV demonstrates high accuracy of DITER in locating and sizing damages. Damages detected in a story have left no effect on the identification of the adjacent stories' properties. Thus, the method may be free from damage leakage problem. In addition, multiple damage cases with varying external loads are captured precisely. Therefore, variation in loading does not impact the DITER results. This is an important aspect of the method, as it is cumbersome to excite a structure with identical dynamic loads every time

that the damage identification is performed. The results verify that for a clean set of data, the DITER performance is completely acceptable for the shear beam model.

Table III-7: Detected damages in the story stiffness, Cases 0i and 0d

Story	Stiffness (kips/in)				DP	DIV
	Undamaged		Damaged			
	Given	Identified	Given	Identified		
1	1800	1800	1440	1440	20%	20%
2	1200	1200	900	900	25%	25%
3	600	600	540	540	10%	10%
4	600	600	480	480	20%	20%
5	550	550	495	495	10%	10%
6	550	550	358	357	35%	35%
7	550	550	550	550	0%	0%

Table III-8: Detected damages in the dashpots, Cases 0i and 0d

Story	Dashpot (kips.s/in)				DP	DIV
	Undamaged		Damaged			
	Given	Identified	Given	Identified		
1	2.7	2.7	2.70	2.70	0%	0%
2	2.5	2.5	2.25	2.25	10%	10%
3	3.7	3.7	3.70	3.70	0%	0%
4	1.5	1.5	0.98	0.98	35%	35%
5	2.0	2.0	1.90	1.90	5%	5%
6	2.0	2.0	1.60	1.60	20%	20%
7	1.0	1.0	0.75	0.75	25%	25%

Table III-9: Detected damages in the nodal mass, Cases 0i and 0d

Story	Mass (kips.s^2/in)				DP	DIV
	Undamaged		Damaged			
	Given	Identified	Given	Identified		
1	2.0	2.0	2.00	2.00	0%	0%
2	2.0	2.0	1.50	1.50	25%	25%
3	2.0	2.0	1.60	1.60	20%	20%
4	1.5	1.5	0.98	0.97	35%	35%
5	1.5	1.5	1.50	1.50	0%	0%
6	1.0	1.0	0.80	0.80	20%	20%
7	1.0	1.0	0.70	0.70	30%	30%

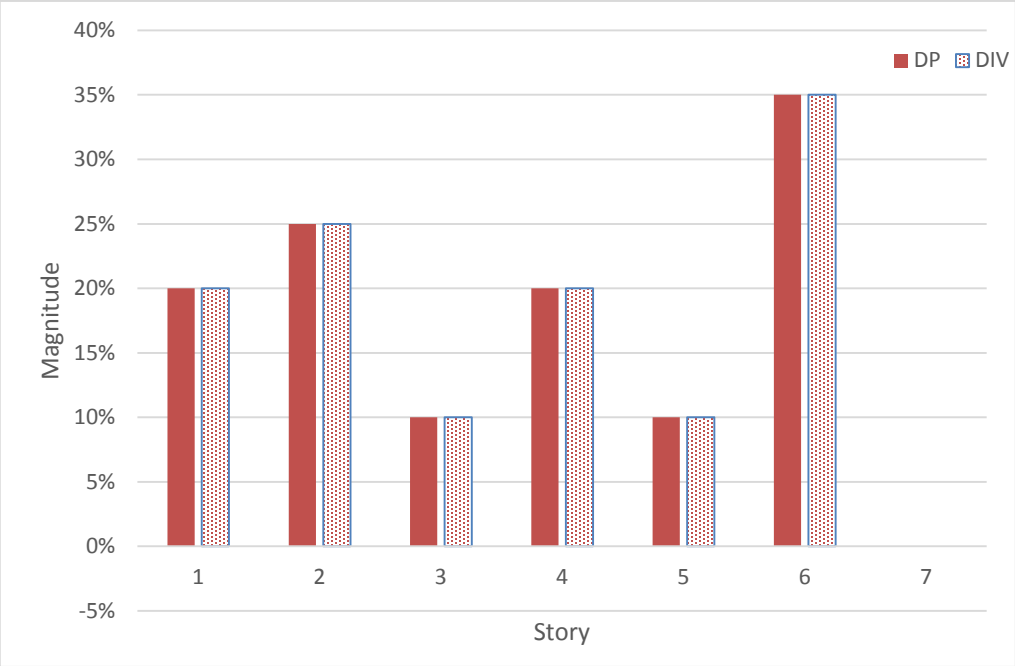

Figure III-3: Detected damages in the stories' stiffness of the shear beam model, Cases 0i and 0d

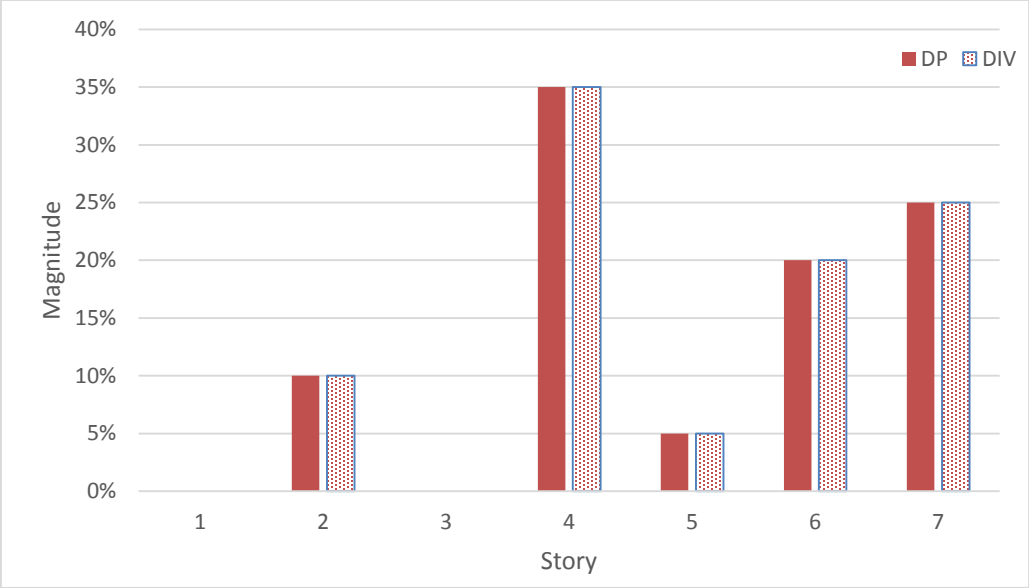

Figure III-4: Detected damages in the dashpots of the shear beam model, Cases 0i and 0d

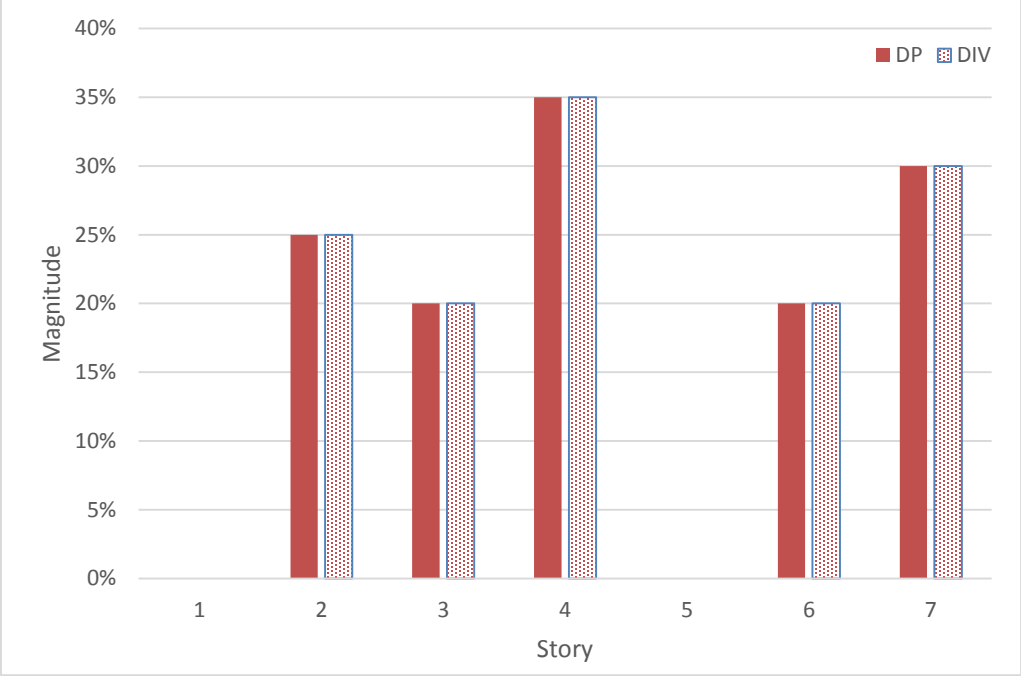

Figure III-5: Detected damages in the masses of the shear beam model, Cases 0i and 0d

2. Case 1i and case 1d

In these cases, four-second duration dynamic response data have been collected with 100 Hz sampling frequency. The applied loads at the 2nd and 7th stories, shown in Figure III-8 and Figure III-9, are considered unknown. The unknown parameters include stiffness and dashpot constants. Similar to the known input procedure, the first step is to baseline structure for which the I-DITER method should be applied. Initial values must be estimated for the unknown excitations at all instants. While the values can be set to zero, the last known structural properties, Table III-6, along with the collected responses have been used to estimate the unknown excitations.

To obtain the work rate boundaries, the maximum expected reduction and healing factors must be selected in advance. In this study, a large value of 80% damage factor and a 10% healing factor are selected for all the stiffness and dashpot values, i.e. $\alpha_k = \alpha_c = 0.8$ and ${}^{H}\alpha_k = {}^{H}\alpha_c = 0.1$. The boundaries are shown in Figure III-6 and Figure III-7 for the intact and damaged states, respectively. The threshold for the convergence criterion is selected to be $\xi = 1$ kip.in/s for the both cases. The errors in the severity of damages are less than 1%, which shows that the selected threshold is adequately small.

The method converged after 172 and 66 iterations for the case 1i and case 1d, respectively.

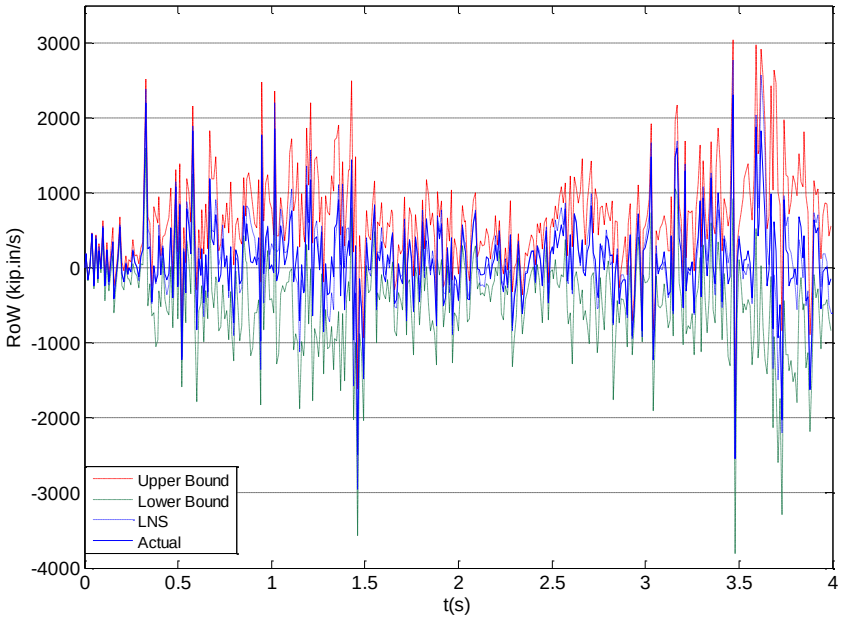

Figure III-6: Applied boundaries to the rate of the work (RoW) of case 1i, LNS is the rate of the work computed based on the last known structural properties.

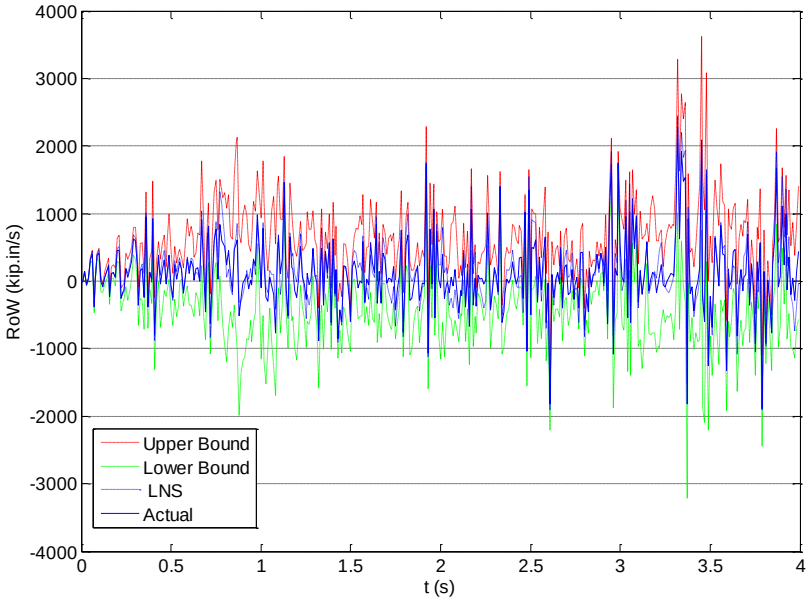

Figure III-7: Applied boundaries to the rate of the work (RoW) of case 1d, LNS is the rate of the work computed based on the last known structural properties.

The results of case 1i are shown in the first three columns of Table III-10 and Table III-11. Variations between the identified and actual properties are less than 1%, which is quite acceptable. Similar to case i1, the structural properties are identified in the damaged states, and correspondingly, the damage index vector is obtained and shown in Table III-10 and Table III-11. Figure III-10 and Figure III-11 compare the introduced damages, DP, and the obtained damage index vector, DIV. The maximum variation between DP and DIV is less than one percent, which verifies the applicability of I-DITER to detect damages in the structural properties for cases with limited input data.

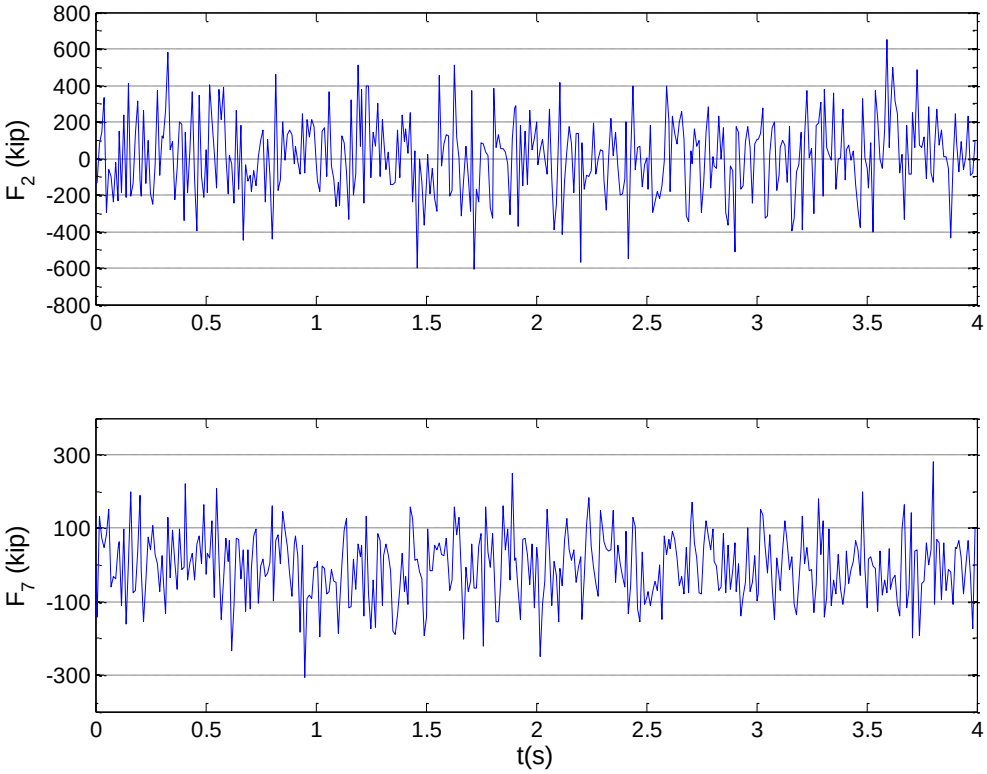

Figure III-8: Loads applied to the 2nd and 7th nodes, Case 1i

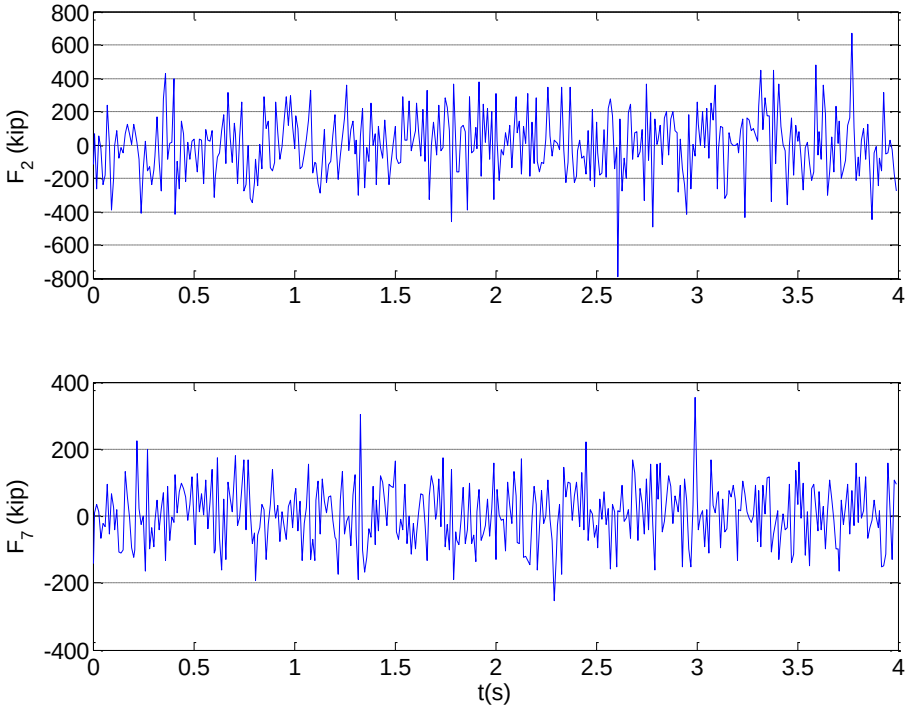

Figure III-9: Loads applied to the 2nd and 7th nodes, Case 1d

Table III-10: Detected damages in the stories' stiffness, Cases 1i and 1d

Story	Stiffness (kips/in)				DP	DIV
	Undamaged		Damaged			
	Given	Identified	Given	Identified		
1	1800	1800	1440	1440	20%	20%
2	1200	1200	900	900	25%	25%
3	600	600	540	540	10%	10%
4	600	600	480	480	20%	20%
5	550	550	495	495	10%	10%
6	550	550	358	358	35%	35%
7	550	550	550	550	0%	0%

Table III-11: Detected damages in dashpot constants, Cases 1i and 1d

Story	Dashpot (kips.s/in)				DP	DIV
	Undamaged		Damaged			
	Given	Identified	Given	Identified		
1	2.70	2.70	2.70	2.70	0%	0%
2	2.50	2.50	2.25	2.25	10%	10%
3	3.70	3.70	3.70	3.70	0%	0%
4	1.50	1.50	0.98	0.97	35%	35%
5	2.00	2.00	1.90	1.90	5%	5%
6	2.00	2.00	1.60	1.60	20%	20%
7	1.00	1.01	0.75	0.75	25%	25%

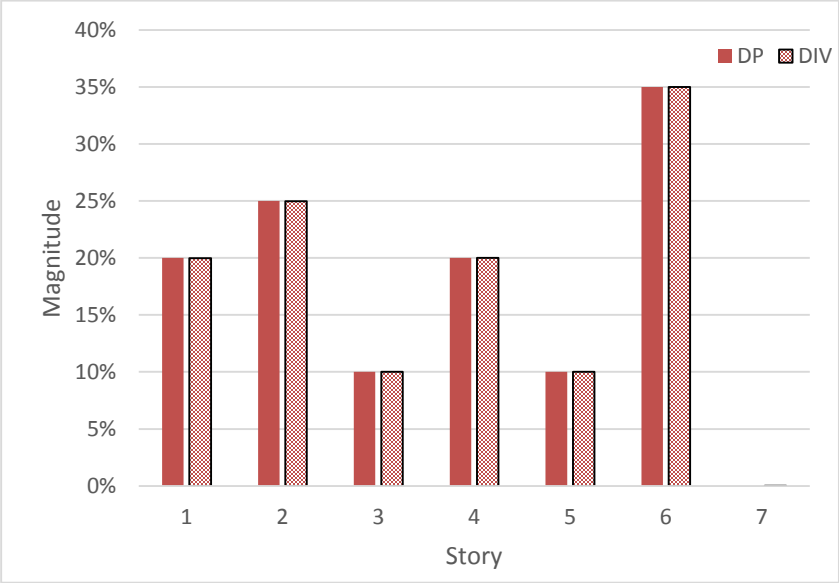

Figure III-10: DIV of story stiffness, Cases 1i and 1d

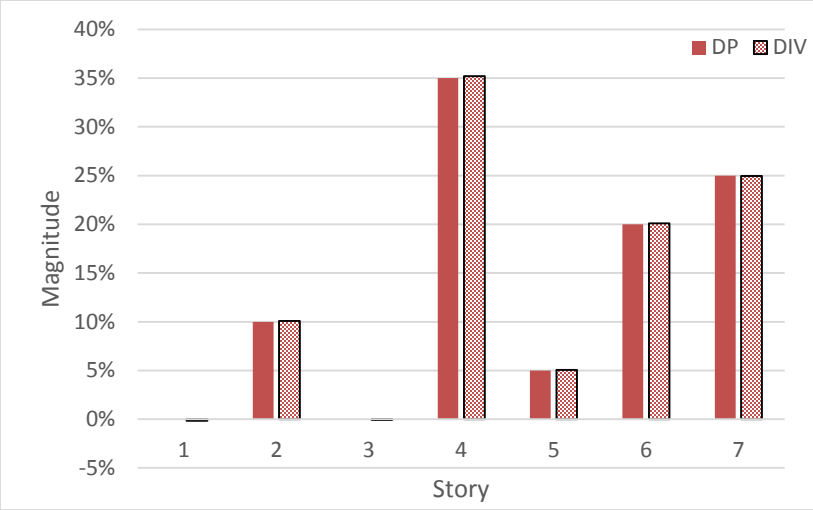

Figure III-11: DIV of dashpot constants, Cases 1i and 1d

In addition to the unknown structural properties, I-DITER is able to estimate the applied excitations. The differences between identified and actual external forces are shown in Figure III-12 and Figure III-13 for the intact and damaged states, respectively. The maximum discrepancy is smaller than 0.1 kips. Note that, regardless of the states of the loads i.e., being known or unknown, I-DITER estimates all the excitations. If it is desired, one may increase the accuracy by choosing a smaller threshold.

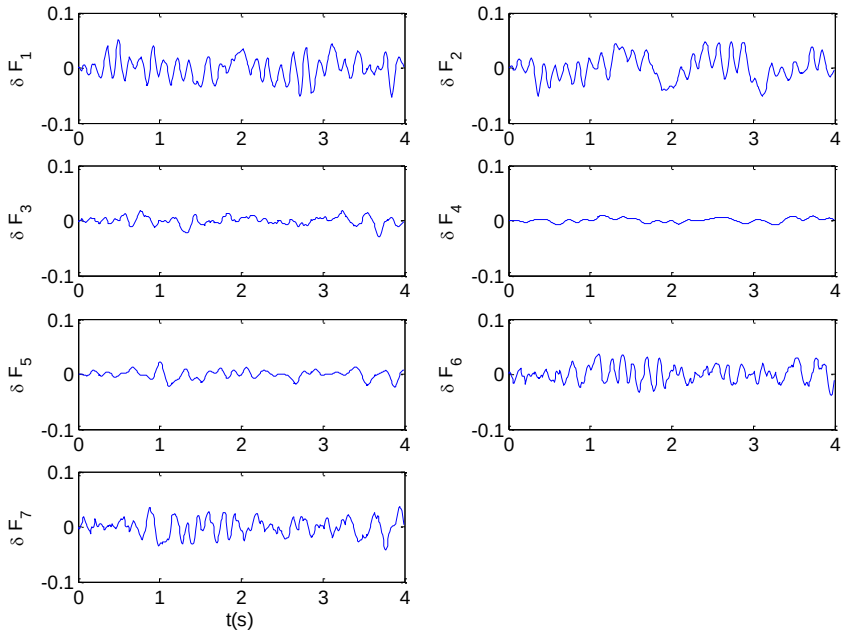

Figure III-12: Variation in the identified loads of case 1i, the vertical axes are in kips, and the horizontal axes show the time in seconds. $\delta F_i = \left(F_{Identified}\right)_i - \left(F_{Actual}\right)_i$

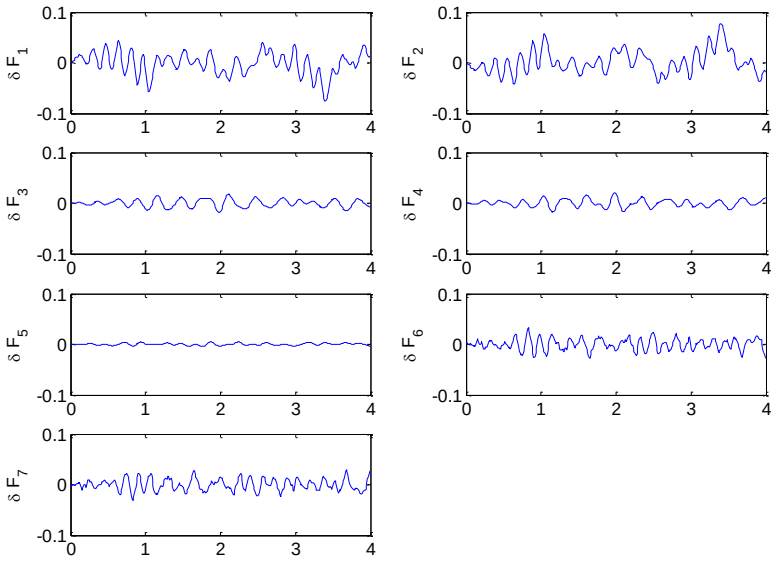

Figure III-13: Variations in the identified loads of case 1d, the vertical axes are in kips, and the horizontal axes show the time in seconds.

Figure III-14 through Figure III-17 demonstrate the convergence of stiffness and dashpot identification of the intact and damaged states. The convergence of I-DITER depends on the applied loads, which is the reason that compared to the damaged state, the intact state demands more iteration to converge.

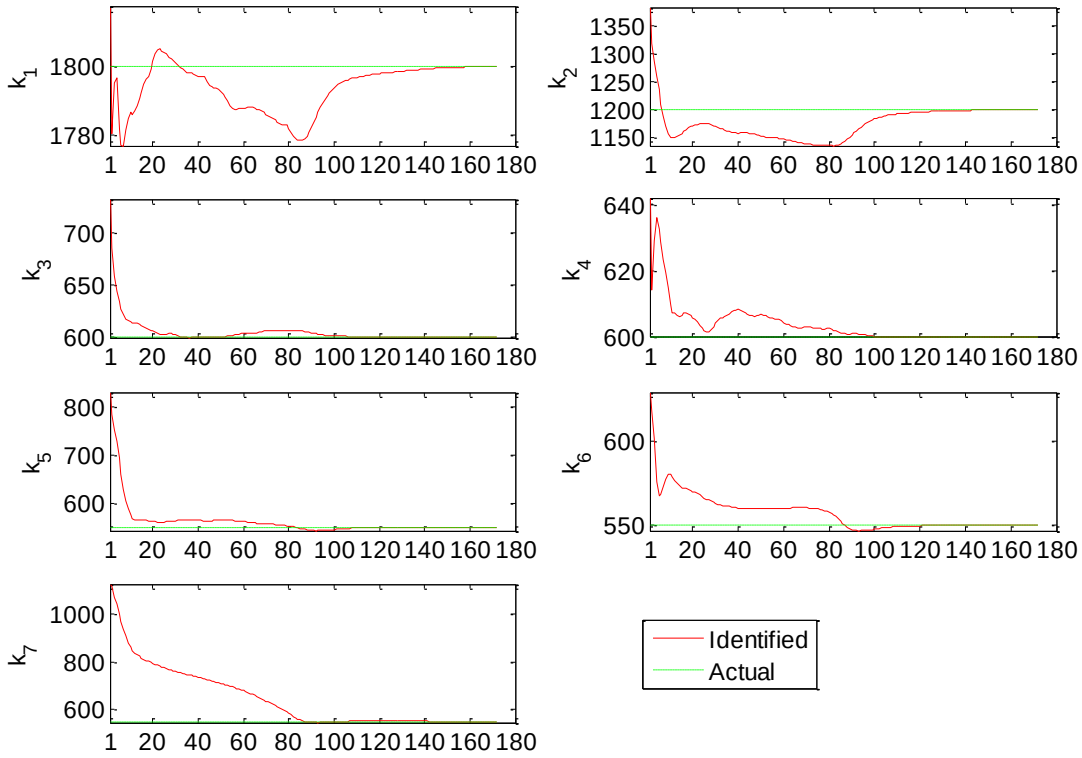

Figure III-14: Convergence of the identified stories' stiffness values of case 1i, vertical axes values are in kips/in, and the horizontal axes show the number of iterations.

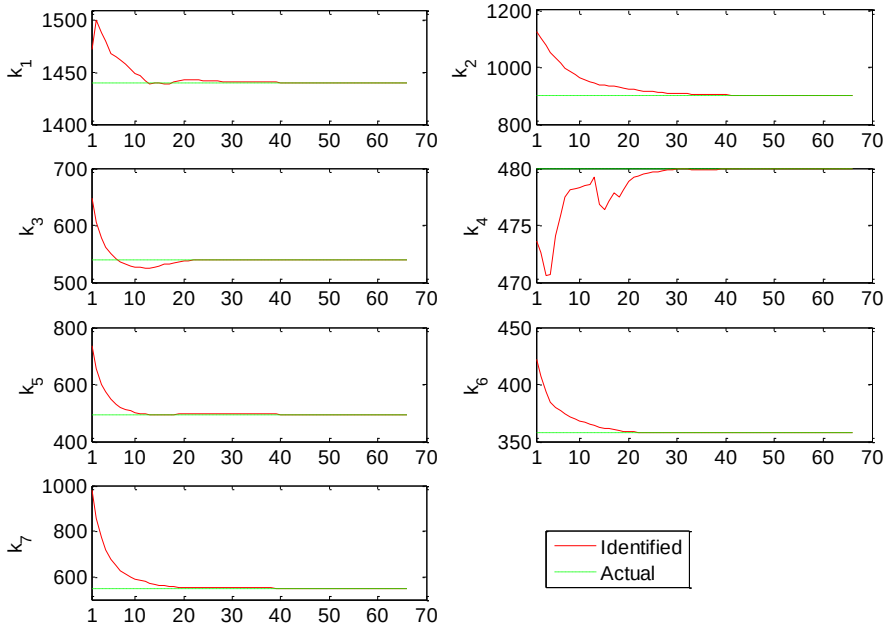

Figure III-15: Convergence of the identified stories' stiffness values of case 1d, vertical axes values are in kips/in, and the horizontal axes show the number of iterations.

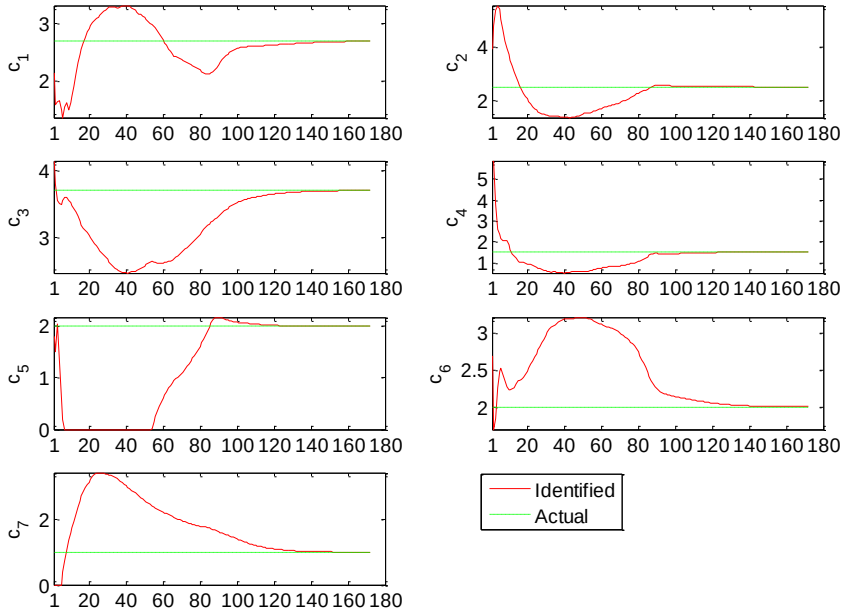

Figure III-16: Convergence of the identified dashpot constants of case 1i, vertical axes values are in kips.s/in, and the horizontal axes show the number of iterations.

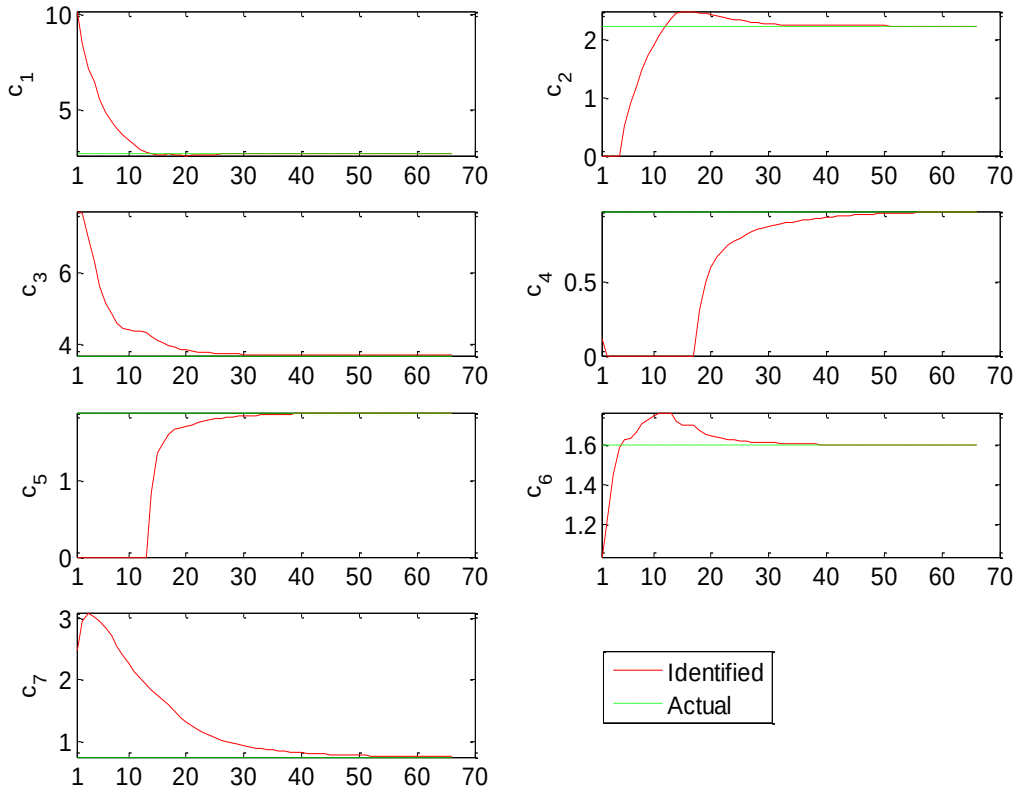

Figure III-17: Convergence of the identified dashpot constants of case 1d, vertical axes values are in kips.s/in, and the horizontal axes show the number of iterations.

3. Case 0in and case 0dn

The finall two cases address the performance of DITER against the noise-polluted data. 1% and 2% noisy data samples have been shown in Figure III-18 and Figure III-19.

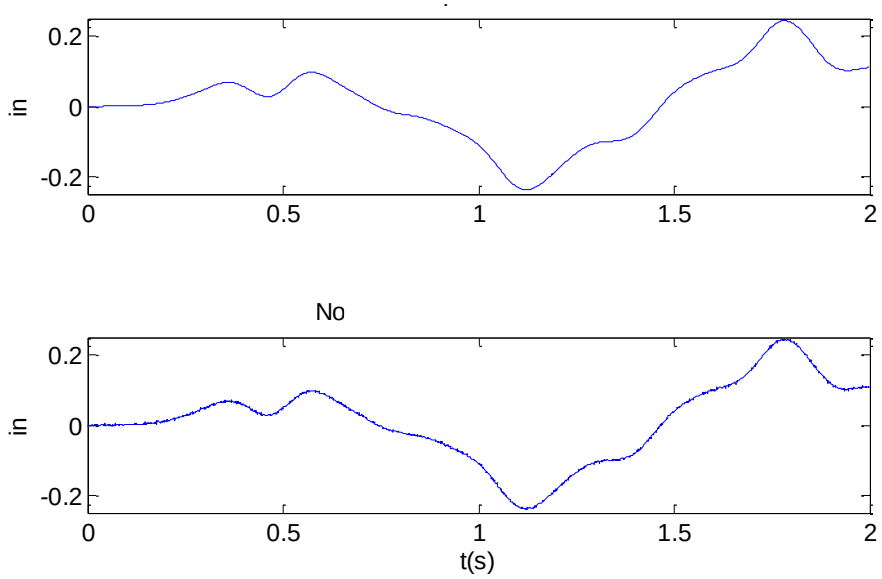

Figure III-18: Top) Noiseless, Bottom) 1% noise-polluted displacement data at the 5th story, Case 0in

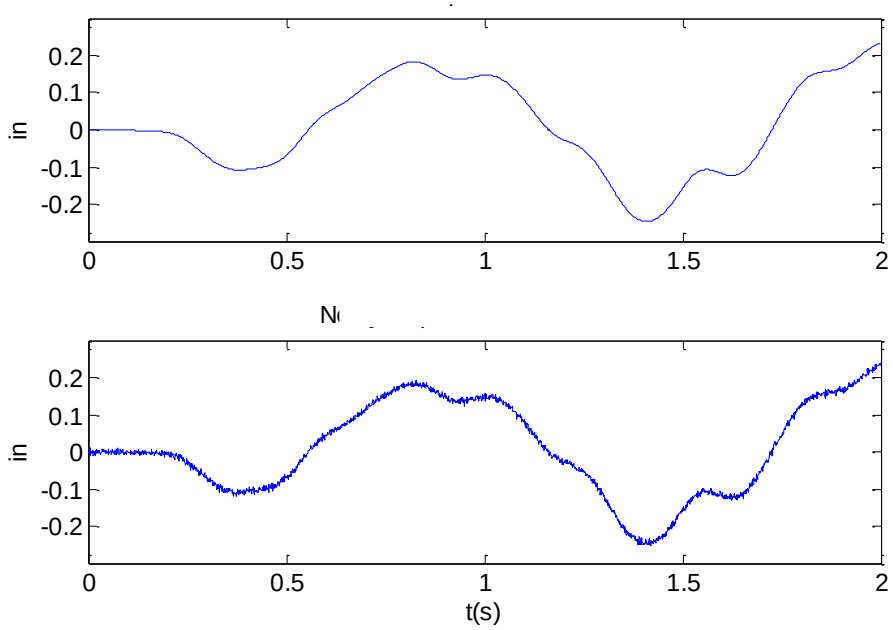

Figure III-19: Top) Noiseless, Bottom) 2% noise-polluted displacement data at the 5th story, Case 0id

Results of the system identification and the obtained DIV are tabulated in Table III-12 through Table III-14 for the one percent noise pollution, Table III-15 through Table III-17 for the two percent noise poluttion, and finally Table III-18 through Table III-20 for the five percent noise intensity. No attempt is performed to remove noises thorugh filtering. In otherwords, the noisy data has been directly fed to DITER to assess the method's sensitivity to the raw noisy data.

It can be observed that in the case of one percent noise, mass and stiffness values are identified accurately. Small deviations in the magnitude of the identified dashpot values can be observed. Nevertheless, DIVs of all the properties are in acceptable range. Similarly, for the two percent noise intensity, the stiffness and mass constants are still identified accurately, and merely small deviations in the detected severity of the dashpot damages can be noticed. Yet, dashpot damages are located perfectly. As the noises become stronger and reach intensities of five percent, false positive damages emerge into the obtained DIVs of mass, stiffness, and dashpot parameters. The accuracy of the identified severities are also adversly affected. Yet, the results are on a conservative side except for the dashpot DIV where the method has skipped a damge that occurred in the dashpot at the fourth story. Figure III-29 through Figure III-31 indicate DP and DIV of all of the studied noisy cases. It is concluded that, even without performing any data cleansing, DITER performance is highly dependable in small and moderately small noise intensities. However, in moderately large noise pollution, before applying DITER, it is suggested to decrease the noise pollution by applying appropriate filtering to the raw data.

Table III-12: Detected damages in the story stiffness, Cases 0i & 0d, 1% noise intensity

Story	Stiffness (kips/in)				Actual Damage	Identified Damage
	Undamaged		Damaged			
	Given	Identified	Given	Identified		
1	1800	1798	1440	1437	20%	20%
2	1200	1199	900	898	25%	25%
3	600	599	540	538	10%	10%
4	600	599	480	478	20%	20%
5	550	548	495	492	10%	10%
6	550	549	358	356	35%	35%
7	550	548	550	546	0%	0%

Table III-13: Detected damages in the dashpots, Cases 0i & 0d, 1% noise intensity

Story	Damping (kips.s/in)				Actual Damage	Identified Damage
	Undamaged		Damaged			
	Given	Identified	Given	Identified		
1	2.7	2.65	2.70	2.77	0%	-4%
2	2.5	2.53	2.25	2.23	10%	12%
3	3.7	3.69	3.70	3.68	0%	0%
4	1.5	1.52	0.98	1.00	35%	34%
5	2.0	1.99	1.90	1.85	5%	7%
6	2.0	1.99	1.60	1.59	20%	20%
7	1.0	0.98	0.75	0.75	25%	24%

Table III-14: Detected damages in mass values, Cases 0i & 0d, 1% noise intensity

Story	Mass (kips.s^2/in)				Actual Damage	Identified Damage
	Undamaged		Damaged			
	Given	Identified	Given	Identified		
1	2.0	2.0	2.00	2.00	0%	0%
2	2.0	2.0	1.50	1.50	25%	25%
3	2.0	2.0	1.60	1.59	20%	20%
4	1.5	1.5	0.98	0.97	35%	35%
5	1.5	1.5	1.50	1.50	0%	0%
6	1.0	1.0	0.80	0.80	20%	20%
7	1.0	1.0	0.70	0.70	30%	30%

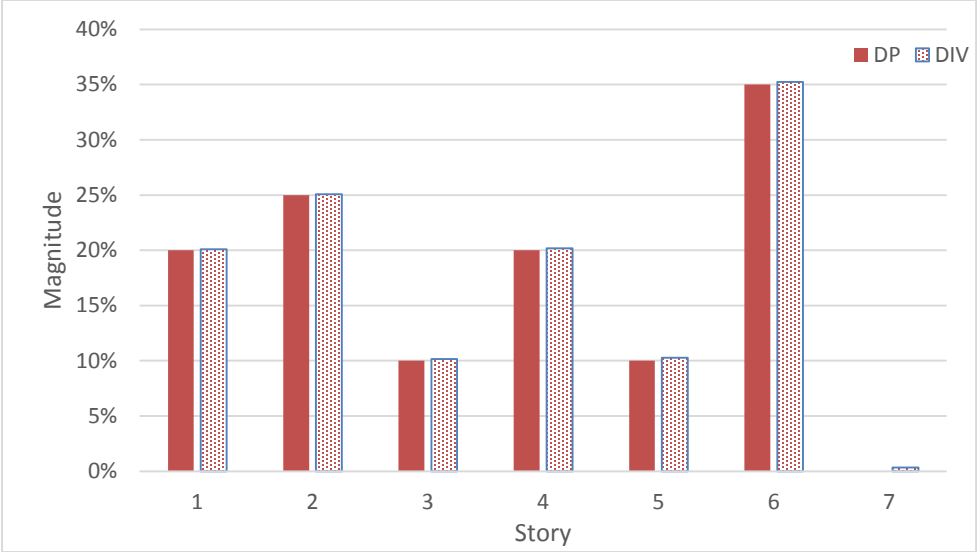

Figure III-20: DIV of story stiffness 1% noise-polluted data

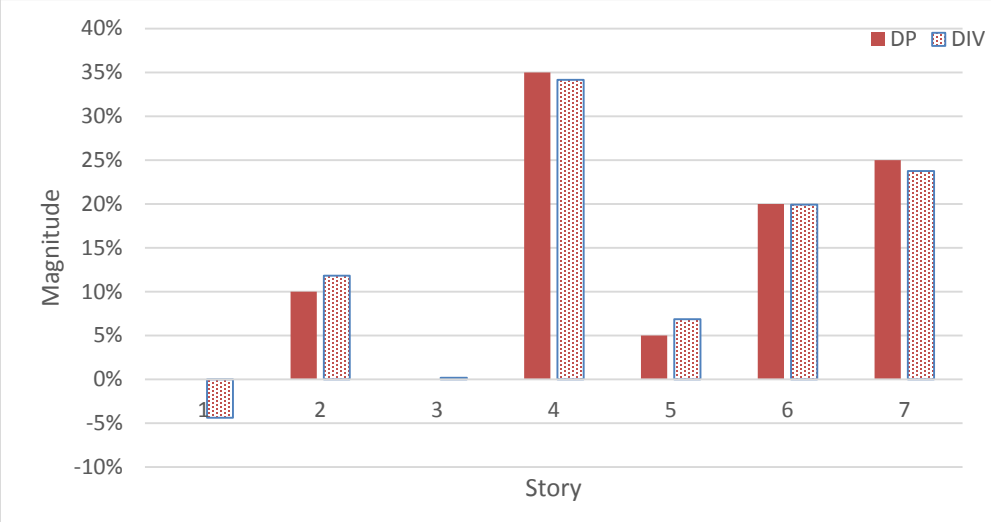

Figure III-21: DIV of dashpot constants, 1% noise-polluted data

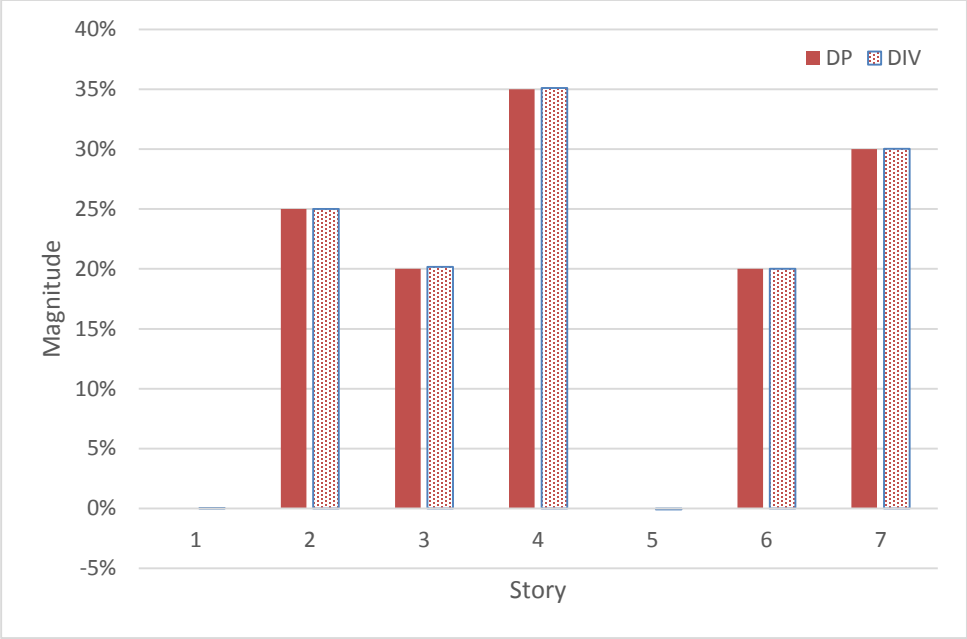

Figure III-22: DIV of mass, 1% noise-polluted data

Table III-15: Detected damages in the stiffness, Cases 0i and 0d, 2% noise intensity

Story	Stiffness (kips/in)				Actual Damage	Identified Damage
	Undamaged		Damaged			
	Given	Identified	Given	Identified		
1	1800	1788	1440	1425	20%	20%
2	1200	1193	900	893	25%	25%
3	600	594	540	532	10%	10%
4	600	594	480	475	20%	20%
5	550	544	495	489	10%	10%
6	550	548	358	354	35%	35%
7	550	538	550	530	0%	2%

Table III-16: Detected damages in the dashpots, Cases 0i & 0d, 2% noise intensity

Story	Damping (kips.s/in)				Actual Damage	Identified Damage
	Undamaged		Damaged			
	Given	Identified	Given	Identified		
1	2.7	2.8	2.70	2.83	0%	-2%
2	2.5	2.6	2.25	2.28	10%	11%
3	3.7	3.6	3.70	3.68	0%	-3%
4	1.5	1.6	0.98	0.95	35%	42%
5	2.0	2.0	1.90	1.85	5%	6%
6	2.0	2.0	1.60	1.57	20%	23%
7	1.0	1.0	0.75	0.76	25%	21%

Table III-17: Detected damages in the mass values, Cases 0i & 0d, 2% noise intensity

Story	Mass (kips.s^2/in)				Actual Damage	Identified Damage
	Undamaged		Damaged			
	Given	Identified	Given	Identified		
1	2.0	2.0	2.00	1.99	0%	0%
2	2.0	2.0	1.50	1.50	25%	25%
3	2.0	2.0	1.60	1.58	20%	20%
4	1.5	1.5	0.98	0.96	35%	35%
5	1.5	1.5	1.50	1.49	0%	0%
6	1.0	1.0	0.80	0.79	20%	20%
7	1.0	1.0	0.70	0.70	30%	30%

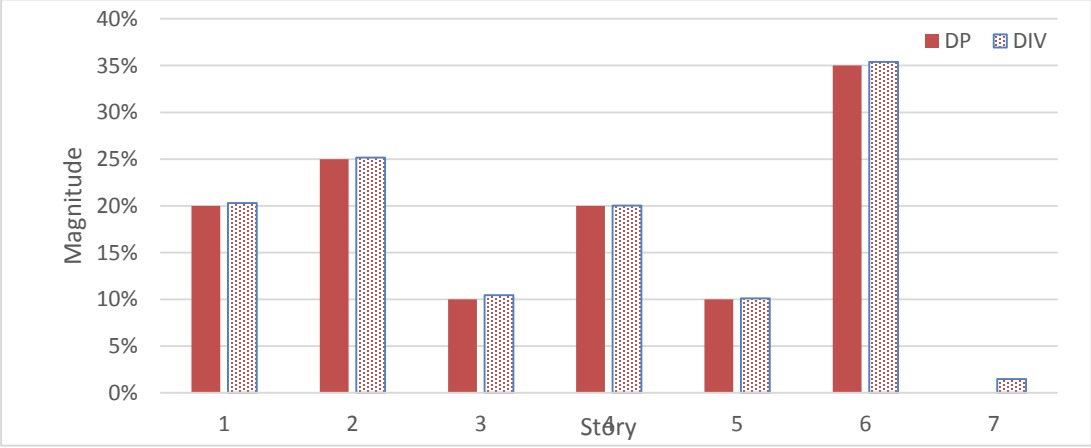

Figure III-23: DIV of story stiffness, 2% noise-polluted data

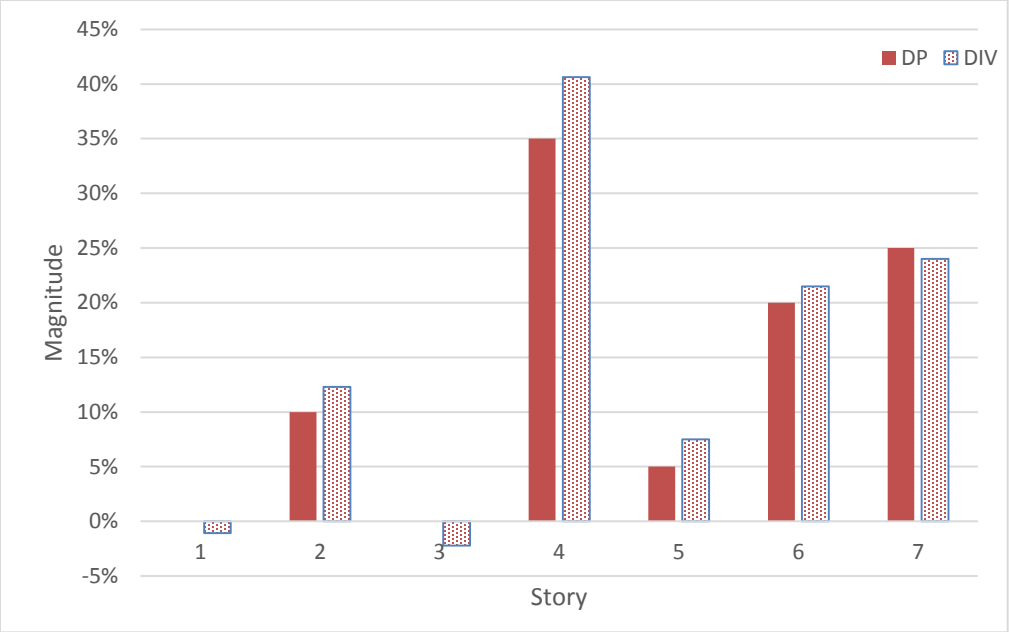

Figure III-24: DIV of dashpot constants, 2% noise-polluted data

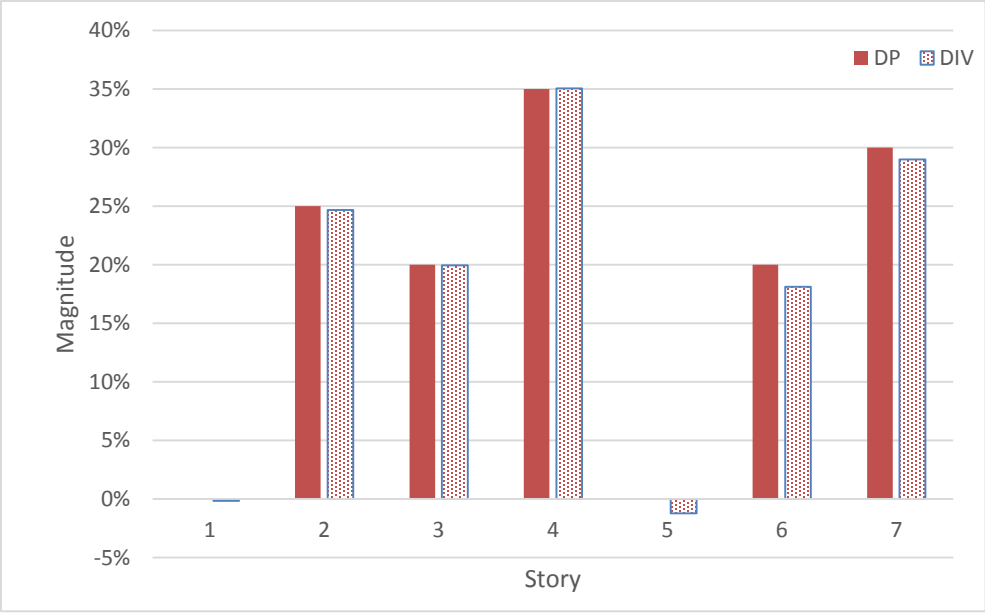

Figure III-25: DIV of mass, 2% noise-polluted data

Table III-18: Detected damages in the stiffness, Cases 0i and 0d, 5% noise intensity

Story	Stiffness (kips/in)				Actual Damage	Identified Damage
	Undamaged		Damaged			
	Given	Identified	Given	Identified		
1	1800	1707	1440	1354	20%	21%
2	1200	1139	900	838	25%	26%
3	600	561	540	498	10%	11%
4	600	550	480	415	20%	25%
5	550	469	495	436	10%	7%
6	550	508	358	306	35%	40%
7	550	496	550	420	0%	15%

Table III-19: Detected damages in the dashpots, Cases 0i & 0d, 5% noise intensity

Story	Damping (kips.s/in)				Actual Damage	Identified Damage
	Undamaged		Damaged			
	Given	Identified	Given	Identified		
1	2.7	2.33	2.70	3.11	0%	-34%
2	2.5	2.85	2.25	2.58	10%	9%
3	3.7	3.81	3.70	3.24	0%	15%
4	1.5	1.11	0.98	1.26	35%	-14%
5	2.0	1.24	1.90	1.10	5%	11%
6	2.0	1.96	1.60	1.54	20%	21%
7	1.0	1.42	0.75	0.86	25%	39%

Table III-20: Detected damages in the mass values, Cases 0i & 0d, 5% noise intensity

Story	Mass (kips.s^2/in)				Actual Damage	Identified Damage
	Undamaged		Damaged			
	Given	Identified	Given	Identified		
1	2.0	1.9	2.00	1.90	0%	-1%
2	2.0	2.0	1.50	1.46	25%	25%
3	2.0	1.9	1.60	1.48	20%	20%
4	1.5	1.4	0.98	0.88	35%	36%
5	1.5	1.4	1.50	1.32	0%	4%
6	1.0	0.9	0.80	0.71	20%	19%
7	1.0	1.0	0.70	0.64	30%	33%

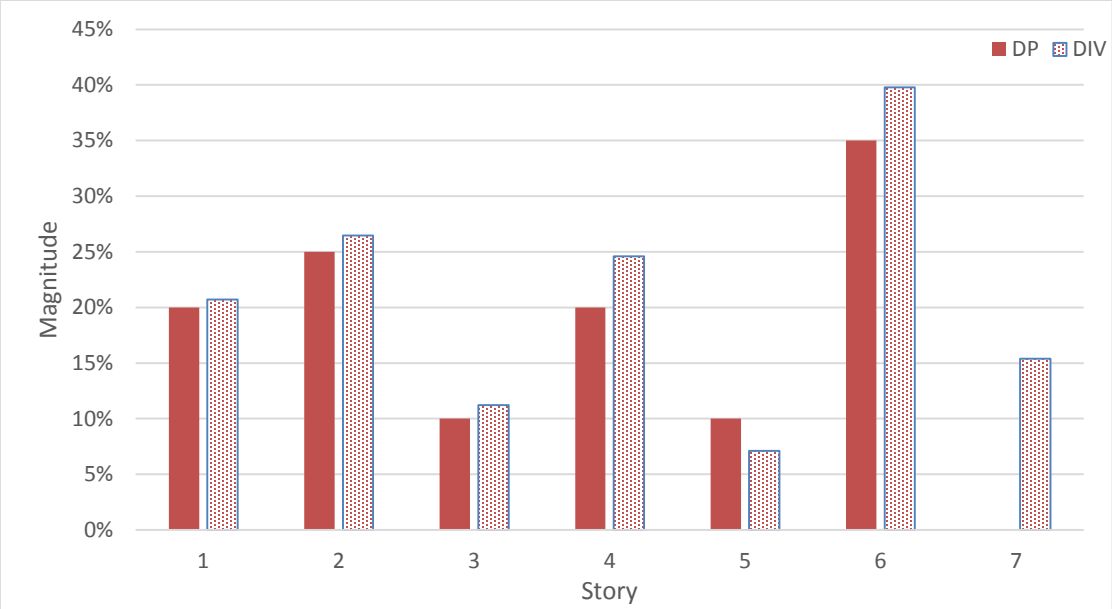

Figure III-26: DIV of story stiffness, 5% noise-polluted data

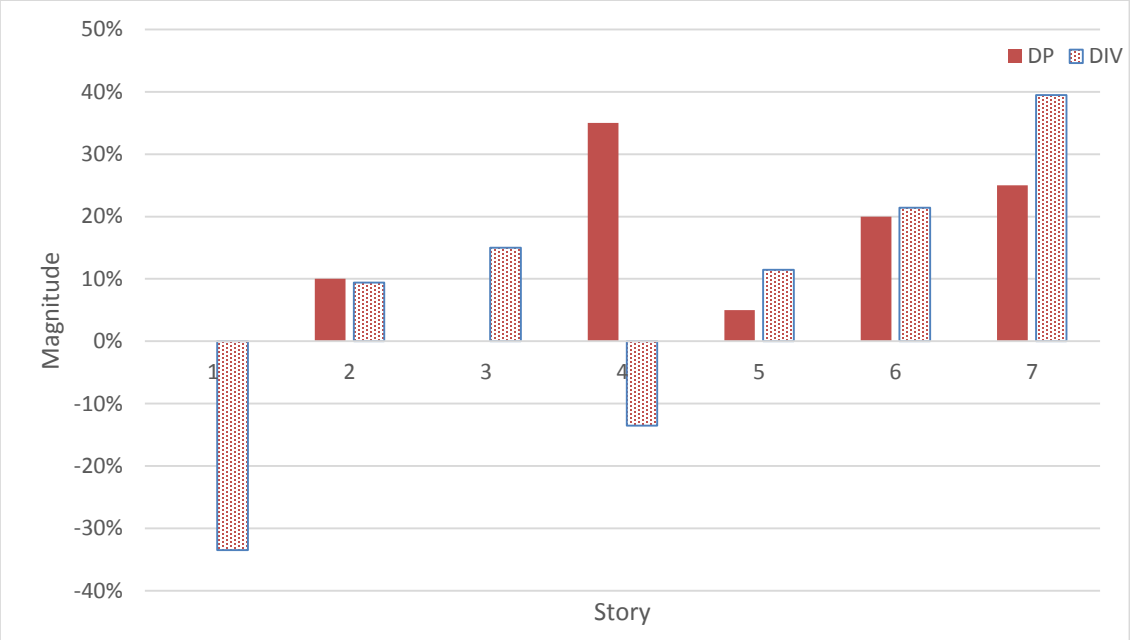

Figure III-27: DIV of dashpot constants, 5% noise-polluted data

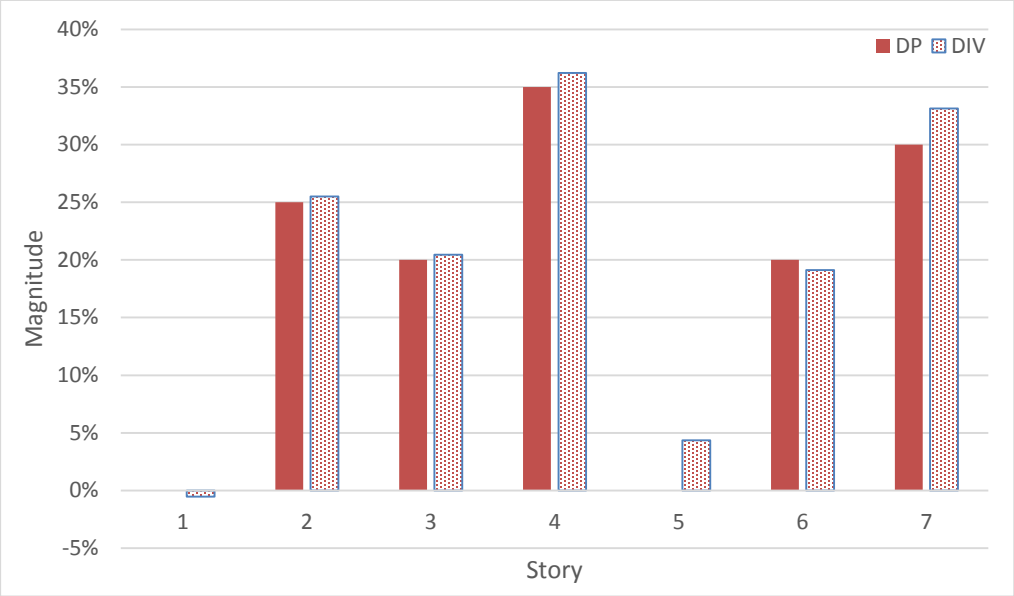

Figure III-28: DIV of mass, 5% noise-polluted data

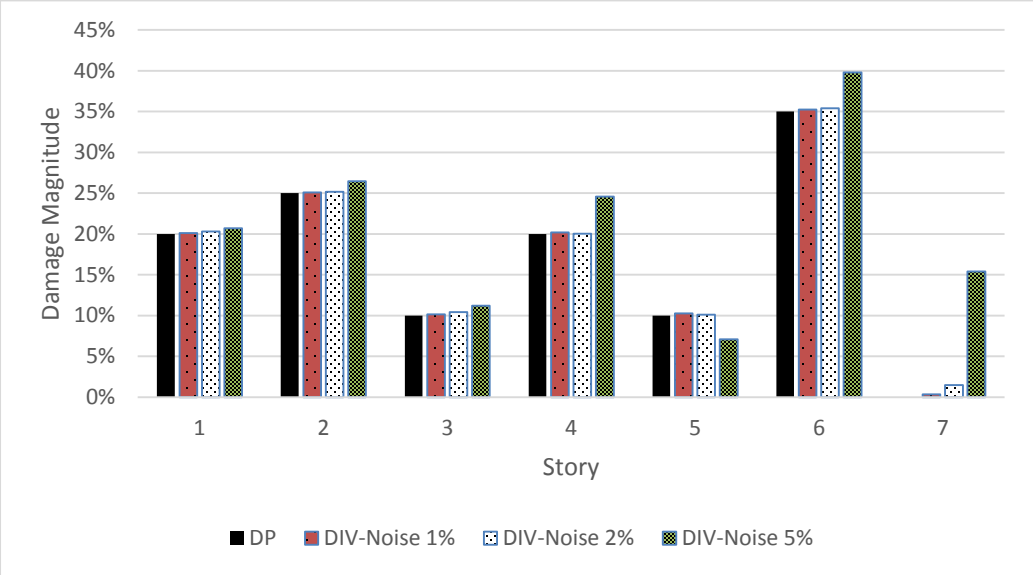

Figure III-29: DIV of story stiffness for all of the noise intensities

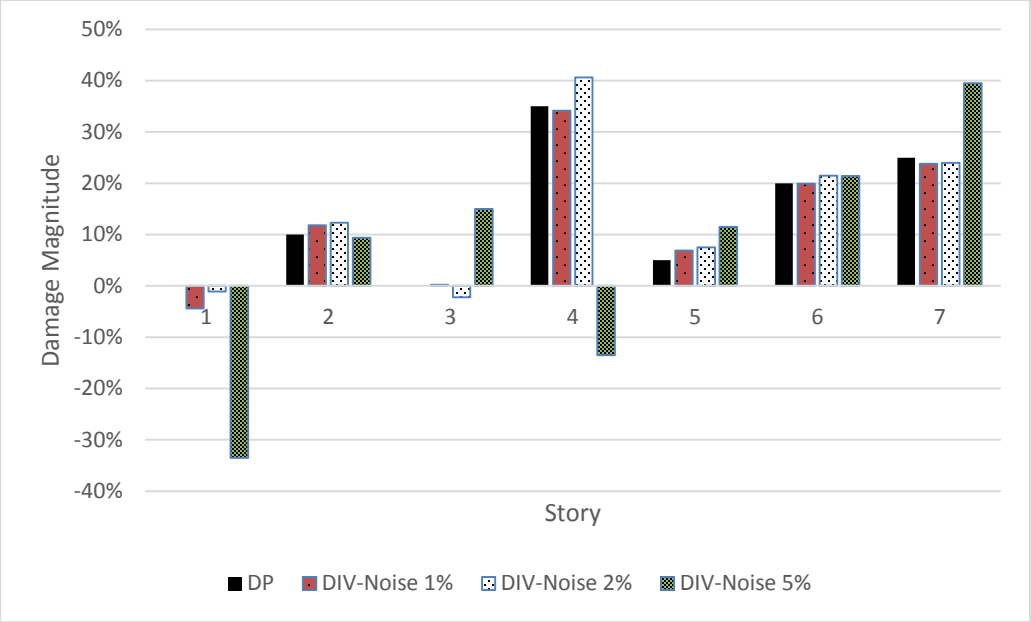

Figure III-30: DIV of dashpot constants for all of the noise intensities

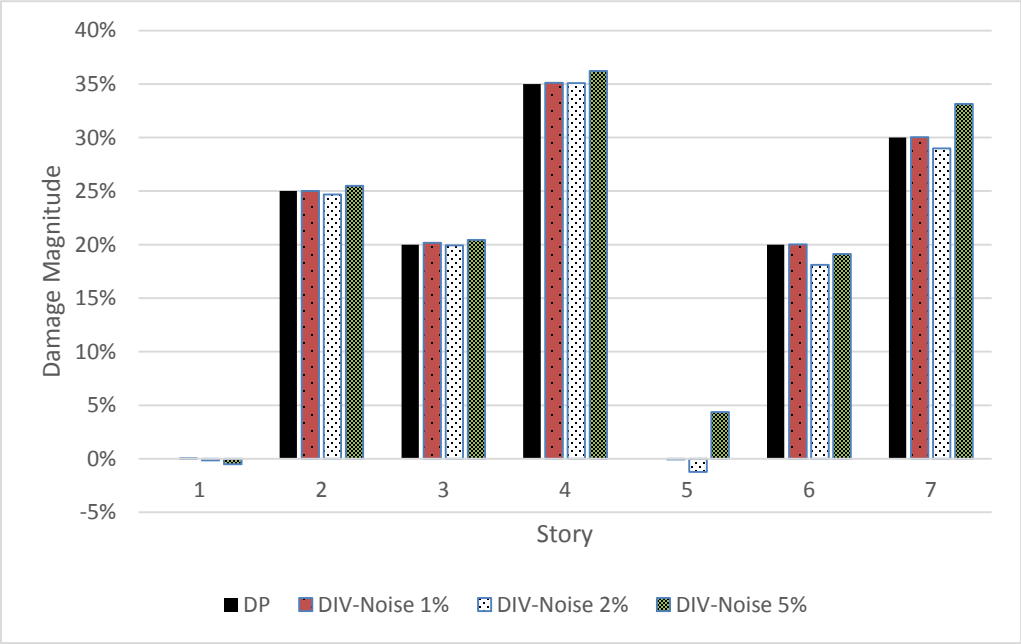

Figure III-31: DIV of mass for all of the noise intensities

The noises do not only affect the observation vector, but also they perturb the left hand side, **H**, of the DITER equation as well. In such cases, a total least square estimation (TLSE) may be preferable to the least square estimation. Therefore, for a case of three percent noise intensity, TLSE has been applied, and the results are compared to the conventional LSE.

According to Golub and Loan (1980), TLSE is intended to minimize the Frobenius norm of the matrix consisted of the perturbation of the data matrix and the observation vector as follows:

$$\begin{aligned} &\min: \left\| [\mathbf{E} \mid \boldsymbol{\varepsilon}] \right\|_F \\ &\text{Subject to: } \mathbf{y} + \boldsymbol{\varepsilon} \in \text{Range}\left([\mathbf{H} + \mathbf{E}] \right) \end{aligned} \tag{3.10}$$

where $\mathbf{E}$ and $\boldsymbol{\varepsilon}$ denote the perturbation in the data and the observation matrix, respectively.

The original formulation also contains weight matrices for $\mathbf{E}$ and $\boldsymbol{\varepsilon}$, which are replaced here by Identity matrices. They proposed a general singular value decomposition based solution for TLS problems and presented the solution to some special cases. For a special case, where $\mathbf{H}$ is a $p+1$ by l matrix with $l < p+1$, $\mathbf{y}$ is a $p+1$ by 1 vector, and matrix $\boldsymbol{\Omega}$ is defined as follow

$$\boldsymbol{\Omega} = [\mathbf{H} \mid \mathbf{y}] \tag{3.11}$$

If $\mathbf{H}$ is a full rank matrix and its l^{th} non-zero singular value, $\sigma_l^{\mathbf{H}}$, is larger than $(l+1)^{th}$ non-zero singular value of $\boldsymbol{\Omega}$, $\sigma_{l+1}^{\boldsymbol{\Omega}}$, then for our non-proportional damping shear beam, the unknown parameters can be found as:

$$\hat{\boldsymbol{\theta}}_{TLS} = \left(\mathbf{H}^T \mathbf{H} - \left(\sigma_{l+1}^{\boldsymbol{\Omega}} \right)^2 \mathbf{I} \right)^{-1} \mathbf{H}^T \mathbf{y} \tag{3.12}$$

As all the above conditions are satisfied for the current shear beam model, the unknown parameters of the last two cases are determined using equation (3.12) with noise pollutions of three percent intensity. The obtained DIVs based on the TLSE and LSE have been provided in Figure III-32 to Figure III-34. Based on the result, the accuracy of the identification, particularly in damage severity estimations, shows improvement once

TLSE has been deployed. Yet, a positive false damage detection in stiffness along with a negative false damage detection in the damping values can be observed.

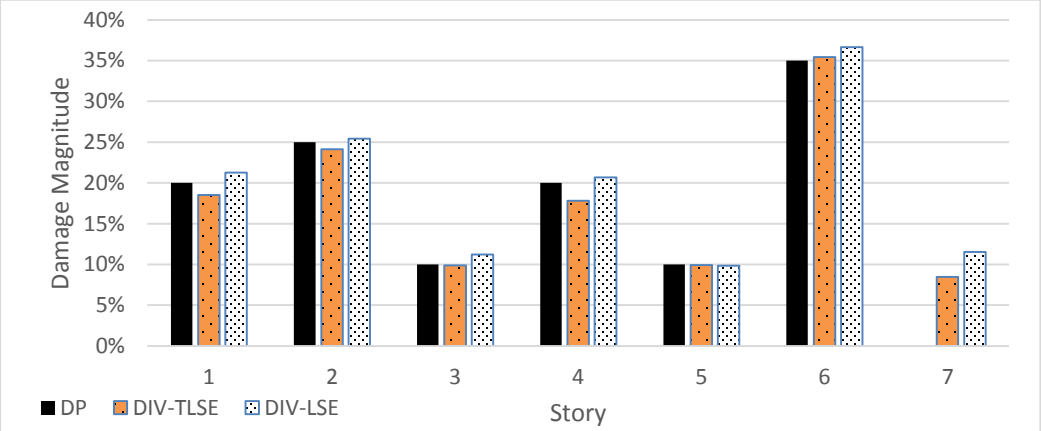

Figure III-32: DIV of story stiffness using total and conventional least square based DITER, 3% noise-polluted data

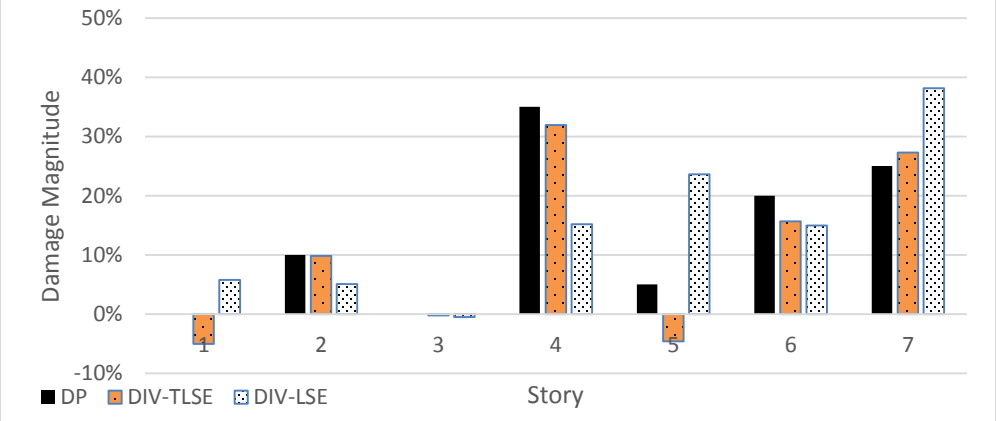

Figure III-33: DIV of dashpot constants using total and conventional least square based DITER, 3% noise-polluted data

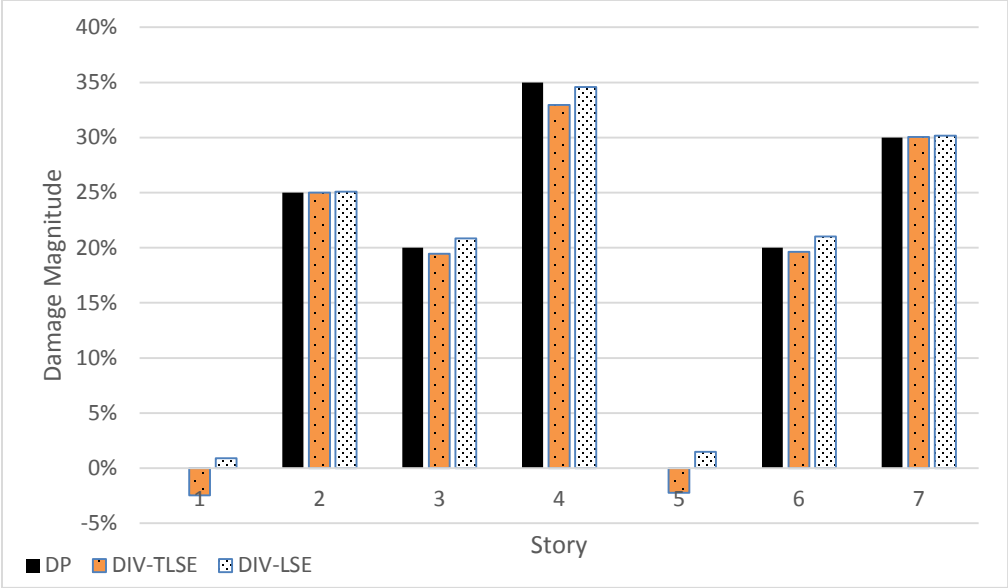

Figure III-34: DIV of mass using total and conventional least square based DITER, 3% noise-polluted data

SUMMARY

In this chapter a seven-story shear beam model was presented for the numerical verification of the proposed DITER and I-DITER methods. Different cases were introduced to study the performance of the methods in dealing with multiple and multi-type damages. The excitation forces were designed to vary case to case to make sure that the methods are not sensitive to the inputs. Also, limited input data were studied by exciting structure with unknown excitations. To keep the generality, loads were chosen to be White Gaussian Noises with varying intensities. In addition, effects of noise pollution on the DITER accuracy were taken into consideration by applying small and moderately large GWN noises to the output data without performing any data cleansing. At the end, DITER performances based on TLSE and LSE were compared for the noisy data. Based on the obtained DIVs, it is concluded that the DITER method has high accuracy in locating and sizing multiple and multi-type damages without any damage leakage problem. For small noise intensities, the method is highly trustworthy. For

moderately large noise pollution data cleansing is recommanded. However, If it is insisted on using raw data, then the TLSE approach is more convincing than the conventional LSE method. The accuracy of the I-DITER outcomes were verified when limited input data was available. To sum up, the numerical example verifies the accuracy and roboustenss of (I-)DITER for the shear beam experiment as a level three damage detection method.

CHAPTER IV
APPLICATION OF THE DITER METHOD TO EULER BERNOULI BEAMS AND FRAMES

INTRODUCTION

In the previous chapter, the application of (I-) DITER was studied on shear beam models that represent highly discrete systems. Shear beams might be considered a proper simplification to structures such as low and high rise ordinary buildings where story damage detections is of interest rather than locating the exact damaged members. Yet, the model is not recommended for structures whose behavior simulation requires larger number of DOFs, such as bridges, or in cases where a more accurate damage assessment is desired. For such structures, beam elements play a crucial rule in analyzing the system responses. Therefore, in this chapter the method is explored for the beam elements with the focus on Euler-Bernoulli (EB) theory.

This chapter begins with the derivation of the DITER equation of EB beams and two dimensional frames. The formulation considers small strain with either small or large rotations. A Rayleigh, external, and viscous resistance to straining of the beam material are considered to model the damping behavior of the beams. The initial static deflection formulation is presented accordingly. Next, the sub-system approach for DITER is detailed and finally, the application of DITER for frames equipped with passive seismic protective devices is discussed. For clarity, the chapter is divided into two parts. Part I is dedicated to the beam/ column elements, and part II contains the discussion of frames, sub-systems, and seismic protective devises.

DITER EQUATION FOR EULER BERNOULLI BEAMS AND FRAMES

DITER is developed to track structural changes under ordinary loads such as in service conditions. Studying the instant behavior under impact, blast, or extreme loads, including large earthquakes, are out of scope of this dissertation. Yet, the consequences of such loadings may be considered after the incidents by collecting data under ordinary load

conditions. Therefore, in EB beams the focus is on the cases with small (infinitesimal) strains. However, due to the slenderness, large loads may cause moderate to large rotations in a beam. Thus the effect of von Kármán nonlinearity is also studied in this chapter. The main effect is the introduction of coupling between the axial and transverse stiffness. A general Rayleigh damping along with straining viscous resistance and external damping characteristics are used to model the damping behavior of the beam. In this part, the DITER equations of motion of an EB beam are developed, and next the effect caused by large rotations are considered.

PART I: BEAMS

Beams with Small Strains and Small Transverse Displacements

Consider a straight beam with a large length to depth ratio. The beam is assumed to undergo small strains with small rotations. Therefore, the coupling between the axial and bending deformations may be ignored, and the Eulerian and Green strain tensors are assumed to be the same. Consider a right hand rectangular Cartesian system originated from the left side of the beam on the neutral axis with "x" axis along the axial axis of the beam where transverse displacements occur along "z" axis. Figure IV-1 shows the beam with the applied forces where $q(x,t)$ and $f(x,t)$ represent the distributed transverse force and axial body force in the local coordinates, respectively. The weight force might be distributed among $q(x,t)$ and $f(x,t)$.

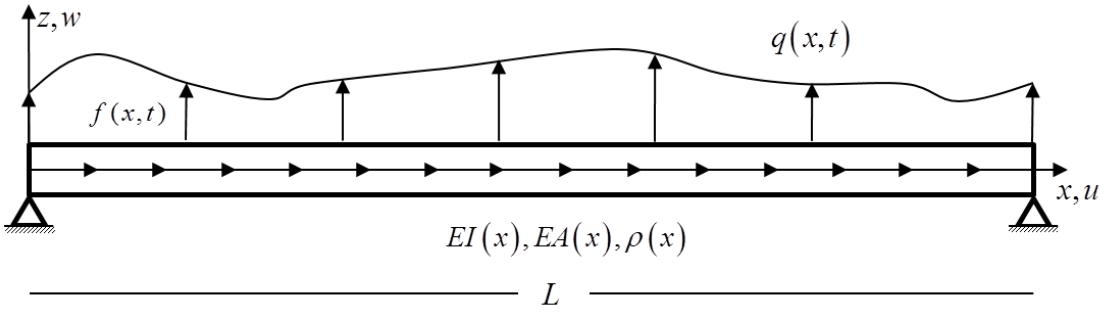

Figure IV-1: Schematic view of a beam

For an elastic behavior, the displacement field can be described as (Reddy 2004):

$$\begin{aligned} u_1 &= u_0 - z\frac{\partial w_0}{\partial x} \\ u_2 &= 0, \\ u_3 &= w_0(x) \end{aligned} \tag{4.1}$$

where (u_1, u_2, u_3) are the displacements along (x, y, z), and the axial and transverse displacement of neutral axis at point χ is shown by $u_0(x)$ and $w_0(x)$, respectively. The rotation of a transverse plane along the y axis is $\theta = -\frac{\partial w_0}{\partial x}$. Ignoring higher order terms, the only non-zero strain is the axial strain, and it is obtained by:

$$\varepsilon_{xx} = \frac{\partial u_1}{\partial x} = \frac{\partial u_0}{\partial x} - z\frac{\partial^2 w_0}{\partial x^2} \tag{4.2}$$

To maintain the equilibrium:

$$-\frac{\partial}{\partial t}\left(\rho A \frac{\partial}{\partial t} u_0\right) + \frac{\partial N}{\partial x} + f = 0 \tag{4.3}$$

$$-\frac{\partial}{\partial t}\left(\rho A \frac{\partial w_0}{\partial t}\right) + \frac{\partial V}{\partial x} + q = 0 \tag{4.4}$$

$$-\frac{\partial M}{\partial x} + V - \frac{\partial}{\partial t}\left(\rho I \frac{\partial}{\partial t}\frac{\partial w_0}{\partial x}\right) = 0 \tag{4.5}$$

where ρ, A, N, V, and M are mass density, cross section area, internal axial force, internal shear force, and internal moment, respectively. Take note that the coupling effect of the axial force in equation (4.4) is neglected. The last term of equation (4.5) originates from the rotary inertia. Up to this point, no damping effect has been considered in the equations. Damping modelling is a difficult task because of the ambiguities in the spatial locations of damping sources and variables that govern the damping forces (Friswell et al. 2007). Yet, for light damped structures, viscous modelling is an acceptable approach. Damping behavior in a beam might originate internally or externally. The application of the latter is discussed later in this chapter for frames with external isolators where it is assumed that the damping behavior is dominated with seismic protective systems i.e., isolators and dampers. The former, however, can originate from the material behavior and be described with Kelvin–Voigt damping model (strain rate damping)(Sorrentino et al. 2003) in which internal friction (Banks and Inman 1991)is assumed to be the dominant dissipated energy mechanism. An alternative way to consider the damping contribution is to introduce a general proportional (Rayleigh) behavior. In the following, both will be discussed and formulated.

The effect of damping behavior may be accounted for considering a transverse displacement viscous resistance, $c(x)$, and a viscous resistance, $c_s(x)$ to straining of the material (see e.g. (Clough and Penzien 1975)and (Reddy 2002). The role of $c_s(x)$ will be seen in the constitutive model; whereas, $c(x)$ is directly implemented in the equation of motion. Therefore, equation (4.4) into might be changed to:

$$-\frac{\partial}{\partial t}\left(\rho A\frac{\partial w_0}{\partial t}\right)+\frac{\partial V}{\partial x}+q-c\frac{\partial w_0}{\partial t}=0 \tag{4.6}$$

The internal axial force and the moment are obtained based on the stresses in the cross section as:

$$N=\int_A \sigma_{xx}dA \tag{4.7}$$

$$M=\int_A \sigma_{xx}zdA \tag{4.8}$$

where

$$\sigma_{xx} = E\varepsilon_{xx} + \sigma_D \tag{4.9}$$

where the first term is the Hooke's law with E as the material Young's modulus, and the second term is coming from the damping characteristic as follows:

$$\sigma_D = c_s \dot{\varepsilon}_{xx} \tag{4.10}$$

Substituting equation (4.9) back into equations (4.7) and (4.8) and taking integration across the cross section, we obtain:

$$N = \int_A \left(E + c_s \frac{\partial}{\partial t} \right) \left(\frac{\partial u_0}{\partial x} - z \frac{\partial^2 w_0}{\partial x^2} \right) dA = EA \frac{\partial u_0}{\partial x} + c_s A \frac{\partial^2 u_0}{\partial t \partial x} \tag{4.11}$$

$$M = \int_A \left(E + c_s \frac{\partial}{\partial t} \right) \left(\frac{\partial u_0}{\partial x} - z \frac{\partial^2 w_0}{\partial x^2} \right) z dA = -EI \frac{\partial^2 w_0}{\partial x^2} - c_s I \frac{\partial^3 w_0}{\partial t \partial x^2} \tag{4.12}$$

where I is the second moment of area across the y axis. In the above derivation the modulus of elasticity is assumed to be constant across the section. Also, it is assumed that the x-axis and the geometric centroid axis (Reddy 2004) coincide by which $\int_A z dA = 0$.

Therefore, the final equations of motion for an EB beam with small strain and small rotations for $0 < x < L$ are:

$$-\frac{\partial}{\partial t} \left(\rho A \frac{\partial}{\partial t} u_0 \right) + \frac{\partial}{\partial x} \left(EA \frac{\partial u_0}{\partial x} + c_s A \frac{\partial^2 u_0}{\partial t \partial x} \right) + f = 0 \tag{4.13}$$

$$-\frac{\partial}{\partial t} \left(\rho A \frac{\partial w_0}{\partial t} \right) + \frac{\partial^2}{\partial t \partial x} \left(\rho I \frac{\partial}{\partial t} \frac{\partial w_0}{\partial x} \right) - \frac{\partial^2}{\partial x^2} \left(EI \frac{\partial^2 w_0}{\partial x^2} + c_s I \frac{\partial^3 w_0}{\partial t \partial x^2} \right) - c \frac{\partial w_0}{\partial t} + q = 0 \tag{4.14}$$

To find element wise mass and stiffness matrices, the method described by Reddy (2005) is used to develop the weak form of the above equations. For an element of length l with start and end nodes of x_a, x_b, respectively, the weak form can be written as follows:

$$\int_{x_a}^{x_b} v_1 \left[-\frac{\partial}{\partial t} \left(\rho A \frac{\partial}{\partial t} u_0 \right) + \frac{\partial}{\partial x} \left(EA \frac{\partial u_0}{\partial x} + c_s A \frac{\partial^2 u_0}{\partial t \partial x} \right) + f \right] dx = 0 \tag{4.15}$$

$$\int_{x_a}^{x_b} v_2 \left[\begin{array}{l} -\dfrac{\partial}{\partial t}\left(\rho A \dfrac{\partial w_0}{\partial t} \right) + \dfrac{\partial^2}{\partial t \partial x}\left(\rho I \dfrac{\partial}{\partial t} \dfrac{\partial w_0}{\partial x} \right) - \dfrac{\partial^2}{\partial x^2}\left(EI \dfrac{\partial^2 w_0}{\partial x^2} + c_s I \dfrac{\partial^3 w_0}{\partial t \partial x^2} \right) \ldots \\ -c \dfrac{\partial w_0}{\partial t} + q \end{array} \right] dx = 0 \qquad (4.16)$$

Where v_1 and v_2 are weight functions for the axial and transverse displacements, respectively. Taking part by part integration of equation (4.15) and considering Q_1 and Q_4 , as shown in equation (4.17)

$$\begin{aligned} Q_1 &= -A\left(E \frac{\partial u_0}{\partial x} + c_s \frac{\partial^2 u_0}{\partial t \partial x} \right)_{x=x_a} \\ Q_4 &= A\left(E \frac{\partial u_0}{\partial x} + c_s \frac{\partial^2 u_0}{\partial t \partial x} \right)_{x=x_b} \end{aligned} \qquad (4.17)$$

to be , respectively, internal axial forces of the start and the end node of the element one finds:

$$\int_l \left[\rho A v_1 \frac{\partial^2 u_0}{\partial t^2} + EA \frac{\partial u_0}{\partial x} \frac{\partial v_1}{\partial x} + c_s A \frac{\partial^2 u_0}{\partial t \partial x} \frac{\partial v_1}{\partial x} - v_1 f \right] dx = v_1(x_a) Q_1 + v_1(x_b) Q_4 \qquad (4.18)$$

which corresponds to equation (4.13) for a typical element , e . ρA is assumed to be time invariant. Take note that if interior nodes are considered for the element i.e., when higher order($r > 1$) Lagrange interpolation functions are employed, technically Q_4 should be changed to Q_r and a new term, $\sum_{i=2}^{r-1} v_1(x_i) Q_i$, needs to be added to the RHS of equation (4.18) to represent the jump in the secondary variables caused by passing the interior nodes. Here, x_i is the location of the interior loads. Nonetheless, if no concentrated external forces are applied to the interior nodes the term $v_1(x_i) \sum_{i=2}^{r-1} Q_i$ is zero. Also, any concentrated load, p , in the element domain equivalently can be modeled as a distributed force of the form $\delta\left(x - x^{Load}\right) p$ where δ is the Dirac delta function and x^{Load} denotes the load location. Therefore, the term $v_1(x_i) \sum_{i=2}^{r-1} Q_i$ becomes zero, and thus it is not shown in equation (4.18).

Similarly, a weak form of the equation (4.14) can be written as for a typical element:

$$\int_{x_a}^{x_b}\left[v_2 \frac{\partial}{\partial t}\left(\rho A \frac{\partial w_0}{\partial t} \right) + \frac{\partial v_2}{\partial x}\frac{\partial}{\partial t}\left(\rho I \frac{\partial}{\partial t}\frac{\partial w_0}{\partial x} \right) + \frac{\partial^2 v_2}{\partial x^2}\left(EI \frac{\partial^2 w_0}{\partial x^2} + c_s I \frac{\partial^3 w_0}{\partial t \partial x^2} \right) + c v_2 \frac{\partial w_0}{\partial t} - q v_2 \right] dx ...$$
$$+ \frac{\partial v_2}{\partial x}\bigg|_{x_a} Q_3 + \frac{\partial v_2}{\partial x}\bigg|_{x_b} Q_6 - v_2\big|_{x_b} Q_2 - v_2\big|_{x_b} Q_5 = 0 \tag{4.19}$$

where

$$Q_2 = \left[\frac{\partial}{\partial x}\left(EI \frac{\partial^2 w_0}{\partial x^2} + c_s I \frac{\partial^3 w_0}{\partial t \partial x^2} \right) - \rho I \frac{\partial^2 w_0}{\partial t \partial x} \right]_{x_a}$$
$$Q_5 = -\left[\frac{\partial}{\partial x}\left(EI \frac{\partial^2 w_0}{\partial x^2} + c_s I \frac{\partial^3 w_0}{\partial t \partial x^2} \right) - \rho I \frac{\partial^2 w_0}{\partial t \partial x} \right]_{x_b} \tag{4.20}$$
$$Q_3 = \left[EI \frac{\partial^2 w_0}{\partial x^2} + c_s I \frac{\partial^3 w_0}{\partial t \partial x^2} \right]_{x_a}$$
$$Q_6 = -\left[EI \frac{\partial^2 w_0}{\partial x^2} + c_s I \frac{\partial^3 w_0}{\partial t \partial x^2} \right]_{x_b}$$

are the internal forces at the boundaries of the element as shown in Figure IV-2 . In derivation of equation (4.19) ρI and ρA are assumed to be time invariant.

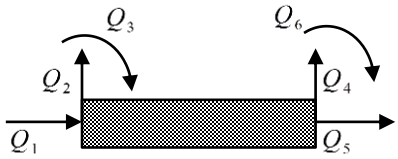

Figure IV-2: Internal forces of a beam element, interior nodes are not shown

The stiffness, damping, and mass matrices of the element can be obtained once the axial and transverse displacements at the element domain are approximated based on the nodal time-instant values and the interpolation functions as:

$$\begin{aligned} u_0(x,t) &= \sum_{j=1:r} u_{0j}^e(t)\varphi_j(x) = \left(\mathbf{u}_0^e\right)^T \boldsymbol{\varphi} \\ w_0(x,t) &= \sum_{J=1:s} w_{0J}^e(t)\psi_J(x) = \left(\boldsymbol{\omega}_o^e\right)^T \boldsymbol{\psi} \end{aligned} \tag{4.21}$$

where φ is a Lagrange interpolation function of order j, and ψ is a cubic Hermite interpolation function (consult Appendix A-2). u_{0j}^e and w_{0j}^e are the generalized nodal displacements corresponding to the employed interpolation functions.

Substituting equation(4.21) in equation (4.19) where the weight functions, v_1 and v_2, are substituted with the corresponding interpolation functions, φ_i and ψ_I, the following FE matrices for the transverse displacements are acquired:

$$\begin{aligned} M_{ij}^{22} &= M_{ij}^t + M_{ij}^r \\ C_{ij}^{22} &= C_{ij}^s + C_{ij}^E \\ K_{ij}^{22} &= \int_l \frac{\partial^2\psi_i}{\partial x^2}\frac{\partial^2\psi_j}{\partial x^2} EI dx \\ q_i^2 &= \int_l q\psi_i dx \end{aligned} \tag{4.22}$$

where

$$M_{ij}^t = \int_l \rho A \psi_i \psi_j dx$$

$$M_{ij}^r = \int_l \frac{\partial\psi_i}{\partial x}\frac{\partial\psi_j}{\partial x}\rho I dx$$

$$C_{ij}^s = \int_l \frac{\partial^2\psi_i}{\partial x^2}\frac{\partial^2\psi_j}{\partial x^2} c_s I dx$$

$$C_{ij}^E = \int_l c\psi_i\psi_j dx$$

Similarly for the axial displacements:

$$
\begin{aligned}
M_{ij}^{11} &= \int_l \rho A \varphi_i \varphi_j dx \\
C_{ij}^{11} &= \int_l \frac{\partial \varphi_i}{\partial x} \frac{\partial \varphi_j}{\partial x} c_s A dx \\
K_{ij}^{11} &= \int_l \frac{\partial \varphi_i}{\partial x} \frac{\partial \varphi_j}{\partial x} EA dx \\
f_i^1 &= \int_l f \varphi_i dx
\end{aligned}
\tag{4.23}
$$

These matrices are defined at element level and no assembly is required. The above equations provide adequate information to construct the data matrix, $\mathbf{H}$, and the observation vector, $\mathbf{y}$, of equation (2.22) to find the structural parameters.

The unknowns at each element are $EI, EA, c_s A, c_s I, \rho A, \rho I$ parameters. To take the unknowns out of the integration, the effective values $EI^e, EA^e, c_s A^e, c_s I^e, \rho A^e, \rho I^e$ are introduced, which remain constant in the element domain and represent each unknown, respectively. Thus, for a beam with N elements:

$$
\begin{aligned}
\boldsymbol{\theta}_m &= \left[\left(\rho I^e\right)_1, ..., \left(\rho I^e\right)_N, \left(\rho A^e\right)_1, ..., \left(\rho A^e\right)_N \right]^T \\
\boldsymbol{\theta}_k &= \left[\left(EI^e\right)_1, ..., \left(EI^e\right)_N, \left(EA^e\right)_1, ..., \left(EA^e\right)_N \right]^T \\
\boldsymbol{\theta}_c &= \left[\left(c_s I^e\right)_1, ..., \left(c_s I^e\right)_N, \left(c_s A^e\right)_1, ..., \left(c_s A^e\right)_N \right]^T
\end{aligned}
\tag{4.24}
$$

where, the external damping behavior of the beam has been neglected.

To construct the data matrix, **H,** it is assumed that *p-1* samples are collected from time instant t_1 to t_p. Consider the j^{th} element's axial and transverse generalized nodal displacement vector be $\mathbf{u}_j^e(t)$, $\boldsymbol{\omega}_j^e(t)$ respectively, where the subscript 0 has been omitted for clarity, then:

$$
\boldsymbol{\Gamma} = \begin{bmatrix}
\dot{\boldsymbol{\omega}}_1^{eT} \boldsymbol{\Lambda}_1'' \boldsymbol{\omega}_1^e \Big|_{t_1} & \cdots & \dot{\boldsymbol{\omega}}_N^{e\,T} \boldsymbol{\Lambda}_N'' \boldsymbol{\omega}_N^e \Big|_{t_1} & \dot{\mathbf{u}}_1^{eT} \mathbf{N}_1' \mathbf{u}_1^e \Big|_{t_1} & \cdots & \dot{\mathbf{u}}_N^{e\,T} \mathbf{N}_N' \mathbf{u}_N^e \Big|_{t_1} \\
 & & \vdots & & & \\
\dot{\boldsymbol{\omega}}_1^{eT} \boldsymbol{\Lambda}_1'' \boldsymbol{\omega}_1^e \Big|_{t_p} & \cdots & \dot{\boldsymbol{\omega}}_N^{e\,T} \boldsymbol{\Lambda}_N'' \boldsymbol{\omega}_N^e \Big|_{t_p} & \dot{\mathbf{u}}_1^{eT} \mathbf{N}_1' \mathbf{u}_1^e \Big|_{t_p} & \cdots & \dot{\mathbf{u}}_N^{e\,T} \mathbf{N}_N' \mathbf{u}_N^e \Big|_{t_p}
\end{bmatrix}
\tag{4.25}
$$

$$\mathbf{D}=\begin{bmatrix} \dot{\boldsymbol{\omega}}_1^{eT}\boldsymbol{\Lambda}_1''\dot{\boldsymbol{\omega}}_1^{e}\Big|_{t_1} & \cdots & \dot{\boldsymbol{\omega}}_N^{e\,T}\boldsymbol{\Lambda}_N''\dot{\boldsymbol{\omega}}_N^{e}\Big|_{t_1} & \dot{\mathbf{u}}_1^{eT}\mathbf{N}_1'\dot{\mathbf{u}}_1^{e}\Big|_{t_1} & \cdots & \dot{\mathbf{u}}_N^{e\,T}\mathbf{N}_N'\dot{\mathbf{u}}_N^{e}\Big|_{t_1} \\ & & \vdots & & & \\ \dot{\boldsymbol{\omega}}_1^{eT}\boldsymbol{\Lambda}_1''\dot{\boldsymbol{\omega}}_1^{e}\Big|_{t_p} & \cdots & \dot{\boldsymbol{\omega}}_N^{e\,T}\boldsymbol{\Lambda}_N''\dot{\boldsymbol{\omega}}_N^{e}\Big|_{t_p} & \dot{\mathbf{u}}_1^{eT}\mathbf{N}_1'\dot{\mathbf{u}}_1^{e}\Big|_{t_p} & \cdots & \dot{\mathbf{u}}_N^{e\,T}\mathbf{N}_N'\dot{\mathbf{u}}_N^{e}\Big|_{t_p} \end{bmatrix} \tag{4.26}$$

$$\mathbf{G}=\begin{bmatrix} \dot{\boldsymbol{\omega}}_1^{eT}\boldsymbol{\Lambda}_1'\ddot{\boldsymbol{\omega}}_1^{e}\Big|_{t_1} & \cdots & \dot{\boldsymbol{\omega}}_N^{e\,T}\boldsymbol{\Lambda}_N'\ddot{\boldsymbol{\omega}}_N^{e}\Big|_{t_1} & \dot{\mathbf{u}}_1^{eT}\mathbf{N}_1\ddot{\mathbf{u}}_1^{e}+\dot{\boldsymbol{\omega}}_1^{eT}\boldsymbol{\Lambda}_1\ddot{\boldsymbol{\omega}}_1^{e}\Big|_{t_1} & \cdots & \dot{\mathbf{u}}_N^{e\,T}\mathbf{N}_N\ddot{\mathbf{u}}_N^{e}+\dot{\boldsymbol{\omega}}_N^{e\,T}\boldsymbol{\Lambda}_N\ddot{\boldsymbol{\omega}}_N^{e}\Big|_{t_1} \\ & & \vdots & & & \\ \dot{\boldsymbol{\omega}}_1^{eT}\boldsymbol{\Lambda}_1'\ddot{\boldsymbol{\omega}}_1^{e}\Big|_{t_p} & \cdots & \dot{\boldsymbol{\omega}}_N^{e\,T}\boldsymbol{\Lambda}_N'\ddot{\boldsymbol{\omega}}_N^{e}\Big|_{t_p} & \dot{\mathbf{u}}_1^{eT}\mathbf{N}_1\ddot{\mathbf{u}}_1^{e}+\dot{\boldsymbol{\omega}}_1^{eT}\boldsymbol{\Lambda}_1\ddot{\boldsymbol{\omega}}_1^{e}\Big|_{t_p} & \cdots & \dot{\mathbf{u}}_N^{e\,T}\mathbf{N}_N\ddot{\mathbf{u}}_N^{e}+\dot{\boldsymbol{\omega}}_N^{e\,T}\boldsymbol{\Lambda}_N'\ddot{\boldsymbol{\omega}}_N^{e}\Big|_{t_p} \end{bmatrix} \tag{4.27}$$

where

$$\boldsymbol{\Lambda}_k=\left[\Lambda_{ij}\right]_k,\ \Lambda_{ij}=\int_l \psi_i\psi_j dx$$

$$\boldsymbol{\Lambda}_k'=\left[\Lambda_{ij}'\right]_k,\ \Lambda_{ij}'=\int_l \frac{\partial\psi_i}{\partial x}\frac{\partial\psi_j}{\partial x}dx$$

$$\boldsymbol{\Lambda}_k''=\left[\Lambda_{ij}''\right]_k,\ \Lambda_{ij}''=\int_l \frac{\partial^2\psi_i}{\partial x^2}\frac{\partial^2\psi_j}{\partial x^2}dx$$

$$\mathbf{N}_k=\left[N_{ij}\right]_k,\ N_{ij}=\int_l \varphi_i\varphi_j dx$$

$$\mathbf{N}_k'=\left[N_{ij}'\right]_k,\ N_{ij}'=\int_l \frac{\partial\varphi_i}{\partial x}\frac{\partial\varphi_j}{\partial x}dx$$

In the unknown mass situation, if it is desired to use the total displacement, the mass data matrix, $\mathbf{G}$, must be modified as discussed later in this chapter in equation (4.68). Note that $\mathbf{u}_j^e(t)$ and $\boldsymbol{\omega}_j^e(t)$ are defined at the sensor locations and are determined from the measurements. The only extra step is to transform the displacements, velocities and accelerations from the global to the local coordinates. The rotations, however, remain the same.

If the external damping behavior of the beam, in the transverse displacement is of interest, the above $\mathbf{D}$ matrix and $\boldsymbol{\theta}_c$ vector must be modified to

$$\mathbf{D}=\begin{bmatrix} \dot{\boldsymbol{\omega}}_1^{eT}\boldsymbol{\Lambda}_1''\dot{\boldsymbol{\omega}}_1^e\big|_{t_1} & \cdots & \dot{\boldsymbol{\omega}}_N^{e\,T}\boldsymbol{\Lambda}_N''\dot{\boldsymbol{\omega}}_N^e\big|_{t_1} & \dot{\mathbf{u}}_1^{eT}\mathbf{N}_1'\dot{\mathbf{u}}_1^e\big|_{t_1} & \cdots & \dot{\mathbf{u}}_N^{e\,T}\mathbf{N}_N'\dot{\mathbf{u}}_N^e\big|_{t_1} & \dot{\boldsymbol{\omega}}_1^{eT}\boldsymbol{\Lambda}_1\dot{\boldsymbol{\omega}}_1^e\big|_{t_1} & \cdots & \dot{\boldsymbol{\omega}}_N^{e\,T}\boldsymbol{\Lambda}_N\dot{\boldsymbol{\omega}}_N^e\big|_{t_1} \\ & & \vdots & & & & & & \\ \dot{\boldsymbol{\omega}}_1^{eT}\boldsymbol{\Lambda}_1''\dot{\boldsymbol{\omega}}_1^e\big|_{t_p} & \cdots & \dot{\boldsymbol{\omega}}_N^{e\,T}\boldsymbol{\Lambda}_N''\dot{\boldsymbol{\omega}}_N^e\big|_{t_p} & \dot{\mathbf{u}}_1^{eT}\mathbf{N}_1'\dot{\mathbf{u}}_1^e\big|_{t_p} & \cdots & \dot{\mathbf{u}}_N^{e\,T}\mathbf{N}_N'\dot{\mathbf{u}}_N^e\big|_{t_p} & \dot{\boldsymbol{\omega}}_1^{eT}\boldsymbol{\Lambda}_1\dot{\boldsymbol{\omega}}_1^e\big|_{t_p} & \cdots & \dot{\boldsymbol{\omega}}_N^{e\,T}\boldsymbol{\Lambda}_N\dot{\boldsymbol{\omega}}_N^e\big|_{t_p} \end{bmatrix}$$

$$\boldsymbol{\theta}_c=\left[\left(c_sI^e\right)_1,...,\left(c_sI^e\right)_N,\left(c_sA^e\right)_1,...,\left(c_sA^e\right)_N,c_1,...,c_N\right]^T \tag{4.28}$$

The observation vector, $\mathbf{y}$, can be find directly from equation (2.20) by computing the work rate of the loads as:

$$\dot{W}=\dot{W}^E+\dot{W}^N \tag{4.29}$$

where $\dot{W}^N$ represents the work rate of the nodal external forces, if any, and is computed by

$$\dot{W}^N=\sum_{j=1}^{NON}\dot{\boldsymbol{\alpha}}_j^T\mathbf{f}_j^N \tag{4.30}$$

in which $\dot{\boldsymbol{\alpha}}$ and $\mathbf{f}^N$ are defined in equation (2.20), and

$$\dot{W}^E\left(t\right)=\sum_{j=1}^{NEL}\dot{W}_j^e\left(t\right) \tag{4.31}$$

is the work rate of the loads distributed in the element domains where

$$\dot{W}_j^e\left(t\right)=\left(\left(\boldsymbol{\omega}_o^e\right)^T\bar{\mathbf{q}}^2+\left(\mathbf{u}_0^e\right)^T\bar{\mathbf{f}}^1\right)_j \tag{4.32}$$

The Derivation of $\dot{W}_j^e\left(t\right)$ is shown in Appendix A-3. Note that in equation (4.32) $\boldsymbol{\omega}_o^e$ and $\mathbf{u}_0^e$ are the same as in equation (4.21) and

$$\begin{aligned}\bar{\mathbf{q}}^2&=\left[\bar{q}_1^2\quad\cdots\quad\bar{q}_s^2\right]^T\\ \bar{\mathbf{f}}^1&=\left[\bar{f}_1^1\quad\cdots\quad\bar{f}_r^1\right]^T\end{aligned} \tag{4.33}$$

where $\bar{q}_i^2$ and $\bar{f}_i^1$ are the same as q_i^2 and f_i^1 defined in equations (4.22) and (4.23), respectively, but once the weight force is eliminated from the calculation of q and f shown in Figure IV-1. Finally the observation vector can be formed as

$$\mathbf{y} = \begin{cases} \left[\dot{W}^E\Big|_{t_1} + \dot{W}^N\Big|_{t_1} \cdots \quad \dot{W}^E\Big|_{t_{p+1}} + \dot{W}^N\Big|_{t_p} \right]^T & \text{For unknown mass situation} \\ \left[\dot{W}^E\Big|_{t_1} + \dot{W}^N\Big|_{t_1} \cdots \quad \dot{W}^E\Big|_{t_{p+1}} + \dot{W}^N\Big|_{t_p} \right]^T - \mathbf{G}\boldsymbol{\theta}_m & \text{For known mass situation} \end{cases} \tag{4.34}$$

Take note that the contribution of the weight force must be eliminated from the calculation of f and q. Also, note that in the known mass situation, terms $\mathbf{G}$ and $\boldsymbol{\theta}_m$ are eliminated from the data matrix, **H**, and unknown vector, $\boldsymbol{\theta}$.

Static Deflection

If the collected displacements data are measured with respect to the static equilibrium configuration, then to account for the static deflection unknowns, $\boldsymbol{\delta}_s$, formation of the extra term $\boldsymbol{\Gamma}_s$ of equation (2.32) is required. Meanwhile, the stiffness data matrix, $\boldsymbol{\Gamma}$, must be replaced by $\bar{\boldsymbol{\Gamma}}$ of equation (2.32), and the body force must be considered in the calculation of the rate of the work as well. In transition from $\boldsymbol{\Gamma}$ to $\bar{\boldsymbol{\Gamma}}$, only the nodal displacements have to be altered with the displacement data measured from the static equilibrium configuration of the structure. The formations for $\bar{\boldsymbol{\Gamma}}$ and $\boldsymbol{\Gamma}$ remain the same. The emergence of $\boldsymbol{\Gamma}_s$, however, is followed by a new unknown vector $\bar{\boldsymbol{\theta}}_k$ as

$$\bar{\boldsymbol{\theta}}_k = \left[EI_1^e \boldsymbol{\delta}_{s_1}^u, ..., EI_N^e \boldsymbol{\delta}_{s_N}^u, EA_1^e \boldsymbol{\delta}_{s_1}^w, ..., EA_N^e \boldsymbol{\delta}_{s_N}^w \right]^T \tag{4.35}$$

where $\boldsymbol{\delta}_{s_k}^u, \boldsymbol{\delta}_{s_k}^w$ are the nodal static deflections of the k^{th} element corresponding to the axial and transverse displacements, respectively. Consequently, the static deflection data matrix can be described as:

$$\boldsymbol{\Gamma}_s = \begin{bmatrix} \dot{\boldsymbol{\omega}}_1^{eT} \boldsymbol{\Lambda}_1''\Big|_{t_1} & \cdots & \dot{\boldsymbol{\omega}}_N^{e\,T} \boldsymbol{\Lambda}_N''\Big|_{t_1} & \dot{\mathbf{u}}_1^{eT} \mathbf{N}_1'\Big|_{t_1} & \cdots & \dot{\mathbf{u}}_N^{e\,T} \mathbf{N}_N'\Big|_{t_1} \\ & & \vdots & & & \\ \dot{\boldsymbol{\omega}}_1^{eT} \boldsymbol{\Lambda}_1''\Big|_{t_p} & \cdots & \dot{\boldsymbol{\omega}}_N^{e\,T} \boldsymbol{\Lambda}_N''\Big|_{t_p} & \dot{\mathbf{u}}_1^{eT} \mathbf{N}_1'\Big|_{t_p} & \cdots & \dot{\mathbf{u}}_N^{e\,T} \mathbf{N}_N'\Big|_{t_p} \end{bmatrix} \tag{4.36}$$

and the data matrix and the unknown vectors should be formed following equation (2.33).

Emergence of the static deflections imply the usage of the total displacements. Thus, in addition to the external excitations, one needs to consider the contribution of the body weight force in the calculation of the rate of the work done on the system. This can be done by using equation (4.34) along with the mass matrix of equation (4.68) . Again, it is noteworthy to mention that $\bar{\boldsymbol{\theta}}_k$ is presented to account for the contribution of the variation of the static deflection in the DITER formulation. Its presence in the unknown vector helps to minimize its interference on the determination of the structural properties of the components. Therefore, the actual values of $\bar{\boldsymbol{\theta}}_k$ is not the main interest.

Proportional Damping

For a general proportional damping model, we set $c = c_s = 0$, and introduce an element-level damping matrix composed of a linear combination of the element's mass and stiffness matrices. The coefficients of this combination, α and β, do not vary from an element to another. Thus, damping matrix of the j^{th} element can be written as:

$$\mathbf{C}_j = \alpha \mathbf{M}_j + \beta \mathbf{K}_j, \qquad \mathrm{j} = 1,..,\mathrm{N} \tag{4.37}$$

where $\mathbf{M}_j$ and $\mathbf{K}_j$ are the mass and stiffness matrices of the j^{th} element, respectively. α and β denote the proportional damping coefficients. Based on the described proportional damping model, the vector of unknown parameters of the damping characteristics changes to:

$$\boldsymbol{\theta}_c = \left[\alpha \boldsymbol{\theta}_m{}^T, \beta \boldsymbol{\theta}_k{}^T \right]^T \tag{4.38}$$

where $\boldsymbol{\theta}_m$ and $\boldsymbol{\theta}_k$ are the same as in equation (4.24). Correspondingly, the damping part of the data matrix should be modified to:

$$\mathbf{D} = \left[\mathbf{D}_m, \mathbf{D}_k \right] \tag{4.39}$$

where

$$\mathbf{D}_m = \begin{bmatrix} \dot{\boldsymbol{\omega}}_1^{eT}\boldsymbol{\Lambda}_1'\dot{\boldsymbol{\omega}}_1^{e}\Big|_{t_1} & \cdots & \dot{\boldsymbol{\omega}}_N^{e\,T}\boldsymbol{\Lambda}_N'\dot{\boldsymbol{\omega}}_N^{e}\Big|_{t_1} & \dot{\mathbf{u}}_1^{eT}\mathbf{N}_1\dot{\mathbf{u}}_1^{e}+\dot{\boldsymbol{\omega}}_1^{eT}\boldsymbol{\Lambda}_1\dot{\boldsymbol{\omega}}_1^{e}\Big|_{t_1} & \cdots & \dot{\mathbf{u}}_N^{e\,T}\mathbf{N}_N\dot{\mathbf{u}}_N^{e}+\dot{\boldsymbol{\omega}}_N^{e\,T}\boldsymbol{\Lambda}_N\dot{\boldsymbol{\omega}}_N^{e}\Big|_{t_1} \\ & & \vdots & & & \\ \dot{\boldsymbol{\omega}}_1^{eT}\boldsymbol{\Lambda}_1'\dot{\boldsymbol{\omega}}_1^{e}\Big|_{t_p} & \cdots & \dot{\boldsymbol{\omega}}_N^{e\,T}\boldsymbol{\Lambda}_N'\dot{\boldsymbol{\omega}}_N^{e}\Big|_{t_p} & \dot{\mathbf{u}}_1^{eT}\mathbf{N}_1\dot{\mathbf{u}}_1^{e}+\dot{\boldsymbol{\omega}}_1^{eT}\boldsymbol{\Lambda}_1\dot{\boldsymbol{\omega}}_1^{e}\Big|_{t_p} & \cdots & \dot{\mathbf{u}}_N^{e\,T}\mathbf{N}_N\dot{\mathbf{u}}_N^{e}+\dot{\boldsymbol{\omega}}_N^{e\,T}\boldsymbol{\Lambda}_N'\dot{\boldsymbol{\omega}}_N^{e}\Big|_{t_p} \end{bmatrix}$$

$$\mathbf{D}_k = \begin{bmatrix} \dot{\boldsymbol{\omega}}_1^{eT}\boldsymbol{\Lambda}_1''\dot{\boldsymbol{\omega}}_1^{e}\Big|_{t_1} & \cdots & \dot{\boldsymbol{\omega}}_N^{e\,T}\boldsymbol{\Lambda}_N''\dot{\boldsymbol{\omega}}_N^{e}\Big|_{t_1} & \dot{\mathbf{u}}_1^{eT}\mathbf{N}_1'\dot{\mathbf{u}}_1^{e}\Big|_{t_1} & \cdots & \dot{\mathbf{u}}_N^{e\,T}\mathbf{N}_N'\dot{\mathbf{u}}_N^{e}\Big|_{t_1} \\ & & \vdots & & & \\ \dot{\boldsymbol{\omega}}_1^{eT}\boldsymbol{\Lambda}_1''\dot{\boldsymbol{\omega}}_1^{e}\Big|_{t_p} & \cdots & \dot{\boldsymbol{\omega}}_N^{e\,T}\boldsymbol{\Lambda}_N''\dot{\boldsymbol{\omega}}_N^{e}\Big|_{t_p} & \dot{\mathbf{u}}_1^{eT}\mathbf{N}_1'\dot{\mathbf{u}}_1^{e}\Big|_{t_p} & \cdots & \dot{\mathbf{u}}_N^{e\,T}\mathbf{N}_N'\dot{\mathbf{u}}_N^{e}\Big|_{t_p} \end{bmatrix}$$

(4.40)

Since the distributed external damping is ignored, $\mathbf{D}_k$ is identical to $\mathbf{D}$ of equation(4.26).

Once the damping data matrix and the unknown vector are formed as in equations (4.39) and (4.38), the unknowns can be determined using equation (2.24).Take note that the uncoupling characteristic of the stiffness and mass matrices between the axial and transverse displacement has been used in derivation of the above damping data matrix.

Beam with Small Strains and Large Rotations

Even under a service loading, due to the slenderness and large loads, it is possible that a beam undergoes of such displacements that the effect of geometric non-linearity adversely affects the results of the currently developed DITER. In such cases, transverse and axial deformations affect each other and their contribution to the energy terms cannot be decoupled. Besides, the assumption of having linear stiffness and damping data matrices may result in poor damage detection outcomes. Therefore, the DITER data matrices must be modified to reduce the effect of this non-linearity on the accuracy of the DITER results. Utilizing a continuum model in the deformed configuration may be a remedy for such cases; however, this demands a solution to a completely non-linear optimization in a sense that the structural unknowns and the dynamic response data are coupled. Yet, to maintain the computational efficiency along with the acceptable DITER results, the effect of this geometric non-linearity can be mitigated through extending the small-strain DITER formulation by considering large rotations.

Consider the beam shown in Figure IV-1. The beam is assumed to undergo small strains but with moderate to large rotations. The difference between deformed and undeformed configuration still can be ignored in terms of the stress and strain calculations i.e., Cauchy stress tensor may be used and the discrepancy between the Green- Lagrange and the Eulerian strain tensors may be neglected (Reddy 2004). The displacement filed of the beam is expressed in equation (4.1). The strain, however, changes as the second order effect of the rotation should not be ignored. Consider the definition of the strain tensor as

$$\boldsymbol{\varepsilon} = \frac{1}{2}\left[\nabla \mathbf{u} + (\nabla \mathbf{u})^T + (\nabla \mathbf{u})^T . \nabla \mathbf{u}\right] \tag{4.41}$$

where ∇ is the gradient operator with respect to $\mathbf{x}$, and $\mathbf{u}$ is the displacement field. All higher order terms in equation(4.41) can be ignored except $\frac{\partial u_3}{\partial x}$. Thus, one can find

$$\varepsilon_{xx} = \frac{\partial u_0}{\partial x} + \frac{1}{2}\left(\frac{\partial w_0}{\partial x}\right)^2 - z\frac{\partial^2 w_0}{\partial x^2} \tag{4.42}$$

The equilibrium relationships remain similar to the small rotation case except that only equation (4.6) modifies to:

$$-\frac{\partial}{\partial t}\left(\rho A \frac{\partial w_0}{\partial t}\right) + \frac{\partial V}{\partial x} + \frac{\partial}{\partial x}\left[N\frac{\partial w_0}{\partial x}\right] + q - c\frac{\partial w_0}{\partial t} = 0 \tag{4.43}$$

The internal axial force and the in plane moment are obtained by substituting equation (4.42) into equation (4.9) and forward the result into equations (4.7) and (4.8) as:

$$N = \int_A \left(E + c_s\frac{\partial}{\partial t}\right)\left(\frac{\partial u_0}{\partial x} - z\frac{\partial^2 w_0}{\partial x^2} + \frac{1}{2}\left(\frac{\partial w_0}{\partial x}\right)^2\right)dA = EA\left(\frac{\partial u_0}{\partial x} + \frac{1}{2}\left(\frac{\partial w_0}{\partial x}\right)^2\right) + c_s A\left(\frac{\partial^2 u_0}{\partial t \partial x} + \frac{\partial^2 w_0}{\partial t \partial x}\right) \tag{4.44}$$

$$M = \int_A \left(E + c_s\frac{\partial}{\partial t}\right)\left(\frac{\partial u_0}{\partial x} - z\frac{\partial^2 w_0}{\partial x^2} + \frac{1}{2}\left(\frac{\partial w_0}{\partial x}\right)^2\right)zdA = -EI\frac{\partial^2 w_0}{\partial x^2} - c_s I\frac{\partial^3 w_0}{\partial t \partial x^2} \tag{4.45}$$

where it is assumed that the x-axis and the geometric centroid axis (Reddy 2004) coincide by which $\int_A z dA = 0$. Therefore, for an EB beam with small strain and moderately large rotations, the equations of motion can be approximated by (for $0 < x < L$) :

$$-\frac{\partial}{\partial t}\left(\rho A\frac{\partial}{\partial t}u_0\right)+\frac{\partial}{\partial x}\left(EA\left(\frac{\partial u_0}{\partial x}+\frac{1}{2}\left(\frac{\partial w_0}{\partial x}\right)^2\right)+c_s A\left(\frac{\partial^2 u_0}{\partial t\partial x}+\frac{\partial^2 w_0}{\partial t\partial x}\right)\right)+f=0 \quad (4.46)$$

$$\begin{aligned}&-\frac{\partial}{\partial t}\left(\rho A\frac{\partial w_0}{\partial t}\right)+\frac{\partial^2}{\partial t\partial x}\left(\rho I\frac{\partial}{\partial t}\frac{\partial w_0}{\partial x}\right)-\frac{\partial^2}{\partial x^2}\left(EI\frac{\partial^2 w_0}{\partial x^2}+c_s I\frac{\partial^3 w_0}{\partial t\partial x^2}\right)...\\&+\frac{\partial}{\partial x}\left(\frac{\partial w_0}{\partial x}EA\left(\frac{\partial u_0}{\partial x}+\frac{1}{2}\left(\frac{\partial w_0}{\partial x}\right)^2\right)\right)+\frac{\partial}{\partial x}\left(\frac{\partial w_0}{\partial x}c_s A\left(\frac{\partial^2 u_0}{\partial t\partial x}+\frac{\partial^2 w_0}{\partial t\partial x}\right)\right)-c\frac{\partial w_0}{\partial t}+q=0\end{aligned} \quad (4.47)$$

Similar to the small rotation case, weak forms of the equations of motion have been developed to find the element wise stiffness, damping and mass matrices. From equation (4.46), a set of discretized equations can be created for the element e as:

$$\mathbf{M}^{11}\ddot{\mathbf{u}}_0^e+\mathbf{C}^{11}\dot{\mathbf{u}}_0^e+\mathbf{C}^{12}\dot{\boldsymbol{\omega}}_o^e+\mathbf{K}^{11}\mathbf{u}_0^e+\mathbf{K}^{12}\boldsymbol{\omega}_o^e=\mathbf{f}^1+\mathbf{Q}^1 \quad (4.48)$$

where

$$\begin{aligned}C_{iJ}^{12}&=\int_l\frac{\partial\varphi_i}{\partial x}\frac{\partial\psi_J}{\partial x}c_s A dx\\K_{iJ}^{12}&=\int_l\frac{1}{2}\frac{\partial\varphi_i}{\partial x}\frac{\partial\psi_J}{\partial x}\sum_{J=1:s}\frac{\partial\psi_J}{\partial x}w_{0J}^e EA dx\end{aligned} \quad (4.49)$$

and M_{ij}^{11}, C_{ij}^{11},and K_{ij}^{11} are the same as in equation (4.23). i, j are determined based on the order of the Lagrange interpolation functions and J is related to the Hermite interpolation function. $\mathbf{f}^1$ is the element wise external forces described in equation (4.23), and $\mathbf{Q}^1$ represents the internal forces. Details of the derivation of equation (4.48) are shown in Appendix A-1. Take note that the structural properties are defined in the element level; however, for clarity, the element sign has been omitted. Also, the emergence of the internal forces in the interior nodes are eliminated as described in the small rotation case.

Similarly, equation (4.47) might be shown by the following set of equations:

$$\mathbf{M}^{22}\ddot{\boldsymbol{\omega}}_o^e + \mathbf{C}^{22}\dot{\boldsymbol{\omega}}_0^e + \mathbf{K}^{22}\boldsymbol{\omega}_o^e + \mathbf{K}^{21}\mathbf{u}_0^e + \mathbf{C}^{21}\dot{\mathbf{u}}_o^e = \mathbf{q}^2 + \mathbf{Q}^2 \tag{4.50}$$

where $\mathbf{q}^2$ is as described in equation (4.22), $\mathbf{Q}^2$ consists of the element internal forces, and

$$\begin{aligned}
M_{IJ}^{22} &= \int_l \rho A \psi_I \psi_J dx + \int_l \frac{\partial \psi_I}{\partial x}\frac{\partial \psi_J}{\partial x}\rho I dx \\
K_{IJ}^{22} &= \int_l \left(\frac{\partial^2 \psi_I}{\partial x^2}\frac{\partial^2 \psi_J}{\partial x^2} EI + \frac{1}{2} EA \frac{\partial \psi_I}{\partial x}\frac{\partial \psi_J}{\partial x}\left(\sum_{J=1:s} \frac{\partial \psi_J}{\partial x} w_{0J}^e \right)^2 dx \right) \\
K_{Ij}^{21} &= \int_l EA \frac{\partial \psi_I}{\partial x}\frac{\partial \varphi_j}{\partial x}\sum_{J=1:s}\frac{\partial \psi_J}{\partial x} w_{0J}^e dx \\
C_{Ij}^{21} &= \int_l c_s A \frac{\partial \psi_I}{\partial x}\frac{\partial \varphi_j}{\partial x}\sum_{J=1:s}\frac{\partial \psi_J}{\partial x} w_{0J}^e dx \\
C_{IJ}^{22} &= \int_l \left(\frac{\partial^2 \psi_I}{\partial x^2}\frac{\partial^2 \psi_J}{\partial x^2} c_s I + c_s A \frac{\partial \psi_I}{\partial x}\frac{\partial \psi_J}{\partial x}\left(\sum_{J=1:s}\frac{\partial \psi_J}{\partial x} w_{0J}^e\right) + c\psi_I \psi_J \right) dx
\end{aligned} \tag{4.51}$$

where capital *I* and *J* refer to the Hermite interpolation functions and small case *i* and *j* are related to the Lagrange interpolation functions. Details of the derivation of equation (4.50) are shown in Appendix A-1.

Once the unknown parameters, $EI, EA, c_s A, c_s I, \rho A, \rho I$, are replaced by their effective values, $EI^e, EA^e, c_s A^e, c_s I^e, \rho A^e, \rho I^e$, the final task will be to create the data matrices form equations (4.48) and (4.50). As, for this situation, it is assumed that the total displacements have been collected, the $\mathbf{G}$ matrix should be formed as in equation(4.68). The damping and stiffness data matrices must be modified as well. For clarity, the followings are defined for the k^{th} element:

$$\bar{\mathbf{A}}'_k = \left[\bar{A}'_{iJ} \right]_k = \int_l \frac{\partial \varphi_i}{\partial x} \frac{\partial \psi_J}{\partial x} dx$$

$$\mathbf{A}'_k = \left[A'_{iJ} \right]_k = \int_l \frac{\partial \varphi_i}{\partial x} \frac{\partial \psi_J}{\partial x} B_k dx$$

$$\mathbf{A}'^T_k = \left[A'_{Ij} \right]_k = \int_l \frac{\partial \psi_I}{\partial x} \frac{\partial \varphi_j}{\partial x} B_k dx \tag{4.52}$$

$$\mathbf{\Xi}'_k = \left[\Xi'_{IJ} \right]_k = \int_l \frac{\partial \psi_I}{\partial x} \frac{\partial \psi_J}{\partial x} B_k dx$$

$$\mathbf{\Xi}'^2_k = \left[\Xi'^2_{IJ} \right]_k = \int_l \frac{\partial \psi_I}{\partial x} \frac{\partial \psi_J}{\partial x} B_k^2 dx$$

where

$$B_k = \sum_{J=1:s} \frac{\partial \psi_J}{\partial x} w^e_{0_J} \tag{4.53}$$

and for linear Lagrange and cubic Hermite interpolation functions:

$$\bar{\mathbf{A}}'_k = \left[\bar{A}'_{iJ} \right]_k = \frac{1}{l_k} \begin{bmatrix} 1 & 0 & -1 & 0 \\ -1 & 0 & 1 & 0 \end{bmatrix}$$

$$\mathbf{A}'_k = \left[A'_{iJ} \right]_k = \begin{bmatrix} \left(\frac{6}{5}(w_3 - w_1) + \frac{l}{10}(w_2 + w_4)\right)/l^2 & \left(\frac{1}{30}(w_4 - 4w_2) + \frac{1}{10l}(w_1 - w_3)\right) & -\left(\frac{6}{5}(w_3 - w_1) + \frac{l}{10}(w_2 + w_4)\right)/l^2 & \left(\frac{1}{30}(w_2 - 4w_4) + \frac{1}{10l}(w_1 - w_3)\right) \\ -\left(\frac{6}{5}(w_3 - w_1) + \frac{l}{10}(w_2 + w_4)\right)/l^2 & -\left(\frac{1}{30}(w_4 - 4w_2) + \frac{1}{10l}(w_1 - w_3)\right) & \left(\frac{6}{5}(w_3 - w_1) + \frac{l}{10}(w_2 + w_4)\right)/l^2 & -\left(\frac{1}{30}(w_2 - 4w_4) + \frac{1}{10l}(w_1 - w_3)\right) \end{bmatrix}_k$$

$$\mathbf{A}'^T_k = \left[A'_{Ij} \right]_k = \left(\mathbf{A}'_k \right)^T$$

$$\mathbf{\Xi}'_k = \left[\Xi'_{IJ} \right]_k = \begin{bmatrix} \left(\frac{54}{35}(w_3 - w_1) + \frac{6l}{35}(w_2 + w_4)\right)/l^2 & \left(\frac{1}{70}(w_4 - 6w_2) + \frac{6}{35l}(w_1 - w_3)\right) & -\left(\frac{54}{35}(w_3 - w_1) + \frac{6l}{35}(w_2 + w_4)\right)/l^2 & \left(\frac{1}{70}(w_2 - 6w_4) + \frac{6}{35l}(w_1 - w_3)\right) \\ \left(\frac{1}{70}(w_4 - 6w_2) + \frac{6}{35l}(w_1 - w_3)\right) & \left(\frac{3}{35}(w_3 - w_1) + \frac{l}{105}(-6w_2 + w_4)\right) & -\left(\frac{1}{70}(w_4 - 6w_2) + \frac{6}{35l}(w_1 - w_3)\right) & \left(\frac{1}{70}(w_1 - w_3) + \frac{l}{105}(w_2 + w_4)\right) \\ -\left(\frac{54}{35}(w_3 - w_1) + \frac{6l}{35}(w_2 + w_4)\right)/l^2 & -\left(\frac{1}{70}(w_4 - 6w_2) + \frac{6}{35l}(w_1 - w_3)\right) & \left(\frac{54}{35}(w_3 - w_1) + \frac{6l}{35}(w_2 + w_4)\right)/l^2 & -\left(\frac{1}{70}(w_2 - 6w_4) + \frac{6}{35l}(w_1 - w_3)\right) \\ \left(\frac{1}{70}(w_2 - 6w_4) + \frac{6}{35l}(w_1 - w_3)\right) & \left(\frac{1}{70}(w_1 - w_3) + \frac{l}{105}(w_2 + w_4)\right) & -\left(\frac{1}{70}(w_2 - 6w_4) + \frac{6}{35l}(w_1 - w_3)\right) & \left(\frac{3}{35}(w_3 - w_1) + \frac{l}{105}(w_2 - 6w_4)\right) \end{bmatrix}_k$$

and

$$\mathbf{\Xi}'^2_k = \left[\Xi'^2_{IJ} \right]_k = \begin{bmatrix} \Xi'^2_{11} & \Xi'^2_{12} & -\Xi'^2_{11} & \Xi'^2_{14} \\ \Xi'^2_{12} & \Xi'^2_{22} & -\Xi'^2_{12} & \Xi'^2_{24} \\ -\Xi'^2_{11} & -\Xi'^2_{12} & \Xi'^2_{11} & -\Xi'^2_{14} \\ \Xi'^2_{14} & \Xi'^2_{24} & -\Xi'^2_{14} & \Xi'^2_{44} \end{bmatrix}$$

where

$$\Xi'^{2}_{11} = \frac{1}{35l^3}\left(3l^2\left(w_2^{\,2} + w_4^{\,2}\right) - 144w_3w_1 - 18l\left(w_1w_2 + w_1w_4 - w_2w_3 - w_3w_4\right) + 72\left(w_1^{\,2} + w_3^{\,2}\right)\right)$$

$$\Xi'^{2}_{12} = \frac{1}{35l^2}\left(18w_3w_1 + 6l\left(w_1w_2 - w_2w_3\right) - 9\left(w_1^{\,2} + w_3^{\,2}\right)\right) - \frac{1}{140}\left(2w_2w_4 - w_2^{\,2} + w_4^{\,2}\right)$$

$$\Xi'^{2}_{14} = \frac{1}{35l^2}\left(18w_3w_1 + 6l\left(w_1w_4 - w_4w_3\right) - 9\left(w_1^{\,2} + w_3^{\,2}\right)\right) - \frac{1}{140}\left(2w_2w_4 + w_2^{\,2} - w_4^{\,2}\right)$$

$$\Xi'^{2}_{22} = \frac{3}{35l}\left(w_1 - w_3\right)^2 + \frac{1}{70}\left(w_1w_2 - w_2w_3 - w_1w_4 + w_4w_3 + l\left(4w_2^{\,2} - w_2w_4 + \frac{w_4^{\,2}}{3}\right)\right)$$

$$\Xi'^{2}_{24} = \frac{1}{140}\left(2w_2w_3 - 2w_1w_4 - 2w_1w_2 + 2w_4w_3 - l\left(w_2^{\,2} + w_4^{\,2}\right)\right) + \frac{l}{105}w_2w_4$$

$$\Xi'^{2}_{44} = \frac{3}{35l}\left(w_1 - w_3\right)^2 - \frac{1}{70}\left(w_1w_2 - w_2w_3 - w_1w_4 + w_4w_3 + l\left(4w_2^{\,2} - w_2w_4 + \frac{w_4^{\,2}}{3}\right)\right)$$

Note that in the derivation of the components of equation (4.52), for clarification, the notation e and subscript 0 are eliminated from $w^e_{0_J}$. Also, it should be noted that w_1 and w_3 have a length unit, while w_2 and w_4 are unitless.

The stiffness and damping matrices of the k^{th} element can be formed as:

$$\mathbf{K}_k = \begin{bmatrix} EA^e\mathbf{N}'_k & \frac{1}{2}EA^e\mathbf{A}'_k \\ EA^e\mathbf{A}'^{T}_k & EI^e\boldsymbol{\Lambda}'' + \frac{1}{2}EA^e\boldsymbol{\Xi}'^{2}_k \end{bmatrix}_{(r+s)\times(r+s)}$$

$$\mathbf{C}_k = \begin{bmatrix} c_sA^e\mathbf{N}'_k & c_sA^e\bar{\mathbf{A}}'_k \\ c_sA^e\mathbf{A}'^{T}_k & c_sI^e\boldsymbol{\Lambda}'' + c_sA^e\boldsymbol{\Xi}'_k + c^e\boldsymbol{\Lambda}_k \end{bmatrix} \tag{4.54}$$

where $\mathbf{N}', \boldsymbol{\Lambda}'', \boldsymbol{\Lambda}', \boldsymbol{\Lambda}$ have the same definition as in equation (4.27), and nodal DOFs are arranged in the form of $\left[\mathbf{u}^e_0, \boldsymbol{\omega}^e_o\right]^T$.

As the element-wise stiffness and damping matrices are formed, next step is to construct the stiffness and damping data matrices. Consider the k^{th} element's axial and transverse nodal displacement vector as $\mathbf{u}^e_k(t)$ and $\boldsymbol{\omega}^e_k(t)$ respectively where the subscript 0 has been omitted for clarity. The rate of the potential and dissipated energy of the element can be obtained as:

$$\dot{U}_k = \left(\dot{\mathbf{u}}^{e^T}\mathbf{K}\mathbf{u}^e\right)_k \simeq EA^e\left(\dot{\mathbf{u}}_k^{e^T}\mathbf{N}_k'\mathbf{u}_k^e + \frac{1}{2}\dot{\mathbf{u}}_k^{e^T}\mathbf{A}_k'\boldsymbol{\omega}_k^e + \dot{\boldsymbol{\omega}}_k^{e^T}\mathbf{A}_k'^T\mathbf{u}_k^e + \frac{1}{2}\dot{\boldsymbol{\omega}}_k^{e^T}\boldsymbol{\Xi}_k'^2\boldsymbol{\omega}_k^e\right) + EI^e\dot{\boldsymbol{\omega}}_k^{e^T}\boldsymbol{\Lambda}''\boldsymbol{\omega}_k^e \tag{4.55}$$

$$\dot{D}_k \simeq c_s A^e\left(\dot{\mathbf{u}}_k^{e^T}\mathbf{N}_k'\dot{\mathbf{u}}_k^e + \dot{\mathbf{u}}_k^{e^T}\mathbf{A}_k'\dot{\boldsymbol{\omega}}_k^e + B_k\dot{\boldsymbol{\omega}}_k^{e^T}\mathbf{A}_k'^T\dot{\mathbf{u}}_k^e + B_k\dot{\boldsymbol{\omega}}_k^{e^T}\boldsymbol{\Lambda}_k'\dot{\boldsymbol{\omega}}_k^e\right) + c_s I^e\dot{\boldsymbol{\omega}}_k^{e^T}\boldsymbol{\Lambda}''\dot{\boldsymbol{\omega}}_k^e + c^e\dot{\boldsymbol{\omega}}_k^{e^T}\boldsymbol{\Lambda}\dot{\boldsymbol{\omega}}_k^e \tag{4.56}$$

Therefore, the stiffness and damping data matrices can be described as:

$$\boldsymbol{\Gamma} = \begin{bmatrix} \dot{\boldsymbol{\omega}}_1^{eT}\boldsymbol{\Lambda}_1''\boldsymbol{\omega}_1^e\big|_{t_1} & \cdots & \dot{\boldsymbol{\omega}}_N^{e^T}\boldsymbol{\Lambda}_N''\boldsymbol{\omega}_N^e\big|_{t_1} & L_1\big|_{t_1} & \cdots & L_N\big|_{t_1} \\ & & \vdots & & & \\ \dot{\boldsymbol{\omega}}_1^{eT}\boldsymbol{\Lambda}_1''\boldsymbol{\omega}_1^e\big|_{t_p} & \cdots & \dot{\boldsymbol{\omega}}_N^{e^T}\boldsymbol{\Lambda}_N''\boldsymbol{\omega}_N^e\big|_{t_p} & L_1\big|_{t_p} & \cdots & L_N\big|_{t_p} \end{bmatrix} \tag{4.57}$$

$$\mathbf{D} = \begin{bmatrix} \dot{\boldsymbol{\omega}}_1^{eT}\boldsymbol{\Lambda}_1''\dot{\boldsymbol{\omega}}_1^e\big|_{t_1} & \cdots & \dot{\boldsymbol{\omega}}_N^{e^T}\boldsymbol{\Lambda}_N''\dot{\boldsymbol{\omega}}_N^e\big|_{t_1} & V_1\big|_{t_1} & \cdots & V_1\big|_{t_1} \\ & & \vdots & & & \\ \dot{\boldsymbol{\omega}}_1^{eT}\boldsymbol{\Lambda}_1''\dot{\boldsymbol{\omega}}_1^e\big|_{t_p} & \cdots & \dot{\boldsymbol{\omega}}_N^{e^T}\boldsymbol{\Lambda}_N''\dot{\boldsymbol{\omega}}_N^e\big|_{t_p} & V_N\big|_{t_p} & \cdots & V_N\big|_{t_p} \end{bmatrix} \tag{4.58}$$

where

$$\begin{aligned} L_k &= \dot{\mathbf{u}}_k^{e^T}\mathbf{N}_k'\mathbf{u}_k^e + \frac{1}{2}\dot{\mathbf{u}}_k^{e^T}\mathbf{A}_k'\boldsymbol{\omega}_k^e + \dot{\boldsymbol{\omega}}_k^{e^T}\mathbf{A}_k'^T\mathbf{u}_k^e + \frac{1}{2}\dot{\boldsymbol{\omega}}_k^{e^T}\boldsymbol{\Xi}_k'^2\boldsymbol{\omega}_k^e \\ V_k &= \dot{\mathbf{u}}_k^{e^T}\mathbf{N}_k'\dot{\mathbf{u}}_k^e + \dot{\mathbf{u}}_k^{e^T}\bar{\mathbf{A}}_k'\dot{\boldsymbol{\omega}}_k^e + \dot{\boldsymbol{\omega}}_k^{e^T}\mathbf{A}_k'^T\dot{\mathbf{u}}_k^e + \dot{\boldsymbol{\omega}}_k^{e^T}\boldsymbol{\Xi}_k'\dot{\boldsymbol{\omega}}_k^e \end{aligned} \tag{4.59}$$

Since the external dampers are studied later in this chapter, in the derivation of equation (4.58) the contribution of the external damping factor, $\mathcal{C}$, has been neglected.

The observation vector, $\mathbf{y}$, is identical to equation (4.34). Again it should be noted that the contribution of the weight forces must be eliminated in the calculation of *f* and *q*. Also, in the known mass situation, the terms $\mathbf{G}$ and $\boldsymbol{\theta}_m$ are eliminated from the data matrix, **H**, and unknown vector, $\boldsymbol{\theta}$.

Proportional damping

For a general proportional damping modeling, equation (4.37) and the damping unknown vector, $\boldsymbol{\theta}_c$, of equation (4.38) need to be taken into consideration. Meanwhile,

the transverse displacement viscous resistance, $c(x)$ along with $c_s(x)$ must be eliminated from the damping data matrix. The mass, $\boldsymbol{\theta}_m$, and stiffness, $\boldsymbol{\theta}_k$, unknown parameters, along with their corresponding data matrices, $\mathbf{G}$ and $\boldsymbol{\Gamma}$, remain the same as described in equations (4.24), (4.68), and (4.57). However, the damping data matrix should be turned into:

$$\mathbf{D} = \left[\mathbf{D}_m, \mathbf{D}_k\right] \tag{4.60}$$

Where $\mathbf{D}_m$ is defined in equation (4.40) and

$$\mathbf{D}_k = \begin{bmatrix} \dot{\boldsymbol{\omega}}_1^{eT} \boldsymbol{\Lambda}_1'' \dot{\boldsymbol{\omega}}_1^e \Big|_{t_1} & \cdots & \dot{\boldsymbol{\omega}}_N^{e\,T} \boldsymbol{\Lambda}_N'' \dot{\boldsymbol{\omega}}_N^e \Big|_{t_1} & \bar{L}_1\Big|_{t_1} & \cdots & \bar{L}_N\Big|_{t_1} \\ & & \vdots & & & \\ \dot{\boldsymbol{\omega}}_1^{eT} \boldsymbol{\Lambda}_1'' \dot{\boldsymbol{\omega}}_1^e \Big|_{t_p} & \cdots & \dot{\boldsymbol{\omega}}_N^{e\,T} \boldsymbol{\Lambda}_N'' \dot{\boldsymbol{\omega}}_N^e \Big|_{t_p} & \bar{L}_1\Big|_{t_p} & \cdots & \bar{L}_N\Big|_{t_p} \end{bmatrix} \tag{4.61}$$

$$\bar{L}_k = \dot{\mathbf{u}}_k^{e\,T} \mathbf{N}_k' \dot{\mathbf{u}}_k^e + \dot{\mathbf{u}}_k^{e\,T} B_k \mathbf{A}_k' \dot{\boldsymbol{\omega}}_k^e + \frac{1}{2} B_k \dot{\boldsymbol{\omega}}_k^{e\,T} \mathbf{A}_k'^T \dot{\mathbf{u}}_k^e + \frac{1}{2} B_k{}^2 \dot{\boldsymbol{\omega}}_k^{e\,T} \boldsymbol{\Lambda}_k' \dot{\boldsymbol{\omega}}_k^e$$

Unknown Mass Modification for the Total Displacement Measurement

If the total displacement measurements are used with an unknown mass situation, the mass data matrix, $\mathbf{G}$, needs to be modified employing the extra term $\bar{\mathbf{m}}_j$ introduced in part b of equation (2.17). Thus, the expression of $\bar{\mathbf{m}}_j$ for the beam elements is derived in this part.

Consider (x_1, x_2, x_3) be the local coordinates of a member or an element and (x, y, z) be the global coordinates as shown in Figure IV-3. Also, consider the counterclockwise angle α_i be measured from the positive global x-axis to the positive local x-axis of the i^{th} element. α_i may be measured from the geometry of the elements at any state of the structure. The matrix that transfers the nodal displacements from the global to the local coordinates is:

$$\mathbf{R}_i = \begin{bmatrix} \cos\alpha_i & 0 & \sin\alpha_i \\ 0 & 1 & 0 \\ -\sin\alpha_i & 0 & \cos\alpha_i \end{bmatrix} \tag{4.62}$$

The reverse transformation can be obtain through $\mathbf{R}_i^T$ .Thus, the global displacement in z-direction of a node in the element can be found as:

$$u_z = u_1 \sin\alpha_i + u_3 \cos\alpha_i \tag{4.63}$$

where u_3 and u_z are the z-direction displacement in the local and global coordinates, respectively. u_1 is the displacement in the x-direction, axial displacement, in the local coordinates.

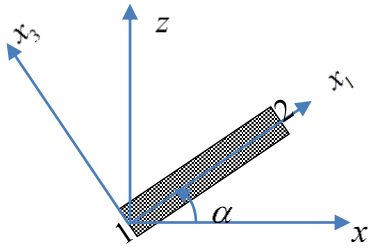

Figure IV-3: A DITER beam element with start node 1 and end note 2 whose local axis oriented with respect to the global coordinates.

Considering the effective $(\rho A)_i^e$ value for the i^{th} element, the rate of the work done by the self-weight can be approximated by:

$$\dot{W}^{mg}(t) = \sum_{i=1}^{N} \dot{W}_i^{mg} = -\sum_{i=1}^{N} g(\rho A)_i^e \int_{l_i} \dot{u}_z(t)\, dx \tag{4.64}$$

or equivalently by:

$$\dot{W}^{mg}(t) = \sum_{i=1}^{N} \dot{W}_i^{mg} = -\sum_{i=1}^{N} g(\rho A)_i^e \left(\left(\dot{\mathbf{u}}_o^e\right)_i^T \sin\alpha_i \int_{l_i} \boldsymbol{\varphi} dx + \left(\dot{\boldsymbol{\omega}}_o^e\right)_i^T \cos\alpha_i \int_{l_i} \boldsymbol{\psi} dx \right) \tag{4.65}$$

Thus, one can introduce

$$\dot{W}_i^{mg} = g \left[\left(\dot{\mathbf{u}}_o^e\right)_i^T \quad \left(\dot{\boldsymbol{\omega}}_0^e\right)_i^T \right] \bar{\mathbf{m}}_i \tag{4.66}$$

where

$$\bar{\mathbf{m}}_i = -\left[\sin\alpha_i \int_{l_i} \boldsymbol{\varphi}^T dx \quad \cos\alpha_i \int_{l_i} \boldsymbol{\psi}^T dx \right]^T \tag{4.67}$$

Finally, the mass data matrix can be written as:

$$\mathbf{G} = \begin{bmatrix} \dot{\boldsymbol{\omega}}_1^{eT} \boldsymbol{\Lambda}_1' \ddot{\boldsymbol{\omega}}_1^e \Big|_{t_1} & \cdots & \dot{\boldsymbol{\omega}}_N^{e\,T} \boldsymbol{\Lambda}_N' \ddot{\boldsymbol{\omega}}_N^e \Big|_{t_1} & \dot{\mathbf{u}}_1^{eT} \mathbf{N}_1 \ddot{\mathbf{u}}_1^e + \dot{\boldsymbol{\omega}}_1^{eT} \boldsymbol{\Lambda}_1 \ddot{\boldsymbol{\omega}}_1^e - \dot{W}_1^{mg} \Big|_{t_1} & \cdots & \dot{\mathbf{u}}_N^{e\,T} \mathbf{N}_N \ddot{\mathbf{u}}_N^e + \dot{\boldsymbol{\omega}}_N^{e\,T} \boldsymbol{\Lambda}_N \ddot{\boldsymbol{\omega}}_N^e - \dot{W}_N^{mg} \Big|_{t_1} \\ & & \vdots & & & \\ \dot{\boldsymbol{\omega}}_1^{eT} \boldsymbol{\Lambda}_1' \ddot{\boldsymbol{\omega}}_1^e \Big|_{t_p} & \cdots & \dot{\boldsymbol{\omega}}_N^{e\,T} \boldsymbol{\Lambda}_N' \ddot{\boldsymbol{\omega}}_N^e \Big|_{t_p} & \dot{\mathbf{u}}_1^{eT} \mathbf{N}_1 \ddot{\mathbf{u}}_1^e + \dot{\boldsymbol{\omega}}_1^{eT} \boldsymbol{\Lambda}_1 \ddot{\boldsymbol{\omega}}_1^e - \dot{W}_1^{mg} \Big|_{t_p} & \cdots & \dot{\mathbf{u}}_N^{e\,T} \mathbf{N}_N \ddot{\mathbf{u}}_N^e + \dot{\boldsymbol{\omega}}_N^{e\,T} \boldsymbol{\Lambda}_N' \ddot{\boldsymbol{\omega}}_N^e - \dot{W}_N^{mg} \Big|_{t_p} \end{bmatrix} \tag{4.68}$$

Once the mass data matrix of equation (4.68) is in use, all the self-weight components must be eliminated from the other loads i.e. f, q .

PART II: FRAMES

DITER for Frames

Once the DITER formulation for beam elements is completed, the same data matrices, $\mathbf{G}, \mathbf{D}, \boldsymbol{\Gamma}$, and observation vector, $\mathbf{y}$, may be applied for the damage detection in two dimensional frames. The module base nature of DITER makes its implementation a convenient task even for large frames. For clarification, assume a frame with *NCOM* number of components. The data and observation matrices of each component (either beam or column) can be constructed individually as described in the first part of this chapter. The assembled observation vector might be found as

$$\mathbf{y} = \sum_{i=1}^{NCOM} \mathbf{y}_i \tag{4.69}$$

where $\mathbf{y}_i$ is the observation vector of the i^{th} component.

To assemble the data matrices, however, different combinations might be employed corresponding to the desirable ordering of the unknown properties. For instance, two assembled sets are presented in equations (4.70) and (4.71).

$$\text{Set 1: } \begin{cases} \mathbf{H} = [\mathbf{H}_1, ..., \mathbf{H}_{NCOM}] \\ \boldsymbol{\theta} = \left[\boldsymbol{\theta}_1^T, ..., \boldsymbol{\theta}_{NCOM}^T \right]^T \end{cases} \tag{4.70}$$

$$\text{Set 2: } \begin{cases} \mathbf{H} = [\boldsymbol{\Gamma}, \mathbf{D}, \mathbf{G}] \\ \boldsymbol{\theta} = \left[\boldsymbol{\theta}_k^T, \boldsymbol{\theta}_c^T, \boldsymbol{\theta}_m^T \right]^T \end{cases} \tag{4.71}$$

where in the second set

$$\boldsymbol{\Gamma} = \begin{cases} \left[\boldsymbol{\Gamma}_1, ..., \boldsymbol{\Gamma}_{NCOM} \right] & \text{No static deflection correction} \\ \left[\bar{\boldsymbol{\Gamma}}_1, \boldsymbol{\Gamma}_{s_1}, ..., \bar{\boldsymbol{\Gamma}}_{NCOM}, \boldsymbol{\Gamma}_{s_{NCOM}} \right] & \text{With static deflection correction} \end{cases}$$

$$\boldsymbol{\theta}_k = \begin{cases} \left[\left(\boldsymbol{\theta}_k^T \right)_1, ..., \left(\boldsymbol{\theta}_k^T \right)_{NCOM} \right]^T & \text{No static deflection correction} \\ \left[\left(\boldsymbol{\theta}_k^T \right)_1, \left(\bar{\boldsymbol{\theta}}_k^T \right)_1 ..., \left(\boldsymbol{\theta}_k^T \right)_{NCOM}, \left(\bar{\boldsymbol{\theta}}_k^T \right)_{NCOM} \right]^T & \text{With static deflection correction} \end{cases}$$

$$\mathbf{D} = \begin{cases} \left[\mathbf{D}_1, ..., \mathbf{D}_{NCOM} \right] \\ \left[\mathbf{D}_m, \mathbf{D}_k \right] \end{cases} \quad \text{For Rayleigh damping model}$$

$$\boldsymbol{\theta}_c = \begin{cases} \left[\left(\boldsymbol{\theta}_c^T \right)_1, ..., \left(\boldsymbol{\theta}_c^T \right)_{NCOM} \right]^T \\ \left[\alpha \left(\boldsymbol{\theta}_m{}^T \right)_1, ..., \alpha \left(\boldsymbol{\theta}_m{}^T \right)_{NCOM}, \beta \left(\boldsymbol{\theta}_k{}^T \right)_1 ..., \left(\beta \boldsymbol{\theta}_k{}^T \right)_{NCOM} \right]^T \end{cases} \text{For Rayleigh damping model}$$

$$\mathbf{G} = \left[\mathbf{G}_1, ..., \mathbf{G}_{NCOM} \right]$$

$$\boldsymbol{\theta}_m = \left[\left(\boldsymbol{\theta}_m^T \right)_1, ..., \left(\boldsymbol{\theta}_m^T \right)_{NCOM} \right]^T$$

Note that in case of using Rayleigh damping model, the term *N* in the equations (4.40) and (4.61) must be changed into *NCOM*. In the case of using the static deflection correction terms for the first set, $\mathbf{H}_i$ and $\boldsymbol{\theta}_i$ should be replaced, respectively, by $\bar{\mathbf{H}}_i$ and $\bar{\boldsymbol{\theta}}_i$ according to equation (2.33) .

DITER for Sub-Systems

In the case of dealing with large structures, monitoring the health of all the elements is a cumbersome task. Reliable damage detection results are heavily dependent on collecting proper data for which a suitable excitation technique is demanded. Evenness in responses helps to avoid ill-conditioned data matrices, which are likely to occur as the number of unknowns keeps growing. Hence, for a large structure, extra care must be taken to excite the system properly. However, it is not always possible to fulfill such a demand

due to the expenses and/or the current service condition of the structure. Besides, instrumenting a large structure with sensors is not always possible. Yet, the problem may be largely overcome if the structure is split into smaller parts, named sub-systems, and each be investigated separately. The process might be more computationally demanding, yet the complexity of excitations, likelihood of ill-conditioning, as well as instrumentation difficulties might be lessened significantly. In addition, an owner might be more interested in identification of some specific areas rather than the whole structure. Hence, DITER should be customizable to the interested components, i.e. the sub-systems, regardless of the behavior of the other parts of the structure.

The important complexity that arises in the sub-system approach is the appearances of new external forces on the boundaries. These newly emerged forces are in fact the current internal forces in the boarding components of the isolated system, whose work or energy had been canceled out previously. Therefore, in order to apply DITER to an isolated part of a structure, it is required to keep tracking the boundaries' forces and calculating them at each time instant. Figure IV-4 illustrates the above discussion for a 2D frame. The internal forces, $\mathbf{F}_{in}$ of an isolated sub-system, separated by the dashed lines, have been shown in in the same figure.

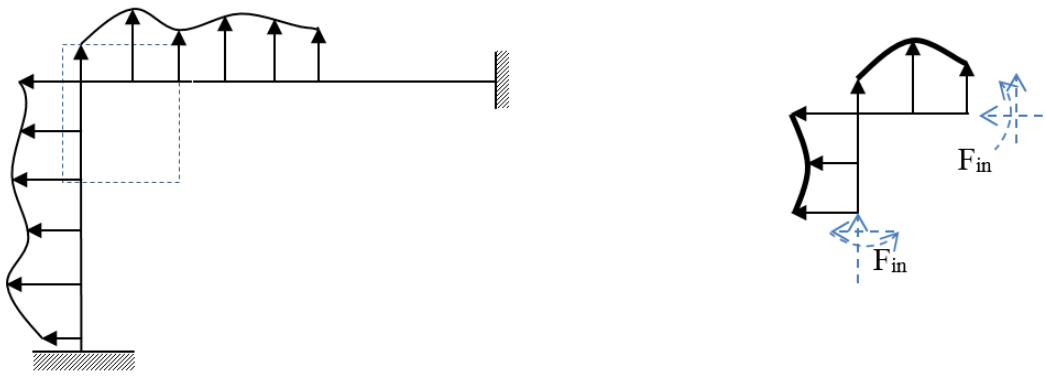

Figure IV-4: Left) Schematic view of a frame with a sub-system showed by the dashed box Right) the sub-system separated from the system

The sub-system, as shown in Figure IV-4, can be presumed to be a new structure excited by unknown loads. One approach to identify damages in the sub-system is to apply I-DITER. This approach, however, is iterative and requires a solution to a FE model of the sub-system updated based on the acquired parameters of each iteration. Thus, it is of interest to look for an alternative approach that is computationally less demanding.

The goal of the alternative approach is to obtain the newly emerged internal forces either directly or through the identification of some new unknowns but without any iteration. To achieve this goal, it is required to install sensors on the immediate adjacent elements to the sub-system to collect their response data. Consider an element of a sub-system whose start node is on the sub-system boundary. This element will be referred to as the 'start element'. The newly emerged internal forces on this element are Q_1, Q_2, Q_3 shown in Figure IV-2. Consider $\mathbf{Q}^{s-s} = [Q_1, Q_2, Q_3]^T$ as the vector which stores the internal forces of the start node of the start element. Thus, $\mathbf{Q}^{s-s}$ should be obtained to apply DITER to the sub-system.

Assume that J_s number of elements located outside the sub-system, called as 'start boundary elements', are attached to the start element. The internal forces at the start node of the start element, $\mathbf{Q}^{s-s}$, can be found by deducting the sum of the generalized forces emerged at the end nodes of the start boundary elements from any existent concentrated load located at the start node as:

$$\mathbf{Q}^{s-s} = \left(\bar{\mathbf{R}}^s\right)^T \left(\mathbf{p}^s - \sum_{i=1}^{J_s} \bar{\mathbf{R}}_i \mathbf{Q}_i^s\right) \tag{4.72}$$

where $\mathbf{p}^s = [p_x, p_z, M_y]^T$ is a vector that contains the concentrated loads applied at the start node location with description in the global coordinates. $\mathbf{Q}_i^s$ is the internal forces of the end node of the i^{th} start boundary element described in the local (member) coordinates. $\bar{\mathbf{R}}^s$ and $\bar{\mathbf{R}}_i$ (see equation (4.73))

$$\bar{\mathbf{R}} = \begin{bmatrix} \cos\alpha & -\sin\alpha & 0 \\ \sin\alpha & \cos\alpha & 0 \\ 0 & 0 & 1 \end{bmatrix} \tag{4.73}$$

are the rotation matrices that transfer nodal DOFs from the local to the global coordinates for the start element and the i^{th} start boundary elements, respectively. α is the angle measured counterclockwise from the positive global x-axis to the positive local x-axis. The internal forces of the i^{th} boundary element can be found from

$$\mathbf{Q}_i^{BE} = \mathbf{M}_i^{BE}\ddot{\mathbf{u}}_i^{BE} + \mathbf{C}_i^{BE}\dot{\mathbf{u}}_i^{BE} + \mathbf{K}_i^{BE}\mathbf{u}_i^{BE} - \mathbf{F}_i^{BE} \tag{4.74}$$

where $\mathbf{F}_i^{BE}$ is a vector that contains values of element wise external forces $\mathfrak{q}$ and $\mathfrak{f}$, defined in part I, applied on the element domain and $\mathbf{Q}_i^{BE} = \left[Q_1, Q_2, Q_3, Q_4, Q_5, Q_6\right]_i^T$. Note that the interest is only on the $\mathbf{Q}_i^s = \left[Q_4, Q_5, Q_6\right]_i^T$ values.

Similarly, any element of the sub-system will be referred to as the 'end element' if its end node is located on the sub-system boundary. Here, the internal forces emerged to the end node of these end elements, $\mathbf{Q}^{s-E} = \left[Q_1, Q_2, Q_3\right]^T$, are of interest. To find $\mathbf{Q}^{s-E}$ similar computation of equation (4.72) might be followed as

$$\mathbf{Q}^{s-E} = \left(\bar{\mathbf{R}}^E\right)^T \left(\mathbf{p}^E - \sum_{i=1}^{J_E} \bar{\mathbf{R}}_i \mathbf{Q}_i^E\right) \tag{4.75}$$

where $\mathbf{Q}_i^E = \left[Q_1, Q_2, Q_3\right]_i^T$ contains the internal forces of the start node of the i^{th} end boundary element, and $\mathbf{p}^E$ is the same as $\mathbf{p}^s$ defined in equation (4.72) but at the location of the end node of the end element. In addition, J_E represents the number of end boundary elements.

The rate of the work done by the internal forces on the boundary nodes of the sub-system at any time instant can then be obtained as

$$\dot{W}^{BN} = \sum_{j=1}^{NBN} \dot{\mathbf{u}}_j^T \mathbf{Q}_j^{BN} \tag{4.76}$$

where superscript BN denotes the boundary nodes, NBN is the number of boundary nodes, and

$$\begin{cases} \mathbf{Q}_j^{BN} = \left[\mathbf{Q}_j^{s_-s^T}, 0, 0, 0 \right]^T \text{ for start nodes} \\ \mathbf{Q}_j^{BN} = \left[0, 0, 0, \mathbf{Q}_j^{s_-E^T} \right]^T \text{ for end nodes} \end{cases} \tag{4.77}$$

Note that $\dot{\mathbf{u}}$ is related either to the start or to the end elements corresponding to the form of $\mathbf{Q}^{BN}$.

Once the values of $\dot{W}^{BN}$ are determined, they must be added to the work rate of the rest of the sub-system domain. Note that concentrated loads applied to the start node of the start element and in the end node of the end elements must be excluded from the calculation of $\dot{W}$. The reason is that the contribution of these loads have already been taken into account in the calculation of $\mathbf{Q}_j^{BN}$. Therefore, if the properties of the boundary elements are known, the data and observation matrices of the sub-system are in the form of

$$\begin{aligned} \mathbf{\Gamma}^{SS} &= \mathbf{\Gamma} \\ \mathbf{D}^{SS} &= \mathbf{D} \\ \mathbf{G}^{SS} &= \mathbf{G} \\ \dot{\mathbf{y}}^{SS}(t) &= \dot{\mathbf{w}} + \dot{\mathbf{w}}^{BN} \end{aligned} \tag{4.78}$$

where $\mathbf{\Gamma}$, $\mathbf{D}$, $\mathbf{G}$, and $\dot{\mathbf{w}}$ are the data and observation matrices of the sub-system obtained neglecting the boundary elements' effect. $\dot{\mathbf{w}}^{BN}$ and $\dot{\mathbf{w}}$ are a column vectors that, respectively, contain the values of $\dot{W}^{BN}$ and $\dot{W}$ at different time instants. Take note that since all the concentrated forces applied on the boundary nodes are already considered in the $\dot{W}^{BN}$, their contribution must be taken out from $\dot{\mathbf{w}}$.

Equation (4.78) is applicable as long as the parameters of the boundary elements are given. However, the values of the stiffness, mass, and damping matrices of equation (4.74) are not always known. In such a case, the unknown values of the boundary elements

are transferred into the unknown vector, and the data matrices must be adjusted correspondingly.

To find the corresponding data matrices of the boundary elements, i.e. $\mathbf{\Gamma}^{BE}, \mathbf{D}^{BE}, \mathbf{G}^{BE}$, $\dot{W}^{BN}$ is examined again. Contribution of the j^{th} boundary element to the $\dot{W}^{BN}$ is

$$\dot{W}_j^{BE} = \begin{cases} -\dot{\mathbf{u}}_j^{S^T}\mathbf{Q}_j^{BE} & \text{start boundary element} \\ -\dot{\mathbf{u}}_j^{E^T}\mathbf{Q}_j^{BE} & \text{end boundary element} \end{cases} \tag{4.79}$$

where $\dot{\mathbf{u}}_j^S$ and $\dot{\mathbf{u}}_j^E$ consist of a part of components of the element velocity DOF vector, $\dot{\mathbf{u}}_j$, as

$$\begin{aligned} \dot{\mathbf{u}}_j^S &= \left[0,0,0,\dot{u}_4,\dot{u}_5,\dot{u}_6\right]_j^T \\ \dot{\mathbf{u}}_j^E &= \left[\dot{u}_1,\dot{u}_2,\dot{u}_3,0,0,0\right]_j^T \end{aligned} \tag{4.80}$$

and vector $\mathbf{Q}_j^{BE}$ holds the element internal forces. Substituting $\mathbf{Q}_j^{BE}$ from equation (4.74) in equation(4.79) yields

$$\dot{W}_j^{BE}(t) = -\begin{cases} \dot{\mathbf{u}}_j^{S^T}\mathbf{M}_j^{BE}\ddot{\mathbf{u}}_j^{BE} + \dot{\mathbf{u}}_j^{S^T}\mathbf{C}_j^{BE}\dot{\mathbf{u}}_j^{BE} + \dot{\mathbf{u}}_j^{S^T}\mathbf{K}_j^{BE}\mathbf{u}_j^{BE} - \dot{\mathbf{u}}_j^{S^T}\mathbf{F}_j^{BE} & \text{start boundary element} \\ \dot{\mathbf{u}}_j^{E^T}\mathbf{M}_j^{BE}\ddot{\mathbf{u}}_j^{BE} + \dot{\mathbf{u}}_j^{E^T}\mathbf{C}_j^{BE}\dot{\mathbf{u}}_j^{BE} + \dot{\mathbf{u}}_j^{E^T}\mathbf{K}_j^{BE}\mathbf{u}_j^{BE} - \dot{\mathbf{u}}_j^{E^T}\mathbf{F}_j^{BE} & \text{end boundary element} \end{cases} \tag{4.81}$$

Equation (4.81) is placed at the RHS of the DITER governing equation where the rate of the work is calculated. However, the first three terms of each equation of equation (4.81) should be transferred to the LHS to account for the unknown parameters of the boundary elements. Consequently, new data matrices must be formed. A simple investigation reveals that the terms of equation (4.81) are exactly the same as terms in equation (2.17) if the multiplied transposed velocity vector is change to either $\dot{\mathbf{u}}_j^S$ or $\dot{\mathbf{u}}_j^E$. Therefore, the data matrices of the boundary elements can be formed exactly in the same way as it has been described for the beam components earlier in this chapter except that the transpose

velocity vectors should be changed to either $\dot{\mathbf{u}}_j^S$ or $\dot{\mathbf{u}}_j^E$. Once the $\mathbf{\Gamma}^{BE}, \mathbf{D}^{BE}$, and $\mathbf{G}^{BE}$ matrices are formed, the final data matrices can be obtained as

$$\begin{aligned}
\mathbf{\Gamma}^{SS} &= \begin{bmatrix} \mathbf{\Gamma} & \mathbf{\Gamma}^{BE} \end{bmatrix} \\
\mathbf{D}^{SS} &= \begin{bmatrix} \mathbf{D} & \mathbf{D}^{BE} \end{bmatrix} \\
\mathbf{G}^{SS} &= \begin{bmatrix} \mathbf{G} & \mathbf{G}^{BE} \end{bmatrix}
\end{aligned} \tag{4.82}$$

where $\mathbf{\Gamma}$, $\mathbf{D}$, and $\mathbf{G}$ are the data matrices of the sub-system obtained neglecting the boundary elements' effect. Also, the rate of the work vector of the sub-system is

$$\dot{\mathbf{y}}^{SS}(t) = \dot{\mathbf{w}} + \bar{\dot{\mathbf{w}}}^{BN} \tag{4.83}$$

where $\dot{\mathbf{w}}$ is the work rate applied to the sub-system including the work of any concentrated load located inside or on the boundary of the sub-system. Note that the effect of the boundary elements have been neglected in calculation of $\dot{\mathbf{w}}$ and

$$\begin{aligned}
\bar{\dot{\mathbf{w}}}^{BN} &= \left[\bar{\dot{W}}^{BN}\Big|_{t_0}, ..., \bar{\dot{W}}^{BN}\Big|_{t_p} \right]^T \\
\bar{\dot{W}}^{BN}(t) &= \sum_{i=1}^{J_S} \dot{\mathbf{u}}_i^{S\,T} \mathbf{F}_i^{BE} + \sum_{i=1}^{J_E} \dot{\mathbf{u}}_i^{E\,T} \mathbf{F}_i^{BE}
\end{aligned} \tag{4.84}$$

To complete the DITER equation, the final task is to create the unknown vector of the sub system, $\boldsymbol{\theta}^{SS}$. $\boldsymbol{\theta}^{SS}$ is a column vector which consists of the sub-system elements properties, $\boldsymbol{\theta}$, and the unknown parameters of the boundary elements, $\boldsymbol{\theta}^{BE}$, as

$$\boldsymbol{\theta}^{SS} = \left[\boldsymbol{\theta}^T, \boldsymbol{\theta}^{BE\,T} \right]^T \tag{4.85}$$

The components of $\boldsymbol{\theta}^{BE}$ must be sorted corresponding to the boundary element data matrices. In addition, to detect damages in the mass properties of the sub-system, external excitation must be applied in the sub-system domain. Otherwise, the mass values must be estimated, for instance from the structure geometry and material densities, or singularity will occur.

DITER for Frames Equipped with Isolators and Dampers

To enhance the structural performance at extreme loadings, such as earthquakes, a common practice is to equip frames with isolators and/or dampers to mitigate the force

transmissibility between the components and dissipate the energy. For instance, common isolator applications may be found in base isolated buildings and in bridges with isolation bearings placed between the deck and the substructure. Thus, existence of seismic protective systems must be considered in a sophisticated damage detection method.

If the behavior of these dampers and isolators can be simplified into a Kelvin spring-dashpot model with constant stiffness and viscous coefficients, it is possible to find their unknown properties by directly adding their data and unknown matrices to the currently assembled $\mathbf{H}$ and $\boldsymbol{\theta}$, respectively. This has been shown later in this chapter. However, most of the time, these systems show strong viscous or hysteretic nonlinear behaviors. Therefore, it is proposed to eliminate the interference of the protective systems in the identification of the structural components and makes them two separated modules. The main objective is to detect damages in the structure; and, should it be desired, the minor objective is to track the conditions of the dissipation devices as well. Once the devices are separated from the structure, each can be modeled as a non-linear SDOF system with known dynamic responses and excitations. Identification of such systems are vastly studied in the literature, e.g. see (Ma et al. 2004; Yang et al. 2006; Yin et al. 2012; Yin et al. 2010; Zhang et al. 2002).

Sliding and elastomeric bearings are examples of isolators being used in the structures. Being amongst common isolators used in bridges (Karalar et al. 2012), elastomeric bearings, such as low damping rubber (LDRB) and lead rubber bearings (LRB), are the main concern in this study. Compared to their large vertical stiffness, these isolators have relatively low horizontal stiffness, and thus can shift the structural period from the excitation loads' and lessen the inertial forces. High lateral displacement may also be avoided as the energy is dissipated through the hysteretic behavior of these isolators.

Behaviors of rubber bearing (RB) isolators are seldom linear and adaptation of a suitable constitutive model is necessary to describe the hysteretic behavior of the RBs. Effective stiffness and effective damping might be used to model the hysteretic behavior of the elastomers for a pre-selected lateral displacement. These effective values are not

constant and are directly affected by the amount of the displacement of the isolator. However, the variations may be neglected in small deformations and effective values might be assumed for the behavior.

For large displacements, the hysteretic behavior of elastomeric isolators in the lateral direction usually is simplified through employing a bilinear force-displacement model ,see Figure IV-5, (Constantinou et al. 2011). However, the characteristics of the bilinear form are not constant; and, for instance, variations in vertical stiffness may change their values.

In the bilinear form, pre yield stiffness, k_e , post yield stiffness, k_d , and the characteristic strength, Q_d , i.e. the force axis intercept of the hysteresis loop, are the main properties based on which one may design the system (see Figure IV-5).

These characteristics are provided by the manufacturer and must be verified by the prototype testing as well as by the tests that are performed under circumstances that the structure is expected to be exposed to, including the required displacement and the applied vertical loads, or the most severe anticipated earthquake loads.

These characteristics are dependent on the applied load's magnitude and frequency, strain rate, temperature, and time. For instance, (Constantinou MC 2007) showed that substantial changes in the stiffness and damping of LDRBs can be observed due to the temperature variation in low temperatures. In addition, the behavior of the shear force-deformation of the LDRBs changed from hysteretic in high temperature into viscoelastic in low temperatures. The same study reveals the dependency of the yield point of a LRB on the applied load's frequency. The reason is mainly attributed to the internal heat that is generating by the lead core during the loading.

To address the above variations, boundaries are provided for the isolator properties for which the design must be checked. For instance, a range of nominal values of the properties of isolators are determined through tests, which are performed in 20 ^{o}C and for various magnitudes of vertical load, lateral load frequency, and displacement.

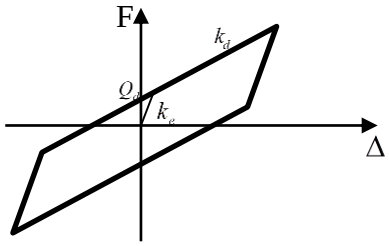

Figure IV-5: Bilinear lateral force-displacement behavior of an isolator

The boundaries might be constructed by multiplying the range of the nominal values with factors that account for the effects of parameters such as temperature, the expected cumulative displacement of the isolator under the service loads, aging, oxidation, and wearing (Constantinou MC 2007). For instance, as the elastomer is aging, the continuation of vulcanization may increase the post yielding stiffness up to 10%, and a drop in temperature may increase the pre-yield stiffness and the characteristic strength by 30% and 80%, respectively (Constantinou MC 2007). Properties limited to these boundaries must satisfy the designing criteria such as the maximum shear deformation and the stability of the isolator that are mostly dependent on the lateral properties.

Compared to the bilinear form, the Bouc–Wen model (Wen 1976) may describe the hysteretic behavior of the isolator more realistically particularly for the dynamic analyses (Ismail et al. 2009). Neglecting pinching effect, which is not an issue for lead rubber and low damping rubber bearings, and assuming no material degradation during data collection, the lateral restoring force of the isolator, *f(t),* can be found as (Lu and Zhou 2002)

$$f(t) = \alpha k_e u(t) + (1-\alpha) k_e u_y Z(t) \tag{4.86}$$

where $f(t)$ is the lateral force developed at the ends of the isolator, u_y is the yield displacement, i.e. the point at which the pre-yield stiffness reduces to the post-yield stiffness, and $\alpha = k_d / k_e$ is a value between zero and one. $Z(t)$ is an imaginary hysteretic component defined as

$$u_y \dot{Z}(t) + \beta Z(t)\left|\dot{u}(t)\right|\left|Z(t)\right|^{n-1} + \gamma \dot{u}(t)\left|Z(t)\right|^{n} - A\dot{u}(t) = 0 \tag{4.87}$$

where A, n, γ, and β are dimensionless shape parameters ($n \geq 1$). The Bouc-Wen parameters may also vary, for instance, due to the variations of the frequency of motion and the variation of the vertical force that are applied to the isolator.

Damage detection of an RB isolator may be attributed to the off limit variations in its pre- and post-yield stiffness values. If the identified values are outside the boundaries that were employed for the design, then a damage state might be reported for further investigations. It has been shown that as long as the lateral responses and excitations of a RB isolator are available, the Bouc-Wen parameters of equation (4.86) and (4.87) may be identified through solving a non-linear optimization problem employing, e.g. least-square (Yin et al. 2010), extended Kalman filter (Yin et al. 2012), or algorithms based on a combination of least square and Kalman filter techniques (Ismail et al. 2009). Therefore, to detect damages in the isolators of a frame, the main contribution of this dissertation will be to provide the required force-displacement of the employed isolators. Note that simplifying the non-linear behavior of RB isolators by using effective damping and stiffness is not beneficial as these values are displacement dependent, and their variation is not comparable to track changes in the isolator.

To provide the force-displacement behavior of non-linear damper or RB isolator devices the sub-system approach might be conducted to first, separate the non-linear contribution of the devices from the rest of the system and identify the structural properties; and second, determine the internal forces applied to the devices from the beam/column components. Here, it is assumed that while the devices behave non-linearly, the structure itself can be in an elastic range. In the rest of the chapter the identification of the force-displacement relation for RB isolators and dampers are discussed separately.

Identification of force-displacement relations of RB isolators

Assume n rubber bearing devices have been placed between columns and beams of a frame. The sensors must be installed at both ends of each rubber bearing to provide the dynamic response data. To determine the lateral force-displacement relation, it is

required to find the internal forces at one of the ends of the device. Compared to the bottom end, more elements are commonly connected to the top surface of an isolator, thus it is simpler to find the internal forces using the boundary elements of the columns instead of the beams; however, either can be selected. During an excitation, the both ends of an isolator may rotate. Therefore, it is helpful to describe the lateral force and displacements of the ends of the isolator with respect to the local coordinates of one of the end plates.

If the end nodes of the k^{th} isolator are denoted by i, j notations, and NEL components are attached to the end i of the isolator, then the forces applied to the end i can be found from:

$$\mathbf{f}_i^k = {}^j\bar{\mathbf{R}}_k^T\left(\mathbf{p}_i^k - \sum_{m=1:NEL}\bar{\mathbf{R}}_m\left(\mathbf{Q}_m^{s/E}\right)\right) \tag{4.88}$$

where $\mathbf{p}_i^k = \left[p_x, p_z, M_y\right]^T$ is a vector that contains the concentrated loads applied at the structural members at node i, and it is described in the global coordinates. $\mathbf{Q}_m^{s/E}$ consists of the internal forces of the end of the m^{th} boundary element that is attached to the end i of the isolator, and it is defined as

$$\mathbf{Q}_m^{s/E} = \begin{cases} \mathbf{Q}_m^s = \left[Q_4, Q_5, Q_6\right]^T{}_m & \text{if element m is an end boundary element} \\ \mathbf{Q}_m^E = \left[Q_1, Q_2, Q_3\right]^T{}_m & \text{if element m is an start boundary element} \end{cases} \tag{4.89}$$

where all the variables are defined in equations (4.72) to (4.75). Note that once the boundary elements' properties are identified, the values of Q_1 to Q_6 can be determined from equation (4.74). $\bar{\mathbf{R}}_m$ is the rotation matrix of the m^{th} boundary element, and ${}^j\bar{\mathbf{R}}_k$ is the rotation matrix of the k^{th} isolator formed at the end j. The rotation matrix is shown in equation(4.73). For the isolator, the local z axis, x_3 , is the axial axis that passes through the area centers of the end plates or cover plates in the opposite direction of gravity, and the x_1 axis must be selected in a way that the out of plane local axis , x_2 , take the same direction as of the out of plane global axis , y, where all the coordinates must follow the

right hand rule. ${}^{j}\bar{\mathbf{R}}_k$ is a function of time, because the angle α_j^k of the isolator rotation matrix (formed at the end-plate j) should be updated to ${}^{j}\alpha_k^u(t)$ as

$${}^{j}\alpha_k^u(t) = \alpha_j^k - \theta_j^k(t) \tag{4.90}$$

where α_j^k is the initial angle of the positive local x-axis of the end-plate j of the isolator measured counterclockwise from the positive global x-axis when the structure is in the static equilibrium configuration. θ_j is the rotation of the end j of the isolator that is measured in the clockwise direction. The corresponding lateral force and displacement, respectively, should be taken as $\bar{f}_i^k$ and u_d^k following

$$\bar{f}_i^k = \mathbf{s}\mathbf{f}_i^k \tag{4.91}$$

$$u_d^k(t) = u_{2,i}^k(t) - u_{2,j}^k(t) - L^k(t)\sin\left(\theta_j^k(t)\right) \tag{4.92}$$

where $\mathbf{s}$ is a transfer vector defined as $\mathbf{s} = \begin{bmatrix}1 & 0 & 0\end{bmatrix}$, $\mathbf{f}_i^k$ is the same as in equation (4.88)

,

and $u_{2,i}^k$, $u_{2,\mathrm{j}}^k$ are the lateral displacements measured at the ends i and j as

$$\begin{aligned} u_{2,i}^k &= \mathbf{s}\left({}^{j}\bar{\mathbf{R}}_k^T\boldsymbol{\delta}_i^k\right) \\ u_{2,j}^k &= \mathbf{s}\left({}^{j}\bar{\mathbf{R}}_k^T\boldsymbol{\delta}_j^k\right) \end{aligned} \tag{4.93}$$

where $\boldsymbol{\delta} = \begin{bmatrix}\delta_x & \delta_z & \delta_r\end{bmatrix}^T$ consists of the measured displacements described in the global coordinates at the time instant t. The last term of equation (4.92) is added to eliminate the contribution of rigid rotations in which L^k is the height of the isolator updated at the last time instant using

$$\begin{aligned} L^k(t) &= L_0^k + \mathbf{s}'\,{}^{j}\bar{\mathbf{R}}_k^T\left(\boldsymbol{\delta}_i^k - \boldsymbol{\delta}_j^k\right) \\ \mathbf{s}' &= \begin{bmatrix}0 & 1 & 0\end{bmatrix} \end{aligned} \tag{4.94}$$

where L_0^k is the initial height of the isolator.

To find the restoring force, the last step is to deduct the inertia force of the isolator mass from the identified lateral force as shown in equation (4.95)

$$f_i^k = \bar{f}_i^k - m^k\ddot{u}_{2,\mathrm{i}}^k \tag{4.95}$$

in which $\ddot{u}^k_{2,\mathrm{i}}$ is the lateral acceleration of the isolator at the end *i* that is obtained from $\ddot{\boldsymbol{\delta}}$ in the same fashion of $u^k_{2,j}$. m^k is the mass of the isolator, and f_i^k is the restoring force that can be compared to the force described in equation (4.86) .

Similar approach may be applied to isolators placed between columns and the ground. The only difference is that the boundary elements must be taken at the end of the isolator that has been attached to the base of the columns.

Identification of force-displacement relations of dampers

If non-linear external dampers exist in the structure, Similar to the isolators, it is required to provide their axial force-displacement relation to create a platform based on which one can track variations in their behavior. However, for the linear viscous dampers the DITER equation might be used directly.

Viscous fluid dampers are rate dependents and develop forces that mathematically can be described by (Symans et al. 2008)

$$f\left(t\right)=C\left|\dot{u}\left(t\right)\right|^{\alpha}\operatorname{sgn}\left[\dot{u}\left(t\right)\right] \tag{4.96}$$

where C is the damping factor and α is the exponent. u is the axial deformation and the superscript dot represents the time derivative. sgn is the signum function. For $\alpha=1$ the damper is called a linear viscous fluid damper. The viscoelastic fluid/solid dampers are similar to the viscous fluid type, but may restore forces from compression of elastomer material that are added to the viscous fluid dampers (Symans et al. 2008).

For a linear viscous fluid damper i.e., $\alpha=1$, the rate of the dissipated energy of the i^{th} damper can be obtained as

$$\mathbf{d}_i^d=\left[\dot{r}_{i,0}{}^2,\cdots\dot{r}_{i,\mathrm{p}}{}^2\right]^T \tag{4.97}$$

where r represents the relative axial displacement of the damper , i.e. $r_{i,k}=u_{x_{end}}\left(t_k\right)-u_{x_{start}}\left(t_k\right)$ at the time instant k . The unknown parameter, C, of the damper can be identified directly by updating the currently assembled $\mathbf{D}^{ND}$ matrix and $\boldsymbol{\theta}_c^{ND}$ vector as

$$\mathbf{D} = \begin{bmatrix} \mathbf{D}^{ND} & \mathbf{d}_1^d & \cdots & \mathbf{d}_n^d \end{bmatrix} \tag{4.98}$$

$$\boldsymbol{\theta}_c = \begin{bmatrix} \boldsymbol{\theta}_c^{ND^T} & {}^c\theta_1^d & \cdots & {}^c\theta_n^d \end{bmatrix}^T \tag{4.99}$$

where n is the number of the linear viscous fluid dampers and ${}^c\theta_i^d = C_i$. $\boldsymbol{\theta}_c^{ND}$ and $\mathbf{D}^{ND}$ are, respectively, the unknown vector of the damping coefficients and damping matrix of the frame in which the existence of dampers have been neglected. The role of the mass, m_i^d, of the i^{th} damper may also be accounted for by forming a 2 by 2 diagonal mass matrix with components of $m_i^d / 2$ and considering the acceleration, $\ddot{\bar{\boldsymbol{\alpha}}}_i$, and velocity, $\dot{\bar{\boldsymbol{\alpha}}}_i$, vectors where they are described in the global coordinates. Consequently, the rate of the kinetic energy of the i^{th} damper is

$$\dot{T}_i^d = \left(\dot{\bar{\boldsymbol{\alpha}}}_i\right)^T \mathbf{M}_i^d \ddot{\bar{\boldsymbol{\alpha}}}_i \tag{4.100}$$

or more simply

$$\dot{T}_i^d = \frac{m_i^d}{2}\left(\dot{\bar{\boldsymbol{\alpha}}}_i\right)^T \ddot{\bar{\boldsymbol{\alpha}}}_i \tag{4.101}$$

where $\mathbf{M}_i^d$ is the diagonal mass matrix of the i^{th} damper where each diagonal component equals to $m_i^d / 2$. Consequently, the mass data matrix of a frame with *n* linear viscous fluid dampers can be formed as

$$\mathbf{G} = \begin{bmatrix} \mathbf{G}^{ND} & \mathbf{G}^d \end{bmatrix} \tag{4.102}$$

where $\mathbf{G}^{ND}$ is the mass data matrix of the same frame but without the dampers, and

$$\mathbf{G}^d = \frac{1}{2}\begin{bmatrix} \left(\dot{\bar{\boldsymbol{\alpha}}}_1\right)^T \ddot{\bar{\boldsymbol{\alpha}}}_1\Big|_{t_1} & \cdots & \left(\dot{\bar{\boldsymbol{\alpha}}}_n\right)^T \ddot{\bar{\boldsymbol{\alpha}}}_n\Big|_{t_1} \\ & \vdots & \\ \left(\dot{\bar{\boldsymbol{\alpha}}}_1\right)^T \ddot{\bar{\boldsymbol{\alpha}}}_1\Big|_{t_p} & \cdots & \left(\dot{\bar{\boldsymbol{\alpha}}}_n\right)^T \ddot{\bar{\boldsymbol{\alpha}}}_n\Big|_{t_P} \end{bmatrix} \tag{4.103}$$

is the mass data matrix of the *n* linear viscous dampers. Since the masses of the dampers are included in the mass data matrix, the mass unknown vector must also be updated as

$$\boldsymbol{\theta}_m = \left[\boldsymbol{\theta}_m^{ND^T} \quad {}^m\theta_1^d \quad \cdots \quad {}^m\theta_n^d \right]^T \tag{4.104}$$

where ${}^m\theta_i^d = m_i^d$.

Once the mass and the damping data matrices have been updated from equations (4.98) and (4.102), the unknowns, $\boldsymbol{\theta}$, can be found directly by DITER as described in chapter II.

To account for a Kelvin type damper, with stiffness K^d, the stiffness data matrix and the unknown vector must be updated as

$$\begin{aligned} \boldsymbol{\Gamma} &= \left[\boldsymbol{\Gamma}^{ND} \quad \boldsymbol{\gamma}_1^d \quad \cdots \quad \boldsymbol{\gamma}_n^d \quad \bar{\boldsymbol{\Gamma}}^d \right] \\ \boldsymbol{\theta}_k &= \left[\boldsymbol{\theta}_k^{ND^T} \quad {}^k\theta_1^d \quad \cdots \quad {}^k\theta_n^d \quad \bar{\boldsymbol{\theta}}^{d^T} \right]^T \end{aligned} \tag{4.105}$$

where $\boldsymbol{\gamma}_i^d = \left[\dot{r}_{i,0} r_{i,0} \quad \cdots \quad \dot{r}_{i,\mathrm{p}} r_{i,p} \right]^T$. ${}^k\theta_i^d$ represents the unknown value of K_i^d. $\boldsymbol{\theta}_k^{ND}$ and $\boldsymbol{\Gamma}^{ND}$ are, respectively, the unknown vector and stiffness data matrix that are formed for the same system neglecting the external dampers. Considering $\dot{\mathbf{r}}_i = \left[\dot{r}_{i,0} \quad \cdots \quad \dot{r}_{i,\mathrm{p}} \right]^T$, the terms $\bar{\boldsymbol{\Gamma}}^d = \left[\dot{\mathbf{r}}_1 \quad \cdots \quad \dot{\mathbf{r}}_n \right]$ and $\bar{\boldsymbol{\theta}}^d = \left[\bar{\theta}_1^d \quad \cdots \quad \bar{\theta}_n^d \right]^T$ are introduced to eliminate the effects of the initial restoring forces of the dampers that might exist due to the compression or tension of the dampers when the structure is at rest.

The viscoelastic solid dampers are built using elastomer material. A Kelvin model might be used to describe the developed forces at the ends of the damper (Symans et al. 2008) as

$$f(t) = Ku(t) + C\dot{u}(t) \tag{4.106}$$

where K and C are the stiffness and damping factors, respectively. However, K and C are dependent on the displacement magnitude, frequency of motion, and temperature. Thus, the factors vary as the response data are being collected.

Similar to the isolators, the sub-system approach may be used to provide the axial force-displacement data of the non-linear viscous fluid, viscoelastic fluid/solid, and viscoelastic solid dampers. To find the axial forces applied at the k^{th} damper with the end

nodes of *i* and *j*, equation (4.88) must be applied to determine the internal forces, $\mathbf{f}_i^k$, at the end *i* of the damper. Here $\mathbf{Q}_j^{s/E}$ is a vector consisted of the internal forces of the end of the boundary elements that are attached to the end *i* of the damper, and it is defined in equation(4.89). $\bar{\mathbf{R}}_j$, and $\bar{\mathbf{R}}_k$ are the rotation matrices of the j^{th} boundary element attached to the damper and the k^{th} damper, respectively. The rotation matrix is shown in equation (4.73); however, to find the forces in the current configuration, it is recommended to update $\bar{\mathbf{R}}_k$ for the current configuration. To update $\bar{\mathbf{R}}_k$, the α_k of the transfer matrix must be updated at each time instant by updating the initial local coordinates into the current local coordinates using the collected displacement data.

Once the internal force at the end *i* is determined for the current local coordinates, the axial force, $\bar{f}_i^k$, can be obtain from equation (4.91) with

$$\mathbf{s} = \begin{bmatrix} 1 & 0 & 0 \end{bmatrix} \tag{4.107}$$

The relative axial deformation can also be found from

$$u_d^k = u_{1,i}^k - u_{1,j}^k \tag{4.108}$$

where $u_{1,i}^k$, $u_{1,\mathrm{j}}^k$ are, respectively, the axial displacements at the i, j ends that are described in the current local coordinates. Similar to the isolator situation, the restoring axial force of the k^{th} can be obtained as

$$f_i^k = \bar{f}_i^k - \frac{m^k}{2}\ddot{u}_{1,\mathrm{i}}^k \tag{4.109}$$

where m^k is the mass of the damper. $\ddot{u}_{1,j}^k$ and $\bar{f}_i^k$ are, respectively, the axial acceleration and force at the node *i* that are described in the current local coordinates. Once the axial force and displacement of the damper are identified, it is require to compare the axial force-displacement of the damper with the boundaries that are used in the design. If the values exceed the boundaries, a damaged state could be reported for further investigations.

SUMMARY

In CHAPTER IV, DITER formulation is developed for Euler Bernoulli beam with small strain but either small or large rotations. The method is extended to include the inherent damping of the structure in the form of Rayleigh or straining viscous resistance. In addition, the application of DITER in two dimensional frames along with formation of the data matrix, unknown vector, and observation vector were discussed. Also, the method was modified to be applicable to the sub-systems using either I-DITER or DITER itself. Finally, the existence of passive seismic protective devices, including viscous fluid, viscoelastic fluid/solid, and viscoelastic solid dampers along with LRB and LDRB isolators were taken into consideration, and the application of DITER for such frames and devices discussed thoroughly.

CHAPTER V
ASSESSMENT OF DITER VIA NUMERICAL EXAMPLE EXPERIMENTS

INTRODUCTION

In this chapter, several numerical examples are developed to verify DITER on EB beams and frames. The experiments are designed to verify the DITER ability in confronting multiple and multi type damage scenarios, different types of supports, large and small rotations, total and relative displacement measurements, Rayleigh and viscous inherent damping characteristics, viscous dampers, and elastomeric isolators. The verification is also studied for the subsystem applications. The DITER applicability on different boundary conditions is studied as well. The first example consists of a simple pinned-pinned beam where the numerical data are generated through an analytical solution. The purpose of the example is to check the correctness of the theory and its implementation with well collected data. Next, more complex examples are considered including cantilever and multi span beams as well as a frame with external isolators and damper to verify the damage detection ability of DITER.

NUMERICAL EXPERIMENTS

Simple Beam Experiment

Description of the experiment and generating data

The first numerical verification is performed on a one span simple EB beam. The responses of the beam are generated using an analytical solution. Therefore, the data are clean and provided a sound theory and implementation, excellent results of DITER may be expected. The first part, Case 1, of the example studies the mass and stiffness identification of the beam. In the second part, an energy dissipation mechanism is introduced to the beam through a Rayleigh damping model. In this particular test, the Rayleigh damping model could be constructed with a combination of transverse and

viscous resistance to the strain of the material. The beam is assumed to be constructed of linear elastic and homogenous material (see Figure V-1). Properties and the cross section of the beam are shown in Table V-1. The height of the cross section and the width of the flanges are 0.2m and 0.1m, respectively. The flanges' thickness are 0.005m, and the thickness of the web is 0.0043m.

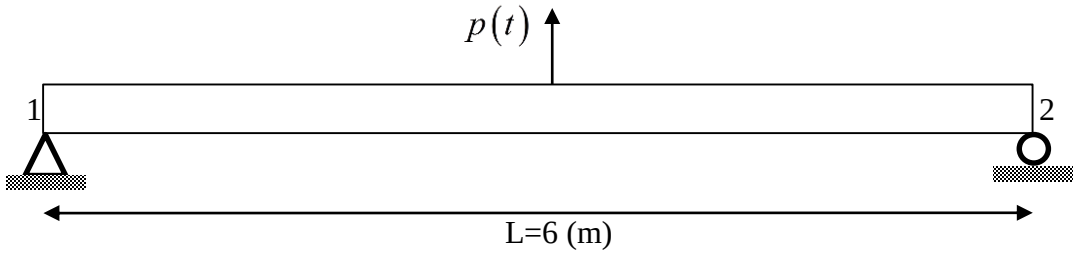

Figure V-1: Schematic view of the one span beam

Table V-1: Properties of the one span beam

Parameter	Unit	Value
Area (A)	m^2	1.817E-3
Young's modulus (E)	GN/m^2	200
2nd Moment of area (I)	m^4	1.197E-5
Length (L)	m	6
Mass density(ρ)	kg/m^3	7849.047

Since the beam length is much larger than its height, the Euler Bernoulli theory might be used to determine the dynamic responses. Neglecting the rotary inertia, the governing equation of the beam is

$$\frac{\partial^2}{\partial x^2}\left(EI\frac{\partial^2 w_0}{\partial x^2} + c_s I\frac{\partial^3 w_0}{\partial t \partial x^2}\right) + c\frac{\partial w_0}{\partial t} + \frac{\partial}{\partial t}\left(m\frac{\partial w_0}{\partial t}\right) = q(x,t) \qquad (4.110)$$

where *EI* is the rigidity of the structure, $m = \rho A$ denotes the mass per unit length, $c(x)$ is the transverse displacement viscous resistance, $c_s(x)$ contains the strain material coefficient of the viscous resistance to the strain of the material, and $q(x,t)$ is the applied excitation. If $c(x)$ and $c_s(x)$ are substituted with

$$\begin{aligned} c &= \beta m(x) \\ c_s &= \alpha E \end{aligned} \tag{4.111}$$

then the beam can have a proportional damping behavior here β and α are the mass and stiffness proportionality constants, respectively.

If the response is approximated in the form of

$$w(x,t) = \sum_{n=1}^{NOM} \phi_n(x) Y_n(t) \tag{4.112}$$

then modal superposition method might be used to find the displacements, velocities and accelerations. If *EI* and m remain constants in the whole length of the beam, then natural frequency, ω_n, and mode shapes, ϕ_n, are (see Appendix B-1)

$$\begin{aligned} \phi_n(x) &= \sin\left(\frac{n\pi x}{2L}\right) \\ \omega_n &= n^2\pi^2\sqrt{\frac{EI}{16mL^4}} \end{aligned} \tag{4.113}$$

Figure V-2 through Figure V-3 demonstrate the first six mode shapes of the beam, and the corresponding frequencies are presented in Table V-2.

Modal displacement $Y_n(t)$, and the beam responses, $u(x,t)$, can be determined using the Duhamel integration (Clough and Penzien 2010) as

$$Y_n(t) = \frac{1}{M_n \omega_{d_n}} \int_0^t P_n(\tau) \sin\omega_{d_n}(t-\tau) e^{-\xi_n \omega_n (t-\tau)} d\tau \tag{4.114}$$

where

$$M_n = \int_0^L \phi_n(x)^2 \, m(x)\, dx$$
$$P_n(t) = \int_0^L \phi_n(x)\, p(x,t)\, dx \qquad (4.115)$$

are the modal mass and modal force respectively, and ξ_n is the damping ratio of the n^{th} mode, which is computed by

$$\xi_n = \frac{\beta}{2\omega_n} + \frac{\alpha\omega_n}{2} \qquad (4.116)$$

where ω_d denotes the free-vibration frequency of the damped system.

$$\omega_{d_n} = \omega_n \sqrt{1-\xi_n^2} \qquad (4.117)$$

Nodal rotations are computed taking spatial derivatives of the mode shapes of equation (4.112), and the velocities and accelerations are calculated taking the corresponding time derivatives of the modal displacement of the same equation. Once the data is acquired, the identification is performed for cases with undamped and damped vibrations. In this experiment, data is collected with respect to the static equilibrium configuration, which remains constant during the experiment, and thus the contribution of the weight force is eliminated in the data matrices.

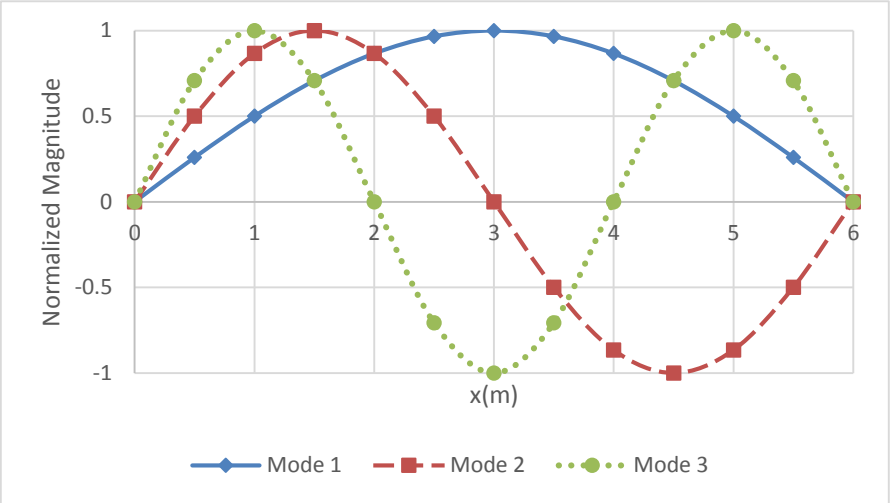

Figure V-2: The first three transverse mode shapes of the beam

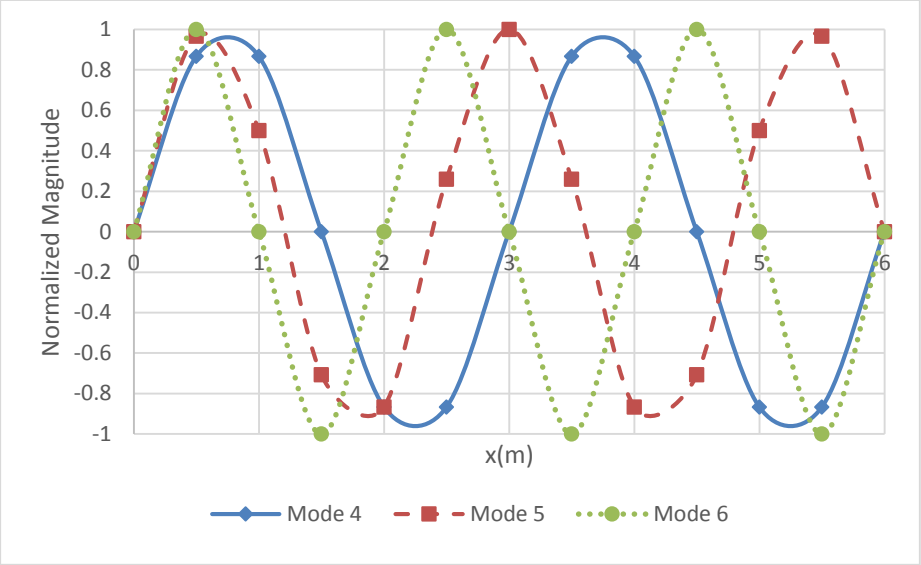

Figure V-3: The sixth transverse mode shapes of the beam

Table V-2: The first six natural frequencies of the beam

No.	ω_n (rad/s)
1	112.278
2	449.111
3	1010.500
4	1796.445
5	2806.946
6	4042.002

Two cases are studied in this experiment. In the first case, an undamped behavior is assumed, i.e. $\xi_n = 0$, and the beam is excited at its midpoint by a sinusoidal force

$$p(t) = 15\sin(20t)\,\text{kN} \qquad (4.118)$$

Figure V-4 shows the displacement and velocity of the midpoint of the beam where the first eleven modes of the structure are used to generate the data.

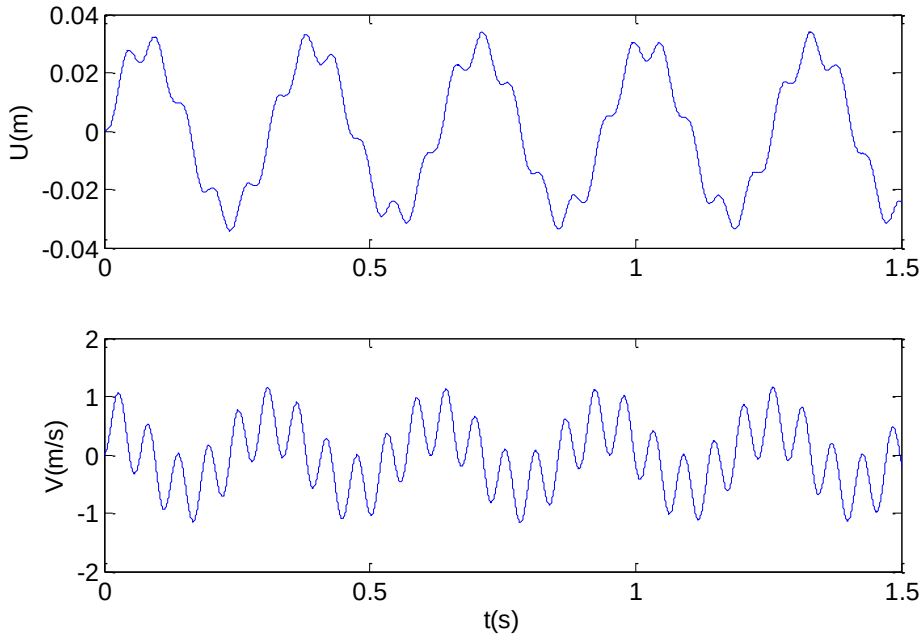

Figure V-4: Displacement and velocity of the midpoint of the beam in case 1

The data of the forced response are collected at 5kHz sampling rate for 1.5 seconds. The data are measurements from the static deformed configuration at thirteen evenly distribured nodes (see Figure V-5). Cubic Hermite shape functions are employed to detrmine the data matrices.

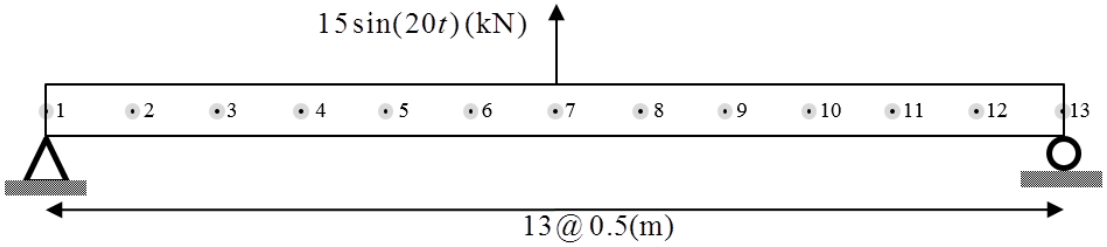

Figure V-5: Nodes layout at which data are collected in case 1

In the second case, Rayleigh damping is added to the beam. Mass and stiffness proportionality constants, β and α, are respectively designed to be $11.06s^{-1}$ and $1.37E-5s$ to have the first and eighth modal damping 5% of the critical damping (see Appendix B-2). To excite the structure, White Noises are applied to the beam at locations $x=\{1.5,3,5\}m$. Figure V-7 demonstrates the applied forces and Table V-3 shows the damping frequencies of the beam. As a comparison to the first case, the displacement and velocity of the middle point are shown in Figure V-8. The data are collected identically to the first case but for one second duration.

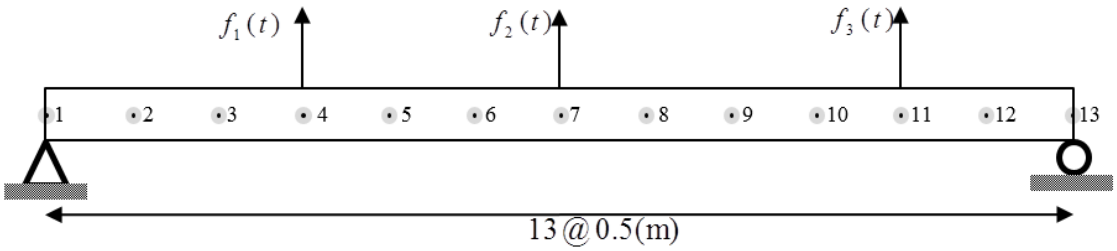

Figure V-6: Sensors layout and excitation forces applied in case 2

Table V-3: The first six damped frequencies of the beam

No.	1	2	3	4	5	6
ω_d (rad/s)	112.137	449.058	1010.423	1796.233	2806.315	4040.295

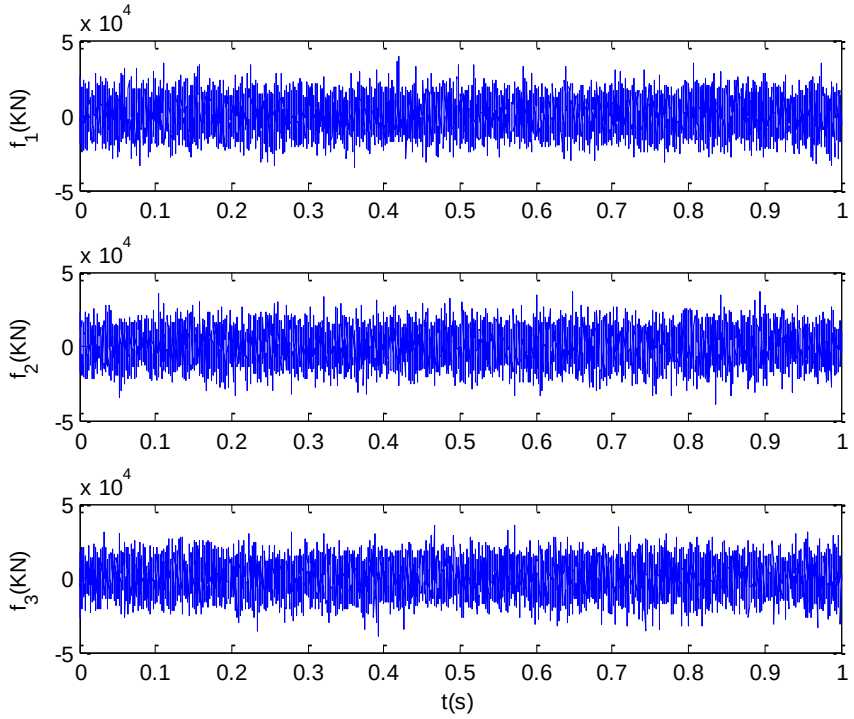

Figure V-7: Loads applied to the beam in case 2

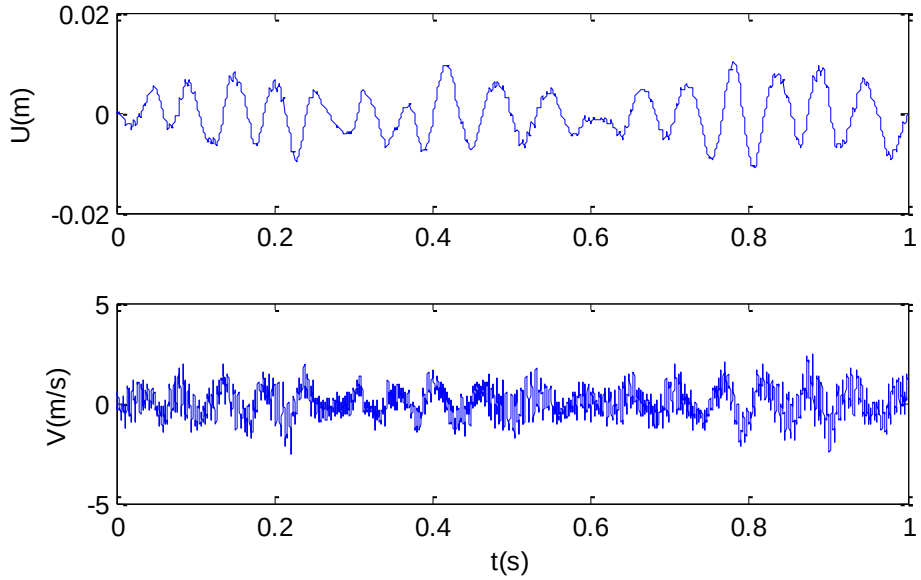

Figure V-8: Displacement and velocity of the middle point of the beam in case 2

Results and discussions

a. Case 1

Figure V-9 and Figure V-10 show the identified element wise mass and flexural rigidity, respectively. The maximum devaition of the identified values from the actual values is less than 1%, which verifies the accuracy of the DITER results.

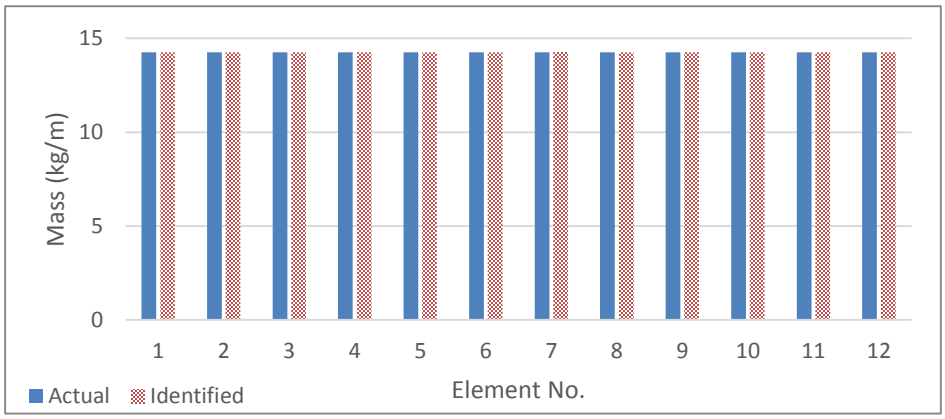

Figure V-9: Mass identification results of the simple beam, Case 1

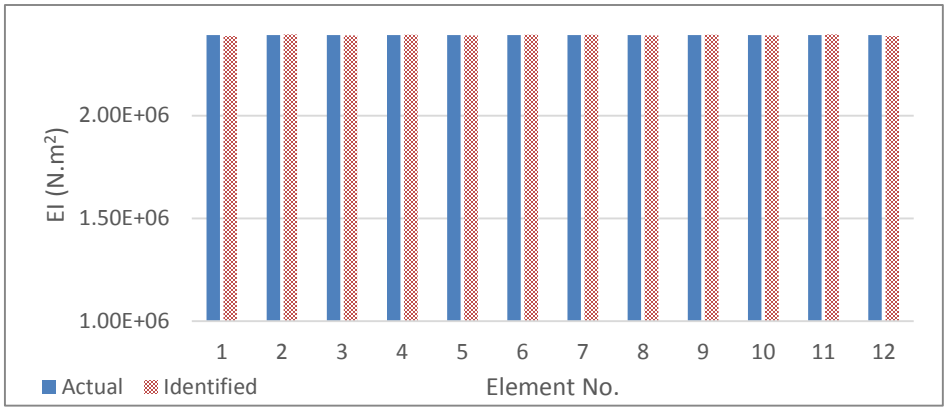

Figure V-10: Identification of the flexural rigidity of the simple beam, Case 1

b. Case 2

In this case, the vector of the unknown parameters, $\boldsymbol{\theta}$, consists of the element wise flexural rigidity and distributed mass along with their corresonding multiplication with the damping factors i.e.

$$\boldsymbol{\theta} = [\boldsymbol{\theta}_k^T, \alpha\boldsymbol{\theta}_k^T, \beta\boldsymbol{\theta}_m^T, \boldsymbol{\theta}_m^T]^T \tag{4.119}$$

Thus, the vector of the independent unknowns should be constructed as:

$$\boldsymbol{\tau} = \left[\boldsymbol{\theta}_k^T, \alpha, \beta, \boldsymbol{\theta}_m^T\right] \tag{4.120}$$

where $\boldsymbol{\theta}_k$ and $\boldsymbol{\theta}_m$ contain the unknown stiffness and mass parameters of each element with the size of 12×1. In addition, the $\boldsymbol{\Lambda}$ matrix of equation (2.25) takes the form of

$$\boldsymbol{\Lambda} = \begin{bmatrix} \mathbf{I} & \mathbf{o} & \mathbf{o} & \mathbf{O} \\ \mathbf{A} & \boldsymbol{\theta}_k & \mathbf{o} & \mathbf{O} \\ \mathbf{O} & \mathbf{o} & \boldsymbol{\theta}_m & \mathbf{B} \\ \mathbf{O} & \mathbf{o} & \mathbf{o} & \mathbf{I} \end{bmatrix} \tag{4.121}$$

where $\mathbf{I}$ and $\mathbf{O}$ are the identity and zero matrices with the size of 12×12, respectively. $\mathbf{o}$ is a zero vector of size 12×1 , and finally

$$\begin{aligned} \mathbf{A} &= \alpha\mathbf{I} \\ \mathbf{B} &= \beta\mathbf{I} \end{aligned} \tag{4.122}$$

The unknowns, however, are determined using the MATLAB constrained optimization toolbox to solve equation (2-24), and the results are shown in Figure V-11 and Figure V-12. The acquired damping proportional constants are provided in Table V-4

Similar to the first case, the outcomes of the element wise rigidity and distributed mass identification are of high accuracy with less than 1% errors. The identified damping Rayleigh constants are also reasonably accurate. This simple experiment verfied the DITER accuracy either in damped or undamped situations for a well defined problem. However, to consider more complex situations in which damages occur in various locations of the domain of the structure, more experiments must be performed and presented.

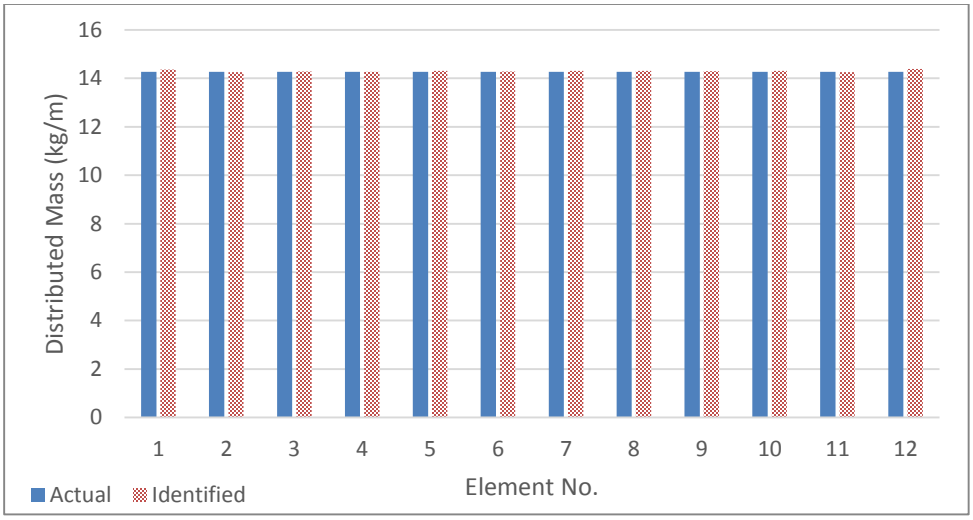

Figure V-11: Mass identification results of the simple beam, Case 2

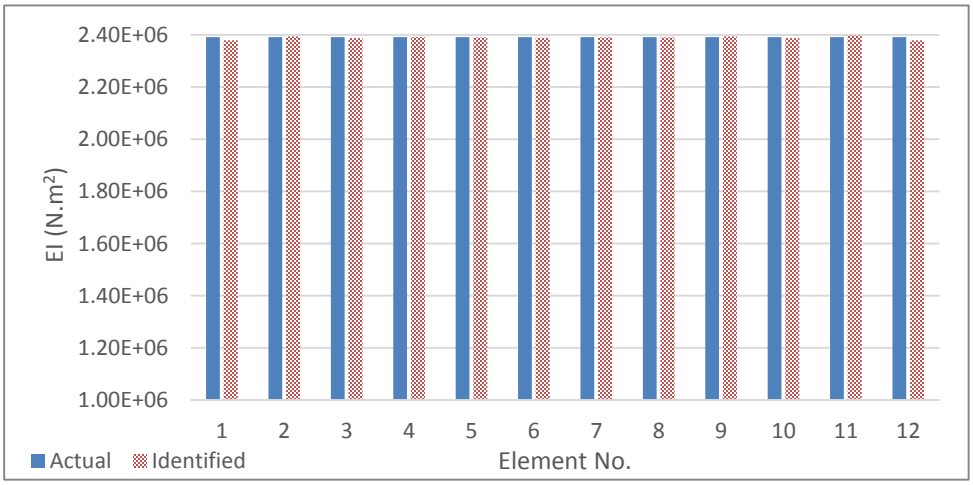

Figure V-12: Identification of the flexural rigidity of the simple beam, Case 2

Table V-4: Identification results of the Rayliegh damping constants, Case 2

α		β	
Actual	Identified	Actual	Identified
1.37E-05	1.41E-05	11.06	10.89

Therefore, in the rest of this chapter several experiments are designed to:

- Investigate the effect of different types of boundary conditions on the damage detection performance of DITER.
- Verify the insensitivity of the method to the variation of loads under which the intact and damaged data are collected.
- Assess the performance of DITER when multiple damages have affected large areas.
- Study the effect of variation of static deflection on DITER with data measured by accelerometers.
- Verify the DITER performance when non-linear seismic protection devices are presented in frames.
- Study the DITER performance in the subsystem applications.

Cantilever Beam Experiment

Description of the experiment

In this experiment, the cantilever beam shown in Figure V-13 is selected to study the damage detection performance of the DITER method when multiple and large area degradations occur in the beam. The experiment is divided into two main parts.

In the first part, the intact properties of the beam are obtained to create a baseline of the system. It is assumed that the beam has no significant damping in its healthy state. Element wise damages are introduced to the beam in the form of stiffness and mass degradations. Some damaged elements are assumed to start dissipating energy through showing viscous resistance to strain of the material. The goal is to locate and size the stiffness and mass reductions as well as to estimate the newly damping behavior of the damaged elements.

The second part of the experiment is dedicated to bold the advantage of applying L-DITER compared to DITER when moderately larger transverse displacements occur. In this part, the goal is to identify the mass and flexural stiffness properties of the beam and locate and size introduced damages. To emphasize on the importance of the large rotation

formulation of DITER, a comparison has been made between the results of DITER with small and large rotation formulation. In the both parts the weight of the beam has been neglected.

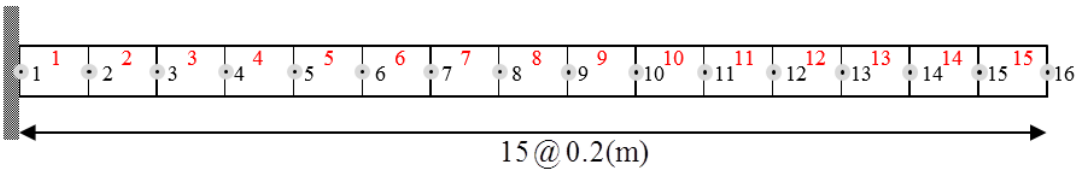

Figure V-13: The cantilever beam of the second experiment

Part I

The selected beam has a length of six meters. It is constructed of a homogenous material with the mass density $\rho = 7849.047\,\text{kg/m}^3$, Poisson's ratio $\nu = 0.3$, and modulus of elasticity $E = 200$ GPa. Similar to the first experiment, an I shape cross section is selected but with a total height of 0.1m. The area and the second moment of area of the beam are $A = 0.139\times10^{-2}\,\text{m}^2$ and $I = 2.52\times10^{-6}\,\text{m}^4$, respectively. The element wise flexural rigidity and per-length mass density of the beam can be found to be $EI = 503.748\,\text{kN.m}^2$ and $m = 10.887\,\text{kg/m}$, respectively. In the healthy state, the beam is assumed to have negligible damping behavior. Table V-5 summarizes the beam properties.

To fulfill the objective of the experiment, an estimation of the intact properties must be provided. To do so, the beam is simulated in Abaqus software using an evenly distributed mesh of 20cm. The dynamic responses are acquired by applying the non-linear direct integration method. The beam is excited with a concentrated White Gaussian Noise type load shown in Figure V-14. The load is intensified by a factor of 50 and applied to the tip of the beam (see Figure V-13). Figure V-15 shows the displacement and velocity of the tip as well.

Table V-5: Properties of the cantilever beam

Parameter	Unit	Value
Area (A)	m^2	1.387E-3
Young's modulus (E)	GN/m^2	200
2^{nd} Moment of area (I)	m^4	2.520E-6
Length (L)	m	6
Mass density(ρ)	kg/m^3	7849.047

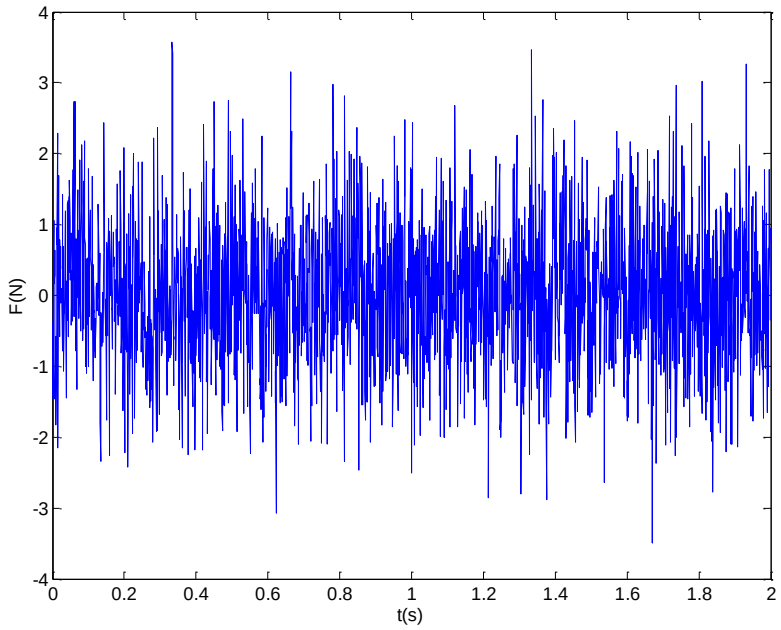

Figure V-14: The normalized WGN load

Data including the force, accelerations, velocities, and displacements are collected at every 0.2m for 2 seconds in 0.001(s) interval. Once the data are collected, the identification process is performed to estimate the structural properties of the intact state. Since no axial load is provided, the obtained axial data are extremely small, and hence not suitable for axial stiffness identitfication.

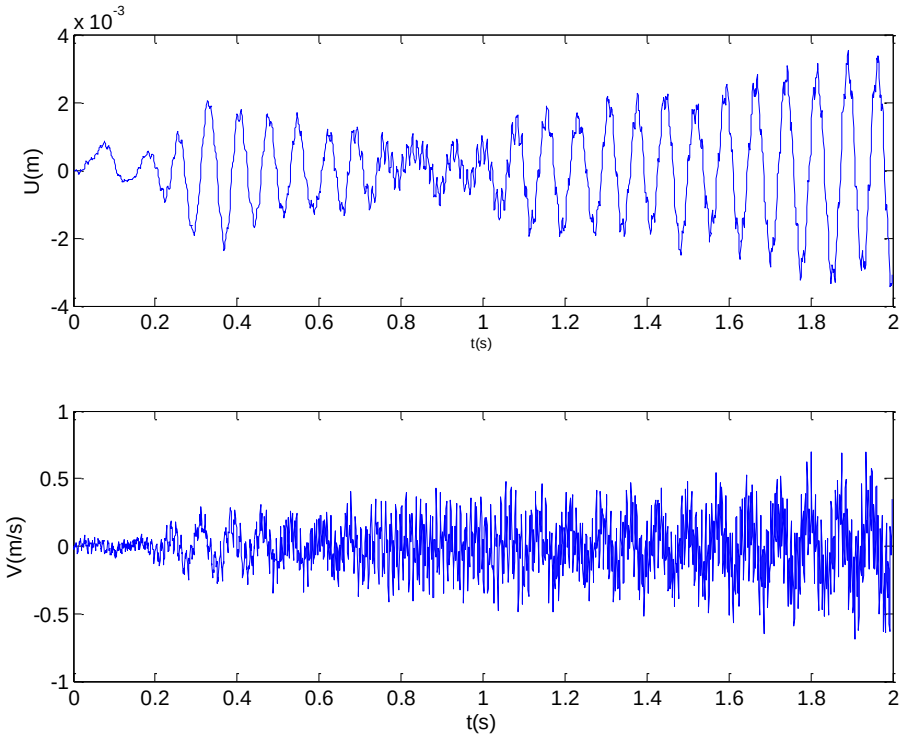

Figure V-15: Velocity and displacement of the tip of the beam in the intact state

To create a damaged state, the modulus of elasticity and the mass of elements 3,4, and 7 are reduced by 15 and 10 percent, respectively. Due to the generated flaws, it is assumed that a viscous resistance to strain of the material with a value of $C_s I = 70.54$ N.s.m^2 has emerged in these damaged elements. In addition, the stiffness of elements number 11 and 12 is degraded by 10 percent. It should be noted that while the damping proportionality is preserved in the element level, the assembled FE formulation of the beam follows a non-proportional damping behavior. Hence, the damping data matrix must follow the form obtained in equations (4.26) or (4.58) and not the proportional one.

To excite the structure, the same load of the intact state is employed in the damaged state. Yet, to consider the effect of the load variation on the DITER performance, the load was relocated to node 13 and magnified by a factor of 60. The responses of the tip of the

cantilever are shown in Figure V-16. Similar to the intact state, the data are collected for 2 seconds in 1 kHz sampling frequency.

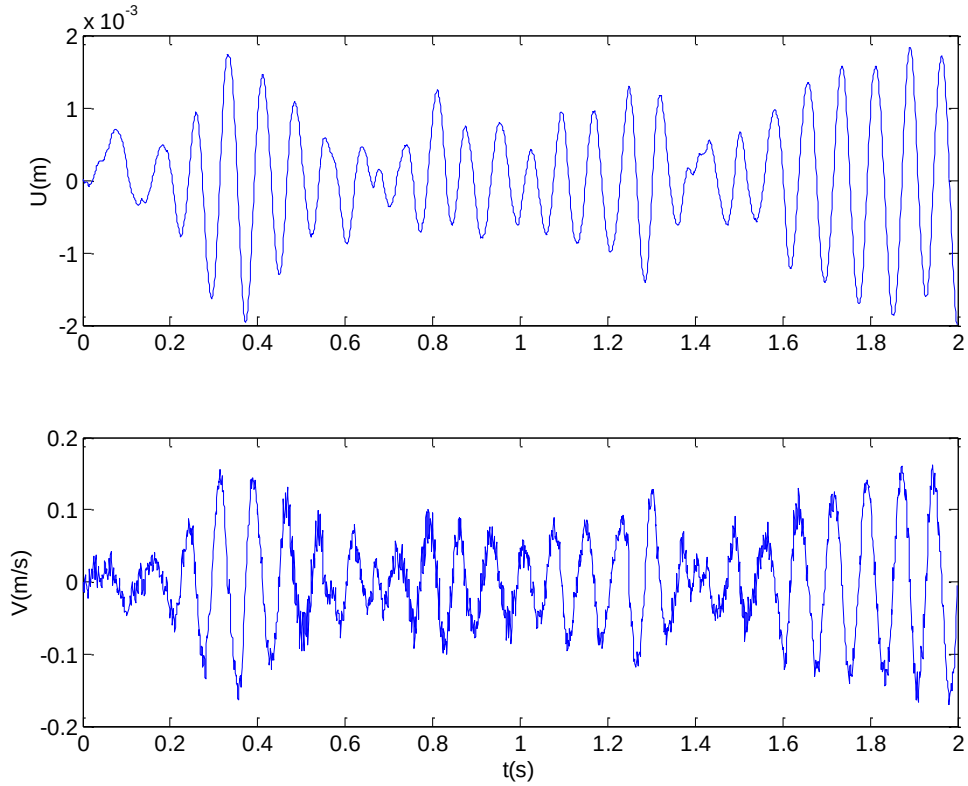

Figure V-16: Velocity and displacement of the tip of the beam in the damaged state

Part II

In the previous part, care had been taken to keep the maximum displacement of the structure in a small range. However, based on the imposed excitations, a beam might experience largerer displacements as well. In such cases, L-DITER may mitigate the model errors and lead to acquire more reasonable outcomes compared to the DITER formulated for small rotations. To investigate the benefit of L-DITER, in this part, the beam is exposed to moderately larger transverse displacements.

The properties of the beam are identical to the previous part and are shown in Table V-5. Similar to the previous part, the first step is to identify the structural properties of the intact structure. The accelerations, velocities, and displacements of the nodes have been fed to the small and large rotations-formulated DITER to obtain the structural baseline. In the next step, damages are introduced to elements 3, 4, and 7 by reducing the mass values and flexural stiffnesses by 15% and 10% respectively. 10% flexural stiffness damage is also assumed of elements 11 and 12.

To acquire the dynamic responses, the beam is modeled in SAP2000 with a uniform element length of 20cm. Data are collected at each node with a sampling rate of 1 kHz for two seconds. In the intact state, the The load shown in Figure V-14 is applied at the tip of the beam in the ‘x’ direcction with magnification factors of 100. The same load is also applied at node 14 in the z direction and magnified by a factor of -350. For the damaged state, node 16 is excited in the ‘z’ and ‘x’ diretcions with the same load, which is magnified by -400 and -50 , respectively. It should be noted that the in SAP2000 small strain assumption is applied even when geometric non-linear is considered. The transverse responses at the tip of the beam are indicated in Figure 23.

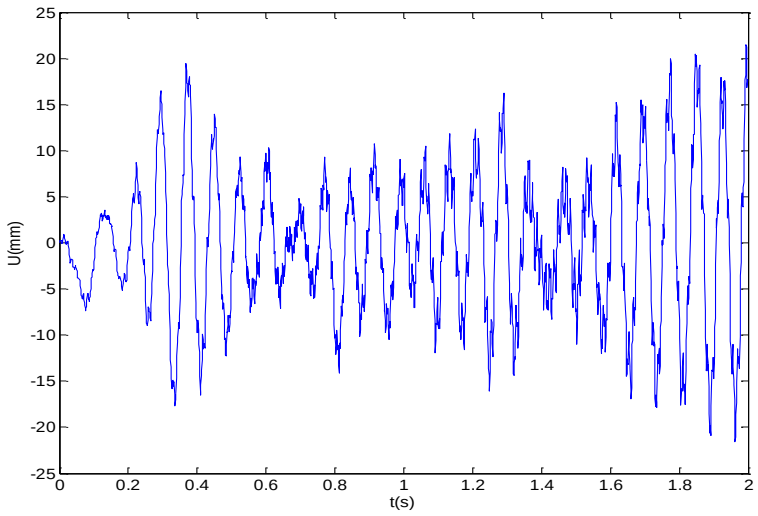

Figure V-17: Transverse displacements at the tip of the beam of the damaged state

Results and discussion

Part I

The identified structural parameters of the intact state are shown in Figure V-18 and Figure V-19. The maximum discrepancy between the identified and actual properties are less than 1%.

Figure V-20 and Figure V-21 show the identified damages. The damages are successfully located and sized with less than 1% error. In addition, the elements with the viscous damping are located accurately. The identified magnitudes of the $C_s I$ coefficients are of high accuracy, with errors less than 1%, as shown in Figure V-22.

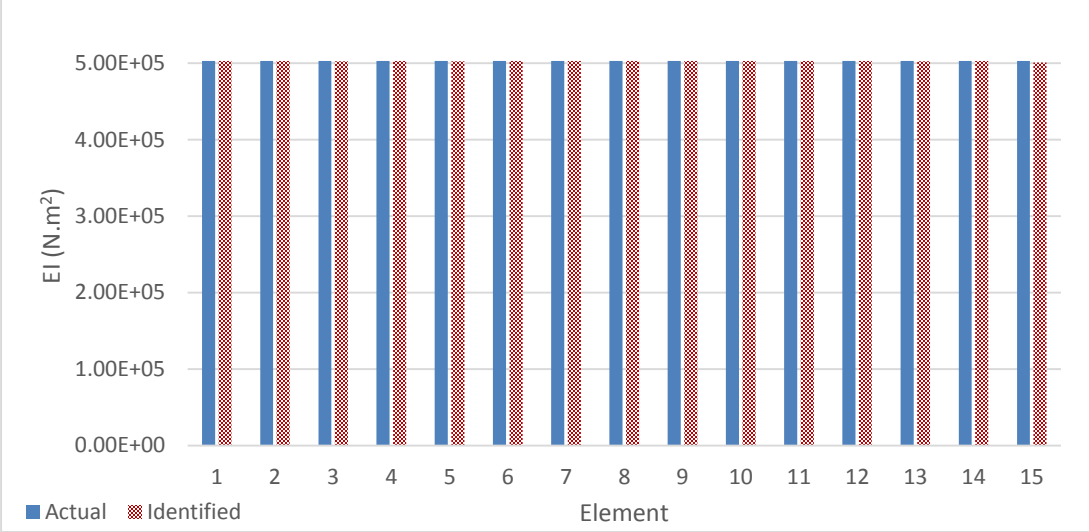

Figure V-18: Identified EI of the intact state, Part 1

Part II

The response data collected in the intact state is fed to the DITER formulated based on small, S-DITER, and large, L-DITER, rotations. Figure V-23 and Figure V-24 shows the identified *EI* and mass values of the intact state.

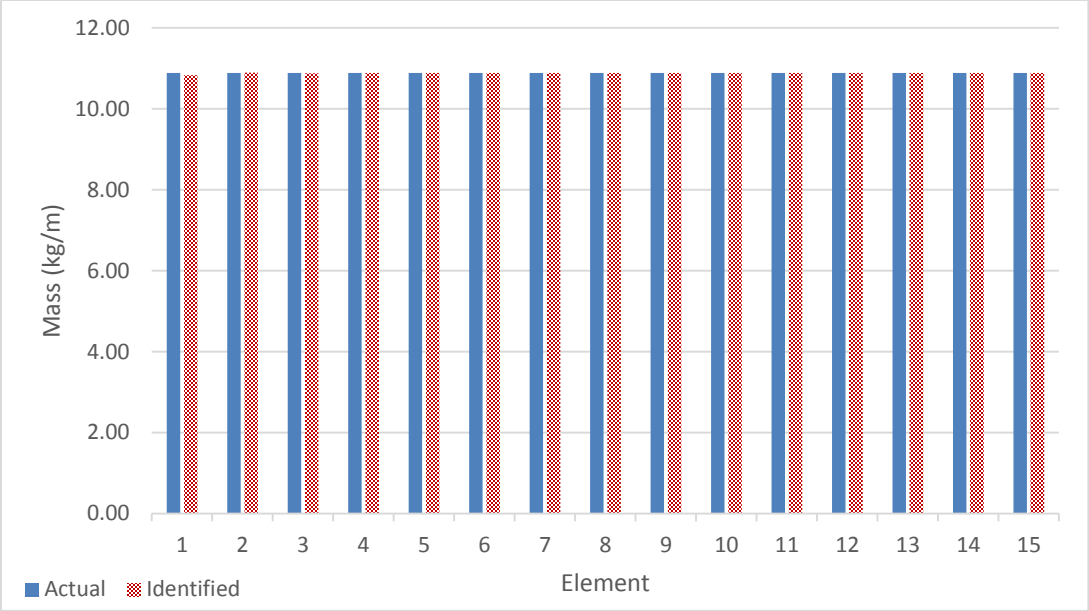

Figure V-19: Mass identification of the intact state, Part 1

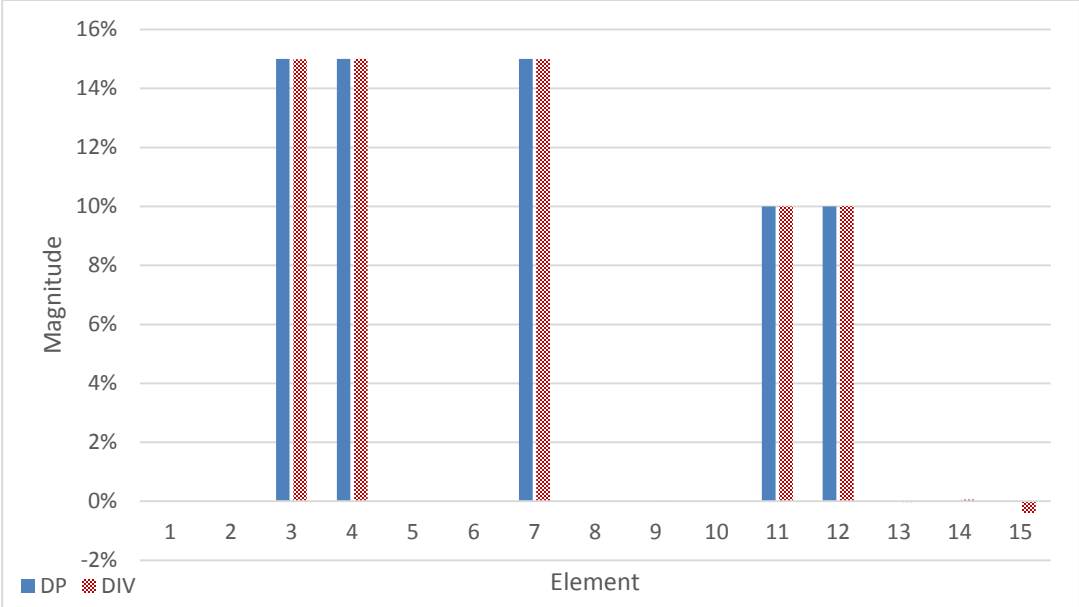

Figure V-20: EI damage detection, Part 1

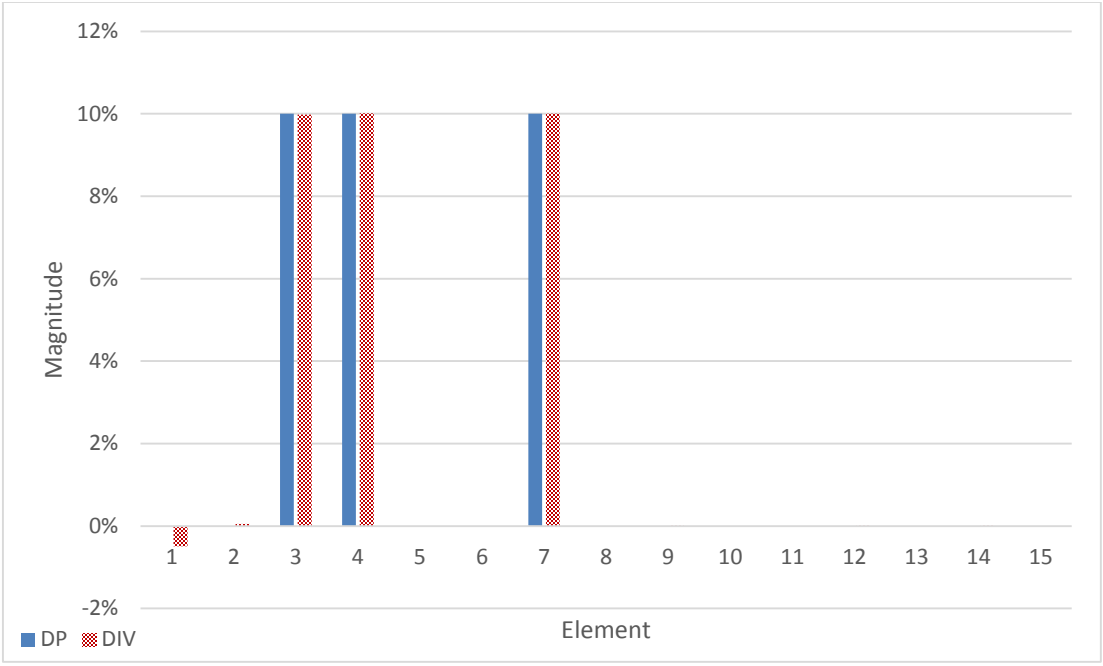

Figure V-21: Mass damage detection, Part 1

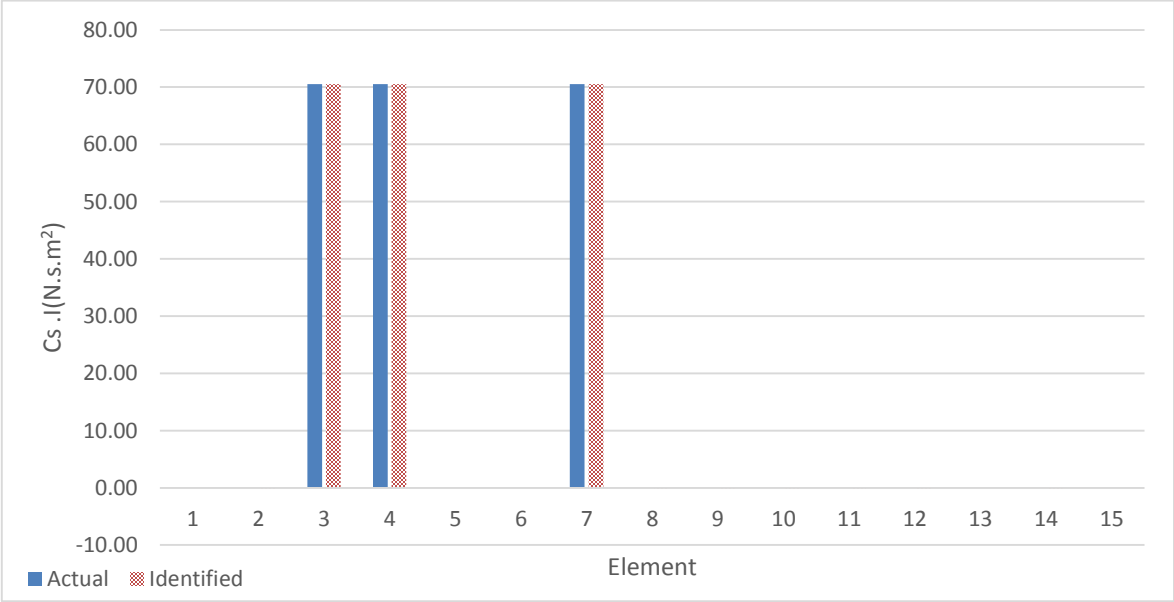

Figure V-22: Identified viscous damping coefficients, Part 1

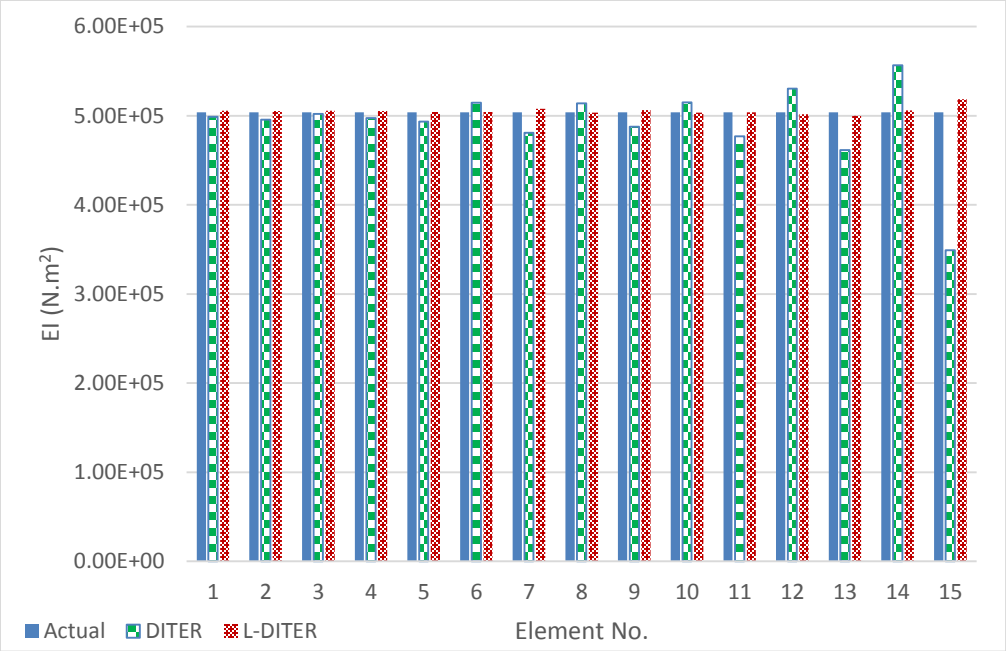

Figure V-23: Identified EI of the intact state, Part 2

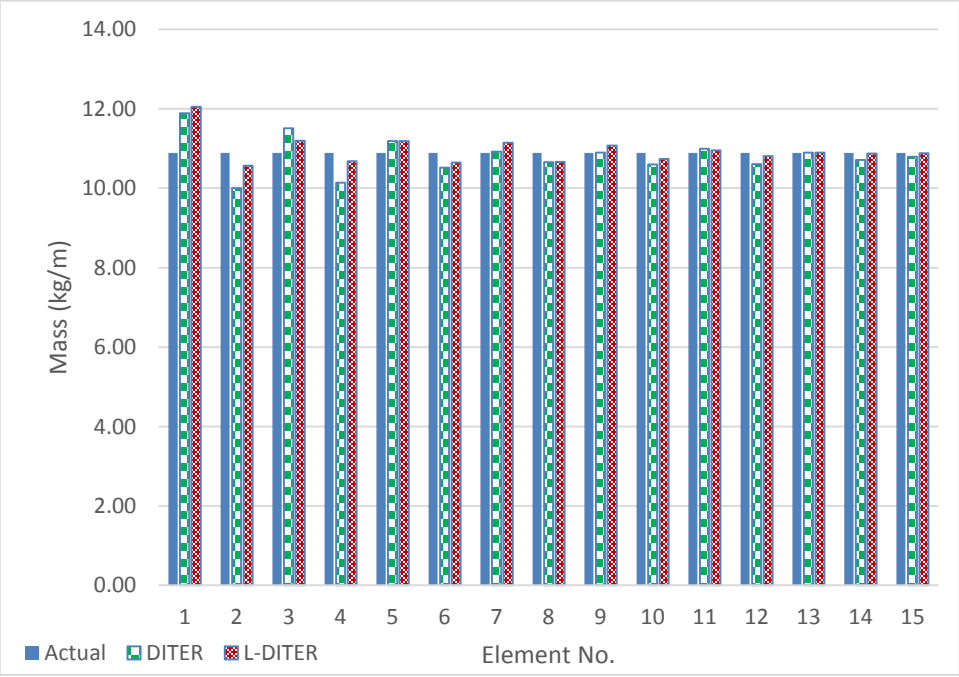

Figure V-24: Mass identification of the intact state, Part 2

As suggested by Figure V-23, the flexural rigidities identified by the DITER formulated for small rotations experienced large deviations from the actual values particularly in regions with larger deformations, i.e. near the tip of the beam. However, the L-DITER results are of acceptable accuracy. Discrepancies between the actual and identified values of the *EI*s can reach up to 40% for the S-DITER. These values, however, drop to 6% for the L-DITER results, which shows a significant improvement. The existence of the latter discrepancies are expected because the geometric non-linearity is not completely considered in the L-DITER formulation. Since no modifications is applied in the mass data matrix of the L-DITER compared to the S-DITER, their performance in the mass identification are close, yet the outcomes of the L-DITER are more sophisticated.

Damage detection results are indicated in Figure V-25 and Figure V-26 . Similar to the structural properties identification of the intact state, the L-DITER outperformed the S-DITER in locating and sizing damages. Large fluctuations and low accuracy in sizing damages are observable in the S-DITER results. Large false positive damage detection has been reported with the usage of S-DIETR for the flexural rigidity. The L-DITER, on the other hand, detected the damages and sized their magnitudes with higher accuracy. Note that L-DITER formulation does not incorporate all the required steps for a large deformation theory and it is benefited from a simpler formulation. Thus, discrepancies between DP and DIV of the L-DITER have been expected.

Summary

In the second experiment DITER successfully located and sized large area and multiple damages when the mass, stiffness and damping properties of the structure were unknown. In addition, the ability of L-DITER for moderately large displacements was successfully verified.

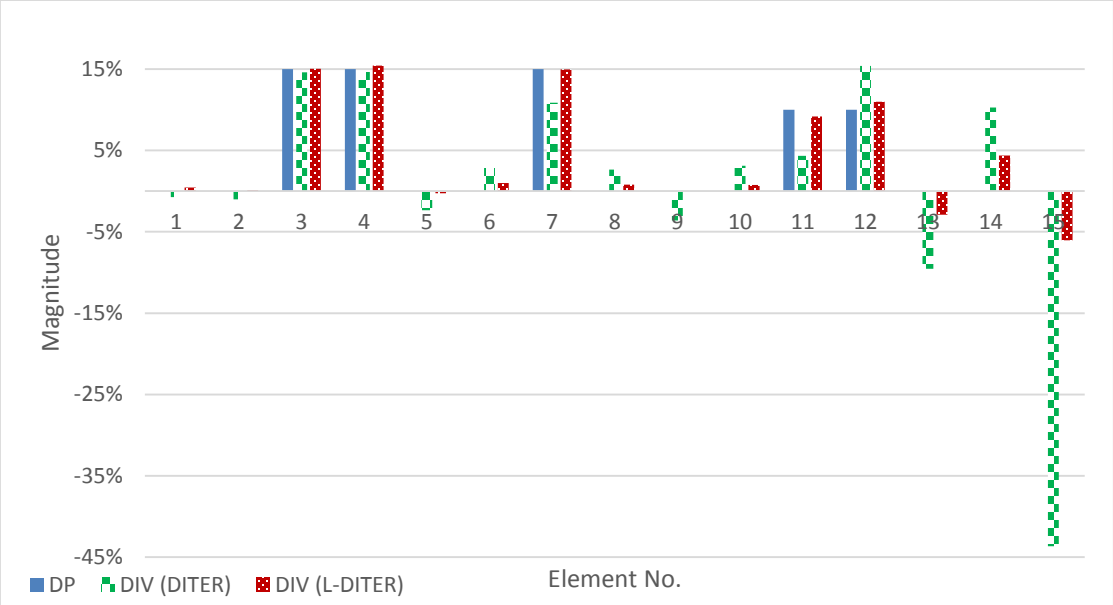

Figure V-25: EI damage detection, Part 2

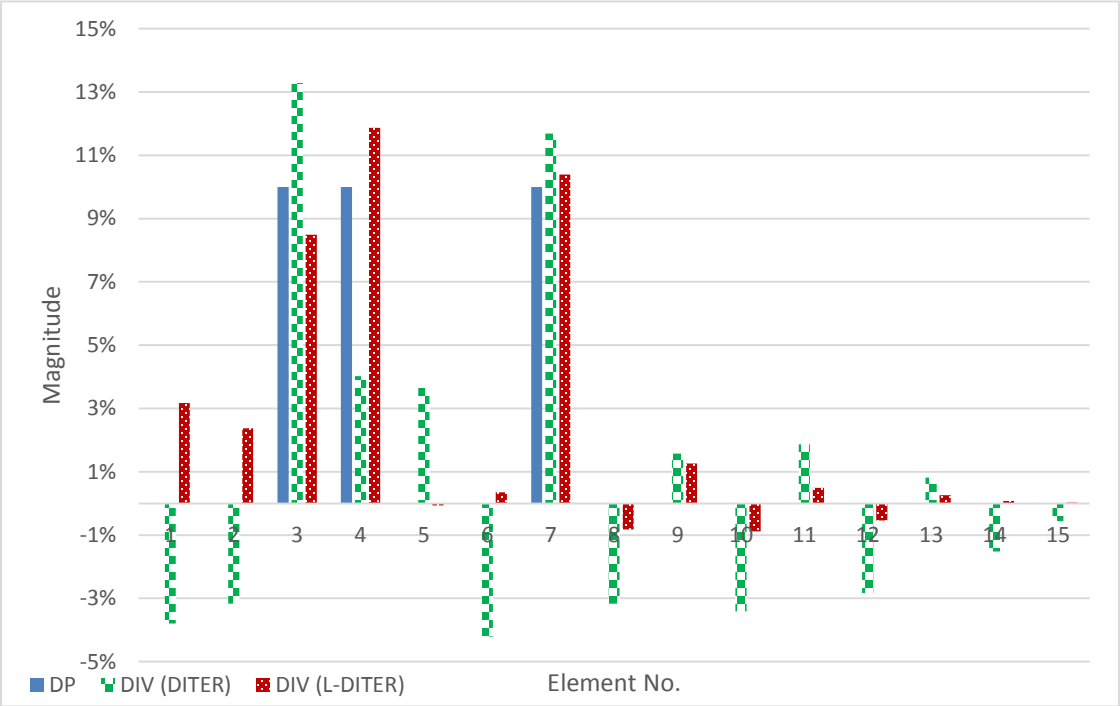

Figure V-26: Mass damage detection, Part 2

Two Span Beam Experiment

Description of the experiment

This experiment is a comprehensive example that investigates the DITER performance on a multi-span beam. This study is important as these beams are common in structures such as bridges and buildings. The experiment is designed to address following aspects of the proposed method:

- System identification
- Locating and sizing damages considering
    - Simultaneous damages in mass, stiffness, and damping properties
    - Large area damage
    - Multiple damage case
- Rayleigh damping
- Application to a sub-system
- Application of the static correction terms

The experiment is divided into six parts. Part 1 is dedicated to identification of the intact state structural properties. In part 2, the structure is affected by multiple damages where mass and stiffness values of some elements are reduced to simulate a structural deterioration. The dynamic response data of this stage are collected and used in DITER to locate and size the damages. The third part of the experiment intends to investigate the sub-system application of DITER where only a specific part of the beam is of interest. In part 4, it is tried to identify a Rayleigh type damping of the beam. The damping is assumed to be the consequence of the damages occurred to the elements. The fifth part studies the difficulties of dealing with data collected form accelerometers when the beam is damaged. The focus is to overcome the errors associated with the variation in the static equilibrium of the structure as it moves from a healthy to a damaged state.

The beam is consisted of two 6m-long spans shown in Figure V-27. The same material and section properties of the cantilever beam experiment is selected for this numerical verification as well. The values are indicated in Table V-5. The element wise

flexural rigidity and per-length mass density of the beam can be computed to be $EI = 503.748\text{kN.m}^2$ and $m = 10.887\text{kg/m}$, respectively.

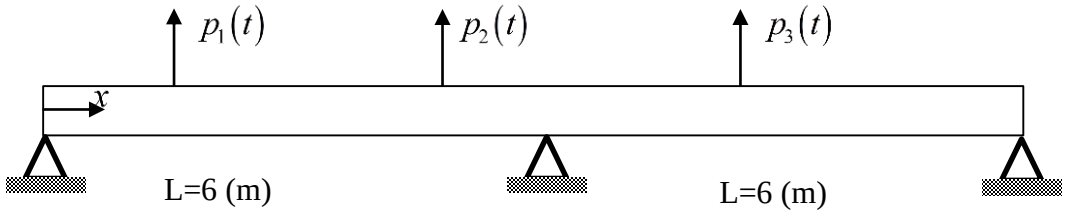

Figure V-27: Two-span beam

To generate required dynamic responses, the beam is modeled in Abaqus software employing WGN type loads. A very fine mesh of 1cm length is used to guarantee the numerical convergence. However, DITER elements, at which data are collected, are taken to be of 20cm length. Thus, while 1201 nodes exist in the FE model, the data are generated and collected only at 60 nodes. The data are collected with respect to the static equilibrium configuration.

In the intact case, i.e. part 1, the beam is excited at locations $x = 1.6, x = 5, x = 8.2$ m by applying concentrated White Gaussian Noise type loads with intensities of -250 N, -150 N, and 350 N, respectively. The loads of intact state are shown in Figure V-29. The maximum displacement response of the beam occurs at $x = 3m$ as demonstrated in Figure V-28.

The collected data are used to prepare the data matrices along with the observation vector to identify the structural properties. These properties form the baseline compared to which the damages will be determined.

The same locations of the intact state are selected to collect data for the other parts. Yet, the excitations are moved from the intact state positions to $x = .8, x = 5$, and $x = 9.2$ m locations, respectively.

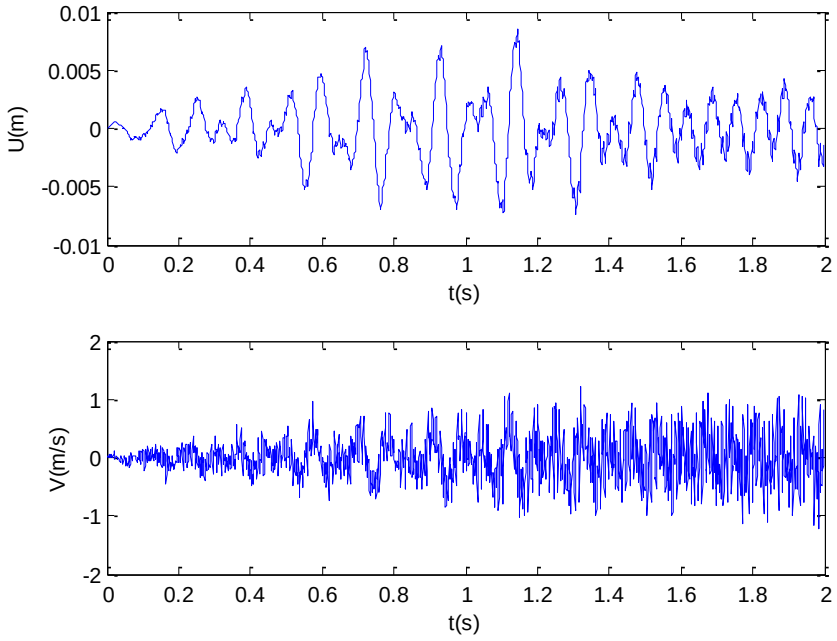

Figure V-28: Displacement and velocity responses at x=3m, Part 1

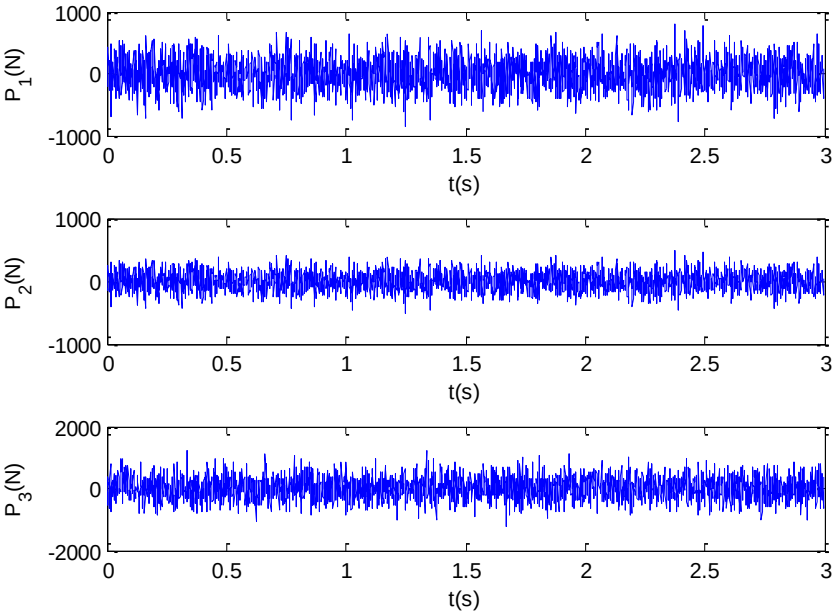

Figure V-29: Applied load to the beam of intact state, P_1) Load at x=1.6 m, P_2) Load at x=5m, P_3) Load at x=8.2m, Part 1

Maximum displacement resposne of an undamped damaged state is shown in Figure V-30.

To simulate damages in the numerical model, stiffness and mass properties of some elements are reduced. Damages are designed to be spreaded in wide and small areas. Table V-6 shows the location, type, and severity of the damages where the numbers reffer to the DITER elements. The numbering is started from the left side of the beam.

Table V-6: Location, severity, and type of damages of the two-span beam

Element No.	15	16	40	42	45	46	49	40	42	45	46	49
Damage Type	EI	EI	EI	EI	EI	EI	EI	m	m	m	m	m
DP%	15	15	10	10	10	10	10	10	10	10	10	10

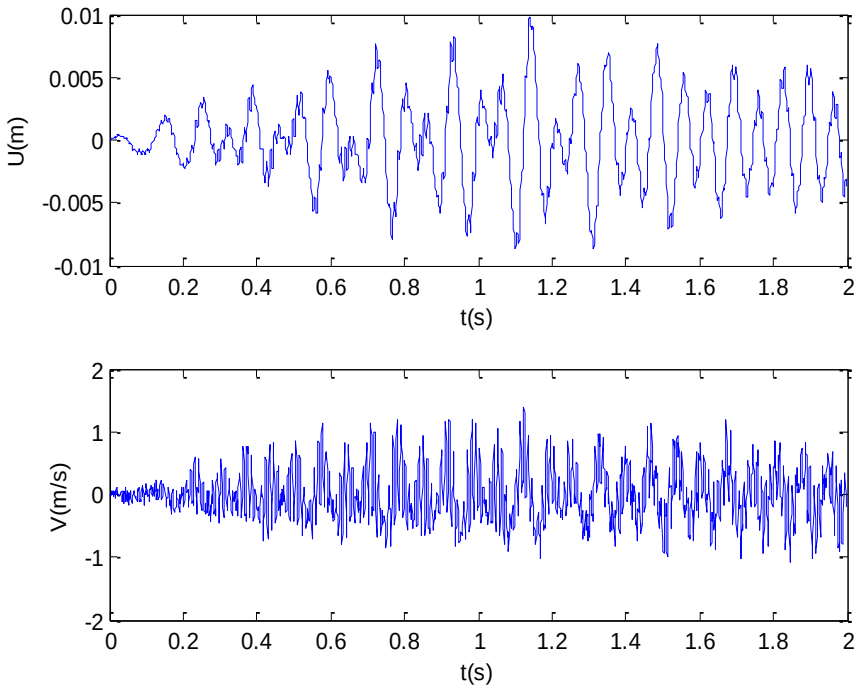

Figure V-30: Maximum displacement response of the beam located at x=3m, Part 2

Results and discussion

Part 1

No dissipiation mechanism is considered in the FE simulation of the intact state. Yet, in the identification process, it is tried to determine mass and stiffness values as well as the material viscous damping coefficients. The data have been collected for a duration of 2 seconds with sampling frequency of 1kHz at each DITER node, i.e. every 20cm. Figure V-31 through Figure V-48 demonstrate the identification results. Less than one percent error is observed in the identifications. In addition, the zero damping values are successfully determined for the beam.

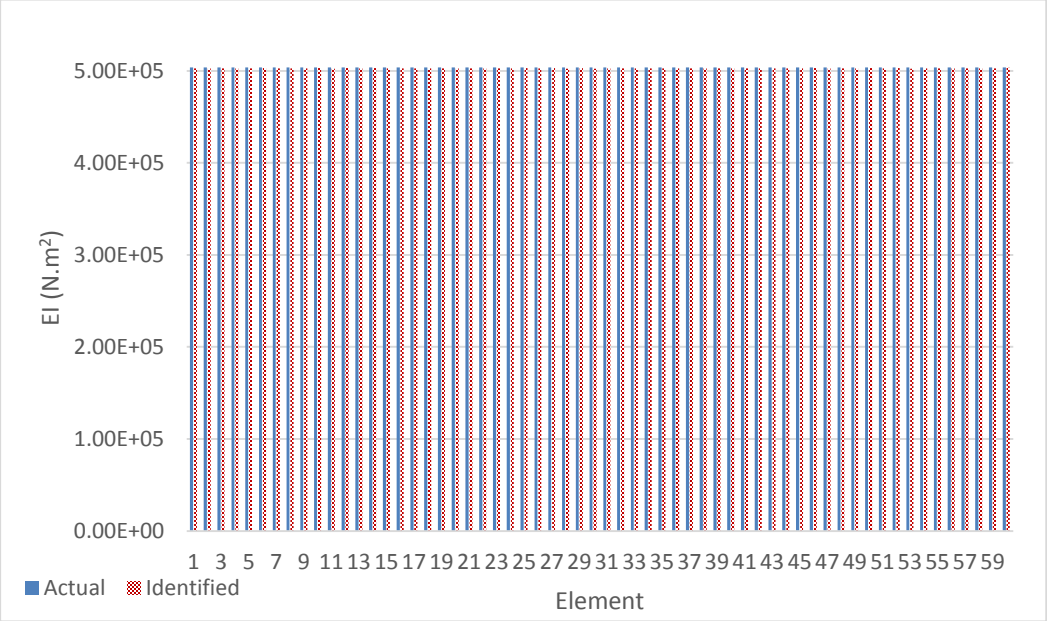

Figure V-31: Identified stiffness of the intact state

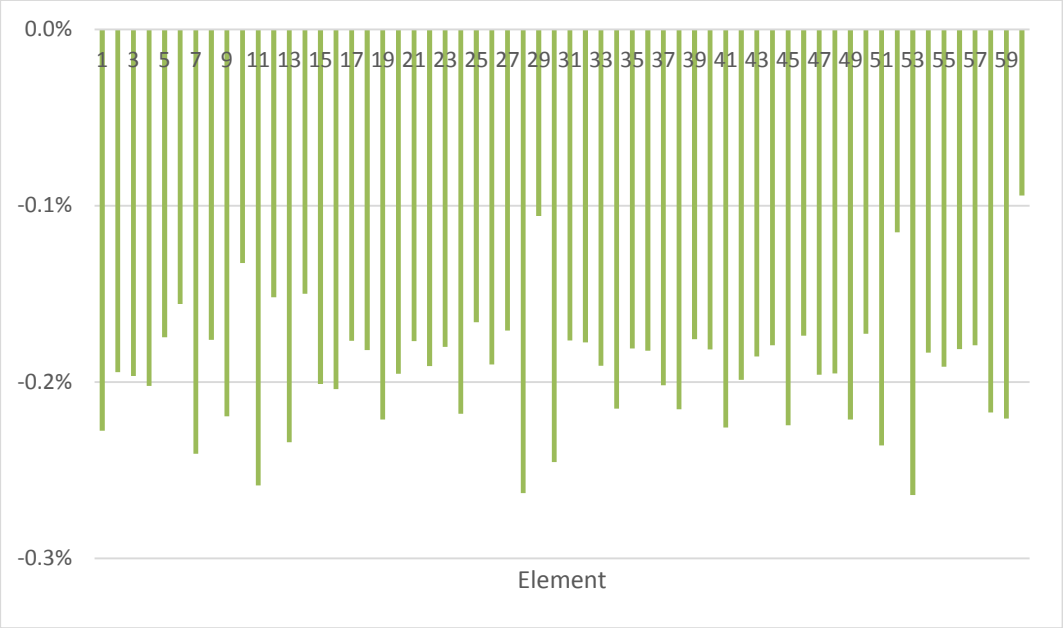

Figure V-32: Errors in the identified stiffness of the intact state

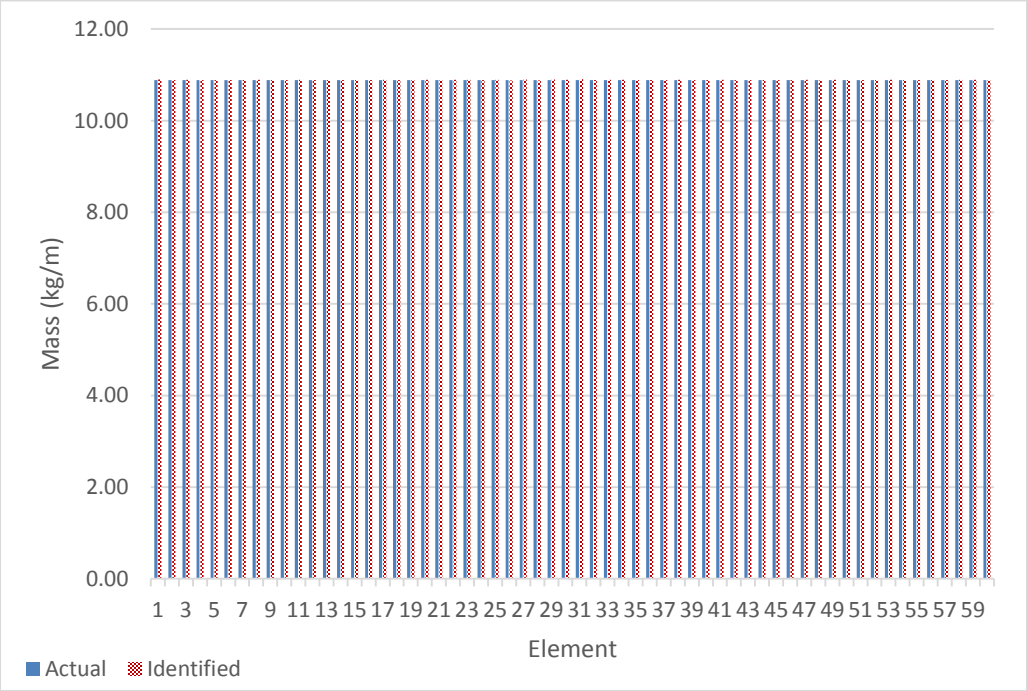

Figure V-33: Identified mass of the intact state

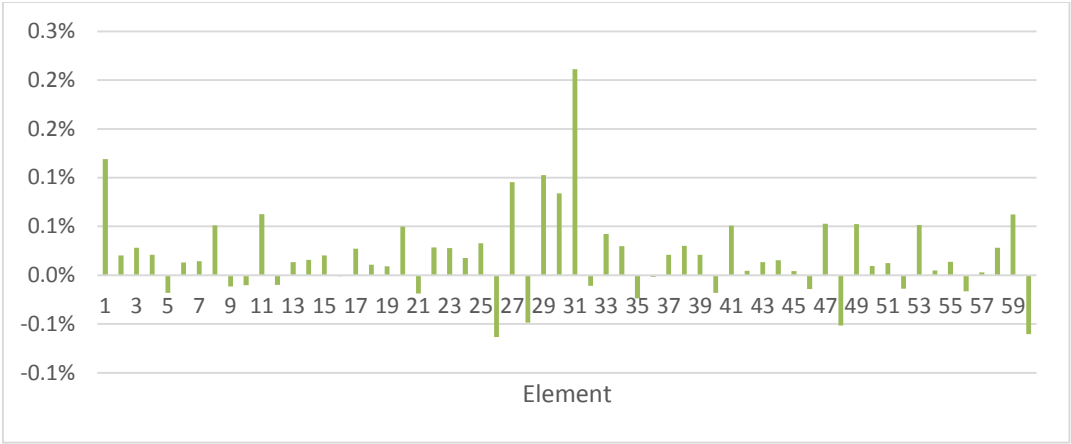

Figure V-34: Errors in the identified mass of the intact state

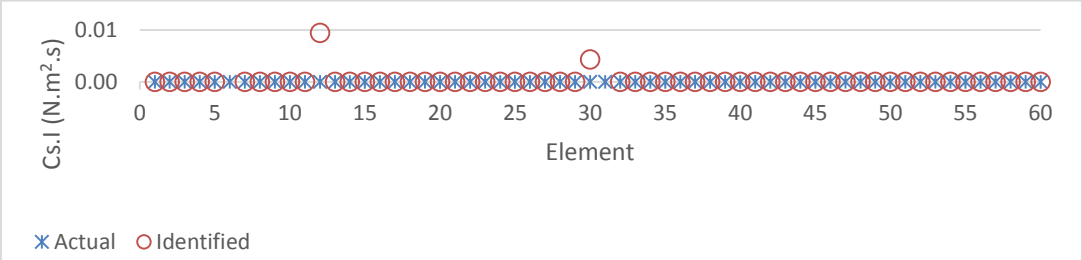

Figure V-35: Identified viscous damping coefficients of the intact state

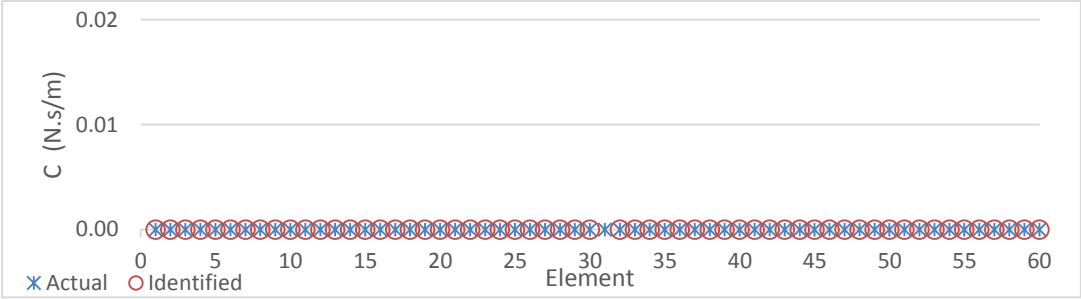

Figure V-36: Identified transverse displacement viscous damping coefficients of the intact state

Part 2

In the damaged state, similar sampling frequency and duration of part 1 are employed. The properties are updated based on the collected data. Finally, comparing the damaged and healthy properties, the damage index vector is determined for the stiffness and mass properties. Results are shown in Figure V-37 through Figure V-40. The damage locations and severities are determined accurately. Slight deviations can be observed in the DP and DIV of the mass properties which are less than one percent. Material damping values are also correctly obtained to be zero.

The experiment was repeated for total displacement data as well. The outcome was almost identical to the above results with an ignorable deviation of less than 0.3%. For an instance, the stiffness DIV are shown in Figure V-41.

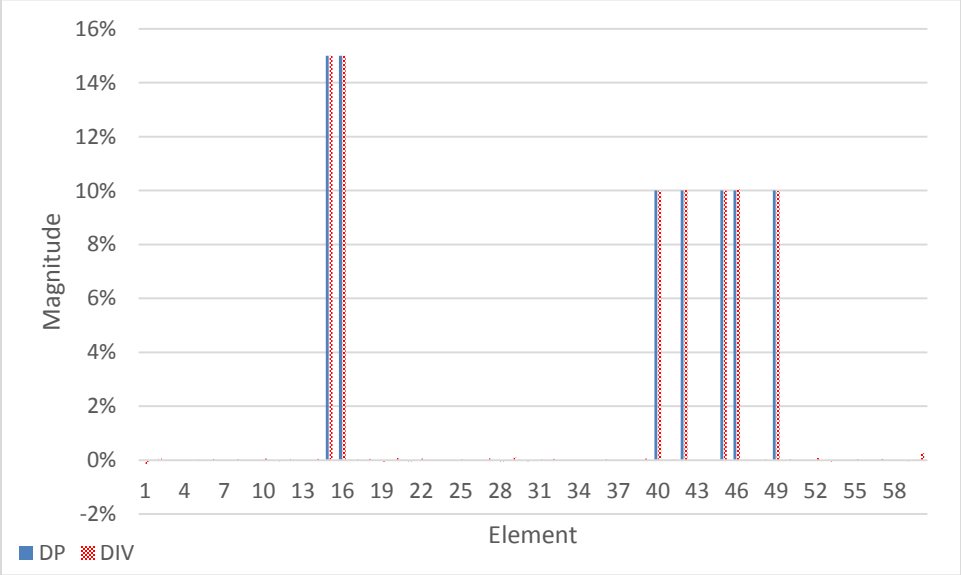

Figure V-37: EI damage detection

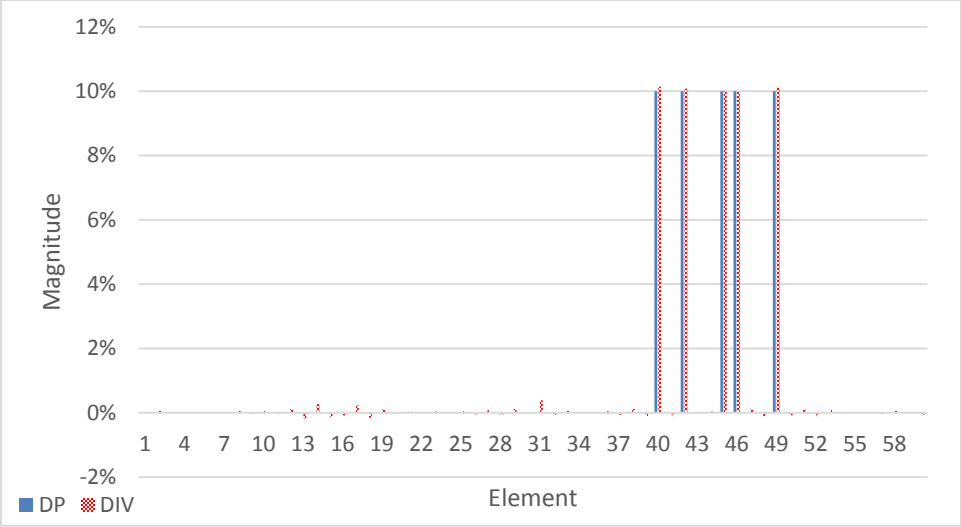

Figure V-38: Mass damage detection

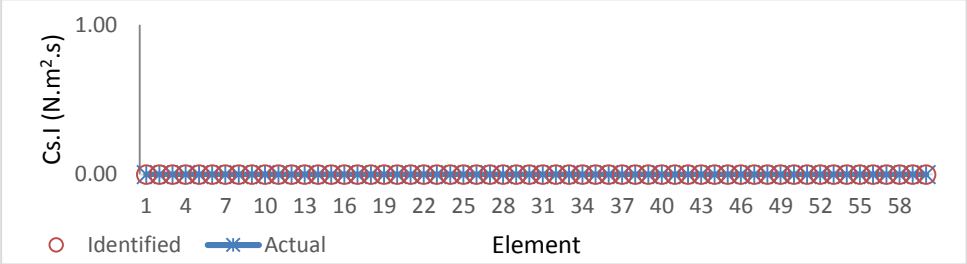

Figure V-39: Identified viscous damping coefficients of the damaged state

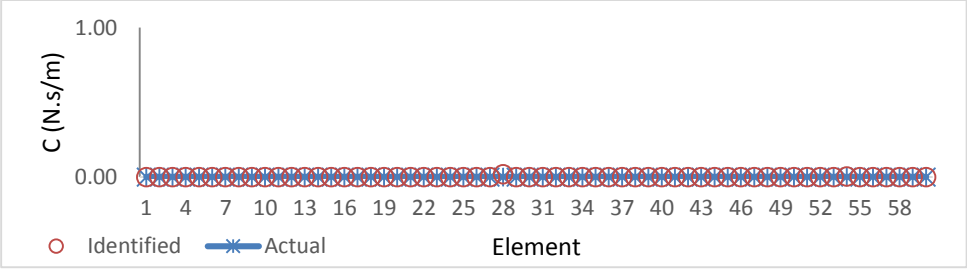

Figure V-40: Identified transverse displacement viscous damping coefficients of the damaged state

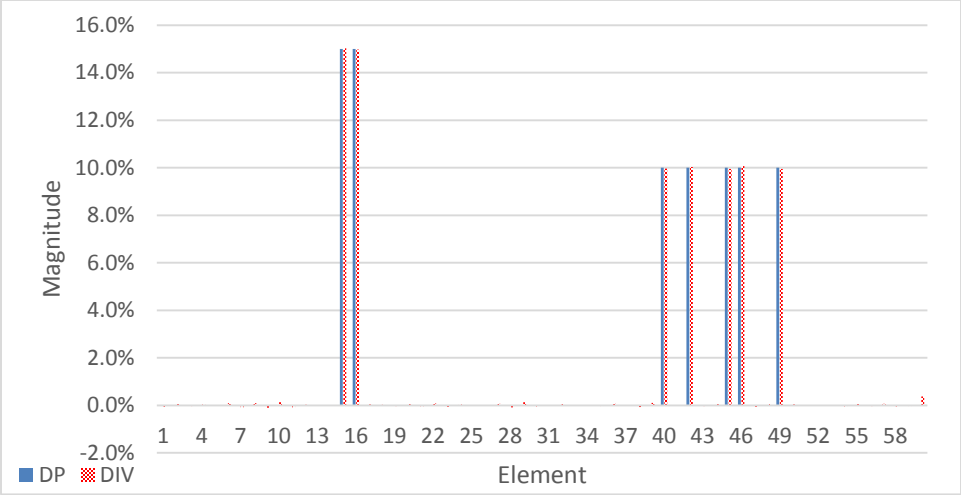

Figure V-41: EI damage identification using total displacement data

Part 3

The sub-system experiment includes the parts located between $x = 7.6m$ to $x = 10.2m$ that corresponds to DITER elements umber 39 to 51. (see Figure V-42).

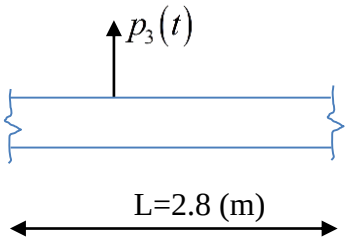

Figure V-42: Sub-system of the two-span beam

In this part data are collected from nodes located in the sub-system only and it is assumed that no information is available from the rest of the system . The load conditions are identical to the previous parts. Once again, the intact properties are

required to be identified. Figure V-43 through Figure V-48 demonstrate the baseline values.

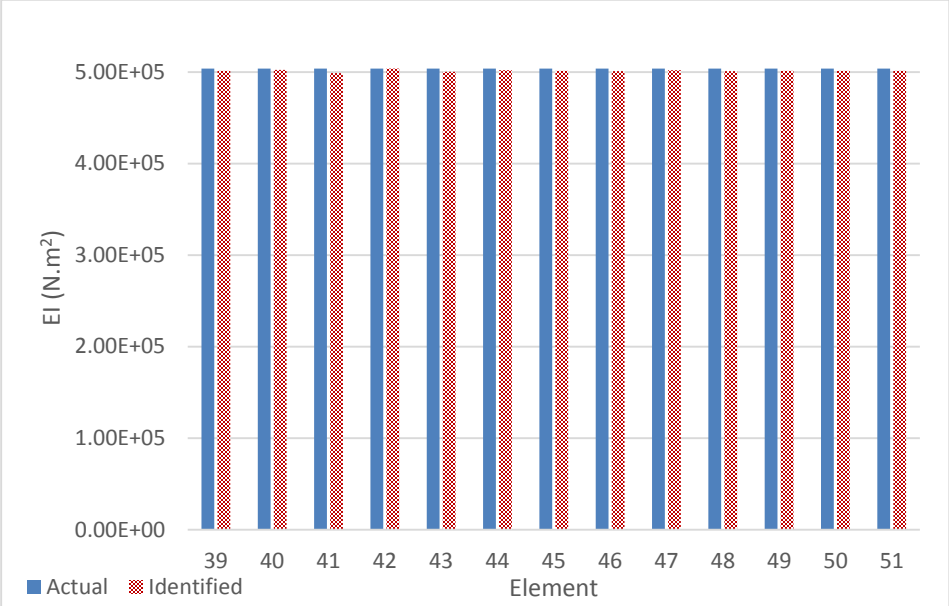

Figure V-43: Identified stiffness of the sub-system, intact state

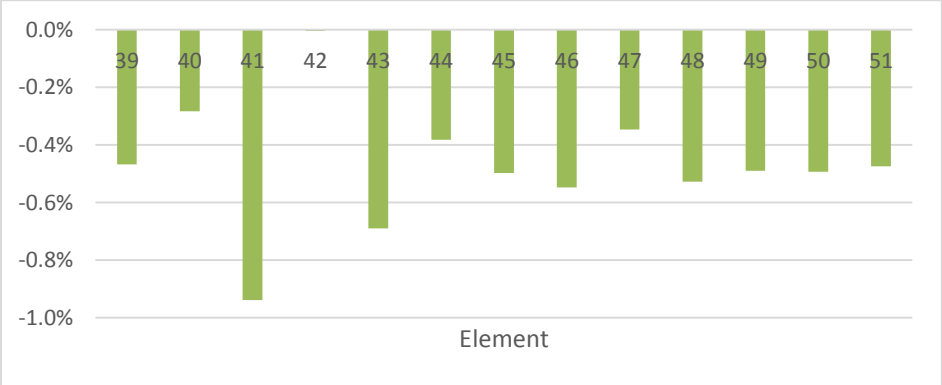

Figure V-44: Errors in the identified stiffness of the sub-system, intact state

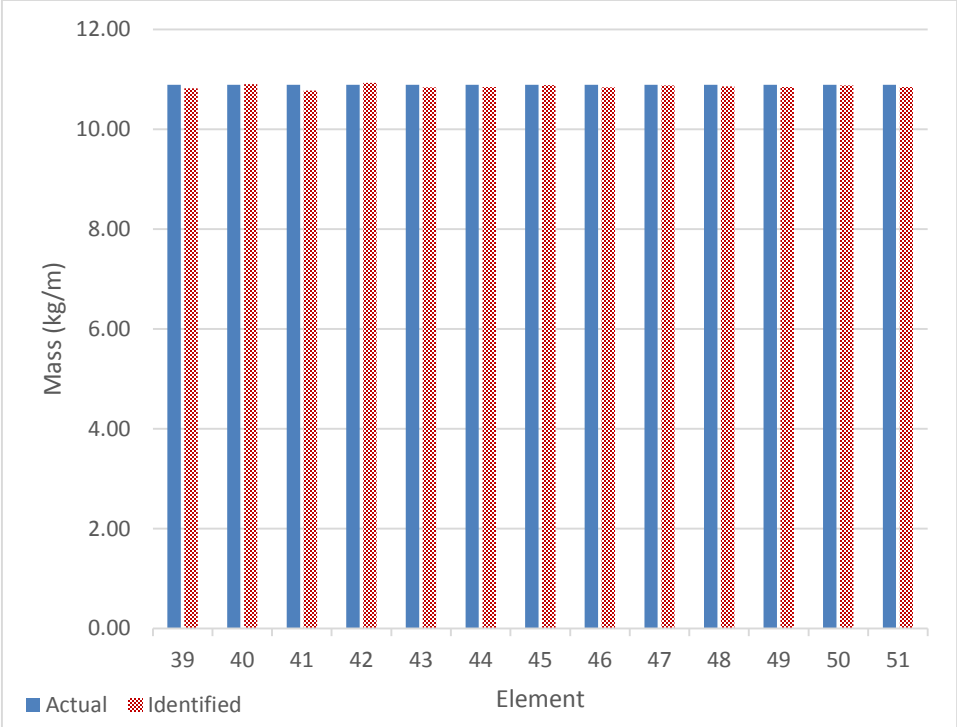

Figure V-45: Identified mass of the sub-system, intact state

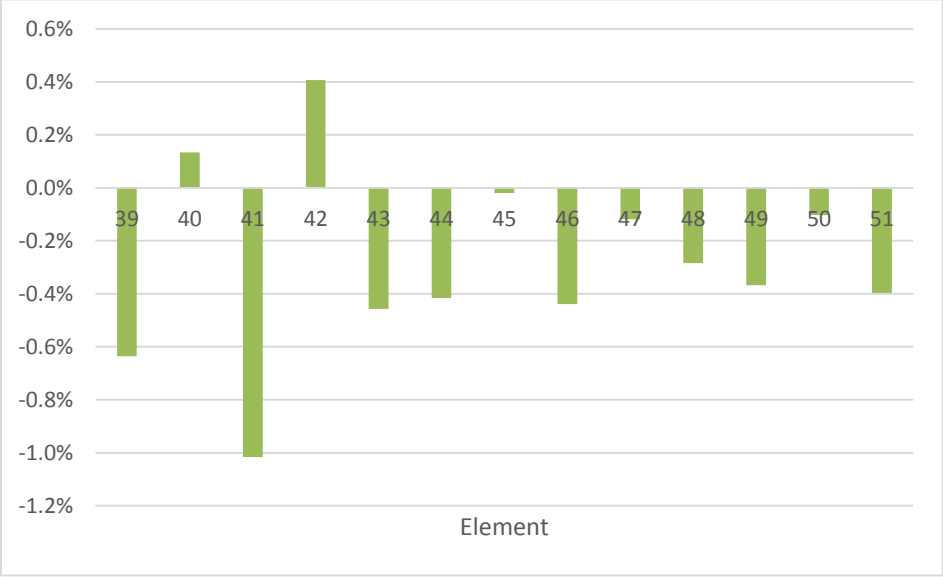

Figure V-46: Errors in the identified mass of the sub system, intact state

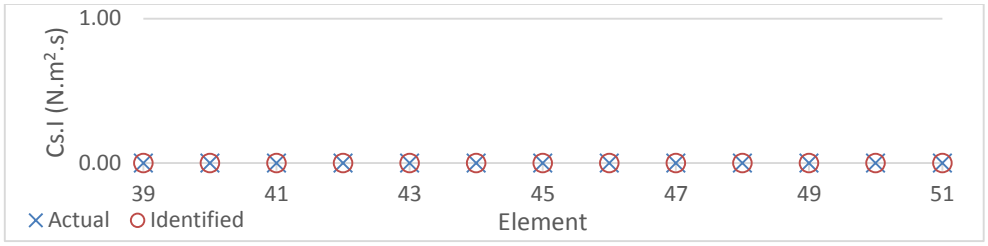

Figure V-47: Identified viscous damping coefficients of the sub-system, intact state

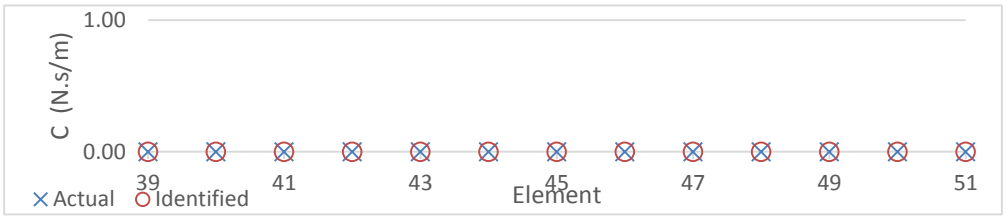

Figure V-48: Identified transverse displacement viscous damping coefficients of the sub-system, intact state

A comparison between the deviations shown in Figure V-32 and Figure V-34 with Figure V-44and Figure V-46 indicates an accuracy reduction in the sub-system identifications. This is the consequence of exercising the boundary elements to estimate the internal loads at the boundary nodes. The errors in the identified properties of the boundary elements are magnified and transferred to the sub-system once the properties are used as inputs, i.e. loads, to the sub-system. Nonetheless, the DITER outcomes are reasonably accurate as it experiences less than two percent errors.

The Next step is to detect damages and their severities in the sub-system. The only excitation load is $p_3(t)$, which has been relocated from the intact to the damaged state. Data collection is performed using a sampling frequency of 1 kHz for 2 seconds. Damage index vector and identified damping values are shown in Figure V-49 through Figure V-52.

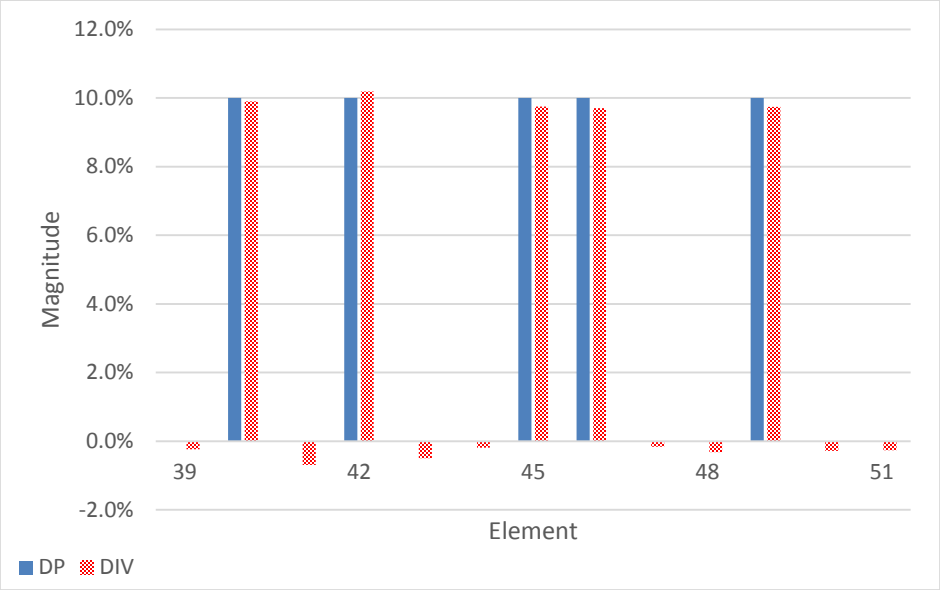

Figure V-49: EI damage identification for the sub-system

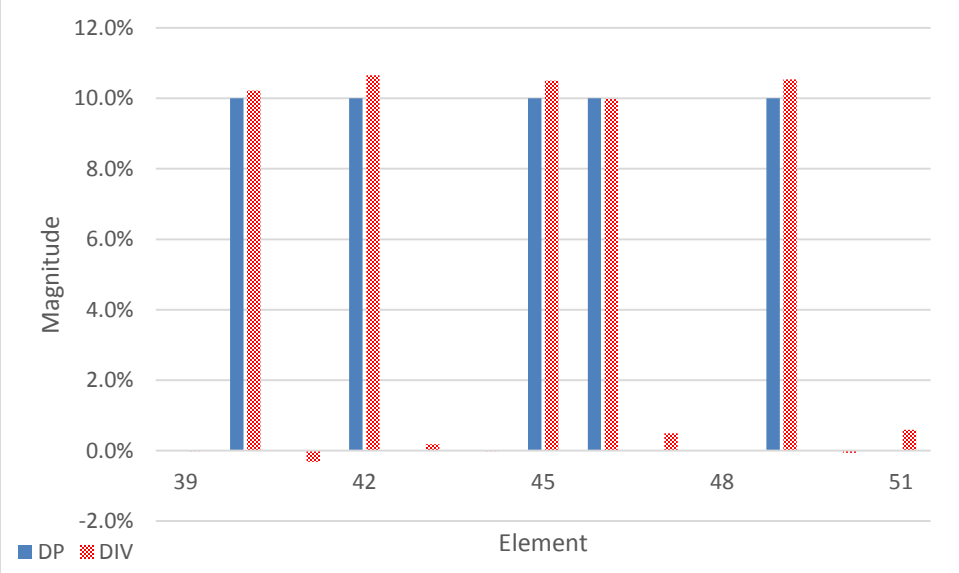

Figure V-50: Mass damage identification for the sub-system

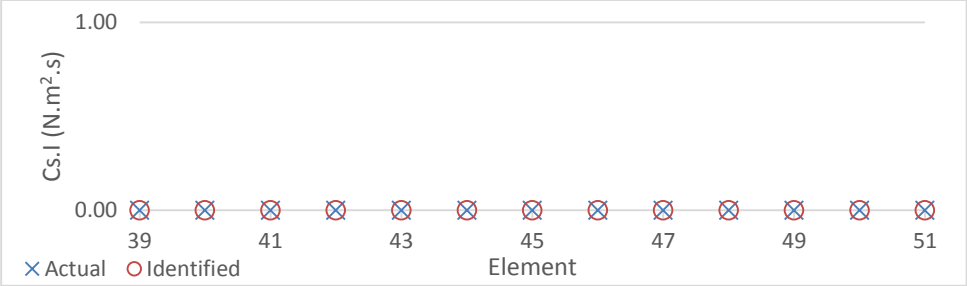

Figure V-51 : Identified viscous damping coefficients of the sub-system, damaged state

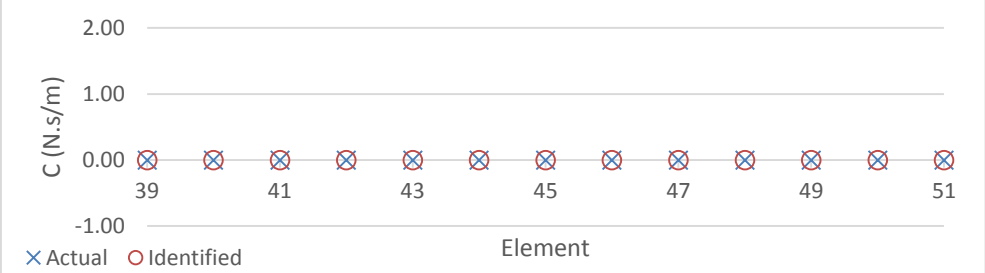

Figure V-52: Identified transverse displacement viscous damping coefficients of the sub-system, damaged state

As the results imply, the damage detection of the sub-system is quite successful. Only small fluctuations are observable in the DIVs, which are less than two percent.

Part 4

In this part, once again, the whole system is taken into consideration. Due to the damages, a Rayleigh damping behavior is assumed to emerge to the structure. The Rayleigh coefficients are selected to impose a 5% modal damping ratio for the first and 100th mode. The corresponding maximum dynamic responses of the beam are shown in Figure V-53, and the given and identified damping values are presented in Table V-7

.

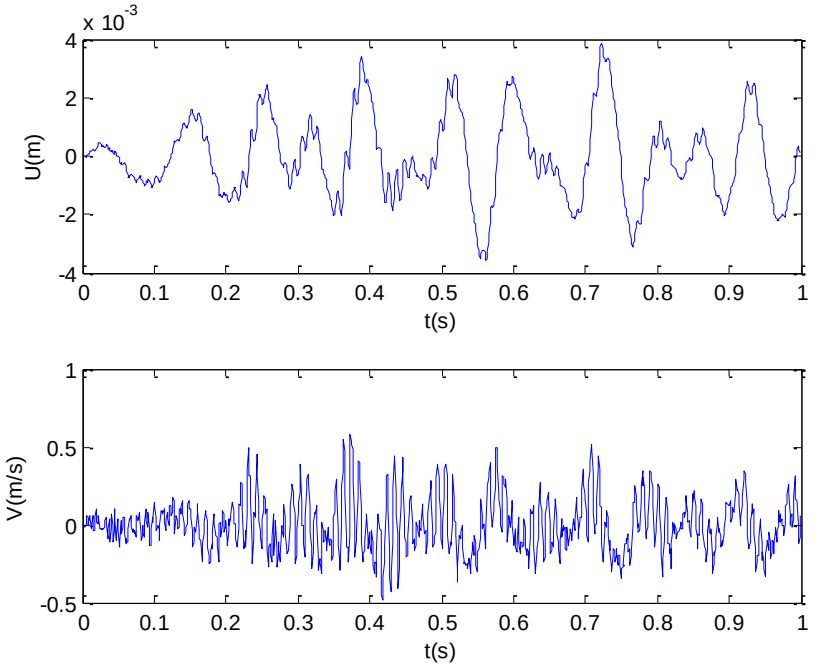

Figure V-53: Maximum dynamic responses of the beam with Rayleigh damping

Table V-7: Rayleigh damping coefficient identification, part 4

α		β	
Actual	Identified	Actual	Identified
1.86E-06	1.83E-06	5.85	5.86

In this part, to obtain the structural properties, the DITER equation in the form of equation (2.24) is solved using the constrained optimization function, fmincon, of MATLAB software. As the problem is non-linear, an initial input must be provided beforehand. An appropriate entry would be the mass and stiffness identification outcomes of the unconstrained linear LSE solution presented in CHAPTER II. The outcome of the first optimizing round may be used as initial guess for the second round optimization. The iteration may be continued until the variation of the evaluated objective function at the solution is insignificant. The obtained damage index vector is shown in Figure V-54 and

Figure V-55. Compared to the undamped case, the results have experienced a relatively larger error amounts. Yet, the error of mass and stiffness DIVs are less than 3% and 2% which are reasonably small to be ignored.

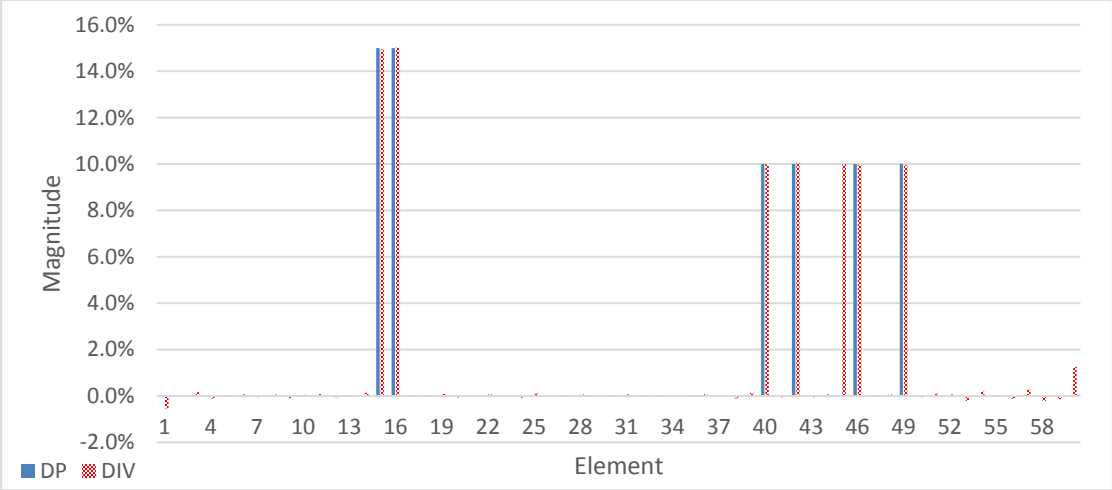

Figure V-54: EI damage identification of the beam with Rayleigh damping

Part 5

This part investigates the effect of variations in static deflections on the accuracy of the DITER method. Two cases have been studied in this part. The first case corresponds to an undamped situation, while in the second case the structure is imposed to the same Rayleigh damping behavior introduced in the fourth part. The damages to mass and stiffness for the both cases are kept to be identical to the second part.

The data are assumed to be collected by accelerometers that were installed in the intact state of the structure. Consequently, the data are measured from the static equilibrium configuration of the intact state of the beam. A comparison is made between the static deflection and the provided dynamic response data in Figure V-56 and Figure V-57. The magnitude of the static deflection can be up to 17% of the maximum

value of the dynamic responses. Thus, for such a measurement, it is expected that variation in the static deflection adversely affect the accuracy of the DITER identification as long as data are measured relative to the static equilibrium configuration of the intact state only.

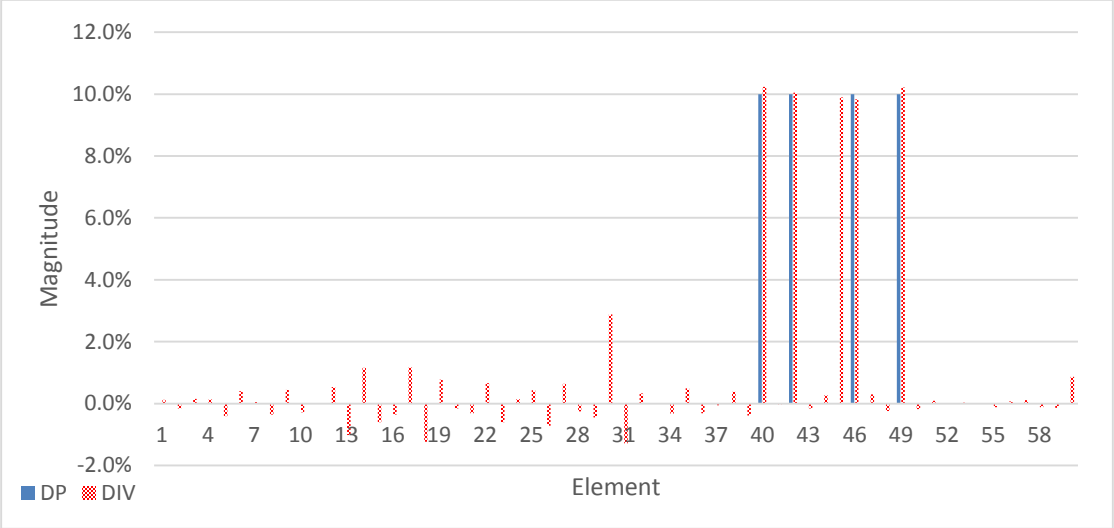

Figure V-55: Mass damage identification of the beam with Rayleigh damping

Figure V-58 and Figure V-59 indicate the obtained DIVs based on the data measured from the static equilibrium configuration of the intact state. The actual damages are located and sized; however, the outcome is too conservative as multiple false positive damages of large magnitudes are observable.

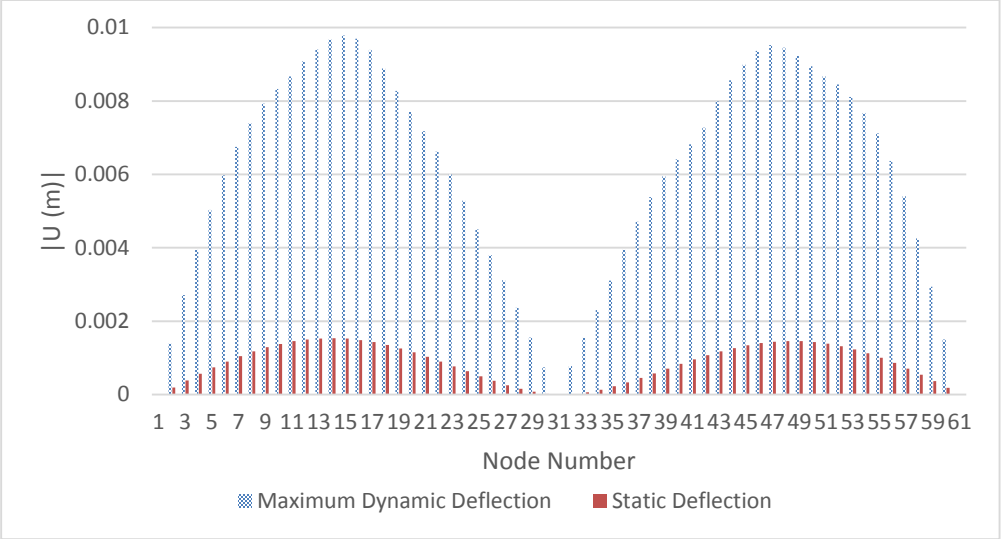

Figure V-56: Static transverse deflection and maximum dynamic transverse deflection of the damaged state of the beam

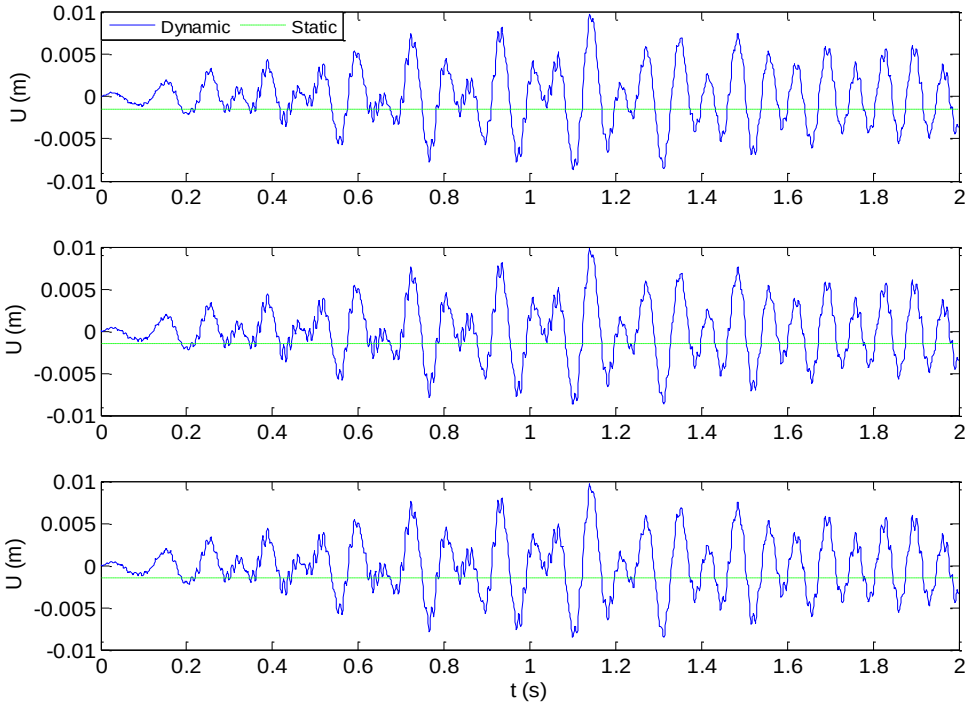

Figure V-57: Transverse static and dynamic displacements for: Top) node 14, Middle) node 15, Bottom) node 16

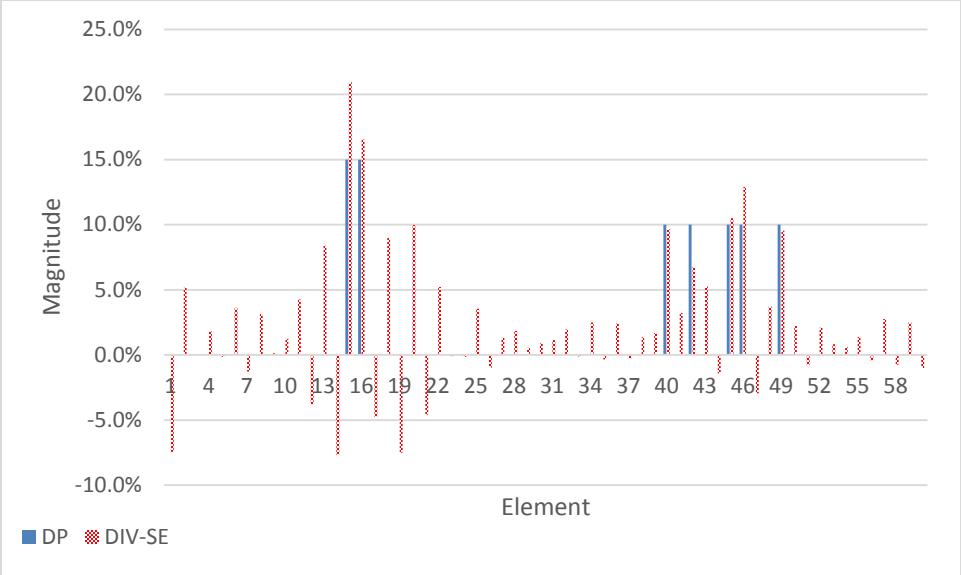

Figure V-58: Stiffness damage identification based on data measured from static equilibrium configuration of the intact state

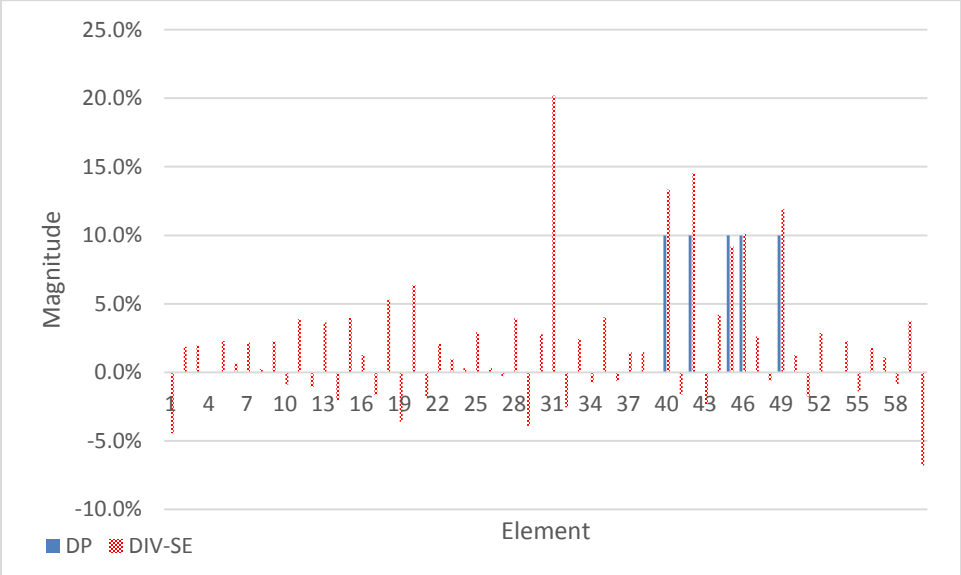

Figure V-59: Mass damage identification based on data measured from static equilibrium configuration of the intact state

Due to the damages, the static equilibrium reaches a new configuration, and consequently the measured data deviate from the static equilibrium of the damaged state. The effect of this deviation is the main reason of the emergence of the large false positive damages obtained in the results. To avoid the errors caused by this deviation, the measured displacements should be converted to the total one considering the static deflection participation as described in CHAPTER III. Here, the main goal is to reduce the errors in the DIVs not an accurate determination of the static deflections. In fact, the mass and stiffness contribution to the optimization function is much larger than what the static deflection values offer. Therefore, the identification of the static deflections are likely to be of less accuracy. Nonetheless, their contribution in the objective function assists to acquire more reliable values for the other structural properties as shown in Figure V-60 and Figure V-61.

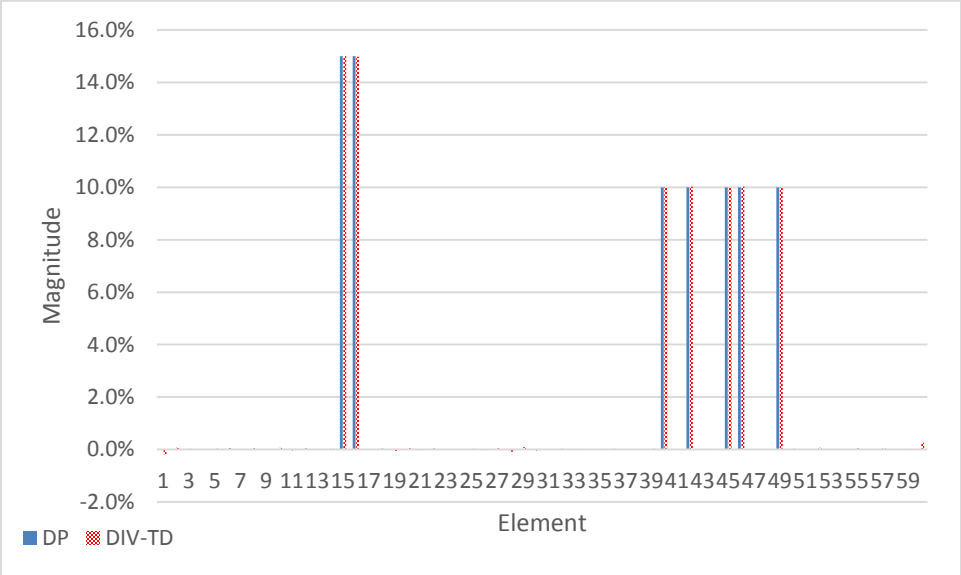

Figure V-60: Stiffness damaged identification considering static deflections, Part 4

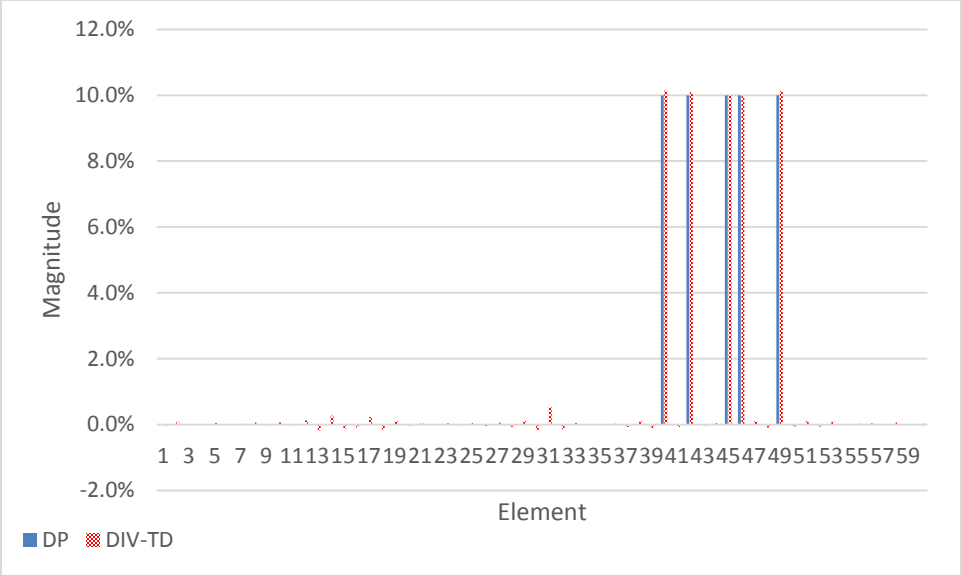

Figure V-61: Mass damaged identification considering static deflections, Part 4

In the second case a similar experiment is performed for a Rayleigh damped state. In this case, ignoring the variation in static deflection significantly affected the damage identification results in a way that some elements are reported to be failed completely, i.e. with zero stiffness. In contrast, damage identification results, shown in Figure V-62 and Figure V-63, are of reasonable accuracy once the static deflections are introduced as extra unknowns. In this experiment, the optimization of equation (2.24) is performed using the MATLAB "fmincon" function. Due to the presence of Rayleigh damping, the optimization was performed several times, with initial values identical to the outcomes of the last optimization result. Iterating the optimization continues until the value of the objective function at the identified properties does not vary significantly.

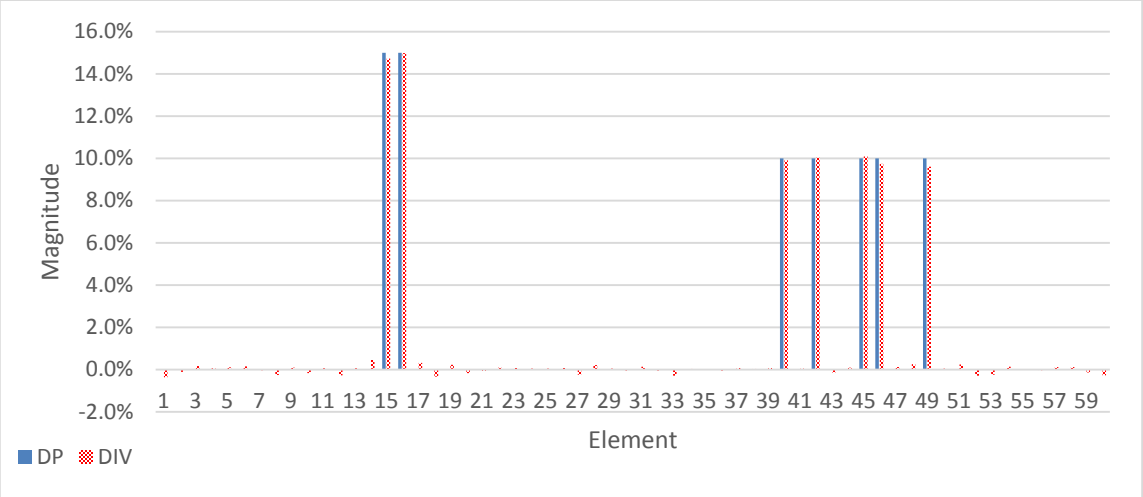

Figure V-62: EI damaged identification considering static deflections, Case 2 of part 5

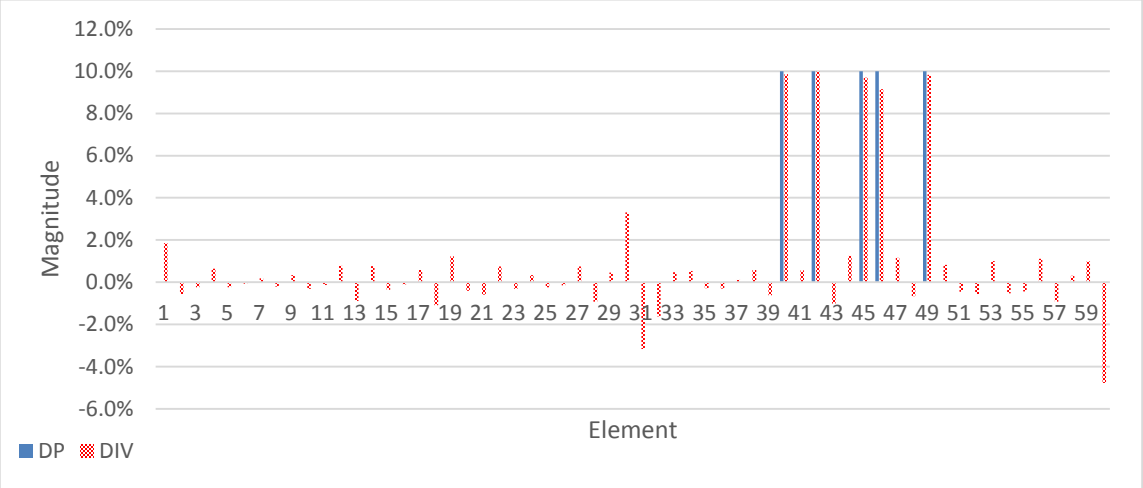

Figure V-63: Mass damaged identification considering static deflections, Case 2, Part 5

Table V-8: Damping coefficient identification, Case 2 of part 5

α		β	
Actual	Identified	Actual	Identified
1.86E-06	1.85E-06	5.85	5.85

Summary

In summary, the third experiment studied a two span beam with a total length of 12m. The beam was modeled in Abaqus software to simulate the dynamic responses of the system under WGN excitations. The FE model has elements of size 0.01m, while the DITER elements are taken to be of length 0.2m. Thus, the data are collected every 0.2m with sampling frequency of 1kHz for a two-second duration. The loads were relocated from the intact into the damaged state to make sure that the variation of the loads has been considered during the experiment. In adddition, to address the DITER performance for sub-system applications, a part of the beam was investigated for probable damages while no other information had been provided from the rest of the system. It was observed that the sub-system damage identification located and sized the dmages but with less accuracy compared to the whole system case. Following the damages, Rayleigh damping behavior was added to the system, and its coefficients successfully identified along with other DIVs. The final part of the experiment studied the DITER reliability when data were collected with acceleramеtors installed in the intact state of the beam. For such cases, it is conluded that DITER outputs are trustable for DIVs and identified damping coefficients as long as the static deflections are placed in the unknown vector.

Frame Experiment

In this part, DITER is numerically verified on a frame with seismic protective systems. The experiment is dedicated to a one-span frame equipped with a pair of low damping rubber bearing isolators and an external Kelvin type viscous damper that is placed near the beam-column joint to dissipate the energy. The interested area is assumed to be confined to the top left corner of the structure. Therefore, DITER with subsystem approach has been implemented to detect damages in this numerical experiment.

Description of the test model

Intact state

A one bay frame with a 8m long span beam, shown in Figure V-64, is considered for this experiment.

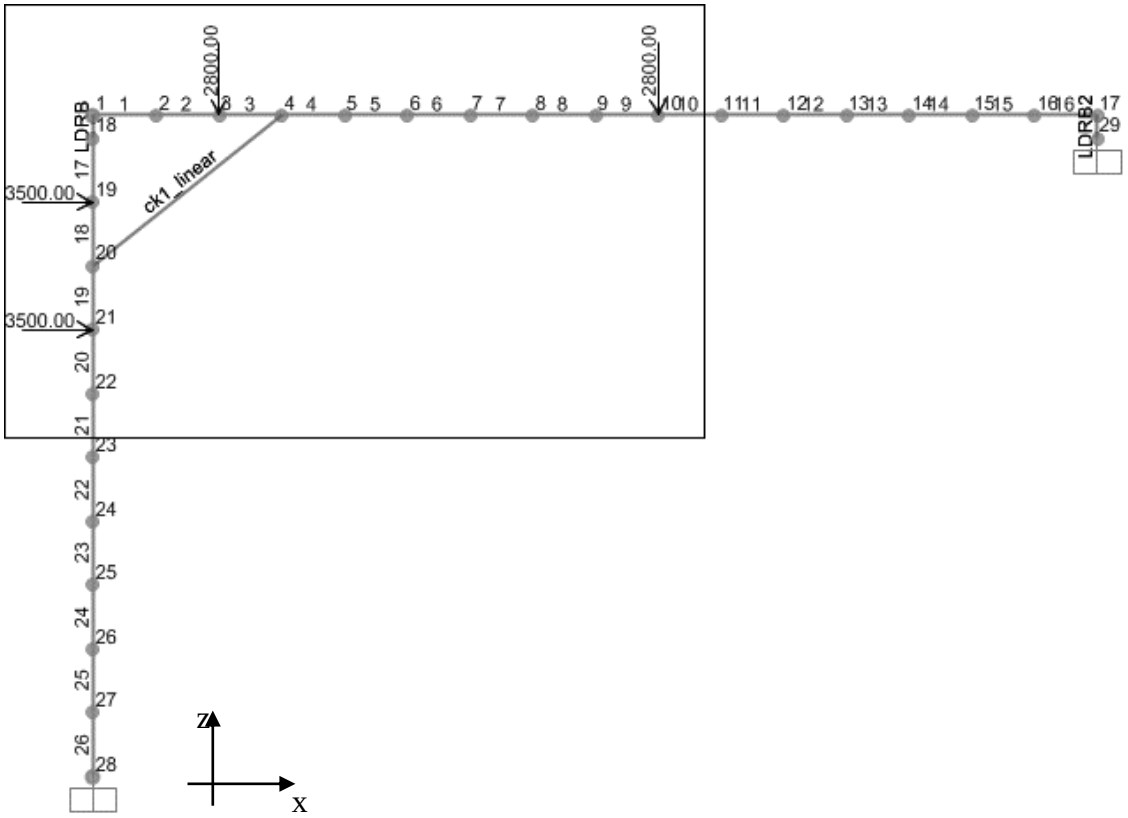

Figure V-64: One bay frame with isolators and external damper. The subsystem is shown by the solid rectangular. The length of the beam and column are 8m and 5m, respectively.

Column and beam sections are selected to be of a compact **I** type section with properties shown in Table V-9. The structure rests on fixed supports at its boundaries. The interested area, for the damage detection purpose, is assumed to be confined to the top left corner of the structure, shown in Figure V-64, where the owner is suspected of some structural issues. Therefore, DITER with subsystem approach must be used in this experiment.

The damper, shown by "ck1" label in Figure V-64, follows a Kelvin model where a spring of effective stiffness 379 kN/m is paralleled to a dashpot with a 7 kN.s/m effective viscous coefficient to resist the movement in the longitudinal direction. It is assumed that the damper parameters are constants during the data collection. As damping and isolator

devices are externally added to the structure, the inherent damping of the frame has been ignored in this example.

Table V-9: Properties of the section used in the frame experiment

Parameter	Unit	Value
Area (A)	m^2	4.797E-3
Young's modulus (E)	GN/m^2	200
2nd Moment of area (I)	m^4	6.854E-5
Mass density(ρ)	kg/m^3	7849.047

Circular low damping rubber bearing isolators are selected for this experiment. The total height of the isolator is taken to be 18cm consisted of 32 layers of rubbers with 3mm thickness and 120mm diameter sandwiched between 31 steel shims of 1.5mm thickness. The thickness of the isolators' top and bottom plates are 19 and 18.5mm, respectively. The shear modulus of the rubbers are assumed to be $0.6N/mm^2$. Table V-10 shows the properties of the isolator, and it is assumed that these properties remain constants during the dynamic simulation. The mass of the isolator is ignored as it is assumed to be merged into the lumped masses located at the top and the bottom of the isolator. One isolator is placed between the beam and column, and two are placed between the beam and the fixed support in a parallel combination.

The Bouc Wen model (Wen 1976) of equation (4.85) and equation (4.86) is used to model the hysteretic behavior of the isolator. The applied parameters are $A=1$, $\alpha=0.15$, $Z_0=0$, $\beta=\gamma=0.5$, $n=2$, and $u_y=0.005m$.

Damaged state

To create a damaged scenario, the beam elements numbered 5, 6, and 9 and the column element number 18 and 19 are damaged as shown in Table V-11. Note that the mass reduction is element wise, i.e. with kg/m unit. Since, the lumped mass model is

employed in this experiment, the element wise mass damage needs to be converted into nodal mass reduction, which is shown in Table V-12.

Table V-10: Properties of the isolator

Item		Value	Unit
Vertical Stiffness	k_v	42414	kN/m
Pre-Yield stiffness	k_e	471.24	kN/m
Post yield stiffness	k_2	70.69	kN/m
Rotational stiffness	k_r	407.17	kN .m
Yield Force	F_y	2.356	kN

Table V-11: Element wise damaged percent values

Element No.	Location	DP		
		EI	EA	mass
5, 6, 9	Beam	15%	10%	10%
18, 19	Column	15%		

Table V-12: Nodal mass damage values

Node No.	DP
5, 7, 9, 10	5%
6	10%

Data generation

The frame is modeled in SAP2000 to generate and collect the structural dynamic responses. Due to the presence of the isolators and damper, the direct integration method, including large deformation, is selected to simulate the dynamic behavior. It should be noted that while the software employs the updated Lagrangian method, it still forms an infinitesimal strain tensor. The structure is discretized into uniform 50cm elements. Data are collected with a sampling frequency of 1 kHz for 5 and 3 seconds for the intact and damaged states, respectively. All the measurements are relative to the static equilibrium configuration, which is updated for the damaged state.

The upper left part of the structure, including the first 5m of the beam and the upper 2.5m of the column, is considered for the damage detection purpose. Consequently, measurements of the responses are limited to this area only, i.e. nodes 1 through 11 and 18 through 23. The responses and the state of the rest of the structure, except the boundary elements, have no impact on the identification of the interested zone.

A normalized White Gaussian Noise, shown in Figure V-65, an impulse, and a sinusoidal force are used to excite the structure. In the intact state, the WGN load applied to the nodes 3 and 10 in the -z direction and intensified by a factor of 2.8kN. The same load applied to the nodes 19 and 21 in the x direction with a magnification factor of 3.5kN. The impulse load is designed to be of a rectangular shaped that lasts for 0.02 second. It applied to the end node of the beam with a total magnitude of 120N in –x direction.

The same loading pattern is used for the damaged state except that the force on the third node is relocated to the node#6 with magnification factor of 2kN; and, in addition to the impulse load, the last node of the beam is excited in the x direction with $f = f_0 \sin(4\pi t)$ where $f_0 = -5.5kN$.

Results and discussion

The structural properties of the intact state are identified and saved to create the baseline structure. Since the isolator behavior is not modeled in the DITER equation, the beam and column attached to the isolator are investigated as two separate isolated systems.

Therefore, there exists four boundary elements, i.e. elements # 1 and 10 for the beam and 17 and 21 for the column. Yet, these subsystems, are coupled through the damper link. Generally, to perform the optimization, it is required to substitute the damper link effect in the subsystems by an unknown force and optimize the subsystems separately through I-DITER approach. However, since the damper contribution to the DITER equation can be modelled directly in the data matrices, it is computationally more efficient to assemble the subsystems into a single DITER equation including the damper data and unknown modules.

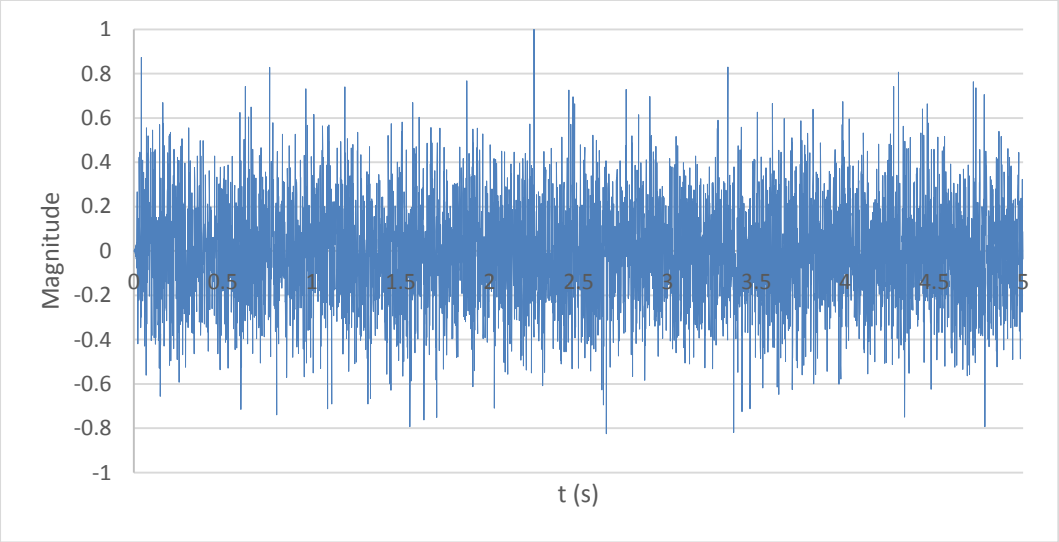

Figure V-65: the White Gaussian Noise applied to the frame experiment

Figure V-66 through Figure V-70 show the DITER identifications of the element wise stiffness values of the sub system. The maximum discrepancy between the identified and actual axial and flexural rigidity of the beam and column is 6%. The maximum axial deformation of the column is less than 0.05mm, and thus the identified values for the column axial stiffness are not dependable. However, the contribution of the axial stiffness

of the column should be kept in the DITER equation to reduce the effect of the model error on the other unknown parameters.

The identified nodal mass values are shown in Figure V-68. Note that the masses of the first and last nodes of the beam and column cannot be identified. The reason is that the beam and column are isolated at their both ends. Meanwhile, the kinetic energies have been computed based on the individual mass values that are lumped at the ends of the elements instead of using an element wise mass, i.e. mass per length, approach. Therefore, the contribution of the end nodes' masses are eliminated. In fact, as long as the mass matrix is modeled with a consistent mass approach, mass identification should be handled accurately. However, in case of element wise-lumped mass modelling of a fully isolated system, errors are likely to be appeared in the individual mass identification. Because the mass data matrix carries data that shares information between the masses of the two adjacent elements. Therefore, the data is sophisticated to identify the summation of the element wise masses rather than the individual mass identification. If one of the ends of the sub-system, is not isolated from the rest of the system, then the individual mass identification might be performed accurately as the mass data matrix carries the information about each mass individually. Thus, when data is generated from a lumped mass FE model and the sub-system is isolated completely from the main system, it is suggested to model the kinetic energy rate based on the nodal masses. This prevents the errors in the lumped mass identification but in the expense of missing the first and last nodal masses identification. Finally, Figure V-69 and Figure V-70 present stiffness and viscous coefficient of the employed damper. Since the behavior of the damper is modeled through a summation of two linear equations, the unknown properties are directly found from adding the damper data modules to the data matrix as discussed in equations (4.97) to (4.105).

Once the bassline structure is created, variations of the structural properties may be followed to detect structural damages. Figure V-71 through Figure V-73 compare the actual damage of the components with the identified damages (DIVs). Two minor false positive damage detections of 4% are reported for the flexural stiffness of the elements

number two and four. In addition, a false positive damage detection of 5% can be observed for the axial rigidity of the 7th element. However, the results show that all the damaged locations have been determined and sized successfully.

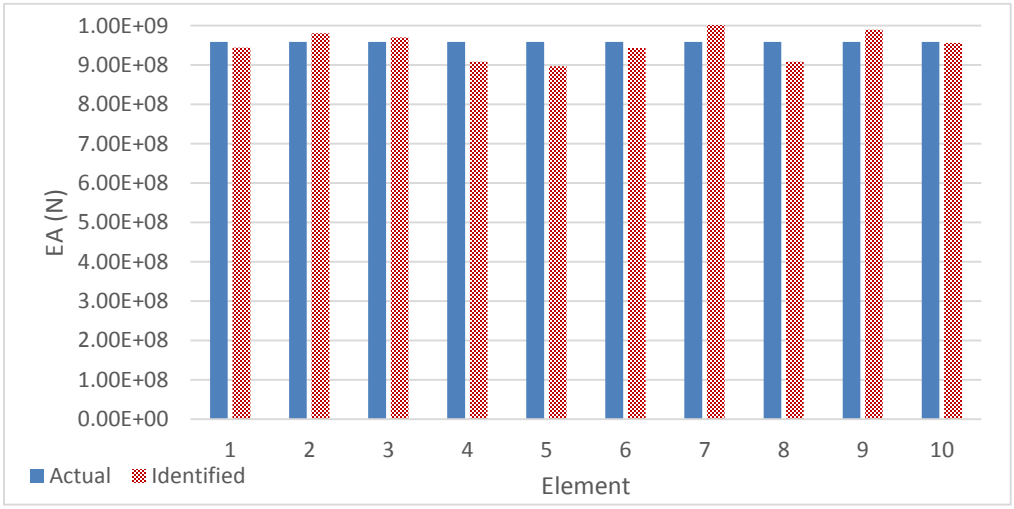

Figure V-66: Axial rigidity identification of the beam of the sub system, Intact State

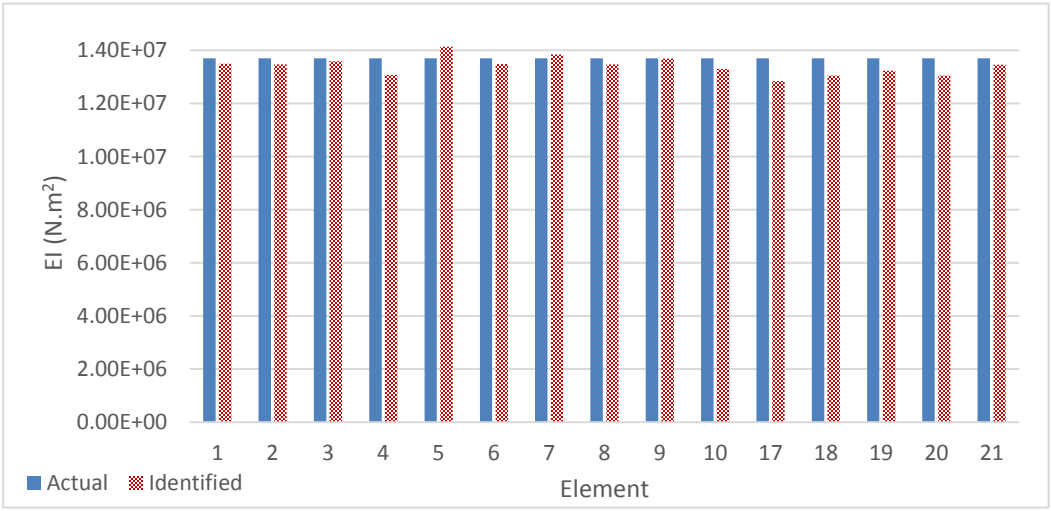

Figure V-67: Flexural rigidity identification of the sub system, Intact State

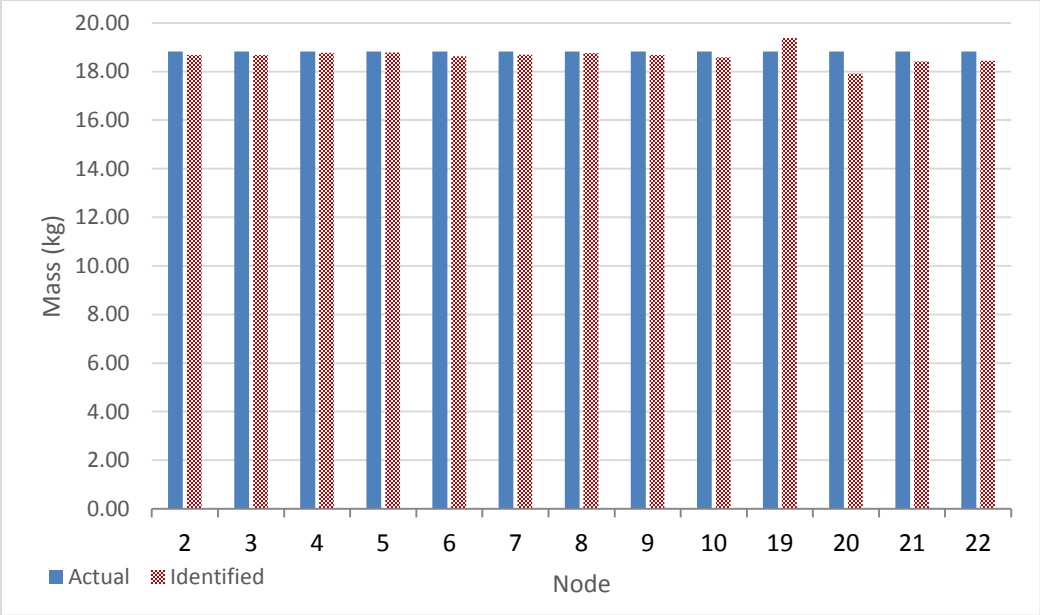

Figure V-68: Nodal mass identification of the sub system

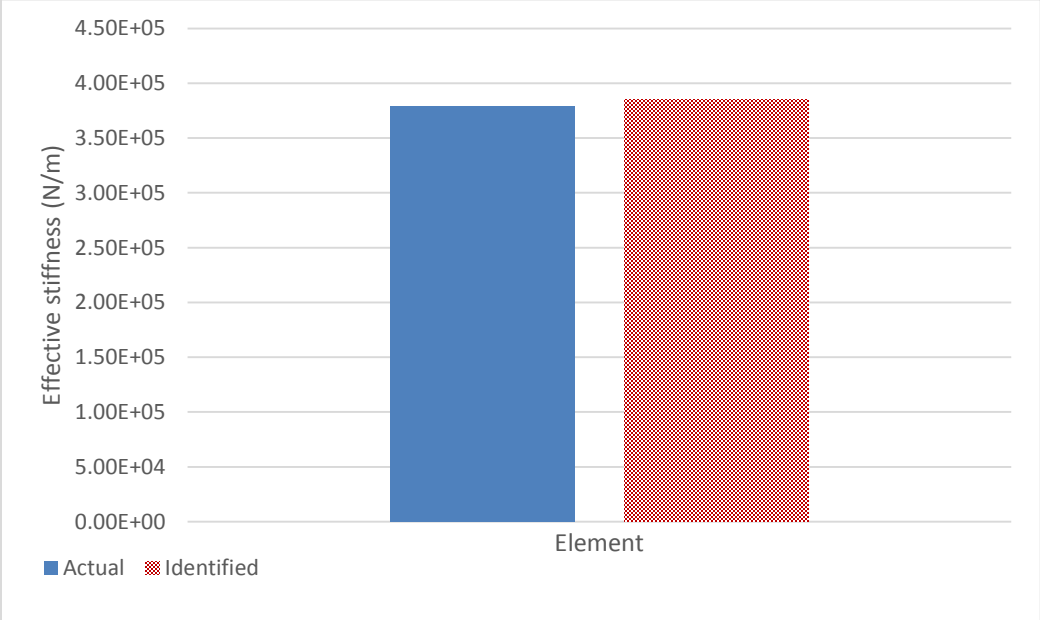

Figure V-69: Identified effective stiffness of the damper

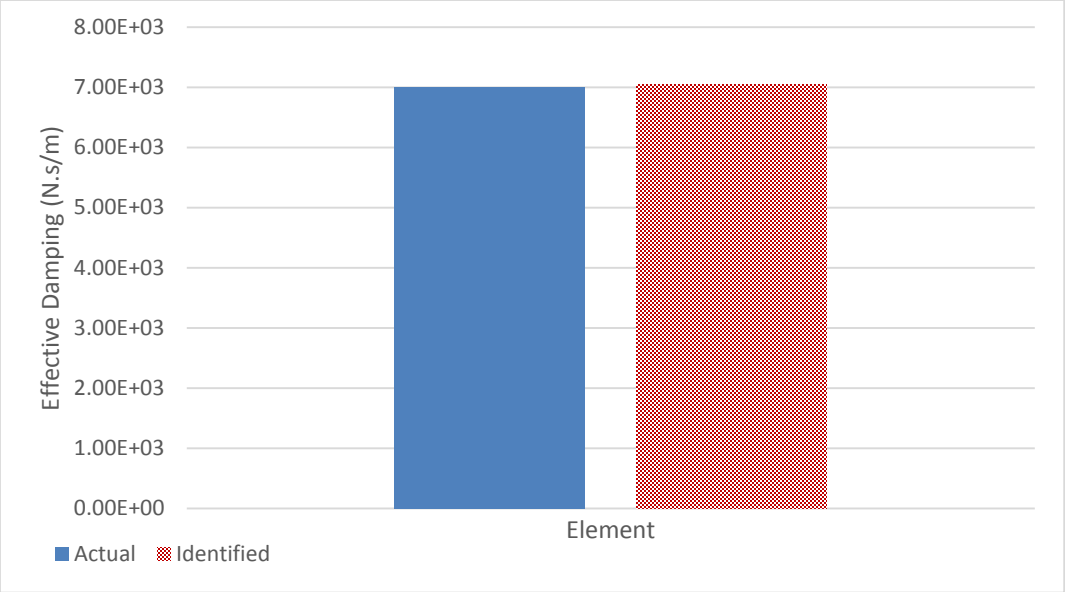

Figure V-70: Identified effective viscous coefficient of the damper

Once the bassline structure is created, variations of the structural properties may be followed to detect structural damages. Figure V-71 through Figure V-73 compare the actual damage of the components with the identified damages (DIVs). Two minor false positive damage detections of 4% are reported for the flexural stiffness of the elements number two and four. In addition, a false positive damage detection of 5% can be observed for the axial rigidity of the 7^{th} element. However, the results show that all the damaged locations have been determined and sized successfully.

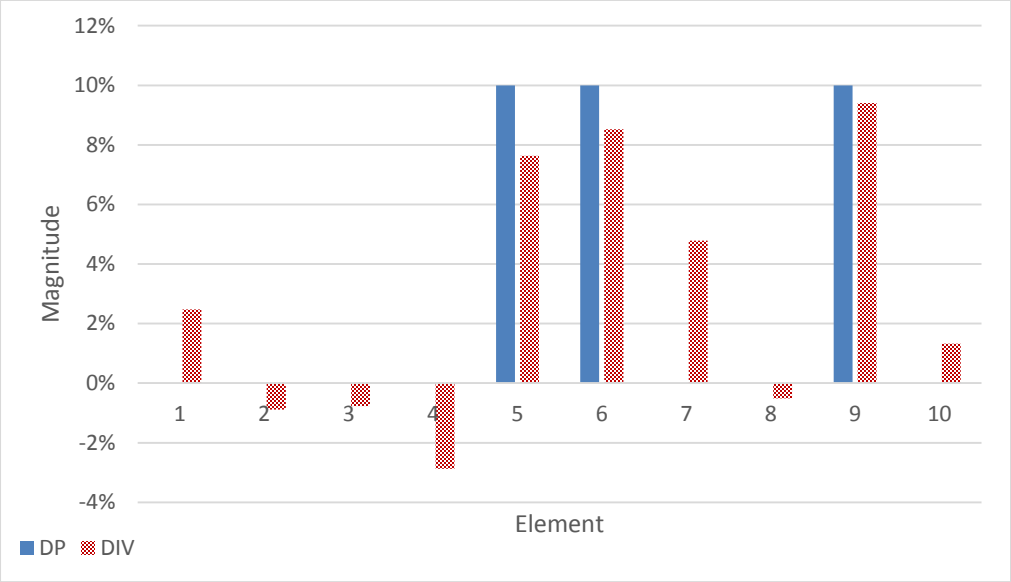

Figure V-71: Axial rigidity damage detection of beam elements

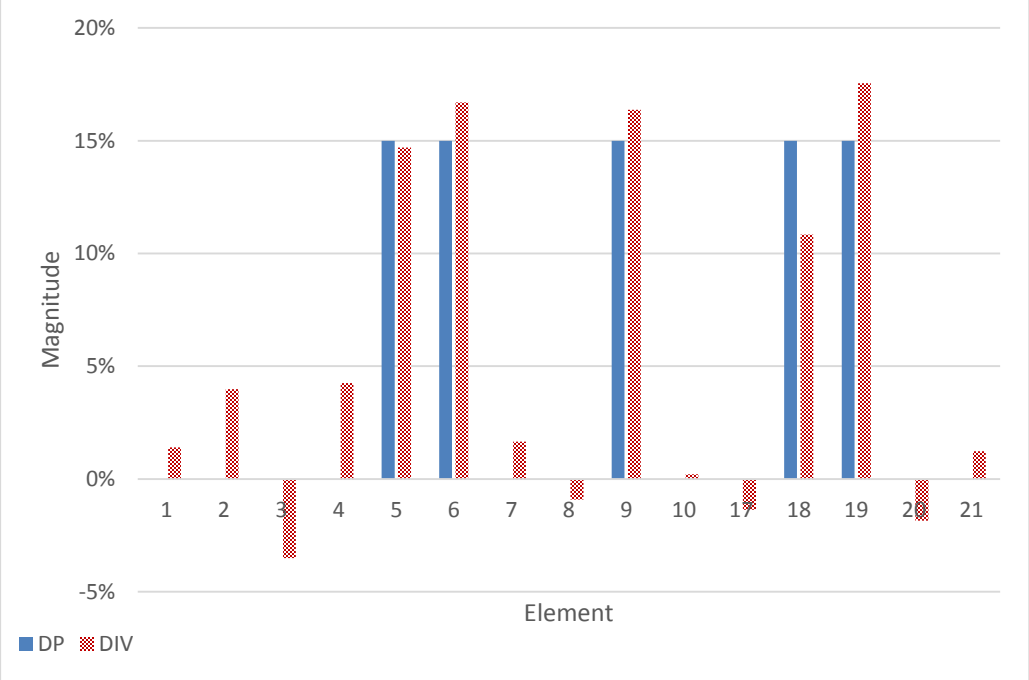

Figure V-72: Flexural rigidity damage detection

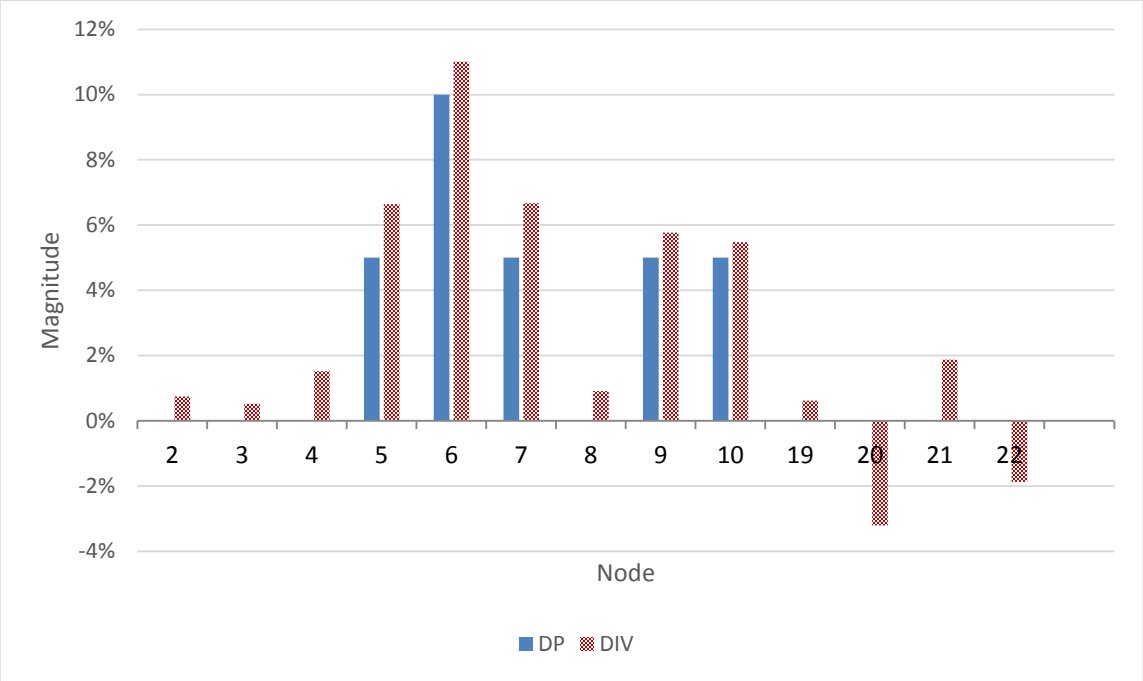

Figure V-73: Nodal mass damage detection

To investigate the state of the isolator, the identified properties of the damaged state of the first element of the beam are used to estimate the applied shear force. As described before, the mass of the first node of the beam cannot be identified due the employed lumped mass modeling. Therefore, the nodal mass must be approximated based on the structural geometry and material densities. In this example, the exact value of the nodal mass is used. Equation (4.88) is used to estimate the force vector applied to the top node of the isolator, where the term $\mathbf{Q}_m^{s/E}$ is substituted by $\mathbf{Q}_m^E$ of equation (4.89) and computed based on the identified EI and EA properties of the element#1 following equation (4.74). In this experiment, $\mathbf{p}_i^k$ is zero and the transformation matrix ${}^j\bar{\mathbf{R}}^T$, $j=19$, has been updated following equation (4.90). Figure V-74 indicates the relation of $f_{18}(t)$ of equation (4.95) and $u_d(t)$ of equation (4.92) along with the obtained values from

SAP2000 simulation. The identified behavior follows the given one; however, due to the errors in the identified values discrepancies are observable.

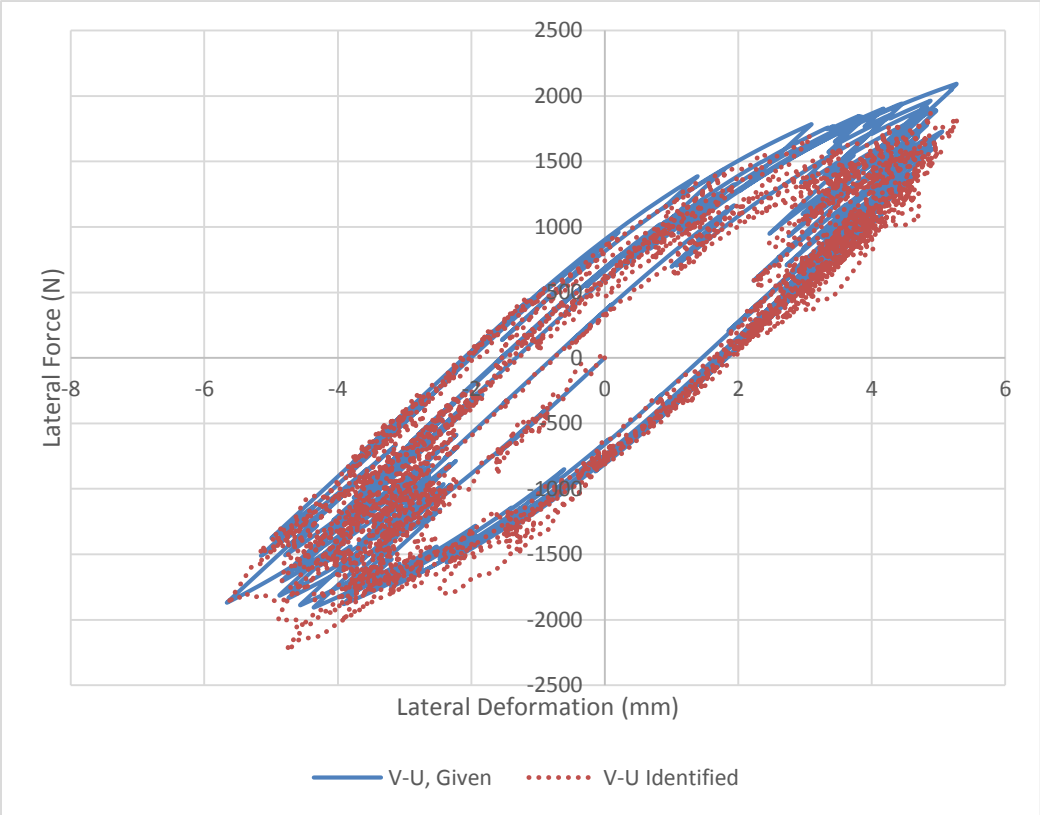

Figure V-74: Identified shear force-displacement behavior of the isolator based on the identified properties of element number 1

Amongst all the Bouc-Wen variables, the pre-yield stiffness of the isolator is of the most concern whose off-limit variation may be attributed to the potential damages. Based on a local sensitivity analysis, Yin et al. (2010) showed that responses of a SDOF system with the Bouc-Wen hysteretic behavior is mostly sensitive to the system stiffness. Consequently, when the lateral deformation of an isolator is modeled as a SDOF system

with the Bouc-Wen hysteretic behavior, the identified elastic stiffness of the isolator should be the most trustable values among the other unknown parameters.

To find the pre-yield stiffness of the isolator, the objective of equation (4.124) is optimized employing the non-linear least square optimization function of MATLAB, i.e. the lsqnonlin function. The value of variable A has been fixed as Ma et al. (2004) showed that there exists functionality redundancy between the Bouc-Wen parameters and, for the identification purposes, the variable A can be valued without affecting the system response. For rubber bearings $A=1$ is recommended (Yin et al. 2010).

$$\begin{aligned}&\min:\Upsilon=\boldsymbol{\varepsilon}^T\boldsymbol{\varepsilon}\\&\text{Subject to}:[50000,0.0001,0.01,-\infty,-\infty,1,-\infty,0.99]^T<\boldsymbol{\theta}<[10^6,0.020,2,\infty,\infty,3,\infty,1.01]^T\\&\hat{\boldsymbol{\theta}}_0=[35000,0.005,0.12,0.1,0.4,2,0.6,1]^T\end{aligned}$$

(4.123)

where

$$\boldsymbol{\theta}=[\mathrm{k}_e,\mathrm{u}_y,\alpha,\mathrm{Z}_0,\beta,\mathrm{n},\gamma,\mathrm{A}]^T \tag{4.124}$$

and

$$\boldsymbol{\varepsilon}=\mathbf{f}_{Identified}-\mathbf{f}_{Bouc-Wen} \tag{4.125}$$

in which $\mathbf{f}_{Identified}$ is a column vector with that holds $f_{18}(t)$ and $\mathbf{f}_{Bouc-Wen}$ is a column vector of the forces obtained from equation (4.86) at each time instant. The identified pre-yield stiffness is $k_{e_{identified}}=452.05$ kN/m that shows only about 4% variation compared to the given value, i.e. $k_e=471.24$ kN/m.

Summary

In conclusion, in this numerical verification experiment, a one-span frame was designed with isolators and an external damper. The damper was assumed to follow a Kelvin type viscous behavior with constant effective stiffness and viscous coefficient. The isolator had a hysteretic shear behavior with constant linear vertical and rotational stiffness. The frame excited by a set of random, impulse, and periodic forces, and the dynamic response data collected for the intact and damaged states of the frame. To

eliminate the effects of the non-linear behavior of the isolator, two sub-systems were created, one for the beam and one for the column, and then the DITER modules of these sub-systems were assembled to include the damper contribution in the DITER equation. The results of the identification of the unknown properties and the damage detections showed that DITER can successfully be applicable on 2D frames equipped with LDRB isolators and viscous dampers. The isolator shear force-displacement relation was also determined and compared to the given values. The results showed that the identified behavior may follow the given one, however, with some discrepancies which mainly was coming from the errors in the identification of the element properties.

SUMMARY

In this chapter, DITER was verified for 2D slender beams by feeding it the data from the pinned-pinned, cantilever, and two span beam tests. The multiple and multi type damage scenarios, large and small displacements, total and relative displacement measurements, and inherent Rayleigh damping and viscous resistance to strain of the material behavior were addressed in the experiments. It showed that DITER were successful in detecting and sizing damages for all the cases. In addition, DITER was applied to a frame with non-linear seismic protective systems. Based on the experiment, it was concluded that the method is applicable to the 2D frames with isolators to identify the structural properties and detect damages.

CHAPTER VI
DAMAGE DETECTION RESULTS USING EXPERIMENTAL MODAL PARAMETERS

INTRODUCTION

In this chapter, modal information acquired from laboratory experiments is utilized to verify the DITER method experimentally. The structure in use is a one-third scale model of a three-story gravity office building. The experimental study was performed by Joseph M. Bracci as a part of his PhD. dissertation in 1992 (Bracci 1992). The structure had been exposed to earthquakes with small to strong severities, and at each stage the modal properties including mode shapes, natural frequencies, and equivalent viscous damping ratios were identified using a simplified three-story shear beam model. As the inputs to the DITER method are in types of accelerations, velocities, and displacements, the modal properties obtained by Bracci are employed to determine the dynamic responses of the structure obtained from different damaged states. Correspondingly, the acquired data are fed to DITER to detect damages, in terms of the stiffness reduction, that occurred in the building due to the earthquake excitations. Finally, the DITER results are compared to the provided structural properties to investigate the accuracy of the method experimentally. Note that, as the mass values are estimated from the structural geometry and material densities, structural damage detection is limited to track reductions in the stories' stiffness values. However, as the mass and damping properties are expected to vary from the estimated values, in the damage detection process, we need to consider these properties unknowns well. Therefore, for the sake of completeness, all the parameters are identified and compared to the provided values of the intact state.

EXPERIMENTAL DATA ACQUISITION

Description of the Structure

Layout and properties

The structure is a one-third scale of an office building. The building is a one-bay by three-bay R/C frames with three stories. This structure had been initially designed to only carry gravity loads. Later, it was retrofitted to be resistant against lateral loads as well. Figure VI-1 and Figure VI-2 show the layout and the section of the building. In addition to the self-weight of the structure components, the mass of the building is increased by adding a total of six 2kip concrete blocks and sixteen 26.5lb lead breaks to the slabs. Special care had been taken to avoid increasing the stiffness of the beams or slabs due to the extra mass mentioned above. The weight of each floor was estimated to be $27(1\pm 0.3)kip$. This chapter focuses on the variation of the stiffness and damping properties of the structural components, rather than the exact details of the structure. Thus, interested readers are guided to (Bracci 1992) for further details of the building.

Instrumentation

The structure had been instrumented with load cells to measure internal axial and shear forces along with bending moments at the mid-story height of the first and second floors. Displacements of the stories were measured using linear displacement transducers. In addition, accelerations in the direction of the excitation load, in the transverse direction, and in the vertical direction were collected at the west and east sides of each story using accelerometers. Linear potentiometers were installed at the beam-column joints to determine the average curvature of the joint members as well.

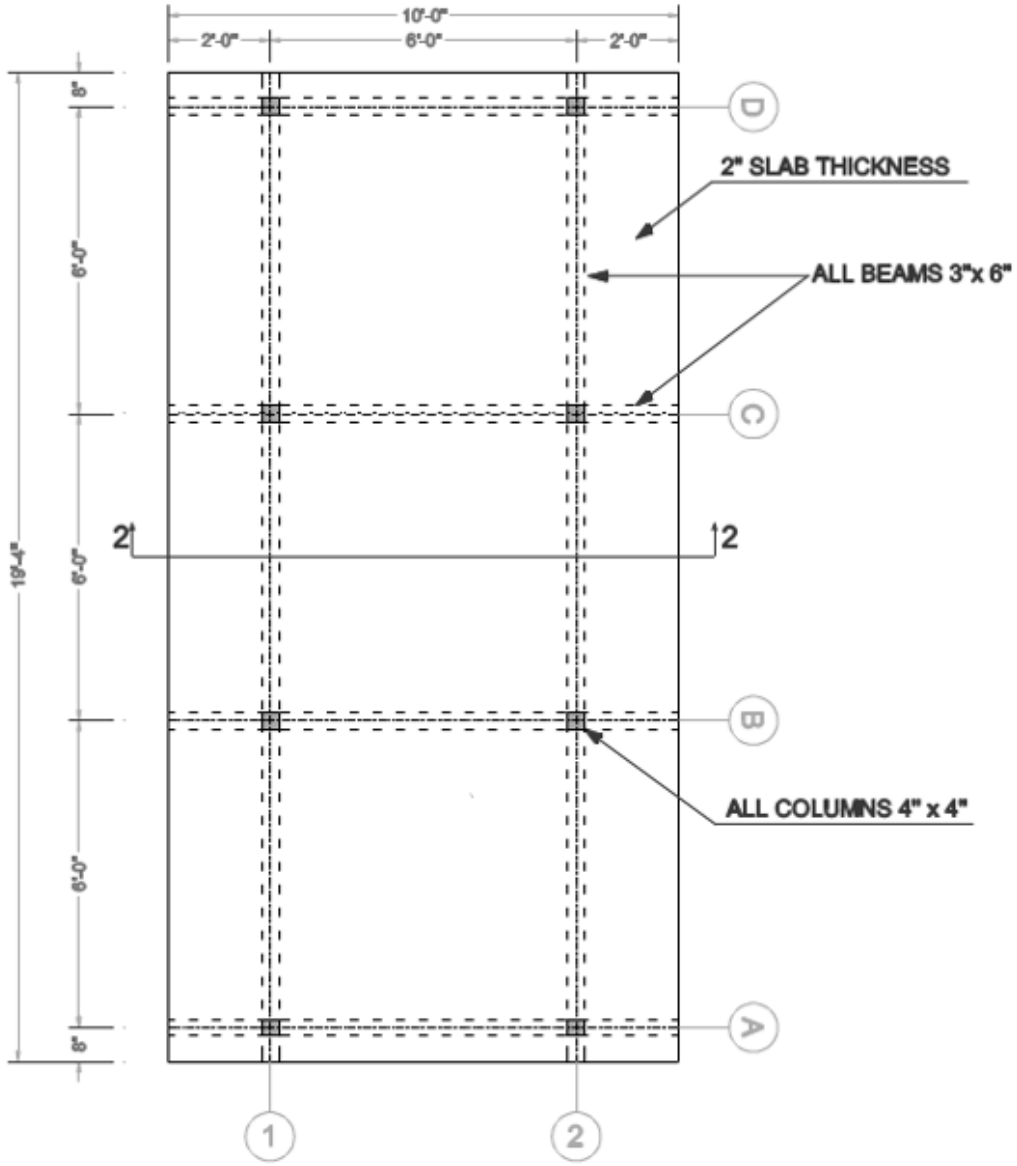

Figure VI-1: Lay out of the experimental model, recreated from (Bracci 1992)

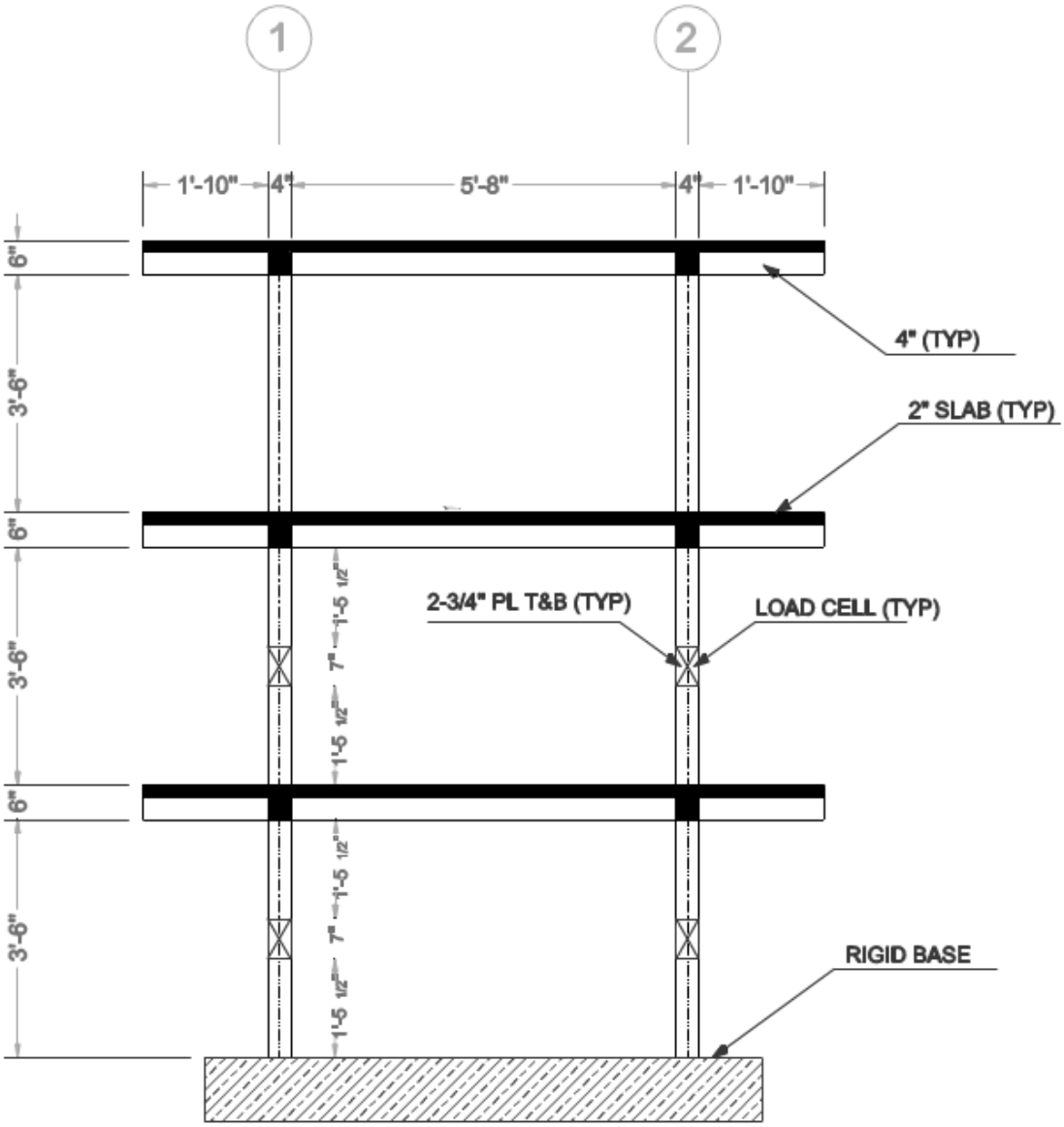

Figure VI-2: Section 2-2 of the experimental building, recreated from (Bracci 1992)

Modal Properties Identification

Bracci employed the impact hammer test, pull back test, snap test, and white noise test to identify the modal properties of the structure in the intact state. All the methods were based upon dynamic response data, except the pull back test in which horizontal

static loads were applied to obtain flexibility and stiffness matrices of the structure. In the pull back test, modal properties were identified through eigen value analysis. In the hammer test, the structure was excited by an impact hammer, and the properties were acquired from the transfer function of the acceleration time histories. Bracci declared that the results of the hammer test were invalid due to large deviations between the identified modal characteristics' values and the analytical predictions. In the snap and white noise tests, he used the Fourier transform of the acceleration time history to identify the modal properties. In the white noise test, the structural characteristics were identified by exciting the structure with a shaking table. Bracci concluded that the identification results based on the white noise test were the most reliable ones amongst other methods.

In the white noise test, care had been taken to ensure that the structure was excited in its linear elastic range to generate and collect proper data for the modal properties identification. The modal properties identification was performed using a transfer function based on the Fourier amplitude of the stories accelerations normalized by the Fourier amplitude of the shaking table acceleration as described in the following paragraphs.

The transfer function, $\mathbf{H}_j(\omega)$, of the j^{th} story was defined as

$$\mathbf{H}_j(\omega) = \frac{\ddot{a}_j(\omega)}{\ddot{x}_g(\omega)} \tag{6.1}$$

where $\ddot{a}_j$ is the absolute acceleration obtained at the j^{th} story, and $\ddot{x}_g$ is the base acceleration. Based on the modal super position method, Bracci used equation (6.2) for the transfer function.

$$\mathbf{H}_j(\omega) = \sum_{k=1}^{n} \mathbf{h}_k(\omega)\phi_{jk} \tag{6.2}$$

where

$$\mathbf{h}_k(\omega) = \frac{-\Gamma_k\left(2i\omega_k\omega\xi_k + \omega_k^2\right)}{\omega_k^2 - \omega^2 + 2i\omega_k\omega_k\xi_k} \tag{6.3}$$

and $\Gamma_k, \xi_k, \phi_{jk}$ are the k[th] modal participation factor($\sum_{j=1:n} \phi_{jk} m_j$),damping ratio for the k[th] mode, and, k[th] mass normalized mode shape function for the j[th] story, respectively. n represents the number of the modes. ω and ω_k are the frequency, and the k[th] structural natural frequency in rad/s.

Dealing with a structure with lightly damped characteristic, he estimated the k[th] natural frequency of the structure by seeking the k[th] peak of the transfer functions. The peaks, however, could be distributed over a frequency range due to the presence of inelastic responses caused by cracks in the RC members. Therefore, he applied a moving average process on the transfer functions signals to determine the peaks. In addition, as the structure had well separated modes, he approximated $\mathbf{H}_j(\omega_k)$ of equation (6.2) with $\mathbf{h}_k(\omega_k)\phi_{jk}$, and thus found the mode shapes magnitude ratio of the structure using

$$\left|\mathbf{H}_j(\omega_k)\right| = \alpha_k \phi_{jk} \tag{6.4}$$

where $\alpha_k = \frac{\Gamma_k \sqrt{1+4\xi_k^2}}{2\xi_k}$ and $\left|\mathbf{H}_j(\omega_k)\right|$ is the peak of the j[th] transfer function at the k[th] natural frequency. As α_k is constant for all the transfer functions at the k[th] natural frequency, the ratio of the mass-normalized mode shape functions at the k[th] natural frequency can be found from the ratio of the corresponding peaks in the transfer functions. He determined the phase angle of the k[th] mode shape from the phase angle of the Fourier transform of the k[th] story acceleration response at ω_k . Having the natural frequencies, he used the half power method (Clough and Penzien 2010) and logarithmic decrement method to estimate the modal viscous damping factors.

He used the N21E ground acceleration component of the July 21, 1952 Taft Earthquake at the Lincoln School Tunnel site in California for the shaking table to excite the structure. He employed three different scales of the Taft N21E where the peak accelerations became 0.05g, 0.20g, and 0.30g. The scales were designed to investigate pre-yield, inelastic, and near collapse behaviors of the model. The structure can be labeled to be at its intact, or as Bracci called “initial” state, slightly (minor) damaged state,

moderately damage state, and heavily (severe) damaged state as it was exposed to no-loading condition, loading with PGA of 0.05g, 0.2g, and 0.3g, respectively. In the moderate damaged state, cracks appeared in the columns of the first and second floors. In the heavily damaged state, cracks were observable in the beams and columns of all the floors.

Bracci modeled the structure using a three-DOF shear beam model, and measured the modal properties of the structure before and after each state. He used a white noise excitation for the shaking table with PGA of 0.024g. The mass of each story was assumed to be concentrated at the deck level and was approximated as

$$m = \frac{27\text{kip.sec}^2}{386.09\text{in}} \simeq 0.07\text{kip.sec}^2/\text{in} \tag{6.5}$$

He identified the corresponding equivalent stories stiffness and equivalent proportional damping matrix using the mass-normalized mode shapes as shown in equation(6.6).

$$\begin{aligned} \mathbf{K} &= \mathbf{M\Phi\Omega\Phi}^T\mathbf{M} \\ \mathbf{C} &= \mathbf{M\Phi\zeta\Phi}^T\mathbf{M} \end{aligned} \tag{6.6}$$

Here $\mathbf{M}$, $\mathbf{\Phi}$, $\mathbf{K}$, and $\mathbf{C}$ are the mass, mass-normalized mode shape, stiffness, and damping matrices, respectively. $\mathbf{\Omega}$ and ζ are diagonal matrices as

$$\begin{aligned} \mathbf{\Omega} &= \begin{bmatrix} \omega_1^2 & & \\ & \ddots & \\ & & \omega_n^2 \end{bmatrix} \\ \zeta &= 2\begin{bmatrix} \xi_1\omega_1 & & \\ & \ddots & \\ & & \xi_n\omega_n \end{bmatrix} \end{aligned} \tag{6.7}$$

where ω and ξ are the cyclic natural frequency and modal damping ratio, respectively. The damping values were only identified for the intact case, while the stiffness values were obtained for all the damaged states. The provided modal values along with the measured and identified values for the intact, minor, moderate, and severe damaged states are shown in Table VI-1through Table VI-4. Take note that the provided modes are not

mass-normalized, and thus they need to be modified before being used in the above formulations.

Table VI-1: Provided data for the intact state, source (Bracci 1992)

No.	f (Hz)	ξ (%)	Floor	ϕ_1	ϕ_2	ϕ_3	m (kip.s^2/in)	k (kip/in)	c (kip.s/in)
1	1.78	2	3	1	-0.82	-0.46	0.07	53.4	0.042
2	5.32	2.4	2	0.8	0.46	1	0.07	54.4	0.029
3	7.89	2	1	0.42	1	-0.83	0.07	50.3	0.083

Table VI-2: Provided data for the minor damaged state, source (Bracci 1992)

No.	f (Hz)	ξ (%)	Floor	ϕ_1	ϕ_2	ϕ_3	m (kip.s^2/in)	k (kip/in)
1	1.71	4.3	3	1	-0.84	-0.42	0.07	46.8
2	5.08	4.2	2	0.79	0.52	1	0.07	47.3
3	7.42	3	1	0.4	1	-0.82	0.07	44.9

Table VI-3: Provided data for the moderate damaged state, source (Bracci 1992)

No.	f (Hz)	ξ (%)	Floor	ϕ_1	ϕ_2	ϕ_3	m (kip.s^2/in)	k (kip/in)
1	1.42	6.6	3	1	-0.95	-0.45	0.07	36.3
2	4.37	5.6	2	0.83	0.55	1	0.07	31.2
3	6.18	2.8	1	0.43	1	-0.78	0.07	28.7

Table VI-4: Provided data for the severe damaged state, source (Bracci 1992)

No.	f (Hz)	ξ (%)	Floor	ϕ_1	ϕ_2	ϕ_3	m (kip.s^2/in)	k (kip/in)
1	1.2	7	3	1	-0.86	-0.46	0.07	24.8
2	3.76	2.3	2	0.75	0.64	1	0.07	22.4
3	5.27	1.8	1	0.33	1	-0.94	0.07	28.5

Data Generation

The provided modal data cannot be used directly in DITER method. Therefore, before performing identification process, an extra step is required to generate applicable data for DITER. In this study, the modal properties including mode shapes, modal damping ratios, and natural frequencies, as well as provided mass values are used to simulate accelerations, velocities, and displacements of the shear beam floors under WGN excitations.

Here, main interest is in assessing the health condition of the stories' stiffness, because the mass values are assumed to be known by estimating them from the weight of the structural and non-structural materials. Yet, in the damage detection process, the mass values are considered unknown. This assists the method to provide more accurate results. To generate the dynamic response data, similar to Bracci's work, the structure is modeled as a three story shear beam shown in Figure VI-3.

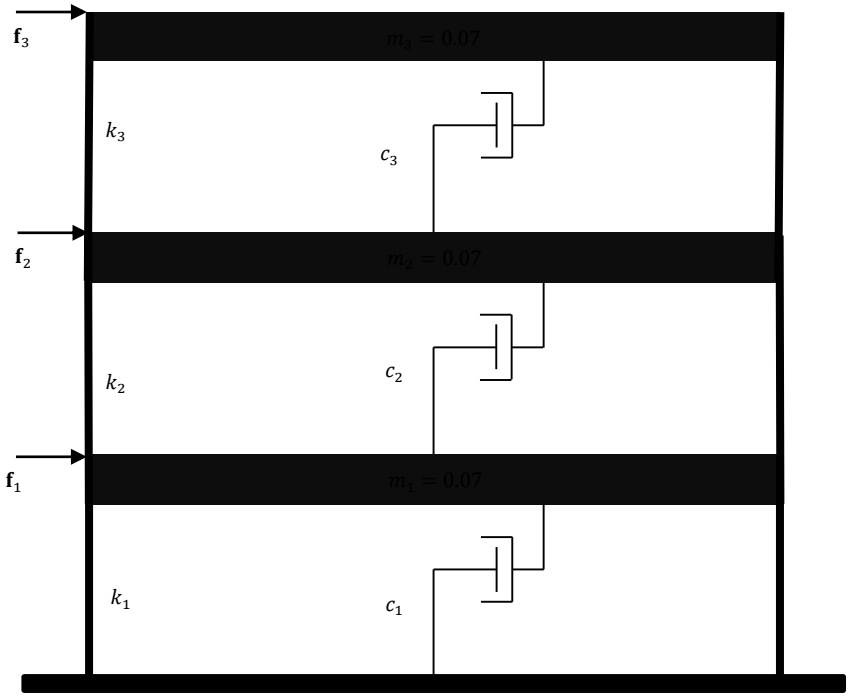

Figure VI-3: Three story shear beam model of the experimental model

The excitation loads are selected to be of WGN type and applied to the all floors as indicated in Figure VI-4.

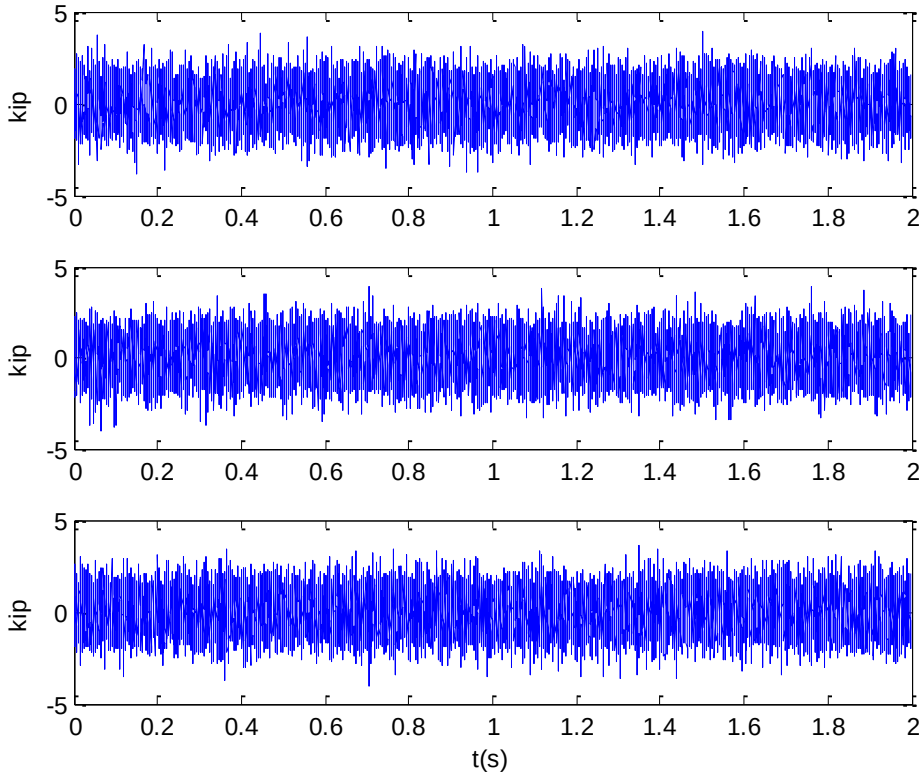

Figure VI-4: Applied loads to the experimental model, Top) at first floor, Middle) at second floor, Bottom) at third floor

The modal superposition method along with the linear acceleration method is used to generate nodal accelerations, $\ddot{u}(t)$, velocities, $\dot{u}(t)$, and displacement $u(t)$ data. Using mass normalized mode shapes, for the kth mode, the following can be written (Clough and Penzien 2010) :

$$\ddot{Y}_n(t) + 2\xi_n \omega_n \dot{Y}_n(t) + \omega_n^2 Y_n(t) = \mathrm{P}_n(t) \tag{6.8}$$

where $Y_n, \dot{Y}_n, \ddot{Y}_n$ are the nth modal displacement, velocity and acceleration ,respectively. $\mathrm{P}_n(t)$ is the nth modal force obtained from

$$\mathrm{P}_n(t) = \sum_{i=1}^{3} \phi_{in}\, \mathrm{f}_i(t) \tag{6.9}$$

where f_i is the applied WGN at the ith story, and ϕ_{in} is the nth mass-normalized mode shape at the ith floor . Equation (6.8) can be solved for the modal displacements by using the linear acceleration method (Chopra 2007). Once Y is found for all the modes, the physical acceleration can be determined using modal superposition as

$$\mathbf{u}(t) = \mathbf{\Phi Y}(t) \tag{6.10}$$

where $\mathbf{Y}$ is the modal displacement vector, and $\mathbf{\Phi}$ is the mass normalized mode shape matrix. The velocities and accelerations can be found by taking the first and second time derivative of equation (6.10), respectively.

The simulation lasts for 2 seconds with time increment of 0.0001 second. The data are acquired in the same duration and with sampling frequency of 10 kHz. During the process, as suggested by Bracci, proportional damping behavior is assumed. It should be noted that the errors on the stiffness and mass damage detection due to the proportionality assumption is ignorable. In fact, the only affected properties of such an assumption are the damping values. In the worst scenario, we are forcing the damping matrix to modify its components to behave as a proportional one, while at the same time the stiffness and mass matrices remain intact. Therefore the identified values should be intact, and only the damping values might be affected.

RESULTS AND DISCUSSIONS

The acquired data from each state are fed to DITER where the loads are assumed to be known. The stiffness values are the properties of main interest for the damage detection. However, as the explicit damping and stiffness properties are provided in the intact state by (Bracci 1992), the corresponding DITER identification results are also shown for this state as well.

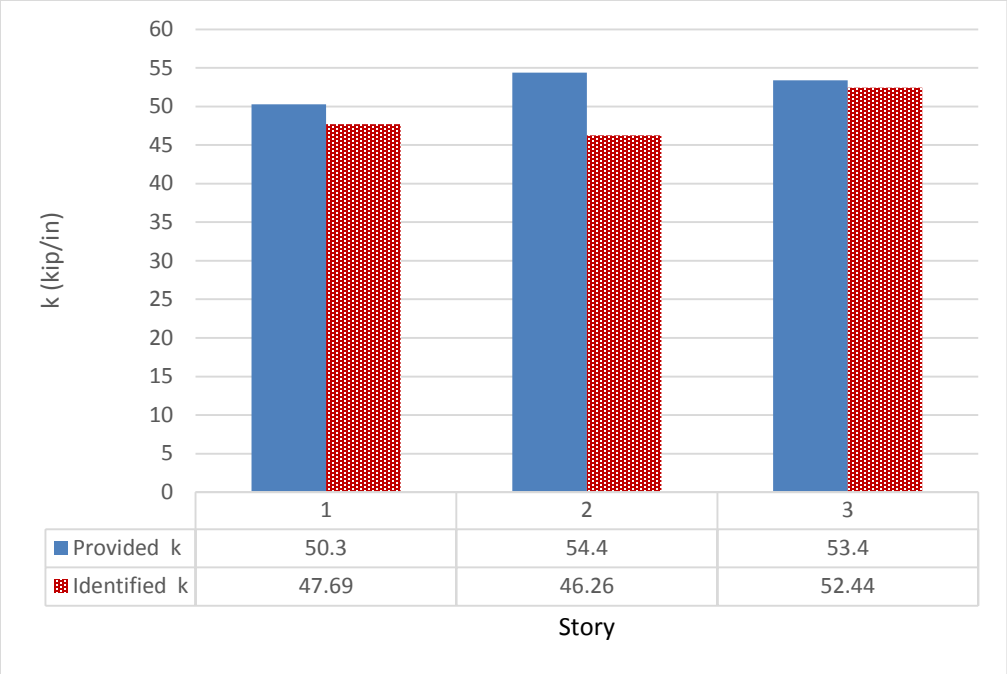

Figure VI-5: Provided and identified story stiffness values of the intact state

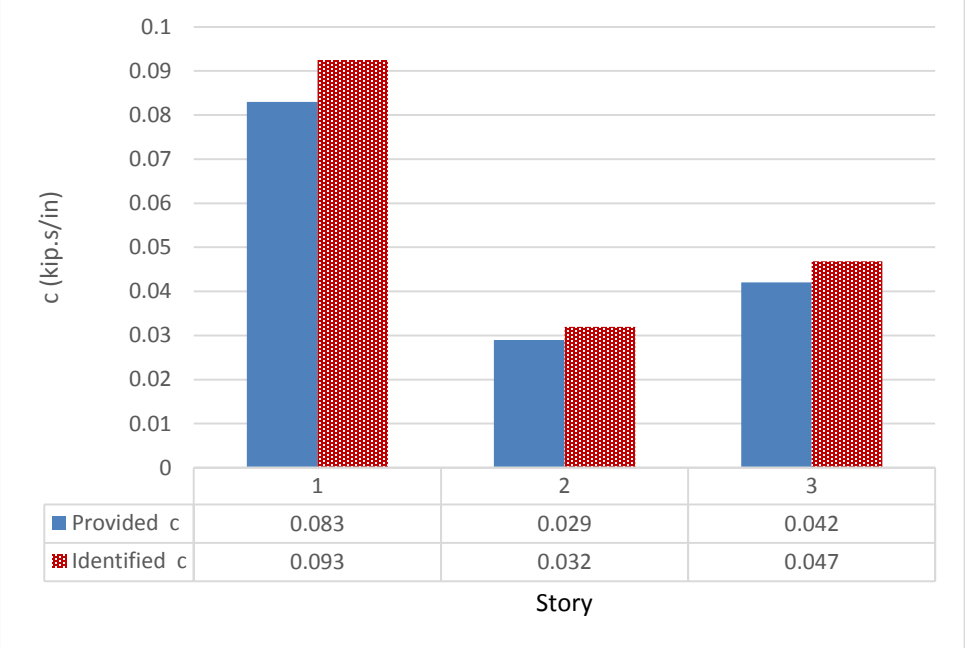

Figure VI-6: Provided and identified equivalent viscous damping of the intact state

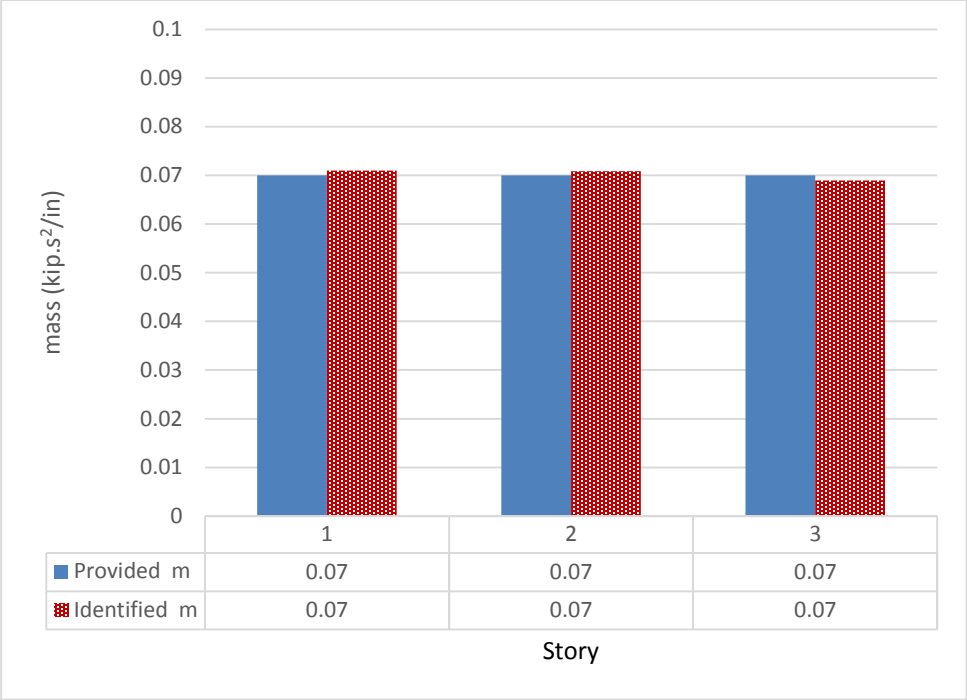

Figure VI-7: Provided and identified mass values of the intact state

As Figure VI-5 through Figure VI-7 imply, the identified values for the intact state are close to the ones provided by (Bracci 1992). The most deviation can be seen in the second story stiffness where the identified value is 15% smaller than the provided one. Also, the magnitude of the identified equivalent viscous damping is about 10% larger than the provided ones for all the stories. However, these deviations are reasonably small for an experimental verification. It should be noted that the measured mode shapes are not perfect. Hence, when the data are generated in a forced response manner, these imperfections add some errors to the modal forces. Thus, the deviations between the measured and identified properties are expectable.

As the ultimate objective of DITER is to detect and size damages, for the rest of the cases, the comparisons are made between the damage parameters and the obtained damage index vectors.

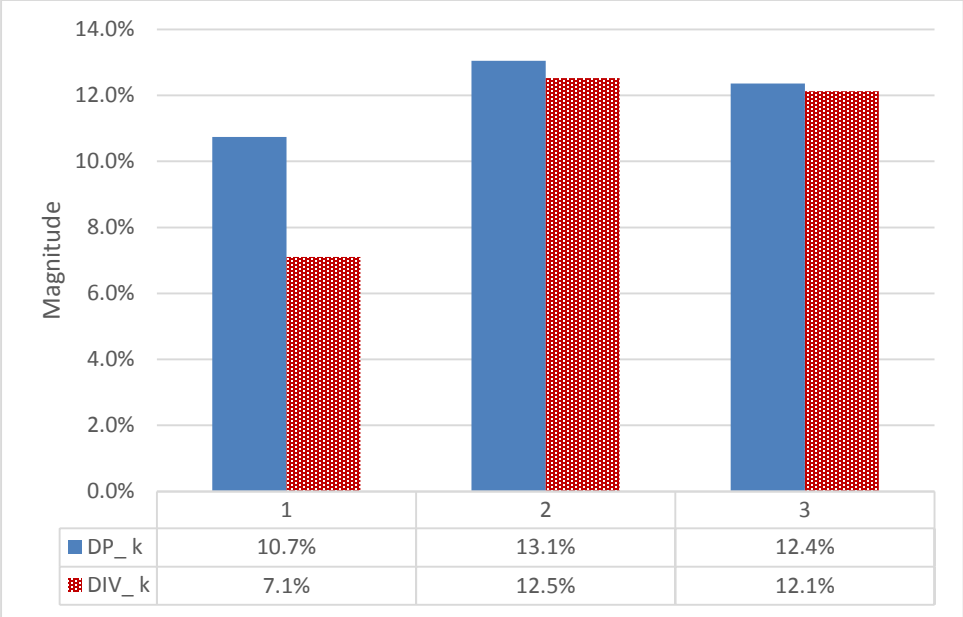

Figure VI-8: Measured damage (DP), and identified (DIV) damages of the stiffness of the slightly damaged state

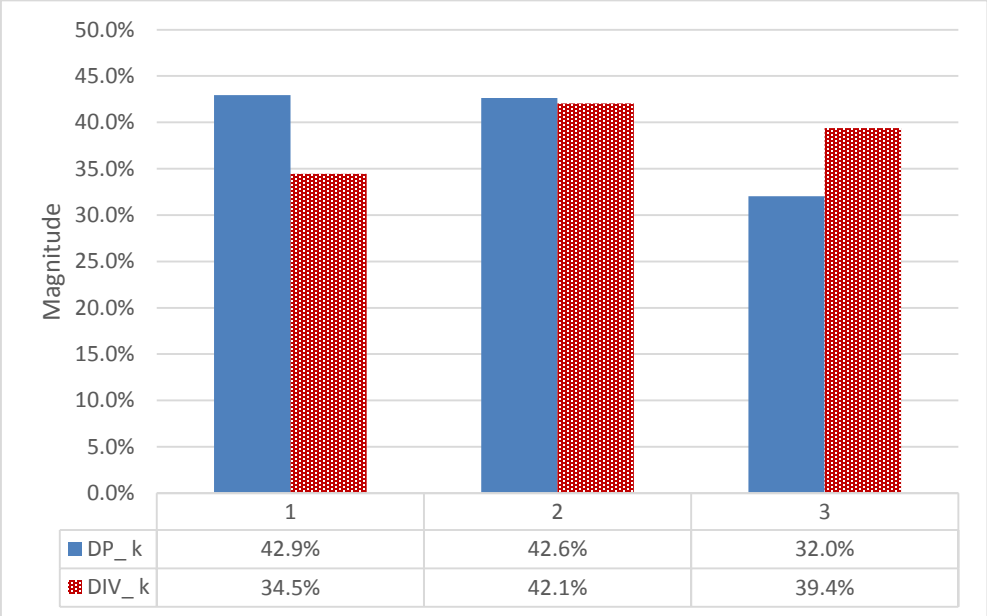

Figure VI-9: Measured damage (DP), and identified (DIV) damages of the stiffness of the moderately damaged state

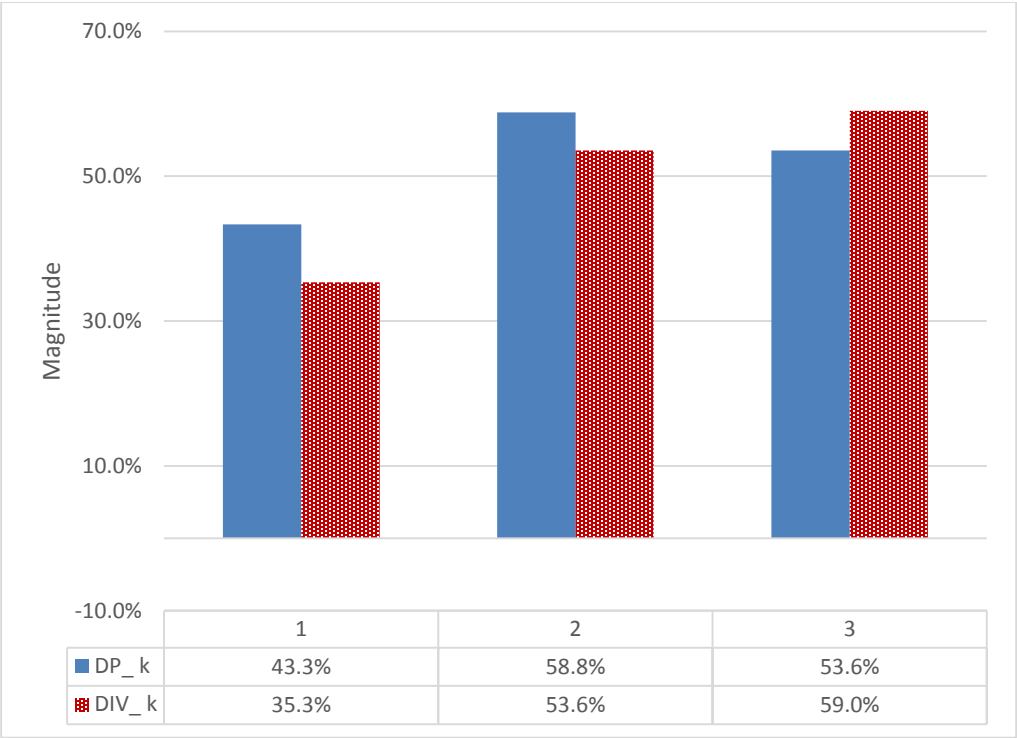

Figure VI-10: Measured damage (DP), and identified (DIV) damages of the stiffness of the heavily damaged state

Figure VI-8 through Figure VI-10 show the measured and identified damages to the story stiffness for the three damage states. In all cases damages are located successfully and the severities are close to what presented by (Bracci 1992).

SUMMARY

In this chapter, a three story lightly reinforced concrete building is used to verify DITER experimentally. The experiment was performed by Bracci (1992) as a part of his PhD. dissertation. The measured modal parameters are used to generate dynamic response data of the building. The building is modeled as a three-DOF shear beam, and the data were collected at each story. The intact state properties were identified in terms of stiffness, mass, and equivalent viscous damping and shown to be close to the provided values. In addition, the damages occurred to the stories' stiffness is obtained and stored in

DIVs and compared to the provided values for minor, moderate, and heavy damaged states. It has been shown that DITER located all the damages and assessed their severity successfully.

CHAPTER VII
CONCLUSION AND FUTURE WORK

SUMMARY AND CONCLUSION

We developed a level III damage detection method in order to detect and size damages in the sense of element wise stiffness and mass degradations and variations in the damping characteristics of a structure with or without seismic protective systems. The method falls under system identification based damage detection methods, as it creates a baseline of the structure with respect to which the variations are tracking in an off-line manner. We discretized a structure into elements and derived the rate of kinetic, potential, and dissipated energy for each along with the rate of the work applied to the structure. Employing the principle of work and energy, the equilibrium for the rate of the energies were constructed on the domain of the structure at discrete time steps corresponding to the sampling frequency and the duration of the collected dynamic response data. The effect of seismic protective systems, in case of existence, were also included in the equations. This set of equations were called the DITER equation in which the element wise stiffness, mass, and damping characteristics of the structure along with the properties of the seismic protective systems were unknown. We assumed that the modulus of elasticity, material density, and the damping coefficient of the structure can be substituted with effective values that remain constant on the element domain during data collection. As model errors and noises do exist in the equations, we solved the DITER equation for the unknowns in a least square optimization manner.

To enhance the applicability of the method, we addressed some practical issues that we may face in a field application. Originally, the DITER inputs are accelerations, velocities, displacements, and external forces. Due to the difficulties in collecting load data from the whole structure, we presented an iterative LSE approach to solve the DITER equation when load data were missing at some nodes, and we called it I-DITER. In addition, neither all the nodes of a structure receive enough energies to be excited, nor

tracking of the states of all the structural components are of interest. Thus, a sub-system approach was added to the DITER by which only a specific domain of a structure might be selected and studied for the damage existence. Moreover, to lessen the model errors, we considered the effect of the variations in the static deflection when data are collected with respect to the initial static equilibrium configuration of the structure.

We explicitly derived the DITER equations for shear beam models and 2D slender beams and frames. The shear beam models are appropriate in dealing with ordinary residential and commercial structures, while the 2D frames might be useful in studying the health state of bridge-like structures.

The implementation of DITER and I-DITER were shown for a seven-story shear beam example with non-proportional damping behavior. We used a total least square method to deal with noisy data, and we recognized that the method is capable to handle small noises with ignorable loss of accuracy. However, data cleansing is necessary for stronger noise pollution.

We constructed the DITER equation for slender beams and frames in which the inherent damping was considered either with the Rayleigh model or element wise straining material viscous resistances. To address the effect of the geometrical non-linearity of the real structures, we developed the DITER equation for the slender beams and frames using von Kármán nonlinearity for the strain tensor and called it L-DITER. The benefit of L-DITER is that it may absorb the geometrical nonlinear effects without adding any further complications to the least square optimization.

We also developed the DITER for frames with dampers and rubber bearing isolators. As long as the behavior of these dampers and isolators can be simplified into a Kelvin spring-dashpot model with constant stiffness and viscous coefficients, we can find their unknown properties by directly adding their corresponding modules into the assembled DITER equation. However, seldom this is a case, and mostly these systems show strong viscous or hysteretic nonlinear behavior. Therefore, we proposed a method in which we eliminated their effects from the rest of the structure and studied them separately.

Finally, we verified the DITER performance for 2D beams and frames by feeding it with data obtained from several numerical examples with different types of loading and supports, and also with or without protective systems. A good way to validate DITER might be considering some well-known bench mark problems such as ones introduced by IASC-ASCE; however, in this study we performed the task by using experimentally identified modal properties of a three story building to generate DITER required data, and we showed that the method was successful in locating and sizing degradations in the stories' stiffness.

Based on the numerical and experimental verifications of the method, it can be concluded that DITER can be used to detect damages in the story stiffness, mass, and damping of shear beam-type buildings with or without isolator where some load data are missing. False positive damage detection might be observable for cases with raw noise-polluted data. DITER is also applicable to slender beams and frames when data are collected with respect to the initial static equilibrium configuration or to the unreformed configuration. It is shown that the ignorance of the variations of the static deflection for data collected with respect to the initial static deflection adversely affects the DITER outcome, which may be avoided by considering the static deflections in the unknown vector. Moreover, DITER may be used as a level III damage detection method for the whole or a part of slender 2D beams and frames with, small or large dynamic displacements, proportional or non-proportional damping behavior, pinned or fixed supports, and with or without seismic protective systems to detect degradations in the element wise mass and stiffness, and variations in the inherent damping.

FUTURE WORK

The DITER equations is derived for a general structure. However, the data and observation matrices are constructed for shear beams and two dimensional beams and frames. Hence, an extension to this dissertation is to develop the matrices for:

- 3D beams and frames.
- plate and shell type structures

These might be performed through employing solid continuum elements.

Other extensions might be addressed by:

- Extending the method to be applicable in on-line damage detections
- Improving the method to be robust against noise-polluted data

REFERENCES

Adams, R., Cawley, P., Pye, C., and Stone, B. (1978). "A vibration technique for non-destructively assessing the integrity of structures." *Journal of Mechanical Engineering Science*, 20(2), 93-100.

Banks, H. T., and Inman, D. J. (1991). "On Damping Mechanisms in Beams." *Journal of Applied Mechanics*, 58(3), 716-723.

Barroso, L., and Rodriguez, R. (2004). "Damage Detection Utilizing the Damage Index Method to a Benchmark Structure." *Journal of Engineering Mechanics*, 130(2), 142-151.

Buckle, I. G., and Mayes, R. L. (1990). "Seismic isolation: history, application, and performance-a world view." *Earthquake spectra*, 6(2), 161-201.

Carden, E. P., and Fanning, P. (2004). "Vibration Based Condition Monitoring: A Review." *Structural Health Monitoring*, 3(4), 355-377.

Catbas, F., Gul, M., and Burkett, J. (2008). "Damage assessment using flexibility and flexibility-based curvature for structural health monitoring." *Smart materials and structures*, 17(1), 015024.

Cawley, P., and Adams, R. (1979). "The location of defects in structures from measurements of natural frequencies." *The Journal of Strain Analysis for Engineering Design*, 14(2), 49-57.

Chang, P. C., Flatau, A., and Liu, S. (2003). "Review paper: health monitoring of civil infrastructure." *Structural health monitoring*, 2(3), 257-267.

Cheraghi, N., Riley, M., and Taheri, F. "A novel approach for detection of damage in adhesively bonded joints in plastic pipes based on vibration method using piezoelectric sensors." *Proc., Systems, Man and Cybernetics, 2005 IEEE International Conference on*, IEEE, 3472-3478.

Cheraghi, N., and Taheri, F. (2007). "A damage index for structural health monitoring based on the empirical mode decomposition." *J. Mech. Mater. Struct*, 2(1), 43-62.

Chopra, A. K. (2007). *Dynamics of Structures: Theory and Applications to Earthquake Engineering*, Pearson/Prentice Hall.

Clough, R. W., and Penzien, J. (1975). *Dynamic of Structures*, McGRAW-HILL.

Clough, R. W., and Penzien, J. (2010). *Dynamics of Structures*, Computers and Structures.

Constantinou, M. C. , Kalpakidis, I. , Filiatrault, A. , and Ecker Lay, R. A. (2011). "LRFD-based analysis and design procedures for bridge bearings and seismic isolators. " *Rep. No. MCEER-11-0004 , Multidisciplinary Center for Earthquake Engineering Research, Buffalo, N.Y.*

Constantinou, M. C. , Whittaker, A. S. , Kalpakidis, Y. , Fenz, D. M. , and Warn, G. P. (2007). "Performance of seismic isolation hardware under service and seismic loading. " *Technical Rep. No. MCEER-07-0012, Multidisciplinary Center for Earthquake Engineering Research, Buffalo, N.Y.*

Das, A. K., Haldar, A., and Chakraborty, S. (2012). "Health Assessment of Large Two Dimensional Structures Using Limited Information: Recent Advances." *Advances in Civil Engineering*, 2012, 16.

Doebling, S. W., Farrar, C. R., and Prime, M. B. (1998). "A summary review of vibration-based damage identification methods." *Shock and vibration digest*, 30(2), 91-105.

Doebling, S. W., Farrar, C. R., Prime, M. B., and Shevitz, D. W. (1996). "Damage identification and health monitoring of structural and mechanical systems from changes in their vibration characteristics: a literature review." *Los Alamos National Lab., NM (United States).*

dos Santos, J. A., Maia, N., Soares, C. M., and Soares, C. M. (2008). "Structural damage identification: a survey." *Trends in Computational Structures Technology, Saxe-Coburg Publications, Stirlingshire, UK*, 1-24.

Esmaeel, R. A., Briand, J., and Taheri, F. (2012). "Computational simulation and experimental verification of a new vibration-based structural health monitoring approach using piezoelectric sensors." *Structural Health Monitoring*, 11(2), 237-250.

Fan, W., and Qiao, P. (2009). "A 2-D continuous wavelet transform of mode shape data for damage detection of plate structures." *International Journal of Solids and Structures*, 46(25–26), 4379-4395.

Fan, W., and Qiao, P. (2011). "Vibration-based damage identification methods: a review and comparative study." *Structural Health Monitoring*, 10(1), 83-111.

Farrar, C., and James III, G. (1997). "System identification from ambient vibration measurements on a bridge." *Journal of Sound and Vibration*, 205(1), 1-18.

Farrar, C. R., and Cone, K. M. (1994). "Vibration testing of the I-40 bridge before and after the introduction of damage." Los Alamos National Lab., NM (United States).

Farrar, C. R., and Doebling, S. W (1997). "An overview of modal-based damage identification methods." *Proc., Proceedings of DAMAS conference*, Citeseer, 269-278.

Farrar, C. R., and Jauregui, D. A. (1998). "Comparative study of damage identification algorithms applied to a bridge: I. Experiment." *Smart materials and structures*, 7(5), 704.

Farrar, C. R., and Worden, K. (2007). "An introduction to structural health monitoring." *Philosophical Transactions of the Royal Society A: Mathematical, Physical and Engineering Sciences*, 365(1851), 303-315.

Friswell, M. I., Adhikari, S., and Lei, Y. (2007). "Non-local finite element analysis of damped beams." *International Journal of Solids and Structures*, 44(22–23), 7564-7576.

Ghrib, F., Li, L., and Wilbur, P. (2012). "Damage Identification of Euler–Bernoulli Beams Using Static Responses." *Journal of Engineering Mechanics*, 138(5), 405-415.

Golub, G. H., and Loan, C. V. (1980). "An Analysis of the Total Least Squares Problem." *Cornell University*.

Haldar, A., Das, A. K., and Al-Hussein, A. (2013). "Data analysis challenges in structural health assessment using measured dynamic responses." *Advances in Adaptive Data Analysis*, 5(04).

Hemez, F. M. (2004). "Uncertainty quantification and the verification and validation of computational models." *Damage Prognosis for Aerospace, Civil and Mechanical Systems*, 201-220.

Hibbeler, R. C. (2010). *Engineering Mechanics: Dynamics*, Prentice Hall.

Hoshiya, M., and Sutoh, A. (1993). "Kalman filter-finite element method in identification." *Journal of engineering mechanics*, 119(2), 197-210.

Housner, G. W., Bergman, L. A., Caughey, T., Chassiakos, A., Claus, R., Masri, S., Skelton, R., Soong, T., Spencer, B., and Yao, J. T. (1997). "Structural control: past, present, and future." *Journal of engineering mechanics*, 123(9), 897-971.

Hua, X., Ni, Y., Chen, Z., and Ko, J. (2009). "Structural Damage Detection of Cable-Stayed Bridges Using Changes in Cable Forces and Model Updating." *Journal of Structural Engineering*, 135(9), 1093-1106.

Huang, H., Yang, J. N., and Zhou, L. (2010). "Adaptive quadratic sum-squares error with unknown inputs for damage identification of structures." *Structural Control and Health Monitoring*, 17(4), 404-426.

Huang, N. E., Shen, Z., Long, S. R., Wu, M. C., Shih, H. H., Zheng, Q., Yen, N.-C., Tung, C. C., and Liu, H. H. (1998). "The empirical mode decomposition and the Hilbert spectrum for nonlinear and non-stationary time series analysis." *Proceedings of the Royal Society of London. Series A: Mathematical, Physical and Engineering Sciences*, 454(1971), 903-995.

Hyung, S. S. (2007). "Nondestructive damage detection by simultaneous identification of stiffness and damping." 3296405 Ph.D., Texas A&M University, Ann Arbor.

Ismail, M., Ikhouane, F., and Rodellar, J. (2009). "The Hysteresis Bouc-Wen Model, a Survey." *Arch Computat Methods Eng*, 16(2), 161-188.

Jauregui, C. R. F. a. D. A. (1998). "Comparative study of damage identification algorithms applied to a bridge: II. Numerical study" *Smart Mater. Struct.* , 7

Ji, X., Fenves, G., Kajiwara, K., and Nakashima, M. (2011). "Seismic Damage Detection of a Full-Scale Shaking Table Test Structure." *Journal of Structural Engineering*, 137(1), 14-21.

Karalar, M., Padgett, J. E., and Dicleli, M. (2012). "Parametric analysis of optimum isolator properties for bridges susceptible to near-fault ground motions." *Engineering Structures*, 40(0), 276-287.

Katkhuda, H., Martinez, R., and Haldar, A. (2005). "Health assessment at local level with unknown input excitation." *Journal of Structural Engineering*, 131(6), 956-965.

Katkhuda, H. N., Dwairi, H. M., and Shatarat, N. (2010). "System identification of steel framed structures with semi-rigid connections." *Structural engineering & mechanics*, 34(3), 351.

Kim, J. T., and Stubbs, N. (2003). "CRACK DETECTION IN BEAM-TYPE STRUCTURES USING FREQUENCY DATA." *Journal of Sound and Vibration*, 259(1), 145-160.

Lee, L. S., Karbhari, V. M., and Sikorsky, C. S. (2004). "Investigation of integrity and effectiveness of RC bridge deck rehabilitated with CFRP composites." *La Jolla, Calif: Dept. of Structural Engineering, University of California, San Diego.*

Li, Y. Y. (2010). "Hypersensitivity of strain-based indicators for structural damage identification: A review." *Mechanical Systems and Signal Processing*, 24(3), 653-664.

Liew, K., and Wang, Q. (1998). "Application of wavelet theory for crack identification in structures." *Journal of Engineering Mechanics*, 124(2), 152-157.

Ling, X., and Haldar, A. (2004). "Element Level System Identification with Unknown Input with Rayleigh Damping." *Journal of Engineering Mechanics*, 130(8), 877-885.

Loutridis, S., Douka, E., Hadjileontiadis, L. J., and Trochidis, A. (2005). "A two-dimensional wavelet transform for detection of cracks in plates." *Engineering Structures*, 27(9), 1327-1338.

Lu, X., and Zhou, Q. (2002). "Dynamic analysis method of a combined energy dissipation system and its experimental verification." *Earthquake Engineering & Structural Dynamics*, 31(6), 1251-1265.

Ma, F., Zhang, H., Bockstedte, A., Foliente, G. C., and Paevere, P. (2004). "Parameter analysis of the differential model of hysteresis." *Journal of Applied Mechanics*, 71(3), 342-349.

Ma, T., Yang, H., and Chang, C. (2005). "Structural Damage Diagnosis and Assessment under Seismic Excitations." *Journal of Engineering Mechanics*, 131(10), 1036-1045.

Messina, A., Williams, E., and Contursi, T. (1998). "Structural damage detection by a sensitivity and statistical-based method." *Journal of Sound and Vibration*, 216(5), 791-808.

Moaveni, B., Stavridis, A., Lombaert, G., Conte, J., and Shing, P. (2013). "Finite-Element Model Updating for Assessment of Progressive Damage in a 3-Story Infilled RC Frame." *Journal of Structural Engineering*, 139(10), 1665-1674.

Mottershead, J., and Friswell, M. (1993). "Model updating in structural dynamics: a survey." *Journal of sound and vibration*, 167(2), 347-375.

Mukhopadhyay, S., Luş, H., and Betti, R. (2014). "Modal parameter based structural identification using input–output data: Minimal instrumentation and global identifiability issues." *Mechanical Systems and Signal Processing, 45(2), 283–301*.

Narkis, Y. (1994). "Identification of crack location in vibrating simply supported beams." *Journal of Sound and Vibration*, 172(4), 549-558.

Pandey, A., and Biswas, M. (1994). "Damage detection in structures using changes in flexibility." *Journal of sound and vibration*, 169(1), 3-17.

Pandey, A., Biswas, M., and Samman, M. (1991). "Damage detection from changes in curvature mode shapes." *Journal of sound and vibration*, 145(2), 321-332.

Ratcliffe, C. P. (1997). "Damage detection using a modified Laplacian operator on mode shape data." *Journal of Sound and Vibration*, 204(3), 505-517.

Reddy, J. N. (2002). *Energy Principles and Variational Methods in Applied Mechanics*, John Wiley.

Reddy, J. N. (2004). *An introduction to nonlinear finite element analysis*, Oxford University Press.

Reddy, J. N. (2005). *An Introduction to the Finite Element Method*, McGraw-Hill Education.

Rytter, A. (1993). "Vibrational based inspection of civil engineering structures." PhD thesis, Dept. of Build. Technol. and Struct. Engrg., Aalborg Univ., Denmark.

Salawu, O. S. (1997). "Detection of structural damage through changes in frequency: a review." *Engineering Structures*, 19(9), 718-723.

Shan, J., Yang, H., Shi, W., Bridges, D., and Hansma, P. (2013). "Structural Damage Diagnosis Using Interstory Drift–Based Acceleration Feedback with Test Validation." *Journal of Engineering Mechanics*, 139(9), 1185-1196.

Slastan, J., and Pietrzko, S. (1993). "Changes of RC-beam modal parameters due to cracks." *Proc., 11th Int. Modal Analysis Conf. , Orlando, 70–76.*

Sorrentino, S., Marchesiello, S., and Piombo, B. A. D. (2003). "A new analytical technique for vibration analysis of non-proportionally damped beams." *Journal of Sound and Vibration*, 265(4), 765-782.

Srinivas, V., Ramanjaneyulu, K., and Jeyasehar, C. A. (2011). "Multi-stage approach for structural damage identification using modal strain energy and evolutionary optimization techniques." *Structural Health Monitoring*, 10(2), 219-230.

Stubbs, N., Broome, T. H., and Osegueda, R. (1990). "Nondestructive construction error detection in large space structures." *AIAA Journal*, 28(1), 146-152.

Stubbs, N., and Kim, J.-T. (1996). "Damage localization in structures without baseline modal parameters." *AIAA Journal*, 34(8), 1644-1649.

Stubbs, N., Kim, J.-T., and Farrar, C. (1995). "Field verification of a nondestructive damage localization and severity estimation algorithm." *Proc., 13th IMAC, Soc. for Experimental Mech., Inc.*, 1, 210–218

Stubbs, N., Kim, J., and Topole, K. (1993). "An efficient and robust algorithm for damage localization in offshore platforms." *Proc., 10th ASCE Structures Conf.*, 543–546.

Stubbs, N., and Osegueda, R. (1990). "Global non-destructive damage evaluation in solids." *International Journal of Analytical and Experimental Modal Analysis*, 5, 67-79.

Stubbs, N., Park, S., Sikorsky, C., and Choi, S. (2000). "A global non-destructive damage assessment methodology for civil engineering structures." *International Journal of Systems Science*, 31(11), 1361-1373.

Symans, M., Charney, F., Whittaker, A., Constantinou, M., Kircher, C., Johnson, M., and McNamara, R. (2008). "Energy Dissipation Systems for Seismic Applications: Current Practice and Recent Developments." *Journal of Structural Engineering*, 134(1), 3-21.

Tang, L., Luo, X., Liu, Z., Liu, Y., He, T., and Fang, D. (2012). "Octonion structural response vector and potential structural damage identification method." *International Journal of Damage Mechanics*.

Topole, K. G. (1993). *Nondestructive Damage Evaluation in Nonlinear Structures*, Texas A&M University. PhD thesis, Dept. of Civil Engineering, Texas A&M University, USA.

Wang, D., and Haldar, A. (1994). "Element-level system identification with unknown input." *Journal of Engineering Mechanics*, 120(1), 159-176.

Wang, D., and Haldar, A. (1994). "Element-Level System Identification with Unknown Input." *Journal of Engineering Mechanics*, 120(1), 159-176.

Wang, D., and Haldar, A. (1997). "System identification with limited observations and without input." *Journal of Engineering Mechanics*, 123(5), 504-511.

Wang, J., and Qiao, P. (2007). "Improved Damage Detection for Beam-type Structures using a Uniform Load Surface." *Structural Health Monitoring*, 6(2), 99-110.

Wen, Y.-K. (1976). "Method for random vibration of hysteretic systems." *Journal of the engineering mechanics division*, 102(2), 249-263.

Worden, K., and Dulieu-Barton, J. (2004). "An overview of intelligent fault detection in systems and structures." *Structural Health Monitoring*, 3(1), 85-98.

Xu, B., He, J., Rovekamp, R., and Dyke, S. J. (2012). "Structural parameters and dynamic loading identification from incomplete measurements: Approach and validation." *Mechanical Systems and Signal Processing*, 28(0), 244-257.

Xu, B., He, J., Rovekamp, R., and Dyke, S. J. (2012). "Structural parameters and dynamic loading identification from incomplete measurements: Approach and validation." *Mechanical Systems and Signal Processing*, 28, 244-257.

Yan, Y., Cheng, L., Wu, Z., and Yam, L. (2007). "Development in vibration-based structural damage detection technique." *Mechanical Systems and Signal Processing*, 21(5), 2198-2211.

Yang, J., Huang, H., and Pan, S. (2009). "Adaptive Quadratic Sum-Squares Error for Structural Damage Identification." *Journal of Engineering Mechanics*, 135(2), 67-77.

Yang, J., Lei, Y., Lin, S., and Huang, N. (2004). "Hilbert-Huang Based Approach for Structural Damage Detection." *Journal of Engineering Mechanics*, 130(1), 85-95.

Yang, J., Xia, Y., and Loh, C. (2014). "Damage Detection of Hysteretic Structures with a Pinching Effect." *Journal of Engineering Mechanics*, 140(3), 462-472.

Yang, J., Xia, Y., and Loh, C. (2014). "Damage Identification of Bolt Connections in a Steel Frame." *Journal of Structural Engineering*, 140(3), 04013064.

Yang, J. N., Huang, H., and Lin, S. (2006). "Sequential non-linear least-square estimation for damage identification of structures." *International Journal of Non-linear mechanics*, 41(1), 124-140.

Yin, Q., Zhou, L., Mu, T., and Yang, J. N. (2012). "751. System identification of rubber-bearing isolators based on experimental tests." *Journal of Vibroengineering*, 14(1).

Yin, Q., Zhou, L., and Wang, X. (2010). "Parameter identification of hysteretic model of rubber-bearing based on sequential nonlinear least-square estimation." *Earthquake Engineering and Engineering Vibration*, 9(3), 375-383.

Young Noh, H., Krishnan Nair, K., Lignos, D., and Kiremidjian, A. (2011). "Use of Wavelet-Based Damage-Sensitive Features for Structural Damage Diagnosis Using Strong Motion Data." *Journal of Structural Engineering*, 137(10), 1215-1228.

Zhang, H., Foliente, G. C., Yang, Y., and Ma, F. (2002). "Parameter identification of inelastic structures under dynamic loads." *Earthquake Engineering & Structural Dynamics*, 31(5), 1113-1130.

Zhang, Z., & Aktan, A. E. (1995). "The damage indices for the constructed facilities". *Proc., 13th Int. Modal Analysis Conf.*, 1520–152

APPENDIX A
SUPPORTIVE EQUATIONS OF CHAPTER IV

A-1: DERIVATION OF EQUATIONS (4.48) AND (4.50)

The weak form of equations (4.46) is developed using a weight function v_1 as follows:

$$0=\int_l v_1\left(\frac{\partial}{\partial t}\left(\rho A\frac{\partial}{\partial t}u_0\right)-\frac{\partial}{\partial x}\left(EA\left(\frac{\partial u_0}{\partial x}+\frac{1}{2}\left(\frac{\partial w_0}{\partial x}\right)^2\right)-c_sA\left(\frac{\partial^2 u_0}{\partial t\partial x}+\frac{\partial^2 w_0}{\partial t\partial x}\right)\right)-f\right)dx$$

Taking part by part integration of the above equation:

$$0=\int_l\left(v_1\frac{\partial}{\partial t}\left(\rho A\frac{\partial}{\partial t}u_0\right)+\left(\frac{\partial v_1}{\partial x}EA\left(\frac{\partial u_0}{\partial x}+\frac{1}{2}\left(\frac{\partial w_0}{\partial x}\right)^2\right)+\frac{\partial v_1}{\partial x}c_sA\left(\frac{\partial^2 u_0}{\partial t\partial x}+\frac{\partial^2 w_0}{\partial t\partial x}\right)\right)-v_1f\right)dx-$$

$$\underbrace{\left(-v_1EA\left(\frac{\partial u_0}{\partial x}+\frac{1}{2}\left(\frac{\partial w_0}{\partial x}\right)^2\right)-v_1c_sA\left(\frac{\partial^2 u_0}{\partial t\partial x}+\frac{\partial^2 w_0}{\partial t\partial x}\right)\right)\Bigg|_{x_a}^{x_b}}_{\text{Contributing to the internal force=Q}^1}$$

Consider the axial and transverse displacements at the element domain to be approximated by the nodal time-instant values and the interpolation functions as follows:

$$\begin{aligned}u_0(x,t)&=\sum_j u_{0j}^e(t)\varphi_j(x)=\left(\mathbf{u}_0^e\right)^T\boldsymbol{\varphi}\\ w_0(x,t)&=\sum_J w_{0j}^e(t)\psi_J(x)=\left(\boldsymbol{\omega}_o^e\right)^T\boldsymbol{\psi}\end{aligned}\qquad(1)$$

where φ is a Lagrange interpolation function of order j, and ψ is a cubic Hermite interpolation function. u_{0j}^e and w_{0j}^e are the nodal displacements corresponding to the employed interpolation functions. Then, the following set of equations can be determined by substituting the weight function v_1 with φ_i and approximating u_0 and w_0 by equation (1).

$$\mathbf{M}^{11}\ddot{\mathbf{u}}_0^e+\mathbf{C}^{11}\dot{\mathbf{u}}_0^e+\mathbf{C}^{12}\dot{\boldsymbol{\omega}}_o^e+\mathbf{K}^{11}\mathbf{u}_0^e+\mathbf{K}^{12}\boldsymbol{\omega}_o^e=\mathbf{f}^1+\mathbf{Q}^1$$

where

$$M_{ij}^{11} = \int_l \rho A \varphi_i \varphi_j dx$$

$$C_{ij}^{11} = \int_l \frac{\partial \varphi_i}{\partial x} \frac{\partial \varphi_j}{\partial x} c_s A dx$$

$$C_{iJ}^{12} = \int_l \frac{\partial \varphi_i}{\partial x} \frac{\partial \psi_J}{\partial x} c_s A dx$$

$$K_{ij}^{11} = \int_l \frac{\partial \varphi_i}{\partial x} \frac{\partial \varphi_j}{\partial x} EA dx$$

$$K_{iJ}^{12} = \int_l \frac{1}{2} \frac{\partial \varphi_i}{\partial x} \frac{\partial \psi_J}{\partial x} \sum_{J=1:m} \frac{\partial \psi_J}{\partial x} w_{0J}^e EA dx$$

Similarly, the weak form formulation of equation (4.47) can be determined using a weight function v_2 as:

$$0 = \int_l v_2 \left(\begin{array}{l} +\frac{\partial}{\partial t}\left(\rho A \frac{\partial w_0}{\partial t} \right) - \frac{\partial^2}{\partial t \partial x}\left(\rho I \frac{\partial}{\partial t} \frac{\partial w_0}{\partial x} \right) + \frac{\partial^2}{\partial x^2}\left(EI \frac{\partial^2 w_0}{\partial x^2} + c_s I \frac{\partial^3 w_0}{\partial t \partial x^2} \right) \ldots \\ +c \frac{\partial w_0}{\partial t} - q \underbrace{- \frac{\partial}{\partial x}\left(\frac{\partial w_0}{\partial x} EA \left(\frac{\partial u_0}{\partial x} + \frac{1}{2}\left(\frac{\partial w_0}{\partial x} \right)^2 \right) \right) + \frac{\partial}{\partial x}\left(\frac{\partial w_0}{\partial x} c_s A \left(\frac{\partial^2 u_0}{\partial t \partial x} + \frac{\partial^2 w_0}{\partial t \partial x} \right) \right)}_{\text{Compared to the small transverse displacement case, all are identical but only these terms}} \end{array} \right) dx$$

The identical set of equations derived for the case of small transverse displacements are obtained here as well except those additional terms that are labeled in the above equation. An investigation on these newly added terms reveals their similarity to the ones that have already been developed on the axial governing equation. Thus, the weak form of the newly added terms must be found and added to the previous set of equations as follows:

$$\int_l -v_2 \frac{\partial}{\partial x}\left(\frac{\partial w_0}{\partial x} EA\left(\frac{\partial u_0}{\partial x}+\frac{1}{2}\left(\frac{\partial w_0}{\partial x}\right)^2\right)\right)dx = \int_l \frac{\partial v_2}{\partial x}\frac{\partial w_0}{\partial x} EA\left(\frac{\partial u_0}{\partial x}+\frac{1}{2}\left(\frac{\partial w_0}{\partial x}\right)^2\right)dx -$$

$$\underbrace{\left(v_2 \frac{\partial w_0}{\partial x} EA\left(\frac{\partial u_0}{\partial x}+\frac{1}{2}\left(\frac{\partial w_0}{\partial x}\right)^2\right)\right)_{x_a}^{x_b}}_{\text{Contribute to the internal forces}}$$

$$\int_l \frac{\partial v_2}{\partial x}\frac{\partial w_0}{\partial x} EA\left(\frac{\partial u_0}{\partial x}+\frac{1}{2}\left(\frac{\partial w_0}{\partial x}\right)^2\right)dx = \int_l EA\frac{\partial v_2}{\partial x}\frac{\partial w_0}{\partial x}\frac{\partial u_0}{\partial x} + \int_l \frac{1}{2} EA\frac{\partial v_2}{\partial x}\frac{\partial w_0}{\partial x}\left(\frac{\partial w_0}{\partial x}\right)^2 dx$$

And

$$\int_l -v_2 \frac{\partial}{\partial x}\left(\frac{\partial w_0}{\partial x} c_s A\left(\frac{\partial^2 u_0}{\partial t\partial x}+\frac{\partial^2 w_0}{\partial t\partial x}\right)\right)dx = \int_l \frac{\partial v_2}{\partial x}\frac{\partial w_0}{\partial x} c_s A\left(\frac{\partial^2 u_0}{\partial t\partial x}+\frac{\partial^2 w_0}{\partial t\partial x}\right)dx -$$

$$\underbrace{\left(v_2 \frac{\partial w_0}{\partial x} c_s A\left(\frac{\partial^2 u_0}{\partial t\partial x}+\frac{\partial^2 w_0}{\partial t\partial x}\right)\right)_{x_a}^{x_b}}_{\text{Contribute to the internal forces}}$$

$$\int_l \frac{\partial v_2}{\partial x}\frac{\partial w_0}{\partial x} c_s A\left(\frac{\partial^2 u_0}{\partial t\partial x}+\frac{\partial^2 w_0}{\partial t\partial x}\right)dx = \int_l c_s A\frac{\partial v_2}{\partial x}\frac{\partial w_0}{\partial x}\frac{\partial \dot{u}_0}{\partial x} + \int_l c_s A\frac{\partial v_2}{\partial x}\frac{\partial w_0}{\partial x}\frac{\partial \dot{w}_0}{\partial x}dx$$

Approximating $u_0(x,t)$ and $w_0(x,t)$ by equation (1) and substituting v_2 with ψ_I, following set of equations are acquired:

$$\mathbf{M}^{22}\ddot{\boldsymbol{\omega}}_o^e + \mathbf{C}^{22}\dot{\boldsymbol{\omega}}_0^e + \mathbf{K}^{22}\boldsymbol{\omega}_o^e + \mathbf{K}^{21}\mathbf{u}_0^e + \mathbf{C}^{21}\dot{\mathbf{u}}_o^e = \mathbf{q}^2 + \mathbf{Q}^2$$

where

$$M_{IJ}^{22} = \int_l \rho A\psi_I\psi_J dx + \int_l \frac{\partial \psi_I}{\partial x}\frac{\partial \psi_J}{\partial x}\rho I dx$$

$$K_{IJ}^{22} = \int_l \left(\frac{\partial^2 \psi_I}{\partial x^2}\frac{\partial^2 \psi_J}{\partial x^2} EI + \frac{1}{2} EA\frac{\partial \psi_I}{\partial x}\frac{\partial \psi_J}{\partial x}\left(\sum_{J=1:s}\frac{\partial \psi_j}{\partial x} w_{0J}^e\right)^2 dx\right)$$

$$K_{Ij}^{21} = \int_l EA\frac{\partial \psi_I}{\partial x}\frac{\partial \varphi_j}{\partial x}\sum_{J=1:s}\frac{\partial \psi_J}{\partial x} w_{0J}^e dx$$

$$C_{Ij}^{21} = \int_l c_s A\frac{\partial \psi_I}{\partial x}\frac{\partial \varphi_j}{\partial x}\sum_{J=1:s}\frac{\partial \psi_J}{\partial x} w_{0J}^e dx$$

$$C_{IJ}^{22} = \int_l \left(\frac{\partial^2 \psi_I}{\partial x^2}\frac{\partial^2 \psi_J}{\partial x^2} c_s I + c_s A\frac{\partial \psi_I}{\partial x}\frac{\partial \psi_J}{\partial x}\left(\sum_{J=1:s}\frac{\partial \psi_J}{\partial x} w_{0J}^e\right) + c\psi_I\psi_J\right)dx$$

A-2: INTERPOLATION FUNCTIONS

In this appendix the Hermite and Lagrange interpolation functions used in Chapter IV are presented. In the case of employing a Cartesian coordinate system that follows the right hand rule, as shown in the following figure, the Hermite interpolation functions can be expressed as

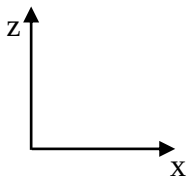

Figure A2-1: Cartesian coordinate system shown in xz plane

$$\begin{cases} \psi_1 = 1-3\xi^2+2\xi^3 \\ \psi_3 = 3\xi^2-2\xi^3 \\ \psi_2 = -l\xi\left(\xi^2-2\xi+1\right) \\ \psi_4 = -l\xi^2\left(\xi-1\right) \end{cases}$$

And a linear Lagrange interpolation functions is expressed as:

$$\begin{cases} \varphi_1 = 1-\xi \\ \varphi_2 = \xi \end{cases}$$

where $\xi = \dfrac{x-x_e}{l}$ and x_e is the start location of the element.

A-3: DERIVATION OF EQUATION (4.32)

The work rate at location x of the element *e* can be written as

$$\frac{\partial W(x,t)}{\partial t}dx_1 = q(x,t)dx_1.\dot{w}(x,t) + f(x,t)dx_1.\dot{u}(x,t)$$

where x_1 stands for the axial axis of the local coordinates of the element, and loads q and f are as shown in Figure IV-1.

$$\dot{W}^e(t) = \int_0^l \left(q(x,t)\dot{w}(x,t) + f(x,t)\dot{u}(x,t) \right) dx_1 \rightarrow$$

$$\dot{W}^e(t) = \int_0^l \left(q(x,t) \sum_{J=1:s} \dot{w}^e_{0j}(t)\psi_J(x) + f(x,t) \sum_{j=1:r} \dot{u}^e_{0j}(t)\varphi_j(x) \right) dx_1 \rightarrow$$

$$\dot{W}^e(t) = \sum_{J=1:s} \dot{w}^e_{0J}(t) \int_0^l q(x,t)\psi_J(x)\, dx_1 + \sum_{j=1:r} \dot{u}^e_{0j}(t) \int_0^l f(x,t)\varphi_j(x)\, dx_1 \rightarrow$$

$$\dot{W}^e(t) = \sum_{J=1:s} \dot{w}^e_{0J}(t) q^2_j + \sum_{j=1:r} \dot{u}^e_{0j}(t)\, f^1_j \rightarrow$$

$$\dot{W}^e(t) = \left(\boldsymbol{\omega}^e_o\right)^T \mathbf{q}^2 + \left(\mathbf{u}^e_0\right)^T \mathbf{f}^1$$

APPENDIX B

SUPPORTIVE EQUATIONS OF THE SIMPLE BEAM EXPERIMENT

B-1: DERIVATION OF MODE SHAPES AND NATURAL FREQUENCIES OF A SIMPLE BEAM

The reference of this derivation can be found in (Clough and Penzien 2010). Assume an EB beam of length L with constant EI and density. Consider m to be the mass per length of the beam. The governing equation of the beam free response can be written as:

$$\frac{\partial^2}{\partial x^2}\left[EI\,\frac{\partial^2 u(x,t)}{\partial x^2} \right] + m\frac{\partial^2 u(x,t)}{\partial t^2} = 0 \tag{1}$$

where the response may be approximated by

$$u(x,t) = \phi(x)Y(t) \tag{2}$$

Substituting equation (2) in the governing equation and dividing the result by ϕ yields

$$EI\,\phi''''/\phi + m\phi\ddot{Y} = 0 \tag{3}$$

where the first term is a function of location only, and the second term is a function of time. To obtain a general solution, the two terms must be equal to a constant. Thus, the above equation turns into

$$\begin{cases} \ddot{Y} + \omega^2 Y = 0 \\ \phi'''' - \alpha^4 \phi = 0 \end{cases} \tag{4}$$

where $\alpha^4 = \dfrac{\omega^2 m}{EI}$.

Considering $\phi = Ge^{sx}$ and substituting it in the second equation of (4) we can find the solution of ϕ as:

$$\phi = A_1 \cos(ax) + A_2 \sin(ax) + A_3 \cosh(ax) + A_4 \sinh(ax) \tag{5}$$

where A_i are real constants.

Boundary conditions of a simple beam imply

$$\begin{aligned} &\phi(0) = \phi(L) = 0 \\ &\phi''(0) = \phi''(L) = 0 \end{aligned} \tag{6}$$

which yield

$$\begin{aligned} &A_1 = A_3 = A_4 = 0 \rightarrow \\ &\phi = A_2 \sin(ax) \end{aligned} \tag{7}$$

Boundary condition $\phi(L) = 0$ demands $\sin(aL) = 0$ for any $A_2 \neq 0$ and therefore

$$a = n\pi / L \qquad n = 0, 1, 2, \cdots \tag{8}$$

and

$$\begin{aligned} &\omega_n = n^2 \pi^2 \sqrt{\frac{EI}{mL^4}} \\ &\phi_n = A_2 \sin\left(\frac{n\pi x}{2L}\right) \end{aligned} \tag{9}$$

Constant A_2 can be determined from the initial values (displacement and velocity at t=0). For a beam with zero initial values, A_2 can be any arbitrary non zero number for which 1 is a convenient value.

B-2: DETERMINATION OF RAYLEIGH DAMPING CONSTANTS

Here the determination of the mass and stiffness proportionality constants, β and α, of the simple beam experiment are presented.

The objective is to have

$$\begin{aligned} &C_m = \xi_m c_{c_m} \\ &C_n = \xi_n c_{c_n} \end{aligned} \tag{10}$$

where C_m and C_n are the mth and nth modal damping coefficients. c_c is the critical damping and is defined by

$$c_c = 2m_n\omega_n \tag{11}$$

Therefore,

$$\xi_n = \xi_m = \xi = 0.05 \tag{12}$$

Writing equation (5.7) as (Clough and Penzien 2010)

$$\begin{bmatrix} \xi_m \\ \xi_n \end{bmatrix} = \frac{1}{2}\begin{bmatrix} \omega_m^{-1} & \omega_m \\ \omega_n^{-1} & \omega_n \end{bmatrix}\begin{bmatrix} \beta \\ \alpha \end{bmatrix} \tag{13}$$

the damping coefficients are acquired as

$$\begin{aligned} \beta &= 2\frac{\omega_m\omega_n}{\omega_n^{\,2} - \omega_m^{\,2}}\left(\omega_n\xi_1 - \omega_m\xi_2\right) = \frac{2\xi\omega_m\omega_n}{\omega_n + \omega_m} \\ \alpha &= 2\frac{\omega_m\omega_2}{\omega_n^{\,2} - \omega_m^{\,2}}\left(-\omega_n^{\,-1}\xi_1 + \omega_m^{\,-1}\xi_2\right) = \frac{2\xi}{\omega_n + \omega_m} \end{aligned} \tag{14}$$